Valentino MM, 2017, Mineral chemistry of fracture coatings in Athabasca Group sandstone as records of element of dispersion, MSc Thesis, 205 p.

NSERC-CMIC Mineral Exploration Footprints Project Contribution 162.

MINERAL CHEMISTRY OF FRACTURE COATINGS IN ATHABASCA GROUP SANDSTONES AS RECORDS OF ELEMENTAL DISPERSION

by

Marissa M. Valentino

A thesis submitted to the Department of Geological Sciences and Geological Engineering

in conformity with the requirements for

the Degree of Master of Science

Queen's University

Kingston, Ontario, Canada

October, 2017

Chapter 1

General Introduction

1.1 Overview

Unconformity-related uranium (U) deposits are hosted in Proterozoic basins, the largest being in the Athabasca Basin, Canada and in the Kombolgie Basin in Northern Territory, Australia (Cuney and Kyser, 2014). Unconformity-related deposits can form as uraninite pods, veins, and massive semi-replacement bodies when oxidized fluids interact with a reduced fluid (Cuney and Kyser, 2014). The deposits are structurally hosted by faults near the unconformity between the Athabasca Group sandstone and underlying Paleoproterozoic and Archean metamorphic basement rocks, and are affected significantly by post-depositional fluids (IAEA, 2009). Fluids associated with these deposits produce alteration zones in the overlying sandstone and in basement rocks surrounding the deposit (Wilson and Kyser, 1987; Kotzer and Kyser, 1995; Fayek and Kyser, 1997), and these alteration zones record the movement of elements prior to, during, and after the formation of the ore body.

The characterization of dispersion around a deposit is commonly used as a geochemical/mineralogical exploration technique, as it is associated with deposit formation, later alteration and fluid-deposit interaction (McQueen, 2005, Figure 1.1). There are two types of dispersion: primary dispersion and secondary dispersion.

Primary dispersion occurs during hydrothermal alteration associated with the emplacement of the deposit wherein elements from the mineralizing system are dispersed into the surrounding rocks beneath the weathering front. This creates a dispersion halo of elements and alteration around the deposit and along surrounding permeable fractures (McQueen, 2005, Figure 1.1). Primary dispersion enhances the target-size of the ore body, and patterns in element

associations are reflected by proximal and distal dispersion (McQueen, 2005).

Secondary dispersion occurs when later fluids, such as low-temperature meteoric water, come into contact with the ore body, allowing the transfer of dissolved ions away from the deposit (Cameron *et al*., 2004; McQueen, 2005; Figure 1.1). Elements in the ore zone and surrounding alteration halo are variably mobilized by hydrostatic, thermal, or electrochemical convection or by microbial interactions. Their transfer is also facilitated by the permeability of open fractures (Cameron *et al*., 2004).

When primary dispersion occurs from ore-forming fluids, fractures act as preferential conduits for the flow of mineralizing fluids and should have mineral assemblages and chemistry that reflect the primary ore-forming fluids and associated alteration of the wall rock. Similarly, if the ore has been affected by later fluids that result in dissolution of ore components during secondary dispersion, the fracture coatings should reflect the geochemistry of elements that are preferentially mobilized from the mineralization, so-called pathfinder elements. Lead is a common pathfinder element as it is produced by the decay of U after the deposit is formed and is easily mobilized. Fracture coatings composed of Fe and Al oxy-hydroxides can form suspended colloidal particles with negative charges that are capable of attracting metal cations, including Pb. Fixation of cations and mobile elements on fracture coating surfaces, such as oxy-hydroxides or clay minerals, restricts their movement (Cameron *et al*., 2004).

The objective of this study is to determine whether the mineralogy and geochemistry of fracture coatings and their wall rocks can be used to detect uranium mineralization at depth (>500 m) in the Athabasca Basin. Using samples from the unconformity-related McArthur River U deposit and Stewardson Lake U project, the study also investigates whether or not components within fractures (from depth to surface) are related to element dispersion. Comparing the mineralogy and geochemistry of fractures from a world-class U deposit (McArthur River) to a U

exploration project (Stewardson Lake) reveals which elements act as pathfinders, as well as what processes are involved in element migration, and whether fracture mineral chemistry can be used as an exploration tool for U deposits. This study is a part of the larger Canadian Mining Innovation Council (CMIC) Exploration Footprints project designed to generate more effective approaches to integrate and visualize multi-parameter data sets and thus improve exploration within the footprint of unconformity-related uranium deposits, as well as orogenic gold and porphyry copper ore systems (e.g. Lesher *et al*., 2017).

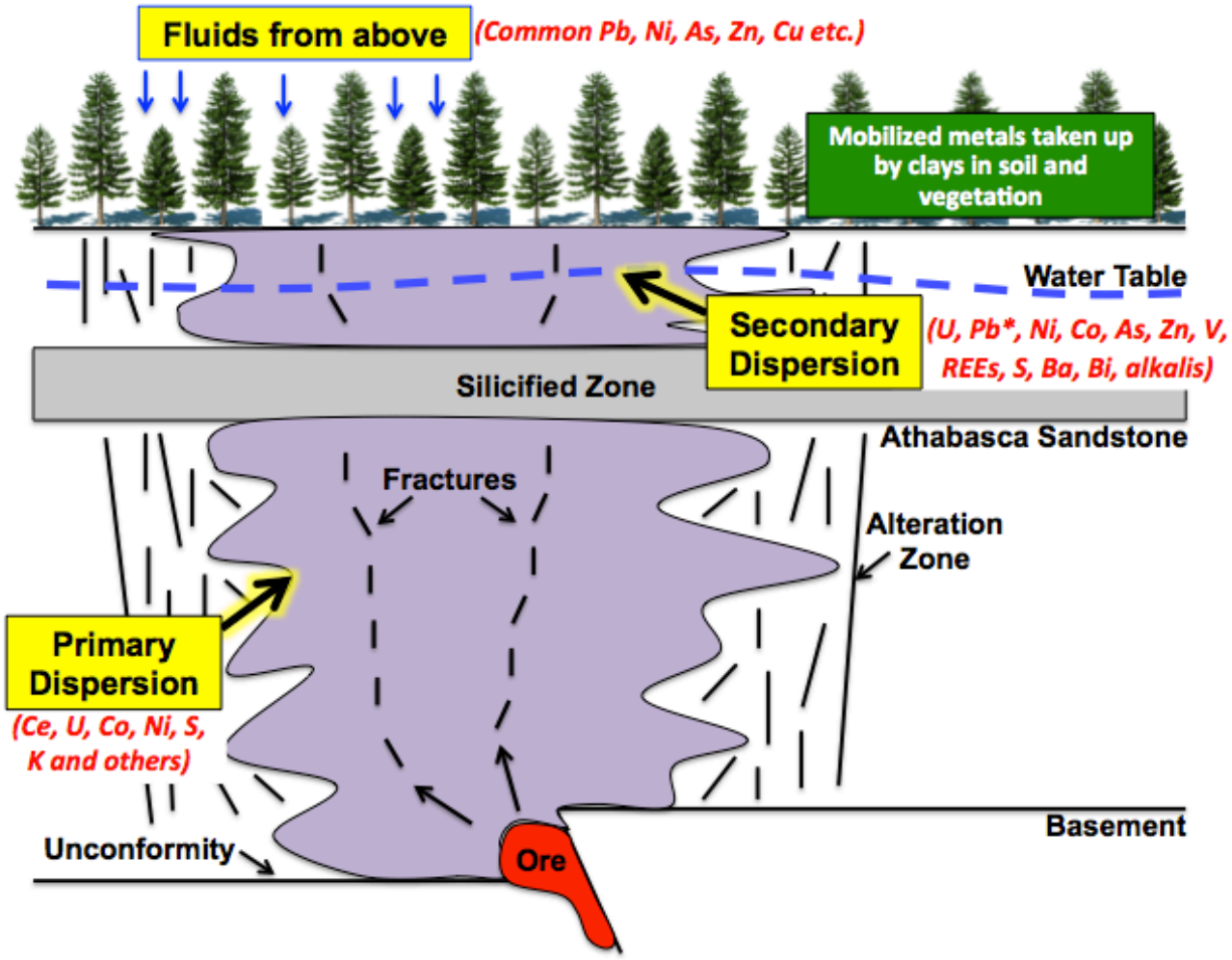

Figure 1.1: Historical rendering of a typical dispersion halo for an unconformity-related U deposit, highlighting primary and secondary dispersion and elements associated with each dispersion event. Figure modified from Cameron *et al.* (2004) and Voinot *et al.* (2015).

1.2 Geological setting of the Athabasca Basin

1.2.1 Basement subdivisions

The Athabasca Basin is an intracratonic basin located in northern Saskatchewan and Alberta (Figure 1.2), which covers an area greater than 85,000 km^2 (Ramaekers, 1990). The basin overlies Archean and Paleoproterozoic basement composed of metamorphosed igneous and sedimentary rocks of the western Churchill Province (Figure 1.2), which have been affected by

three Paleoproterozoic orogenic events: the *ca*. 2.02-1.91 Ga Thelon Orogen, between the Slave and Rae Provinces, the *ca*. 1.92-1.85 Ga Snowbird Orogen, between the Rae and Hearne Provinces, and the *ca*. 1.91-1.81 Ga Trans-Hudson Orogen, between the Hearne and Wyoming provinces and the Superior Province (Hoffman, 1988). The western Churchill Province is located between the remains of two orogenic belts: the Taltson magmatic zone to Thelon tectonic zone (*ca*. 1.9 Ga) and the Trans-Hudson Orogen (*ca*. 1.8 Ga) (Hoffman, 1988). In Figure 1.2, the Rae and Hearne provinces divide the western Churchill province. The contact between the Rae and Hearne provinces is the Snowbird Tectonic Zone (Hoffman, 1988), comprised of the Virgin River shear zones at the south of the Athabasca Basin, and the Black Lake shear zone to the north (Figure 1.2).

There are three domains within the Hearne Province that unconformably underlie the basin, from east to west: the Wollaston domain, the Mudjatik domain and the Virgin River domain (Hoffman, 1988). The three domains are primarily composed of Archean granitoids, which are overlain by Paleoproterozoic supracrustal sequences, all of which have been metamorphosed and multiply deformed; boundaries between the domains are defined by variations in lithology, structural, and metamorphic grade (Lewry and Sibbald, 1980).

1.2.2 Athabasca Basin

The Athabasca Basin is composed of clastic sediments, which likely originated from mountain ranges associated with the Trans-Hudson Orogen (Kyser *et al*., 2000). Basin formation has been attributed to the uplift of the Trans-Hudson foundation at *ca*. 1750 Ma (Kyser *et al*., 2000). This is evidenced by the basal sediments in the basin which were sourced from the east after rapid uplift during the Trans-Hudson Orogen, which occurred at *ca.* 1750 Ma (Kyser *et al*., 2000).

The Athabasca Group (Figure 1.2) consists of flat-lying, quartz-rich sandstone and conglomerate, which was deposited in major river systems and near-shore to shallow-shelf environments (Ramaekers, 1990; Ramaekers *et al*., 2007). Sedimentary basin fill is 1-2 km deep, although temperature estimates from fluid inclusions suggest that these sequences reached depths of up to 5 km during peak diagenesis (Pagel *et al*., 1980). The units are cut by reactivated Hudsonian-age faults that have been periodically active to the present day (Hoeve and Quirt, 1984; Kyser *et al*., 2000). The northwest-trending 1267 Ma Mackenzie dike swarm (LeCheminant and Heaman, 1989) also cuts the sedimentary sequences of the Athabasca Basin and underlying basement rocks. These dikes and the reactivated post-Athabasca structures act as pathways for fluid movement (Kyser *et al*., 2000).

Four unconformity-bound stratigraphic sequences divide the Athabasca Group (Figure 1.2; Yeo *et al*., 2002; Ramaekers and Catuneanu, 2004; Ramaekers *et al*., 2007). In ascending order, these are: (1) Fair Point; (2) Smart and Manitou Falls Formations; (3) Lazenby Lake and Wolverine Point Formations; and (4) Locker Lake, Otherside, Douglas, and Carswell Formations (Figure 1.2; Ramaekers *et al*., 1979, 1980; Ramaekers, 1990, Rainbird *et al*., 2007).

The Manitou Falls Formation is the most important unit in the eastern Athabasca Basin and is divided into four members, youngest to oldest: the MFd, MFc, MFb, and MFa (Figure 1.2; Ramaekers, 1990). The MFa, MFb and MFc members consist of clastic sediments deposited primarily within alluvial fans (MFa) and high energy proximal braided streams (MFa, MFb, MFc) (Ramaekers, 1990). The MFd, on the other hand, reflects distal portions of a braided stream, such as an estuary or a braided delta setting (Hiatt and Kyser, 2007). The MFa is composed of interbedded matrix-supported quartz pebble conglomerate and well-to-poorly sorted, medium-grained sandstone, accompanied by minor hematitic siltstone beds (Ramaekers, 1990). The MFb consists of medium-grained sandstone, with significant poorly-sorted and clast-

supported conglomerate sandstone (Ramaekers, 1990). The MFc contains sandstone that is characterized by conglomerate beds less than 2 cm thick and less than 1% clay intraclasts (Ramaekers, 1990). The MFd gradationally overlays the MFc, and is composed of well-sorted sandstone, with greater than 1% clay intraclast-rich layers (Ramaekers, 1990). Within the MFd, bedded siltstone and mudstone can occur up to 5 cm thick (Ramaekers, 1990). This thesis uses nomenclature from Ramaekers (1990) to remain consistent with historical literature and current exploration practices.

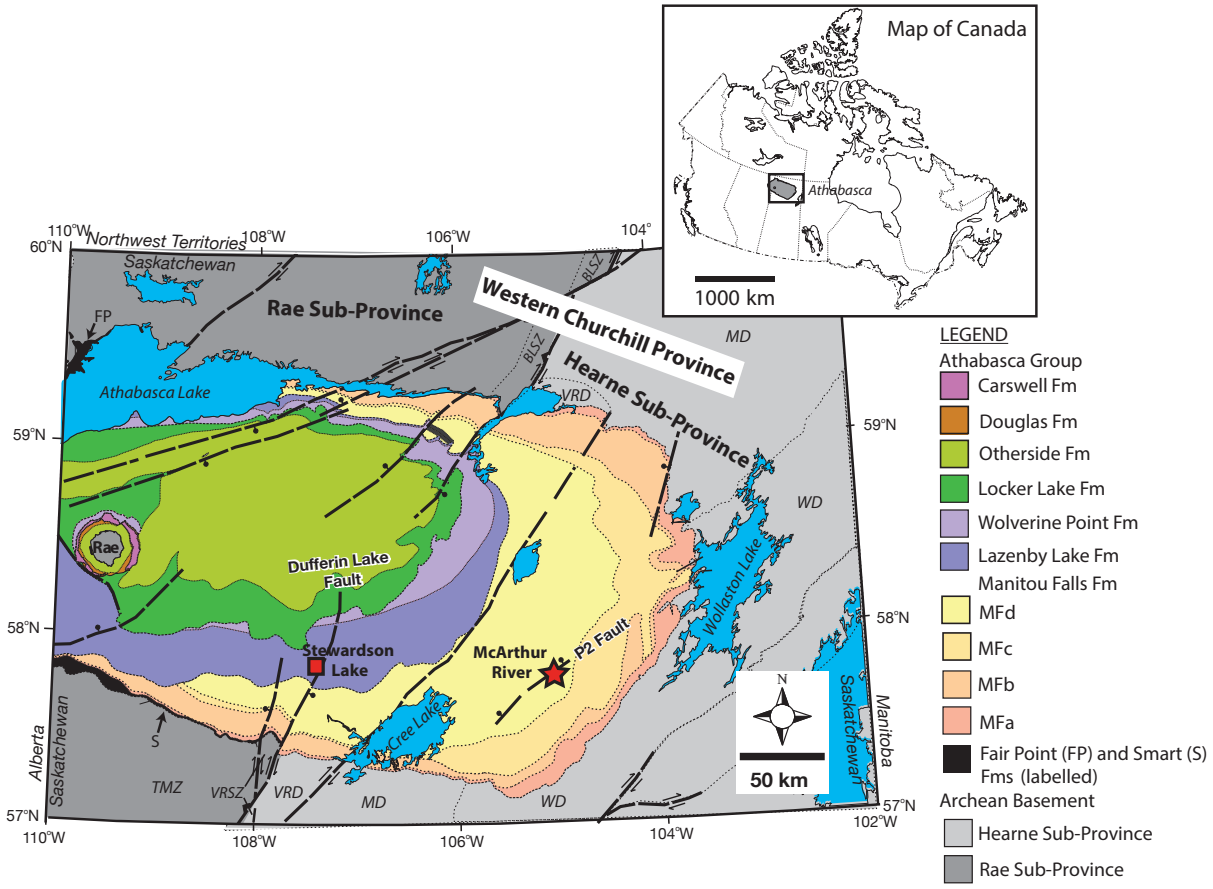

Figure 1.2: Geological map of the Athabasca Basin in Saskatchewan, highlighting the major basement provinces (in bold), fault structures (dashed lines), stratigraphic subdivisions of the Athabasca Group, the McArthur River deposit (red star), and Stewardson Lake project (red square). Figure modified after Ng *et al.* (2013). Domain abbreviations: VRD = Virgin

River, MD = Mudjatik, WD = Wollaston. Shear/magmatic zones: BLSZ = Black Lake shear zone, VRSZ = Virgin River shear zone, TMZ = Taltson magmatic zone.

1.3 Models for unconformity-related U deposits in the Athabasca Basin

Elements respond to specific environments by staying in solution or precipitating. For example, uranium is redox-sensitive and precipitates in reducing depositional environments as insoluble U^{4+} (UO_2) and stays in solution as soluble U^{6+} in oxidized environments (Cuney and Kyser, 2014). In addition, different isotopes of elements fractionate between different redox states because of the different bonding environments in reduced and oxidized species. Consequently, variations in the isotopic composition of redox active elements in uranium deposits are expected and can be used to trace the extent and intensity of the deposit forming process and subsequent interactions with fluids in the basin (e.g. Cuney and Kyser, 2014). The flow of fluids that ultimately lead to the formation of the deposits and associated alteration are spatially associated with high-angle fault structures that are concentrated within graphite-rich gneisses in the basement and between rocks with competency contrasts (Kyser *et al*., 1989). These fault systems are reactivated after the formation of the Athabasca Basin (i.e. fractures in the overlying sandstone), and ultimately control uranium deposition (Kyser *et al*., 1989).

There are two end-member styles of mineralization in unconformity-related deposits, ingress and egress deposit styles that can be distinguished based on the location of uranium mineralization relative to the unconformity, and their associated sulfide mineral assemblages (Figure 1.3; Fayek and Kyser, 1997). Egress-style deposits form at the unconformity where uranium mineralization is partially hosted in the overlying sandstone, and are associated with Ni-Co-As-Fe-Cu-Pb sulphides and arsenides with enrichments in Mo, V, Zn, Ag, Au, Se, S, Bi and Te (Hoeve and Quirt, 1984; Fayek and Kyser, 1997). High sulphide contents indicate uranium

deposition formed under reducing conditions, possibly when a reducing basement fluid interacted with an oxidizing basinal brine (Fayek and Kyser, 1997). Egress-style deposits can be characterized by a significant amount of sandstone alteration (Fayek and Kyser, 1997).

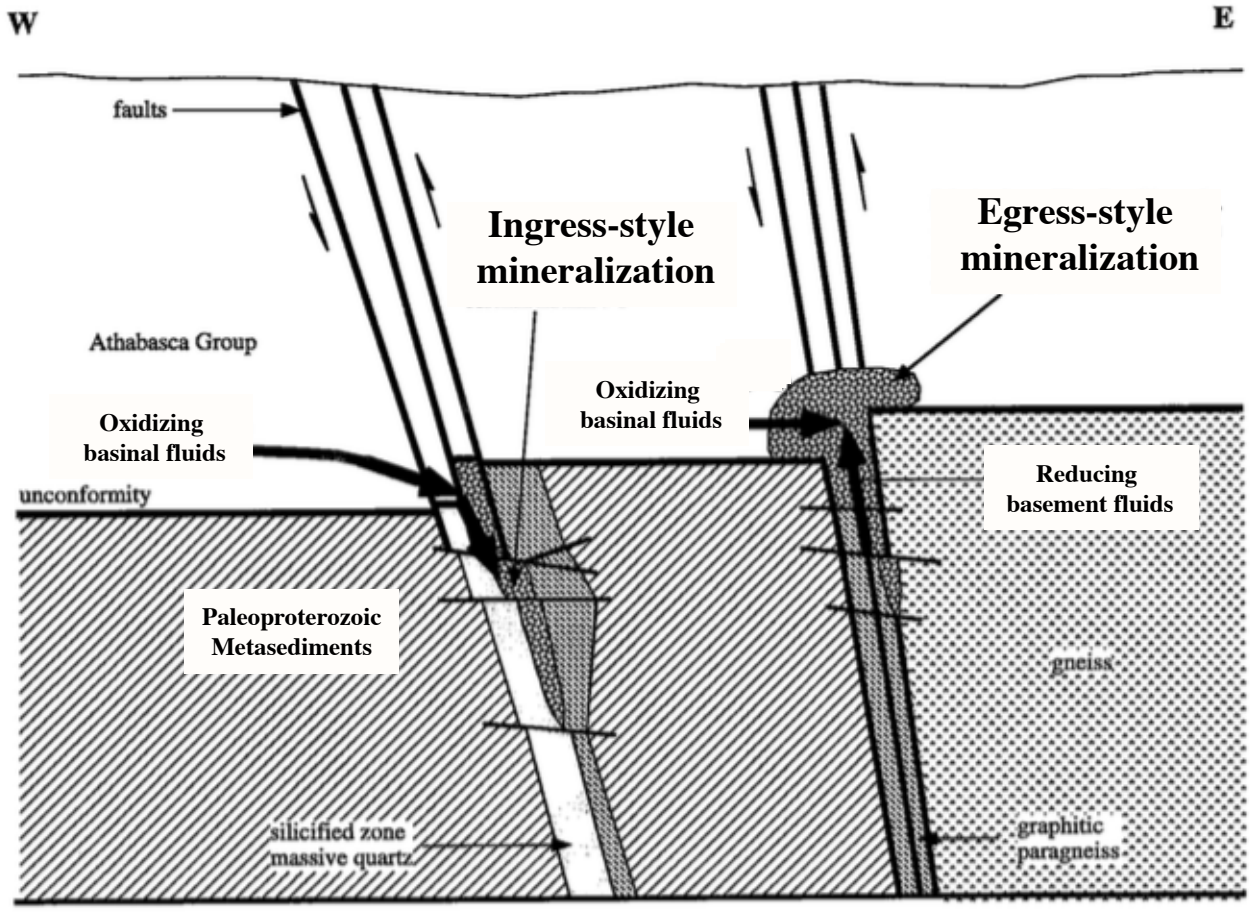

Figure 1.3: Schematic cross section of the two major styles of mineralization in unconformity-related U deposits in the Athabasca Basin, highlighting basinal and basement fluid movement surrounding the unconformity. Figure modified from Fayek and Kyser, 1997.

Ingress-style deposits form within structures in the underlying basement rock and are associated with only trace amounts of sulphides and arsenides (Fayek and Kyser, 1997). Low sulphide contents indicate that this type of deposit formed under less reducing conditions than egress deposits, when reduction of the oxidizing basinal brine occurred as the brine interacted

with basement rocks, with potentially little influence from basement fluids. There is an insignificant amount of sandstone alteration associated with ingress deposit types (Fayek and Kyser, 1997).

Surrounding uranium deposits of both types are hydrothermal alteration halos of variable size and may consist of illitized sandstone with local enrichments of K, Mg, Ca, B, U, Ni, Co, As, Cu and Fe within the sandstone and basement gneisses and metasediments caused by intense hydrothermal alteration (Hoeve *et al*., 1980; Wallis *et al*., 1985; Bruneton, 1993; Kotzer and Kyser, 1990a, 1995), although these features are less significant in ingress-style deposits (Fayek and Kyser, 1997). Beneath the unconformity, paleo-weathering-related alteration extends several meters down where basement gneisses become strongly altered to illite, hematite, chlorite and kaolinite (Hoeve and Quirt, 1984). A dravite, kaolinite, and chlorite signature is typical of several deposits in the south-eastern area of the Athabasca Basin and can be associated with extensive areas of silicification, specifically at the McArthur River deposit (Marlatt *et al*., 1992).

1.4 Exploration techniques related to primary and secondary dispersion in the Athabasca Basin

Geochemical exploration techniques for unconformity-type U deposits largely involve primary and secondary dispersion. Fluids associated with U deposits can create massive alteration halos, which surround the deposit and lead to elevated concentrations of pathfinder elements and many other radioactive decay products (Cuney and Kyser, 2014). Pathfinder elements such as S, V, Mo, Se, As, Cu, Ag, Cr, Pb, Zn, Ni, Co, Re, Ba, P, Mn, rare earth elements (REEs), He, Rn and U are mobilized under oxidizing conditions and create a large geochemical footprint thereby increasing the size of the exploration target. The size of the

alteration halo depends largely on the lithology of its host rock (Sopuck *et al*., 1983). In sandstone, mineralogical halos can extend up to 15 times farther than those occurring in more complex basement lithologies (Sopuck *et al*., 1983). Boron anomalies (indicative of dravite alteration) and clay minerals can be present hundreds of metres from the mineralization, whereas Ni, Co and As typically have smaller alteration halos of a few tens of metres (Cuney and Kyser, 2014). Graphite and organic matter reductants within alteration zones are also major indicators of environments likely to produce U enrichment (Hoeve and Quirt, 1984; Cuney and Kyser, 2014). Holk et al. (2003) used Pb isotopes to reflect post-mineralization dispersion processes distal from the ore body: drusy quartz fracture coatings located in the Kombolgie Basin showed high $^{206}Pb/^{204}Pb$ ratios, suggesting that radiogenic Pb was being transported from the ore body through fractures. This observation is key for exploration purposes as dispersion from the ore body increases the size of the target and it can be cost-effective in exploration if it is understood and quantified.

Clay minerals, such as illite and kaolinite, are abundant on fracture coatings in Athabasca Basin samples. Historically, X-ray diffraction (XRD) techniques have been used to determine the variations in clay mineralogy with respect to depth. In a study by Hoeve and Quirt (1984), a clay fraction of <2 μm was separated from whole-rock samples and used to define normative clay mineral proportions, including illitic and chloritic trends. Proximal to the mineralization, the intensity of clay alteration increases, as does illite and sudoite abundance (sudoite>illite as mineralization is approached), while kaolinite abundance decreases (Kister, 2006). Portable short-wave infrared (SWIR) spectrometers have been used to identify clay minerals in-situ, which is faster and less expensive than XRD analysis (Zhang *et al*., 2001).

Surface sampling techniques are used to detect anomalies in the surficial environment through vegetation, soil and boulder samples that can be used to vector back to the ore.

Anomalies present in glaciated terranes result from the action of several mechanisms, including the formation of glacial till. This includes minerals and boulders from the ore body which are transported and deposited within glacial landforms (Campbell *et al*., 2007). Anomalies caused by secondary dispersion occur as pathfinder elements move away from the ore body and interact with the surficial environment (McQueen, 2005). Mobile pathfinder elements migrate to the surface through faults and fractures as a result of dilatancy pumping, groundwater movement, and electro-migration through redox gradients linked to the contrast between the reducing ore body and oxidized bedrock, producing redox gradients (Aspandiar *et al*., 2008). Soil sampling is a common surface sampling technique wherein surveys that detect anomalies in element concentrations in specific soil horizons. The soil horizons of importance are those where ore-related elements are adsorbed, chelated or co-precipitated (Mann *et al*., 2005) and typically include the surface of clay minerals, hydrous Fe-Mn oxides and humic-fulvic components of humus material (Hall, 1998). Plants are also important in exploration as they use their roots to penetrate deep into the soil and are able to uptake elements that have migrated up from an ore body. Chemical dispersion can also arise from microbial activity related to reducing environments; as microbes produce CO_2 and CH_4 gas, heavy metals bind to these gases and travel to the surface through fractures, faults and permeable sediments (Kelley *et al*., 2006).

Geophysical exploration techniques include gamma-ray spectrometry used in airborne, regional and local surveys, as well as on outcrops with hand-held units and in down-hole logging (Cuney and Kyser, 2014). On the surface, U, K and Th can be directly measured by airborne gamma-ray spectrometry surveys (Cuney and Kyser, 2014). Spectral responses of typical alteration minerals can also be mapped by remote sensing, which can detect visible and mid-infrared sections of the electromagnetic spectrum (Cuney and Kyser, 2014).

1.4 McArthur River unconformity-related U deposit

The Athabasca Basin is host to several high-grade, world-class U deposits, including McArthur River. The McArthur River deposit is the largest and highest grade unconformity-related deposit in the world and is located in the eastern part of the basin (Figure 1.2; Ng *et al*., 2013; Cuney and Kyser, 2014). The deposit has an average grade of 21% U_3O_8 and tonnage greater than 100 kt U (Cuney and Kyser, 2014). It also has combined proven and probable reserves of 332.6 million pounds U_3O_8 and a past production of 225 million pounds U_3O_8 (Bronkhorst *et al*., 2009).

High grade U mineralization occurs in six mineralized zones (1, 2, 3, 4, A, and B) with massive U mineralization occurring at the top of the hanging-wall block of the P2 fault (Figure 1.4). The McArthur River area contains both sandstone-hosted (Zone 1, 3, 4, A and B) and basement-hosted (Zone 2) U ore bodies (Ng *et al*., 2013). Zone 4 (Figure 1.4) is largely monometallic with the principal ore mineral, uraninite, accompanied by sulfides, including minor galena, pyrite, chalcopyrite, and Ni-Co-As sulfides (Ng *et al*., 2013). Silicification at approximately 200-400 m depth, above the deposit has limited the spatial extent of hydrothermal alteration and the anomalies detectable in surficial geochemistry (Ng *et al*., 2013).

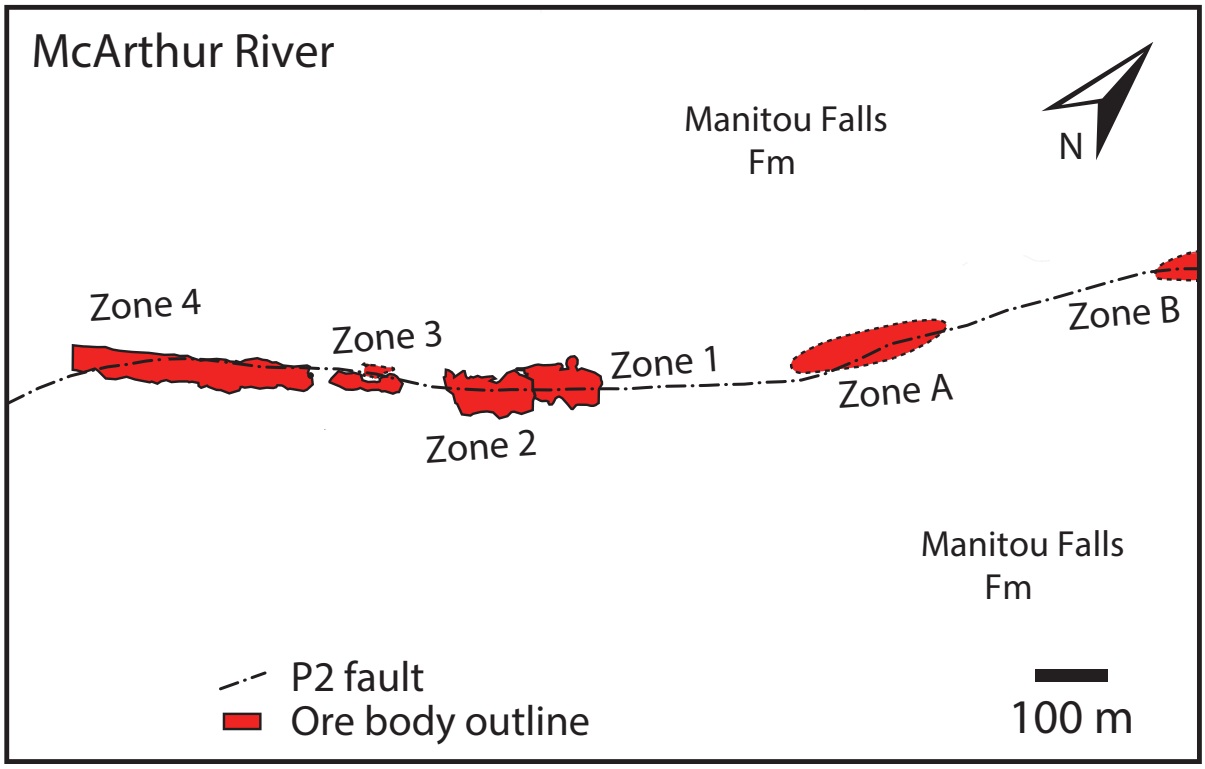

Figure 1.4: Location of mineralized zones within the McArthur River area. Figure modified after Ng *et al.* (2013).

1.5 Stewardson Lake unconformity-related U project

The Stewardson Lake area is a U project under exploration by Uravan Minerals Inc. This property is located in the south-central region of the Athabasca Basin and overlies two strands of the Dufferin Lake reverse fault, which trends NE-SW (Figure 1.2) (Uravan Minerals Inc. Assessment Report, 2016). Sediments at the surface within the Stewardson Lake area include the Lazenby Lake Formation, composed of pebbly quartz arenites (Ramaekers *et al*., 2007), which overlies the Manitou Falls Formation. Alteration chimneys exist and extend more than 300 m into the sandstone above the unconformity (Uravan Minerals Inc. corporate website, 2010). The Athabasca Group sandstone is greater than 800 m in thickness and overlies crystalline basement

rocks of felsic gneiss, metavolcanic rocks and graphitic pelitic schist of the Virgin Schist Group along the Virgin River Shear Zone (Leppin and Goldak, 2005).

1.6 Thesis objectives and rationale

Earlier studies of fractures in sandstone at McArthur River have examined radiogenic Pb mobility around the deposit and geochronology (Holk *et al*., 2003), mineral paragenesis (Kotzer and Kyser, 1995; Fayek and Kyser, 1997; Ng *et al*., 2013), isotope characteristics of specific fluids and temperatures associated with mineral formation (Kotzer and Kyser, 1995), host rock geology and stratigraphy (Ramaekers and Dunn, 1977; Pagel *et al*., 1980; LeCheminant and Heaman, 1989; Cumming and Krstic, 1992; Ey *et al*., 1992; Kyser *et al*., 2000; Yeo *et al*., 2002; Ramaekers and Chatuneanu, 2004; Hiatt and Kyser, 2007; Rainbird *et al*., 2007; Ramaekers *et al*., 1979, *et al*., 1980, 1990, *et al*., 2007; Ng *et al*., 2013), and deposit geology (Ramaekers, 1990; McGill *et al*., 1993; Kotzer and Kyser, 1995; Fayek and Kyser, 1997; Lorilleux *et al*., 2002; Mwenifumbo *et al*., 2004; Alexandre *et al*., 2005; Derome *et al*., 2005; Hiatt *et al*., 2007; Yeo *et al*., 2007; Ng *et al*., 2013). Cameron *et al*., (2004) and McQueen (2005) discuss primary and secondary dispersion in surrounding rocks from mineralizing systems, as well as the enrichment of elements on fracture surfaces.

This study is one of a number of research projects focused on the U site as part of the Canadian Mining Innovation Council (CMIC) Footprints project and involves collaboration from various researchers and projects. The main objective of this study is to determine if fracture coatings and their wall rocks in Athabasca Group sandstones record the primary and secondary dispersion of components from the McArthur River U deposit. These data enhance the deposit footprint and link elements from the deposit to their surficial geochemical signatures. This study also provides the petrographic context of fractures, characterized by optical, scanning electron

microscopy (SEM), X-ray diffraction (XRD), and short-wave infrared spectrometry (SWIR). The geochemistry of fracture coatings was determined by weak acid leach (WAL), *aqua regia* (AR), and continuous leach inductively-coupled plasma mass spectrometry (CL-ICP-MS) techniques. This study also determines the geochemistry of mineralizing fluids through stable isotope analyses, and reveals which elements act as pathfinders in surface samples and their respective migration pathways and processes. Results from the analysis of fracture surfaces from a known Athabasca deposit are compared with the chemistry from similar analyses from the Stewardson Lake U project, to help discern whether fractures are a viable prospective tool for U. Furthermore, geochemical and mineralogical analyses aid in distinguishing the type of depositional control (primary or secondary dispersion). This research has the potential to lead to the development of new U exploration techniques in the Athabasca Basin, by enhancing the footprint of the deposit.

1.7 Thesis structure

Chapters 2, 3, and 4 are presented as manuscripts and contain the main research of this study. Chapter 2 focuses on the McArthur River fractures through a petrographic context of fracture coatings, which aided in the determination of fracture types as well as mineral paragenesis. Stable isotope data from McArthur River fractures is also presented in Chapter 2 that address the origin and character of the fluids recorded on the fractures. Chapter 3 presents CL-ICP-MS data, model ages of various fracture types, and the comparison between fracture surfaces and adjacent wall rock at McArthur River. Chapter 4 introduces the Stewardson Lake fractures through a petrographic context, similar to the McArthur River fractures, which aided in determination of the mineral paragenesis. Model ages of various fracture types and the

comparison between the fracture surface and adjacent wall rock will also be presented in Chapter 4. Lastly, Chapter 5 consists of a discussion and future recommendations for this study.

References

Alexandre, P., Kyser, K., Polito, P. and Thomas, D. 2005. Alteration mineralogy and stable isotope geochemistry of Paleoproterozoic basement-hosted unconformity-type uranium deposits in the Athabasca Basin, Canada. Economic Geology, 100(8), 1547-1563.

Aspandiar, M.F., Anand, R.R. and Gray, D.J. 2008. Geochemical dispersion mechanisms through transported cover: implications for mineral exploration in Australia: CRC Leme, Open File Report 246, 84 p.

Bronkhorst, D., Edwards, C.R., Mainville, A.G., Murdock, G.M., Yesnik, L.D. 2009. McArthur River operation, Northern Saskatchewan, Canada. Cameco Corporation, NI 43-101 Technical Report. (207 pp.).

Bruneton, P. 1993. Geological environment of the Cigar Lake uranium deposit. Canadian Journal of Earth Sciences, 30(4), 653-673.

Cameron, E.M., Hamilton, S.M., Leybourne, M.I., Hall, G.E.M., McClenaghan, M.B. 2004. Finding deeply buried deposits using geochemistry; Geochemistry: Exploration, Environments and Analysis. Vol. 4, p. 7-32.

Campbell, J. 2007. Quaternary geology of the eastern Athabasca Basin, Saskatchewan, in Jefferson, C.W., and Delaney, G., eds., EXTECH IV: Geology and Uranium Exploration TECHNology of the Proterozoic Athabasca basin, Saskatchewan and Alberta, Geological Survey of Canada Bulletin 588, Saskatchewan Geological Society Special Publication 18, Mineral Deposit Division (GAC) Special Publication 4, p. 211-228.

Cumming, G. L. and Krstic, D. 1992. The age of unconformity-related uranium mineralization in the Athabasca Basin, northern Saskatchewan. Canadian Journal of Earth Sciences, 29(8), 1623-1639.

Cuney, M. and Kyser, K. (Eds.). 2014. Recent and not-so-recent developments in uranium deposits and implications for exploration.

Derome, D., Cathelineau, M., Cuney, M., Fabre, C., Lhomme, T. and Banks, D. A. 2005. Mixing of sodic and calcic brines and uranium deposition at McArthur River, Saskatchewan, Canada: a Raman and laser-induced breakdown spectroscopic study of fluid inclusions. Economic Geology, 100(8), 1529-1545

Ey, F., Piquard, J. P., Baudemont, D. and Zimmerman, J. 1992. The sue uranium deposits, Saskatchewan, Canada (No. IAEA-TECDOC--650).

Fayek, M. and Kyser, T.K. 1997. Characterization of multiple fluid-flow events and rare-earth-element mobility associated with formation of unconformity-type uranium deposits in the Athabasca Basin, Saskatchewan: The Canadian Mineralogist, v. 35, p. 627-658.

Hiatt, E. E. and Kyser, T. K. 2007. Sequence stratigraphy, hydrostratigraphy, and mineralizing fluid flow in the Proterozoic Manitou Falls Formation, eastern Athabasca Basin, Saskatchewan. BULLETIN-GEOLOGICAL SURVEY OF CANADA, 588, 489.

Hiatt, E. E., Kyser, T. K., Fayek, M., Polito, P., Holk, G. J. and Riciputi, L. R. 2007. Early quartz cements and evolution of paleohydraulic properties of basal sandstones in three Paleoproterozoic continental basins: Evidence from in situ δ 18 O analysis of quartz cements. Chemical Geology, 238(1), 19-37.

Hall, G.E. 1998. Analytical perspective on trace element species of interest in exploration: Journal of Geochemical Exploration, v. 61, p. 1-19.

Hoeve, J., Sibbald, T. I. I., Ramaekers, P. and Lewry, J. F. 1980. Athabasca basin unconformity-type uranium deposits. A special class of sandstone-type deposits. In Uranium in the Pine Creek geosyncline.

Hoeve, J. and Quirt, D. 1984. Mineralization and host rock alteration in relation to clay mineral diagenesis and evolution of the Middle-Proterozoic, Athabasca Basin, Northern Saskatchewan, Canada: Saskatchewan Research Council Technical Report No. 187, 187 p.

Hoffman, P. F. 1988. United Plates of America, the birth of a craton-Early Proterozoic assembly and growth of Laurentia. Annual Review of Earth and Planetary Sciences, 16, 543-603.

Holk, G.J., Kyser, T.K., Chipley, D., Hiatt, E.E. and Marlatt, J. 2003. Mobile Pb-isotopes in Proterozoic sedimentary basins as guides for exploration of uranium deposits: Journal of Geochemical Exploration, v. 80, p. 297-320.

International Atomic Energy Agency. 2009. World distribution of uranium deposits (UDEPO), with uranium deposit classification: IAEA-TECDOC-1629, Vienna, 117 p.

Kelley, D.L., Kelley, K.D., Coker, W.B., Caughlin, B. and Doherty, M.E. 2006. Beyond the obvious limits of ore deposits: the use of mineralogical, geochemical, and biological features for the remote detection of mineralization: Economic Geology, v. 101, p. 729-752.

Kister, P., Laverret, E., Quirt, D., Cuney, M., Mas, P.P., Beaufort, D. and Bruneton, P. 2006. Mineralogy and geochemistry of the host-rock alterations associated with the Shea Creek unconformity-type uranium deposits (Athabasca Basin, Saskatchewan, Canada). Part 2. Regional-scale spatial distribution of the Athabasca group sandstone matrix minerals:

Clays and Clay Minerals, v. 54, p. 295-313.

Kotzer, T. and Kyser, T. K. 1990. The use of stable and radiogenic isotopes in the identification of fluids and processes associated with unconformity-type uranium deposits.

Kotzer, T. G. and Kyser, T. K. 1995. Petrogenesis of the Proterozoic Athabasca Basin, northern Saskatchewan, Canada, and its relation to diagenesis, hydrothermal uranium mineralization and paleohydrogeology. Chemical Geology, 120(1), 45-89.

Kyser, T. K., Wilson, M. R. and Ruhrmann, G. 1989. Stable isotope constraints on the role of graphite in the genesis of unconformity-type uranium deposits. Canadian Journal of Earth Sciences, 26(3), 490-498.

Kyser, K., Hiatt, E., Renac, C., Durocher, K., Holk, G. and Deckart, K. 2000. Diagenetic fluids in Paleo-and Meso-Proterozoic sedimentary basins and their implications for long protracted fluid histories: Fluids and basin evolution: Mineralogical Association of Canada Short Course, v. 28, p. 225-262.

LeCheminant, A. N. and Heaman, L. M. 1989. Mackenzie igneous events, Canada: Middle Proterozoic hotspot magmatism associated with ocean opening. Earth and Planetary Science Letters, 96(1-2), 38-48.

Leppin, M. and Goldak, D. 2005. Mapping deep sandstone alteration and basement conductors utilizing audio magnetotellurics: exploration for uranium in the Virgin River area, Athabasca basin, Saskatchewan, Canada. In 2005 SEG Annual Meeting. Society of Exploration Geophysicists.

Lesher, M., Hannington, M., Galley, A., Ansdell, K., Astic, T., Banerjee, N., Beauchamp, S., Beaudoin, G., Bertelli, M., Bérubé, C., Beyer, S., Blacklock, N., Byrne, K., Cheng, L.-Z., Chouinard, R., Chouteau, M., Clark, J., D'Angelo, M., Darijani, M., Devine, M., Dupuis, C., El Goumi, N., Enkin, R., Farquharson, C., Fayol, N., Feltrin, L., Feng, J., Gaillard, N., Gleeson, S., Gouiza, M., Grenon, C., Guffey, S., Guilmette, C., Guo, K., Hart, C., Hattori, K., Hollings, P., Joyce, N., Kamal, D., King, J., Kyser, K., Layton-Matthews, D., Lee, R., Lesage, G., Leybourne, M., Linnen, R., Lypaczewski, P., McGaughey, J., Mitchinson, D., Milkereit, B., Mir, R., Morris, W., Oldenburg, D., Olivo, G., Perrouty, S., Piercey, S., Piette-Lauzière, N., Raskevicius, T., Reman, A., Rivard, B., Ross, M., Samson, I., Scott, S., Shamsipour, P., Shi, D., Smith, R., Sundaralingam, N., Taves, R., Taylor, C., Valentino, M., Vallée, M., Wasyliuk, K. and Williams-Jones, A., Winterburn, P. 2017. Integrated Multi-Parameter Exploration Footprints of the Canadian Malartic Disseminated Au, McArthur River-Millennium Unconformity U, and Highland Valley Porphyry Cu Deposits: Preliminary Results from the NSERC-CMIC Mineral Exploration Footprints Research Network. Available at: http://cmic-footprints.ca/home/ publications.

Lewry, J.F. and Sibbald, T.I. 1980. Thermotectonic evolution of the Churchill Province in northern Saskatchewan: Tectonophysics, v. 68, p. 45-82.

Lorilleux, G., Jébrak, M., Cuney, M. and Baudemont, D. 2002. Polyphase hydrothermal breccias associated with unconformity-related uranium mineralization (Canada): from fractal analysis to structural significance. Journal of Structural Geology, 24(2), 323-338.

Mann, A., Birrell, R., Fedikow, M. and De Souza, H. 2005. Vertical ionic migration: mechanisms, soil anomalies, and sampling depth for mineral exploration: Geochemistry: Exploration, Environment, Analysis, v. 5, p. 201-210.

Marlatt, J., McGill, B., Matthews, R., Sopuck, V. and Pollock, G. 1992. The discovery of the McArthur River uranium deposit, Saskatchewan, Canada (No. IAEA-TECDOC--650).

McGill, B. D., Marlatt, J. L., Matthews, R. B., Sopuck, V. J., Homeniuk, L. A. and Hubregtse, J. J. 1993. The P2 north uranium deposit, Saskatchewan, Canada. Exploration and Mining Geology, 2(4), 321-331.

McQueen, K. G. 2005. Ore deposit types and their primary expressions. Regolith Expression of Australian Ore Systems. CRC LEME, Perth, website: http://www. crcleme. org. au/Pubs/Monographs/RegExpOre. html [Last accessed January 2013.].

Mwenifumbo, C. J., Elliott, B. E., Jefferson, C. W., Bernius, G. R. and Pflug, K. A. 2004. Physical rock properties from the Athabasca Group: designing geophysical exploration models for unconformity uranium deposits. Journal of Applied Geophysics, 55(1), 117-135.

Ng, R., Alexandre, P. and Kyser, K. 2013. Mineralogical and geochemical evolution of the unconformity-related McArthur River Zone 4 Orebody in the Athabasca Basin, Canada: implications of a silicified zone. Economic Geology, 108(7), 1657-1689.

Pagel, M., Poty, B. and Sheppard, S. M. F. 1980. Contribution to some Saskatchewan uranium deposits mainly from fluid inclusion and isotopic data. In Uranium in the Pine Creek Geosyncline.

Rainbird, R. H., Stern, R. A., Rayner, N. and Jefferson, C. W. 2007. Age, provenance, and regional correlation of the Athabasca Group, Saskatchewan and Alberta, constrained by igneous and detrital zircon geochronology. BULLETIN-GEOLOGICAL SURVEY OF CANADA, 588, 193.

Ramaekers, P. P. and Dunn, C. E. 1977. Geology and geochemistry of the eastern margin of the Athabasca Basin.

Ramaekers, P., Christopher, J.E., and MacDonald, R. 1979. Stratigraphy of the Athabasca Basin; in Summary of Investigations 1979; Saskatchewan Geological Survey; Saskatchewan Mineral Resources, Miscellaneous Report 79-10, p. 154–160.

Ramaekers, P., Christopher, J.E., and MacDonald, R. 1980. Stratigraphy and tectonic history of the Athabasca Group (Helikian) of northern Saskatchewan; in Summary of Investigations 1980; Saskatchewan Geological Survey, Saskatchewan Mineral Resources, Miscellaneous

Report 80-4, p. 99–106.

Ramaekers, P. 1990. Geological Maps of the Athabasca Group (Helikian) in Northern Saskatchewan. Saskatchewan Energy and Mines, Saskatchewan Geology Survey.

Ramaekers, P. and Catuneanu, O. 2004. Development and sequences of the Athabasca basin, early Proterozoic, Saskatchewan and Alberta, Canada. The Precambrian Earth: Tempos and Events. Developments in Precambrian Geology, 12, 705-723.

Ramaekers, P., Yeo, G. M., Jefferson, C. W., Collier, B., Long, D. G. F., Catuneanu, O., Bernier, S., Kupsch, B., Post, R., Drever, G., McHardy, S., Jiricka, D., Cutts, C. and Wheatley, K. 2007. Revised geological map and stratigraphy of the Athabasca Group, Saskatchewan and Alberta. Bulletin-Geological Survey of Canada, 588, 155.

Sopuck, V., de Carla, A., Wray, E. and Cooper, B. 1983. The application of lithogeochemistry in the search for unconformity-type uranium deposits, northern Saskatchewan, Canada: Journal of Geochemical Exploration, v. 19, p. 77-99.

Stewardson Lake, Uravan Minerals Inc. 2010. Retrieved from http://www.uravanminerals.com/properties/outer_ring_project/

Stewart, P., Beyer, S. and Bzdel, L. 2016. Stewardson Lake Project 2015 Exploration Report.

Voinot, A., Chipley, D. and Kyser, K. 2015. Mo, Tl and U Isotopes in U-Ore Deposits: Proxies of Redox-Driven Formation Processes. Poster originally presented at the Goldschmidt conference series, Prague, Czech Republic.

Wallis, R. H., Saracoglu, N., Brummer, J. J., and Golightly, J. P. 1985. The geology of the McClean uranium deposits, northern Saskatchewan; in Sibbald, T.I.I. and Petruk, W. (eds.), Geology of Uranium Deposits, CIM Spec. Vol. 32, p101-131.

Wilson, M. R. and Kyser, T. K. 1987. Stable isotope geochemistry of alteration associated with the Key Lake uranium deposit, Canada. Economic Geology, 82(6), 1540-1557.

Yeo, G., Jefferson, C. W. and Ramaekers, P. 2002. A preliminary comparison of Mantiou Falls Formation stratigraphy in Four Athabasca Basin Deposystems. Summary of Investigations, 2, 2002-4.

Yeo, G., Jefferson, C.W. and Ramaekers, P., 2007. Comparison of lower Athabasca Group stratigraphy among depositional systems, Saskatchewan and Alberta: Geological Survey of Canada, Bulletin 588, p. 465–488.

Zhang, G., Wasyliuk, K. and Pan, Y. 2001. The characterization and quantitative analysis of clay minerals in the Athabasca Basin, Saskatchewan: Application of shortwave infrared reflectance spectroscopy: The Canadian Mineralogist, v. 39, p. 1347-1363.

Chapter 2

Mineral Chemistry and Petrogenesis of Fracture Coatings in Athabasca Group Sandstones from the McArthur River Uranium Deposit

M. Valentino[1], T.K. Kyser[1], M. Leybourne[2], T. Kotzer[3], D. Quirt[4], P. Lypaczewski[5]

[1]Department of Geological Sciences and Geological Engineering, Queen's University, Kingston, ON;
[2]Mineral Exploration Research Centre, Department of Earth Sciences, Laurentian University, Sudbury, ON;
[3]Cameco Corporation, Saskatoon, SK;
[4]AREVA Resources Canada Inc., Saskatoon, SK;
[5]Department of Earth and Atmospheric Sciences, University of Alberta, Edmonton, AB

Abstract

The McArthur River unconformity-related uranium deposit in the Athabasca Basin, Saskatchewan, Canada, is structurally-hosted near the unconformity between Archean to Paleoproterozoic metasedimentary basement and about 600 meters of Proterozoic Athabasca Group sandstones. In this study, the mineralogy and geochemistry of fracture materials in the Athabasca Group sandstones and their wall (host) rock from the McArthur River area were used to determine the paragenetic sequence and origin of minerals on and near fractures to determine if the minerals they host record elements associated with the uranium deposit at depth and can be used to guide exploration (vectoring). Fracture orientations indicate that most fractures are moderately to steeply-dipping (<50°) providing permeable pathways for fluid movement within the basin from below and through the overlying sedimentary rocks. Many of the fractures and their adjacent wall rocks record multiple distinct fluid events.

Seven types of fracture fillings were identified, representing distinct colors, mineralogies, and chemical features. Brown (type 1) and pink (type 7) fractures host paragenetically-late botryoidal goethite, Mn-oxides and poorly crystallized kaolinite that formed from relatively recent low-temperature meteoric fluids as indicated by poor crystallinity and low δ^2H values of -

198 to -115 ‰. These minerals variably replaced higher-temperature minerals that are rarely preserved on the fractures or in wall rock near the fractures. Hydrothermal alteration associated with the mineralizing system at *ca*. 200°C is recorded in assemblages of dickite, well-crystallized kaolinite, illite, and spherulitic dravite in some white and yellow (type 2), white (type 3), and drusy quartz (type 6) fractures as reflected by their habits and high δ^2H values of -155 to -44 ‰. Fibrous goethite in white and yellow (type 2) and black and orange (type 5) fractures and microfibrous Mn oxy-hydroxides in black (type 4) fractures, also formed from hydrothermal fluids, but at temperatures less than 200°C.

White and yellow fractures (type 2) containing fibrous goethite reflect fracture networks indicative of hydrothermal fluids associated with the mineralizing system during primary dispersion of pathfinder elements, and therefore extend the deposit footprint. Brown (type 1) and pink (type 7) fractures are indicative of meteoric fluids due to low δ^2H values in botryoidal goethite and poorly crystalline kaolinite. Secondary dispersion of elements from the deposit to the surface on some fractures is evidence that fractures are pathways for element migration from the deposit to the surface, over distances exceeding ~500 meters.

2.1 Introduction

The Athabasca Basin is a Paleo- to Mesoproterozoic basin located in northern Saskatchewan and Alberta (Figure 2.1) that hosts significant uranium deposits in faults near the unconformity between the Athabasca Group sandstone and underlying Paleoproterozoic and Archean metamorphic basement rocks (IAEA, 2009). These unconformity-related uranium deposits formed under reducing conditions near the unconformity, by interaction between oxidizing basinal fluids and reduced basement lithologies or a reducing basement fluid (Hoeve and Sibbald, 1978; Hoeve and Quirt, 1984; Wallis *et al*., 1985; Wilson and Kyser, 1987; Kotzer

and Kyser, 1995; Fayek and Kyser, 1997). Fluids associated with these deposits produced alteration zones of variable extent in the overlying sandstone or more restricted zones in basement rocks surrounding the deposit (Wilson and Kyser, 1987; Kotzer and Kyser, 1995; Fayek and Kyser, 1997). The flow of fluids that affect the formation of the deposits and subsequent alteration of them are associated with high-angle fault structures most commonly are associated with graphite-rich gneisses and pelites and quartzites that form a competency contrast (Kyser *et al*., 1989). These fault systems are pre-cursors for later structural features (i.e. fractures in the overlying sandstone), which ultimately control uranium deposition (Kyser *et al*., 1989). The alteration zones associated with unconformity-related U deposits can be used for exploration because they significantly enhance the footprint of the deposit by up to several hundred meters from the mineralization (Gustafson and Curtis, 1983; Wilde *et al*., 1989), extending along structural discontinuities including permeable zones such as faults, fractures, and breccias on both sides of the unconformity (Beaufort *et al*., 2005).

The mineralogy and geochemistry of some alteration zones are related to two temporarily distinct processes directly associated with the mineralizing system: (1) primary (syn-mineralization) and (2) secondary (post-mineralization) dispersion. Primary dispersion occurs during hydrothermal alteration associated with the mineralizing system, wherein elements are dispersed to the surrounding rocks, creating a dispersion halo around the deposit itself and along fractures with enhanced permeability (McQueen, 2005). Secondary dispersion occurs when post-ore events such as hydrothermal, low-temperature meteoric, or microbial activity (Cameron *et al*., 2004) variably mobilize elements from the ore zone and/or surrounding alteration halo; a process also facilitated by enhanced permeability of open fractures. In addition, post-mineralization elements can be present in fracture coatings where they are absorbed onto Fe- and Al-oxy-hydroxides and Fe-Mn hydroxides that can precipitate from fluids that flow down fractures from

the surface. These oxy-hydroxide phases typically have negative charges that are capable of attracting metal cations including elements that may be mobilized from the deposit, thereby trapping them on fracture surfaces during secondary dispersion from the deposit (e.g. Cameron *et al*., 2004). Fractures are important to both primary and secondary dispersion processes and are therefore critical in defining the extended footprint of the deposit and the possible processes by which elements in surface media can reflect the deposit at depth.

Fluids interacting with mineral assemblages in fracture fillings may originate from a number of sources (Kerrich and Kyser, 1990), including diagenetic basinal fluids, hydrothermal fluids, and meteoric fluids. Diagenetic basinal fluids interacted with Athabasca Group sandstones and formed mineral assemblages of clay and silicate minerals at 200ºC (Kotzer and Kyser, 1995). Hydrothermal fluids formed as mixing occurred between diagenetic basinal fluids and basement fluids, in the immediate vicinity of unconformity-related U deposits in the Athabasca Basin (Kotzer and Kyser, 1995). In the upper Athabasca Group sandstones, the infiltration of meteoric waters from above occurred, due to the enhanced permeability of open fractures (Kotzer and Kyser, 1995). From past studies (e.g. Wood and Hewett, 1982; Hoeve and Quirt, 1984) it is difficult to distinguish diagenetic basinal fluids and hydrothermal fluids, as both occur at high-temperatures (~200 ºC) and are represented by similar mineral assemblages (Hoeve and Quirt, 1984). Notwithstanding these difficulties, in this study the distinction of origins is based on the crystallinities of minerals and $\delta^{18}O$ and $\delta^{2}H$ values of the primary minerals in the fracture fillings, but recognizing these are operational distinctions.

The geology and stratigraphy of the Athabasca Group including the Manitou Falls Formation sandstones, which lies above the unconformity at the McArthur River uranium deposit which is the focus of this study, and the metallogenesis of unconformity-type uranium deposits,

have been documented in many previous studies (Ramaekers and Dunn, 1977; Pagel *et al*., 1980; Hoeve and Quirt, 1984; Wallis *et al*., 1985; LeCheminant and Heaman, 1989; Cumming and Krstic, 1992; Ey *et al*., 1992; Kyser *et al*., 2000; Yeo *et al*., 2002; Ramaekers and Catuneanu, 2004; Hiatt and Kyser, 2007; Rainbird *et al*., 2007; Ramaekers *et al*., 1979, *et al*., 1980, 1990, *et al*., 2007; Ng *et al*., 2013). In addition, the geology of the deposit has been well documented (Ramaekers, 1990; McGill *et al*., 1993; Kotzer and Kyser, 1995; Fayek and Kyser, 1997; Lorilleux *et al*., 2002; Mwenifumbo *et al*., 2004; Alexandre *et al*., 2005; Derome *et al*., 2005; Hiatt *et al*., 2007; Jefferson *et al*., 2007; Yeo *et al*., 2007; Ng *et al*., 2013; among others). The mineral paragenesis of the McArthur River deposit and surrounding area (Figure 2.1) was described by Kotzer and Kyser (1995), Fayek and Kyser (1997) and Ng *et al*. (2013). These authors reported that the $\delta^{18}O$ and $\delta^{2}H$ isotopic compositions of early hydrothermal fluids and the crystal chemistry of minerals that formed from them were consistent with derivation from evolved basinal brines at *ca*. 200°C, but also that the deposits and basin minerals were affected by later low-temperature meteoric fluids associated with clay and oxide minerals, including late pervasive kaolinite and limonite staining (also Hoeve and Quirt, 1984; Wilson and Kyser, 1987). Cameron *et al*. (2004) and McQueen (2005) discussed primary and secondary dispersion from buried mineralization into surrounding rocks and overburden as well as the enhancement of elements through various systems including unconformity-related uranium deposits. Devine (2016) analyzed surficial fracture coatings within 100 m of the surface from the McArthur River U deposit using sequential leach extractions to determine the potential mineralogical hosts of various elements and compared these results to radium distributions. This work showed that surficial fracture coatings include illite, kaolinite, and Fe-Mn oxy-hydroxides, and that the abundance of Ra (≤ 32.2 pg/g) on fracture coatings is likely impacted by groundwater and the Fe

and Mn concentrations on fracture surfaces. A selection of these fractures were analyzed as part of this study to understand the surficial geochemical signature at the McArthur River uranium deposit.

In this study, the mineralogy and geochemistry of coatings from fractures and adjacent wall rock in the Athabasca Group sandstones above the McArthur River deposit were evaluated to develop a mineral paragenesis for the coatings. The purpose of this study is to investigate components within fractures from depth to surface and determine if they constitute an effective exploration tool. This study is part of the Canadian Mining Innovation Council (CMIC) NSERC-CRD Footprints project to determine the footprint of the McArthur River U deposit and to provide data and information to aid in the generation of more effective approaches to integrate and visualize multi-parameter data sets and thus improve exploration within the footprint of unconformity-related uranium deposits (e.g. Lesher *et al*., 2017).

2.2 Geological setting

2.2.1 Regional geology

The Athabasca Basin is an intracratonic basin located in northern Saskatchewan and Alberta (Figure 2.1), and covers an area greater than 85,000 km^2 (Ramaekers, 1990). The Paleo- to Mesoproterozoic basin unconformably overlies Archean and Paleoproterozoic basement composed of metamorphosed sedimentary and igneous rocks of the western Churchill Province (Figure 2.1), which is further divided into the Rae and Hearne Sub-Provinces. The western Churchill province is located between two orogenic belts, the Taltson-Thelon orogenic Belt (*ca*. 1.9 Ga) and the Trans-Hudson Orogen (*ca*. 1.8 Ga) (Hoffman, 1988). In the Athabasca region, the contact between the Rae and Hearne Provinces is the Snowbird Tectonic Zone (Hoffman, 1988), comprised of the Virgin River shear zones at the south of the Athabasca Basin, and the Black

Lake shear zone to the north (Figure 2.1).

There are three domains within the Hearne Province in the Athabasca region, all containing metamorphosed Archean and Paleoproterozoic granitic gneiss and overlying the supracrustal meta-sedimentary sequences. The domains are defined by variations in lithology, structural character, and metamorphic grade (Lewry and Sibbald, 1980). From east to west the domains are: the Wollaston Domain, the Mudjatik Domain, and the Virgin River Domain (Annesley *et al*., 2005; Tran *et al*., 2008), with the Wollaston-Mudjatik Transition Zone (WMTZ) separating the Wollaston and Mudjatik domains (Annesley *et al*., 2005; Jeanneret *et al*., 2016). Most of the unconformity-type U deposits in the eastern Athabasca region are located within the WMTZ.

The Wollaston Group basement in the vicinity of the McArthur River deposit is composed of pelitic, semipelitic and arkosic gneissic rocks, with calc-silicate and quartzite units in the footwall, and a 25 m thick sequence of graphite-bearing pelitic gneiss and pegmatitic veins in the hanging wall of the P2 fault zone with which the deposit is associated (McGill *et al*., 1993). Prior to the deposition of the Athabasca Group, a paleoweathering profile, partially preserved up to 50 m thick, was established on basement rocks (Ramaekers, 1990). The upper portion of the paleoweathering profile contains pervasive hematite staining; however, the profile can be altered in some areas to chlorite by superimposed reduction (Ramaekers, 1990). The circa 1700-1500 Ma Athabasca Group (Figure 2.1) consists of flat-lying, quartz-rich sandstone and conglomerate, which was deposited in major river systems and near-shore to shallow-shelf environments (Ramaekers, 1990; Ramaekers *et al*., 2007). Sedimentary basin fill has a maximum current thickness around 1.5 km, although temperature estimates from fluid inclusions suggest that these sequences reached depths of up to 5 km during peak diagenesis (Pagel *et al*., 1980). The units are cut by reactivated Hudsonian faults that are periodically active to the present day

(Hoeve and Quirt, 1984; Kyser *et al*., 2000). The northwest-trending 1267 Ma Mackenzie dike swarm (LeCheminant and Heaman, 1989) also cuts the sedimentary sequences of the Athabasca Basin and underlying basement rocks.

Four unconformity-bound stratigraphic sequences form the Athabasca Group (Figure 2.1; Yeo *et al*., 2002; Ramaekers and Catuneanu, 2004; Ramaekers *et al*., 2007). In ascending order they are the: 1) Fair Point Formation; 2) Smart and Manitou Falls formations, which make up the majority of the Athabasca Group (Ramaekers *et al*., 2007); 3) Lazenby Lake and Wolverine Point formations; and 4) Locker Lake, Otherside, Douglas, and Carswell formations (Ramaekers *et al*., 1979, 1980; Ramaekers, 1990). The Athabasca Group strata present in the McArthur River area consist of Manitou Falls Formation sandstone and microconglomerate.

2.2.2 Manitou Falls Formation

The Manitou Falls Formation is divided into four members which are, from youngest to oldest, the MFd, MFc, MFb and MFa (Figure 2.1; Ramaekers, 1990). Members a, b, and c were formed from clastic sediments deposited primarily within alluvial fans (MFa) and high energy proximal braided streams (MFa, MFb, MFc) (Ramaekers, 1990). MFd reflects deposition in more distal portions of a braided stream, such as an estuary or a braided delta setting (Hiatt and Kyser, 2007).

The MFa is composed of interbedded matrix-supported quartz pebble conglomerate and well-to-poorly-sorted, medium-grained sandstone, accompanied by minor hematitic siltstone beds (Ramaekers, 1990), while the MFb consists of medium-grained sandstone with significant poorly-sorted and clast-supported conglomerate sandstone (Ramaekers, 1990). The MFc contains sandstone that has very minor conglomerate beds less than 2 cm thick and contains less than 1% clay intraclasts (Ramaekers, 1990). The MFd is gradational from the MFc and is composed of

well-sorted sandstone with greater than 1% clay intraclast-rich layers (Ramaekers, 1990). In the MFd, bedded siltstone and mudstone can occur as up to 5 cm thick (Ramaekers, 1990). This study uses nomenclature from Ramaekers (1990) to remain consistent with historical literature and current exploration terminology.

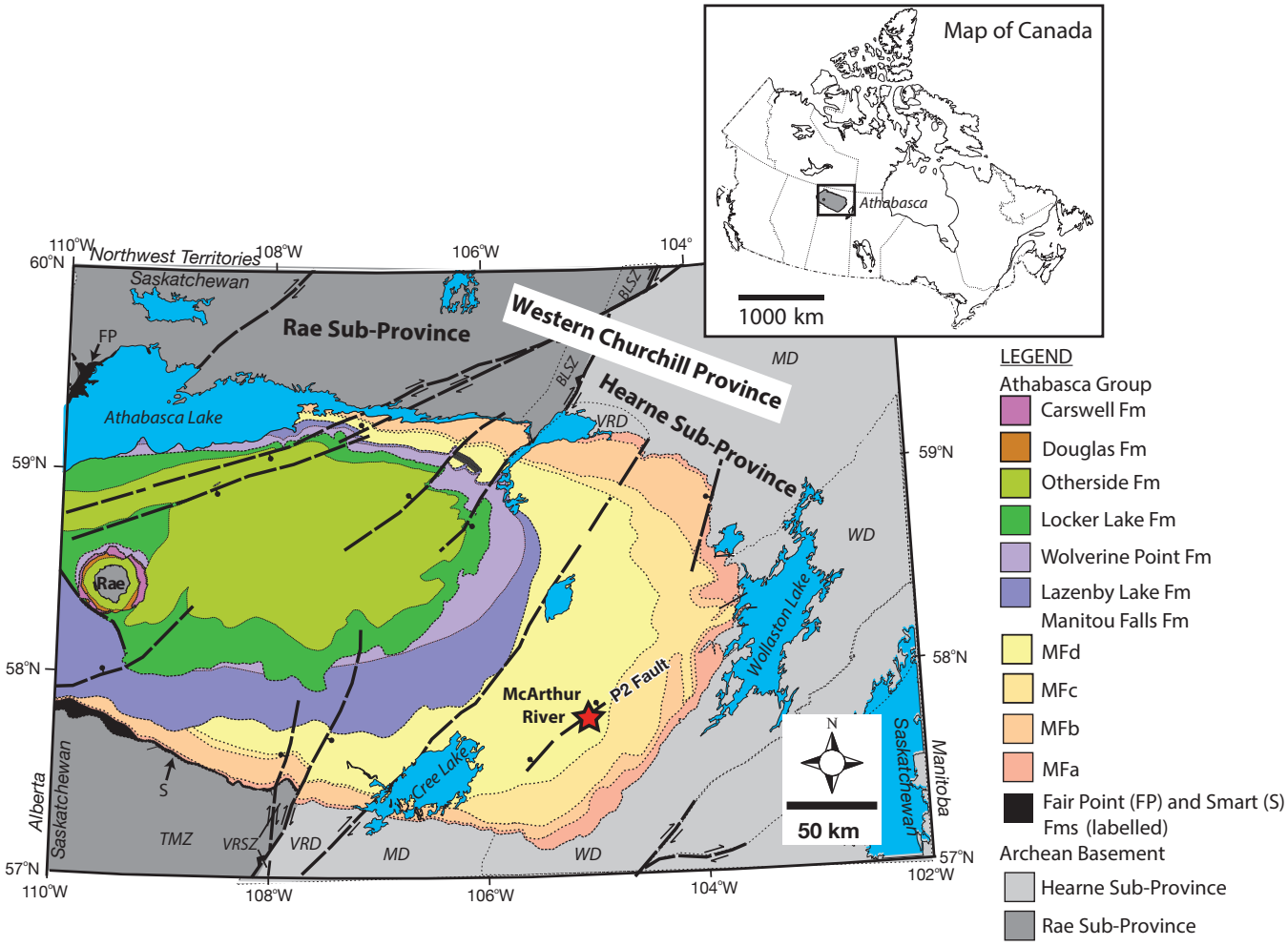

Figure 2.1: Geological map of the Athabasca Basin, highlighting basement provinces (grey; names in bold), fault structures (dashed lines) such as the P2 fault, stratigraphic sections of the Athabasca Group, and the McArthur River deposit (red star). Figure modified from Ng *et al.* (2013). Domain abbreviations: VRD = Virgin River, MD = Mudjatik, WD = Wollaston. Shear/magmatic zones: BLSZ = Black Lake shear zone, VRSZ = Virgin River shear zone, TMZ = Taltson magmatic zone.

2.2.3 McArthur River unconformity-related U deposit

The McArthur River unconformity-related U deposit (Figure 2.1) occurs around the unconformity between the Manitou Falls Formation of the Athabasca Group and Wollaston Group basement rocks, along the P2 structure (Ng *et al*., 2013). The P2 fault is a major reverse thrust fault with a strike length of approximately 13 km, striking N45°E, and dipping 40° to 45° SE (McGill *et al*., 1993). The P2 fault has been traced seismically at least 2 km below the unconformity (Hajnal *et al*., 2010). As displacement along the fault occurred along the graphite-rich basement rocks, the hanging wall block was uplifted by 60-80 m (Figure 2.2). The P2 structure underwent multiple episodes of reactivation during sedimentation (Bernier, 2004; Yeo *et al*., 2007) and was displaced by three sets of steeply-dipping transcurrent faults, which strike 100° to 110° (McGill *et al*., 1993).

Intense silicification is present within the Manitou Falls Formation, especially in the lower 200 m (MFa and MFb) of the Manitou Falls Formation at Zone 4 (Figure 2.2b; Ng *et al*., 2013). Hiatt *et al*. (2007) suggested that this silicified zone formed primarily due to early pre-compaction quartz cementation, whereas Derome *et al*. (2005) suggested that silicification was post-diagenetic, but pre-ore in timing. Pan *et al*. (2006), who used electron paramagnetic resonance (EPR) spectroscopy to observe the effects of U on quartz cements, suggested that both previously mentioned processes operated. Either process would limit syn-mineralization or post-mineralization dispersion of elements from the deposit to fracture-controlled migration (Kyser *et al*., 2000; Holk *et al*., 2003; Hiatt and Kyser, 2007; Ng *et al*., 2013; Joyce, 2016). Reactivation of the P2 fault later caused widespread fracturing of silicified sandstone, with a 50-75 m fracture zone being present in the lower MFa (McGill *et al*., 1993; Mwenifumbo *et al*., 2004).

Alteration mineralogy within the Manitou Falls Formation includes quartz cements, iron oxides, dravite, dickite, sudoite and illite (McGill *et al*., 1993). Chlorite-dravite solution breccias

are associated with massive quartz dissolution (Lorilleux *et al*., 2002; Derome *et al*., 2005). Basement alteration proximal to the P2 fault zone consists of an inner illite-sudoite alteration and a distal clinochlore alteration (Ng *et al*., 2013). At the hanging wall of the P2 fault, dravite, apatite and carbonate are locally present, (McGill *et al*., 1993; Alexandre *et al*., 2005) together with intense uranium mineralization associated with significant hematite alteration (Ng *et al*., 2013). In proximity to hydrothermally-altered fault zones, these early formed diagenetic and hydrothermal assemblages, were altered and overprinted by late meteoric fluids (Kotzer and Kyser, 1995). Kaolinite mainly occurs within fractures in the upper Manitou Falls Formation, (MFc and MFd) and formed during meteoric fluid infiltration, but kaolinite is also found adjacent to the P2 fault zone in the sandstone and formed from hydrothermal fluids (Kotzer and Kyser, 1995).

The Zone 4 ore body is a strongly mineralized region located at a depth of 500-570 m along the P2 fault (McGill *et al*., 1993; Ng *et al*., 2013). It is partially hosted within the uplifted Wollaston Group basement hanging wall and adjacent Athabasca Group sedimentary rocks (Ng *et al*., 2013). The Zone 4 ore body is dominantly monometallic and composed of uraninite, with minor galena, pyrite, chalcopyrite, and Ni-Co-Au sulfides (Ng *et al*., 2013). Late coffinite, late poorly-crystallized uraninite, and recent secondary uranyl minerals also occur in the deposit (McGill *et al*., 1993; Fayek and Kyser, 1997).

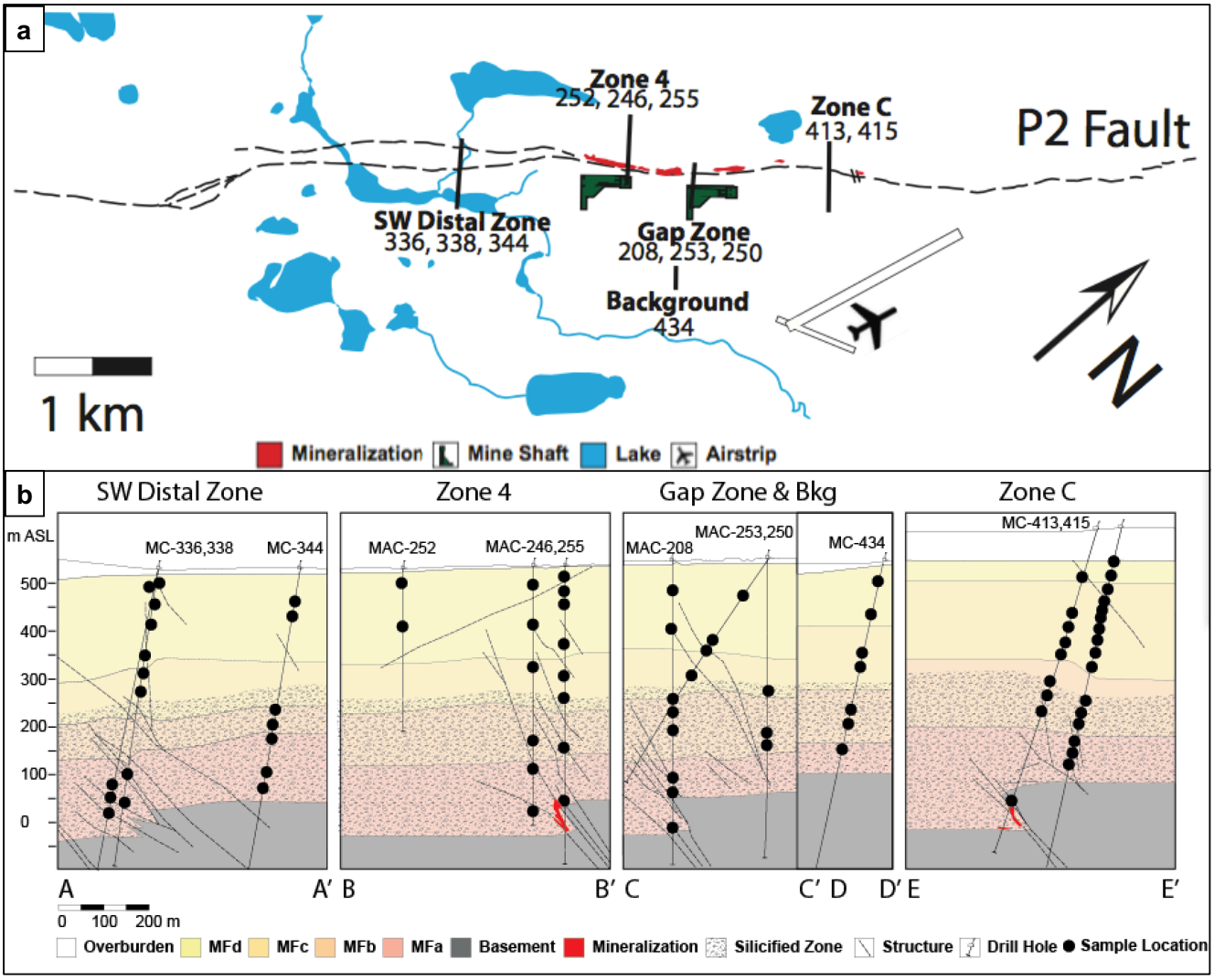

Figure 2.2: a) Map view of the McArthur River area, highlighting the five zones and drill holes where the fractures for this study were collected; b) Cross section of the McArthur River area, showing the five zones and drill holes where the fractures for this study were collected. Sample locations indicated as a solid circle. Figure modified from Joyce (2016).

The Athabasca sandstones and conglomerates in the McArthur River area consist of *ca*. 95% quartz (+ minor heavy minerals) and 0-5% matrix minerals by volume (Kotzer and Kyser, 1995; Hiatt *et al*., 2007). The underlying Paleoproterozoic Wollaston Group metasedimentary rocks contain mainly quartz, plagioclase, biotite, cordierite, garnet, and minor tourmaline, with anatectic pegmatite and graphite layers, and unconformably overlie Archean granitoid gneiss (Ey

et al., 1991; Marlatt *et al*., 1992). The graphite layers include a 25 m thick sequence of graphitic pelitic gneiss (McGill *et al*., 1993). Early diagenesis of the basin formed quartz overgrowths, an APS (aluminum-phosphate-sulphate) mineral, and hematite on detrital quartz of the Manitou Falls Formation (Kotzer and Kyser, 1993, 1995; Derome *et al*., 2005). The Aluminum-Phosphate-Sulphate (APS) group mineral is associated with the clay and silicate minerals that comprise the alteration halo of U deposits in the basin (Cuney and Kyser, 2014). Kotzer and Kyser (1995) used increasing $\delta^{18}O$ values, high salinities and homogenization temperatures in fluid inclusions in diagenetic quartz to indicate that continual water-rock interactions chemically and isotopically modified the basinal fluids, and to some extent, basement fluids. Prior to interaction of fluids along fractures, illite and dickite were produced throughout the entire basin by alteration of detrital silicates during peak diagenesis of the Athabasca Group (Percival, 1993; Kotzer and Kyser, 1995; Laverret *et al*., 2006). Therefore, the predominant clay assemblage of the Athabasca Group is dickite (+/- kaolinite) +/- illite (Hoeve and Quirt, 1984).

The study examined five zones in the McArthur River deposit area, represented by drill fences that are perpendicular to the structural trend of the P2 fault (Figure 2.2). These areas include, from southwest to northeast, the South West Distal Zone (weakly mineralized), Zone 4 (strongly mineralized), the Gap Zone (between zones of mineralization), Background (drill hole MC-434) and Zone C (moderately mineralized) (Figure 2.2).

2.3 Methods

Open fracture surfaces may have fracture coatings which have been used in this study as the primary criteria for classifying fractures into seven types. The near-fracture surface material, adjacent to the fracture, is considered to contain a local background signature or a signature of a

prior fluid event experienced by that fracture. Sixty-seven fractures that cut Manitou Falls Formation sandstones, from depths >100 m below the surface, and from 12 drill holes were sampled for detailed study (Figure 2.2b), while an additional fifteen near-surface fractures (<100 m from the surface from the Devine (2016) study) were also investigated. They represent the spectrum of fracture coating types observed in drill core from the McArthur River U deposit. Abbreviations of minerals are those of Whitney and Evans (2010).

Fracture types were classified based on color, mineralogy, and geochemistry of fracture coatings and wall rock material. The orientation (α) relative to vertical of fractures (degrees TCA) was used to assess orientations of the fractures as pathways for fluid movement. The open faces of the fractures were documented by photography.

Petrography was carried out on fracture coatings using a Leica E24D microscope for transmitted and reflected light optical petrography to document mineralogy, grain size, and color. A section of each fracture surface was mounted on a SEM (scanning electron microscopy) sample stub for high-magnification visual examination to determine the mineralogy and paragenesis of each fracture coating using a FEI Quanta 650 field emission gun environmental scanning electron microscope (FEG ESEM) equipped with a back-scatter detector (BSED) and two Bruker XFlash Si-Drift energy dispersive spectrometers (EDS). Analyses were conducted at 25 kV in Low Vacuum mode at a chamber pressure of 0.45 torr.

The fracture coatings were removed as a fine powder from the fracture surface using a dental drill. A portion of the fine powder was used to verify the mineralogy by X-ray diffraction (XRD) using a Panalytical X'Pert Pro MPD diffractometer using Co Kα radiation (1.79 Å) over the 2θ range from 5-100 degrees. Data was analyzed using Panalytical Highscore 4.0 software and the ICDD PDF-2 2015 database.

A separate portion of the fracture coating materials was used for geochemical analysis by weak acid leach (WAL), a technique to leach mobile elements with 2% HNO_3, following the method of Holk *et al*. (2003). WAL was also done on twenty samples of wall rock material to determine the elemental differences between the near-fracture material and the fracture coating. The wall rock material was isolated from the fracture surface using a diamond rock saw, crushed using a ceramic jaw crusher, and sieved to a <0.5 mm fraction. *Aqua regia* (AR), a more aggressive leaching technique, using a modified 1:1:1 mixture of distilled $HCl:HNO_3:H_2O$ was only used on the fracture powder for elemental and isotope geochemistry (Table 2.1). Leach/digestion solutions were analyzed using a Thermo Scientific Element II XR high-resolution inductively coupled plasma mass spectrometry (HR-ICP-MS) to determine major elements and trace element concentrations, and Pb isotope ratios including $^{207}Pb/^{206}Pb$, $^{208}Pb/^{206}Pb$, $^{206}Pb/^{204}Pb$, $^{207}Pb/^{204}Pb$ and $^{208}Pb/^{204}Pb$. A list of parameters used for the Thermo Scientific Element II XR HR-ICP-MS are specified in appendix D.

Table 2.1: Sample preparation summary for WAL and AR.

Method	Amount of sample (g)	Acid added (mL)	Reaction time (hr)	Acid removed (mL)	Dilution (g)
WAL	0.1	2	2 at 44°C	1	5
AR	0.1	0.5:0.5:0.5	1 at 95°C		5

SWIR (Shortwave Infrared reflectance) spectroscopy was also used to characterize the clay mineralogy. A Terraspec 4 (ASD Inc.) contact probe analyzer was used to obtain SWIR spectra using a 10 mm spot diameter, a 100 ms scanning time, and a 3-10 μm spectral resolution across a wavelength range of 350-2500 nm. Reflectance spectra in the SWIR (Shortwave Infrared Reflectance Spectrometer) were collected on the open fracture face and on the side of the core sample away from the fracture. The spectral data were interpreted using MinSpec4 software

(Earle, 1997, *et al*., 1999), which is calibrated to report relative abundances (%) of illite, chlorite, dickite, kaolinite, and dravite as well as signal-to-noise ratios (Appendix E). Signal-to-noise ratios of less than 10 were considered to be unusable.

Hyperspectral SWIR imaging of the fracture surface and the near-fracture surface area for mineral identification was acquired between 1000-2500 nm using Specim's SisuROCK hyperspectral scanner at the University of Alberta. The instrument was fitted with a OLES56 (high-resolution) lens, yielding infrared data at a spatial resolution of 0.2 mm/pixel. Each sample was scanned twice, once with the fracture facing the camera for the fracture surface, and once with the fracture perpendicular to the camera for the near-fracture surface area. Similar to the Terraspec spectral data processing, raw data were automatically converted to reflectance by normalizing radiance-at-sensor data to a 99% reflectance Spectralon panel fixed to the instrument. In SWIR, kaolinite shows a characteristic doublet absorption at 2160 nm (weak) and 2205 nm (strong), whereas white mica has a single broader absorption around 2200 nm (strong). The presence of a sharp absorption at 2160 nm therefore uniquely identifies kaolinite, and its second absorption is always located at 2205 nm. For white mica, the exact position of the 2200 nm absorption feature varies with composition. Muscovite end member has an absorption at 2192 nm, which increases up to 2215nm with decreasing Al (Post and Noble, 1993; Duke 1994). Reflectance data was analysed on a pixel-by-pixel basis to locate the exact position of the 2160 nm and 2200 nm absorption features and create mineral maps.

An indication of the pH of fluids that interacted with the fracture surfaces was determined by means of pH measurement on fracture coatings following the method of Vorres (1995). A small amount (0.1 g) of fracture coating material was suspended as a slurry ~0.5 mL of distilled

water; each slurry was agitated and then left to react for 10-20 minutes, before a pH measurement was made using Fisherbrand 4-7 plastic pH indicator strips, with a precision of +/- 0.5 pH units.

Hydrogen and oxygen isotope analyses were conducted on eighteen fracture coatings to constrain fluid sources and temperatures associated with the formation of fracture coating minerals. A portion of fine powder from the fracture surface was used for analysis. Samples were chosen from the most mineralogically homogeneous fracture fillings. Oxygen isotopic compositions were determined by extracting oxygen from 5 mg of fracture coating powder at 550-600°C according to the conventional BrF_5 procedure of Clayton and Mayeda (1963) and analyzed using a Thermo-Finnigan Delta^{Plus} XP Isotope-Ratio Mass Spectrometer (IRMS). The $\delta^{18}O$ values are reported using the delta (δ) notation in units of permil (‰) relative to the Vienna Standard Mean Ocean Water (VSMOW) international standard, with a precision of 0.2‰. Hydrogen isotopic compositions were determined by weighing ~1 mg of fracture coating powder into silver capsules, followed by degassing for 1 hour at 100°C. The samples were then crushed and loaded into a zero-blank auto sampler purged with ultrahigh-pressure (UHP) helium. The hydrogen isotopic composition was measured using a Thermo-Finnigan thermo-combustion elemental analyzer (TC/EA) coupled to a Thermo-Finnigan DeltaPlus XP Continuous-Flow Isotope-Ratio Mass Spectrometer (CF-IRMS). The $\delta^{2}H$ values are reported using delta (δ) notation in per mil (‰), relative to Vienna Standard Mean Ocean Water (VSMOW), with a precision of 3‰. Oxygen isotope fractionation factors used throughout this study are those experimentally-derived from Sheppard and Gilg (1996) for kaolinite-water and illite-water, and Yapp (1987, 1990) for goethite-water. Hydrogen isotope fractionation factors used for kaolinite-water are those experimentally derived from Sheppard and Gilg (1996) and for goethite-water are those derived from Yapp and Pedley (1985). Although hydrogen isotope fractionation factors have not been determined for reactions between illite and water, smectite has been used to

approximate reactions between illite and water due to similarities in structure (Yeh, 1980). Therefore, the fractionation factor for clay (illite-smectite mixture)-water used throughout this study and empirically derived from Capuano (1992), represents both illite-water and smectite-water.

2.4 Results

2.4.1 Fracture characteristics

Fracture coatings were grouped into seven types based on color, mineralogy, and chemistry. All fracture types reflect minerals that were formed on the fracture surface and are normally visible in hand specimen.

Type 1 is the most abundant fracture type in the McArthur River drill core (30 samples). It contains brown-stained fracture fillings/coatings of Mn oxides, goethite, and hematite, and minor kaolinite, illite, and dravite (Figure 2.3). Type 2 is the second most abundant fracture type (20 samples) and these fractures contain white and yellow crusted or stained fracture coatings of goethite on dravite, kaolinite, and illite (Figure 2.4). Type 3 fractures are white (15 samples) and contain one or more of dravite, illite, and/or kaolinite (Figure 2.5). Type 4 is characterized by black-stained fracture coatings (9 samples) of Mn oxides on illite, kaolinite, and minor dravite (Figure 2.6), whereas type 5 are black and orange crusted fracture coatings (3 samples) with goethite and Mn oxide on illite and kaolinite (Figure 2.7). Type 6 fractures contain drusy quartz (3 samples from McArthur River), the crystals of which are commonly overgrown by later goethite and Mn oxide crusts (Figure 2.8). Type 7 is pink (2 samples) and contains illite, kaolinite, and disseminated Fe oxide (Figure 2.9).

The dominant fracture coating minerals include clay minerals (kaolinite, illite, chlorite and dickite), dravite, Fe oxides/hydroxides (goethite and hematite), Mn oxides, and drusy quartz.

Fracture coating minerals only present in minor quantities, detectable using SEM and/or XRD, include APS (aluminum-phosphate-sulfate) minerals, lepidocrocite, Ti oxides, pyrite, siderite and organic matter.

The crystal habits of the dominant fracture coating minerals are also a function of fracture type. For example, goethite exhibits a botryoidal habit in most brown fractures (type 1; Figure 2.3), but has a fibrous habit in most white and yellow (type 2; Figure 2.4) and black and orange (type 5; Figure 2.7) fracture types. Pink fractures (type 7) have amorphous Fe oxide and poorly crystalline kaolinite (Figure 2.9). Mn oxides exhibit a fibrous habit in most black fractures (type 4; Figure 2.6) and quartz in type 6 fractures is euhedral (Figure 2.8). White fractures (type 3) contain abundant of clay minerals, including variably crystalline kaolinite (Figure 2.5). So, the habit of major fracture coating minerals can also be used with color and geochemistry to identify fracture types.

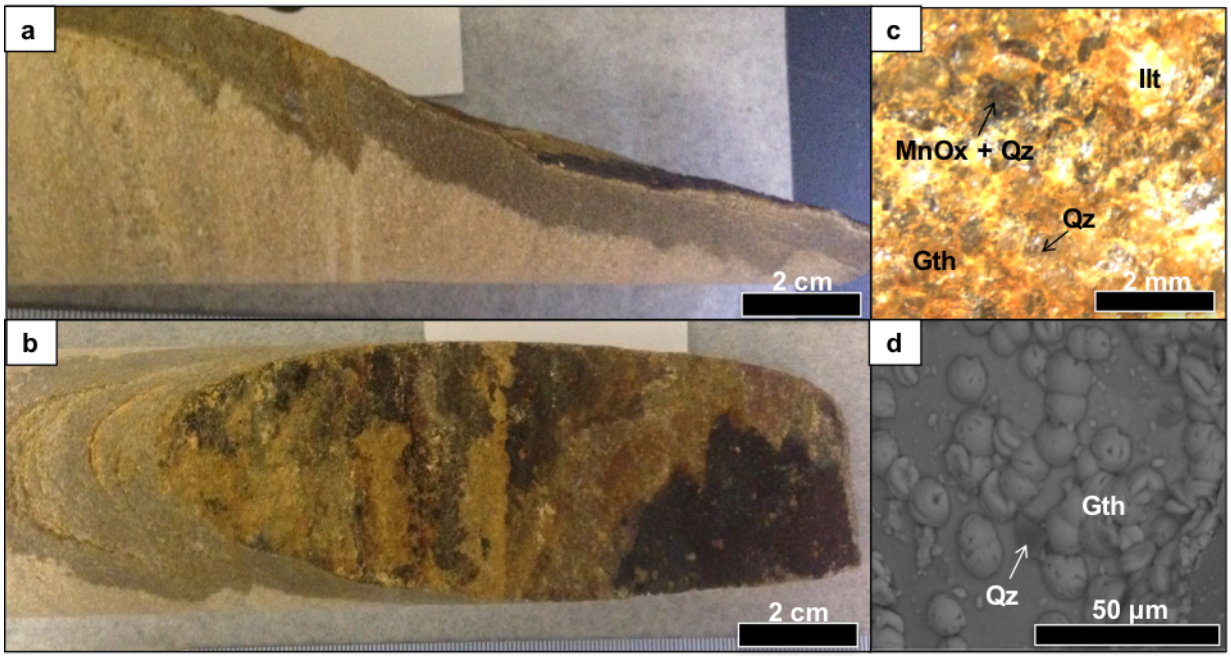

Figure 2.3: Type 1 - Brown fracture coating (MC-344-379.3), showing (a) open fracture face, (b) fracture orientation, (c) optical mineralogy, and (d) SEM mineralogy.

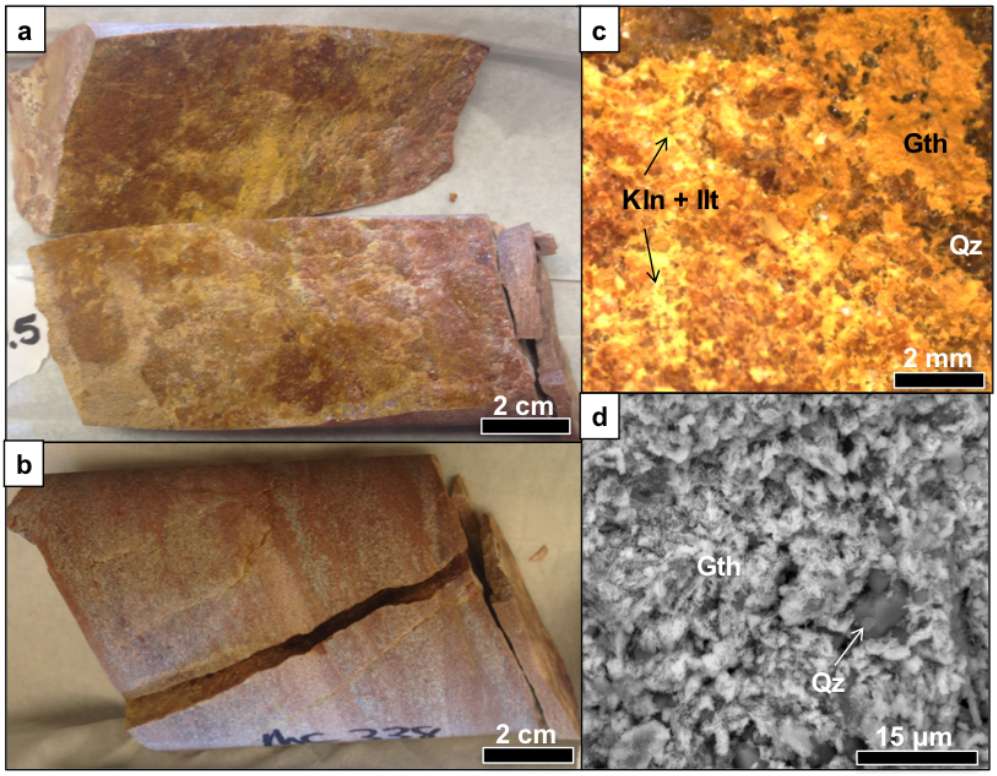

Figure 2.4: Type 2 - White and Yellow fracture coating (MC-338-504.5), showing (a) open fracture face, (b) fracture orientation, (c) optical mineralogy, and (d) SEM mineralogy.

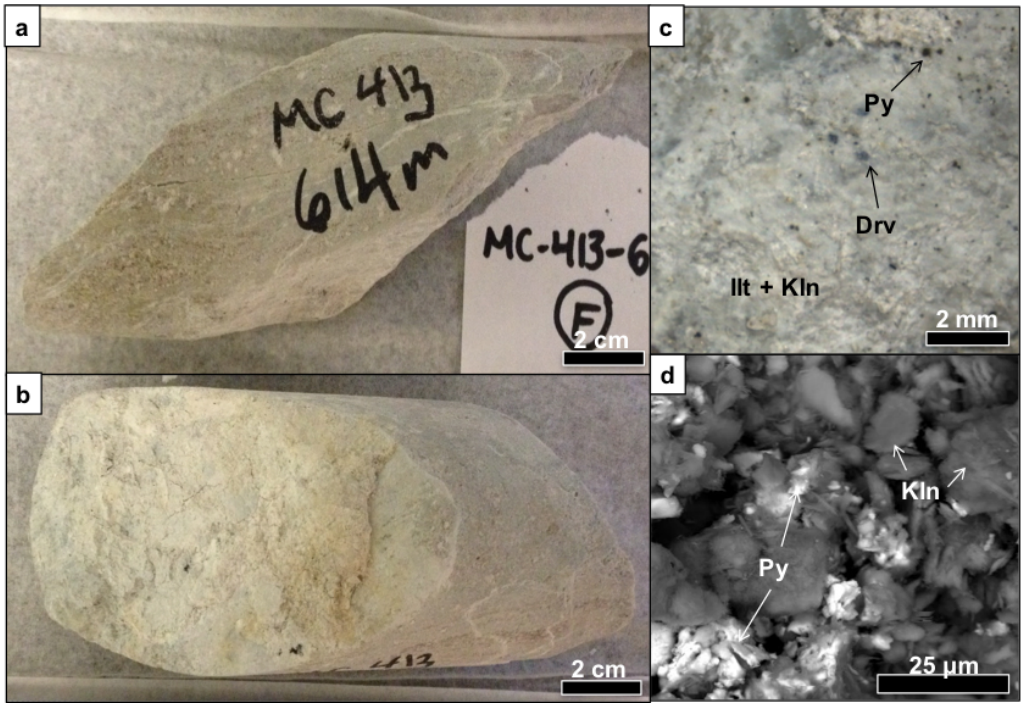

Figure 2.5: Type 3 - White fracture coating (MC-413-614), showing (a) open fracture face, (b) fracture orientation, (c) optical mineralogy, and (d) SEM mineralogy.

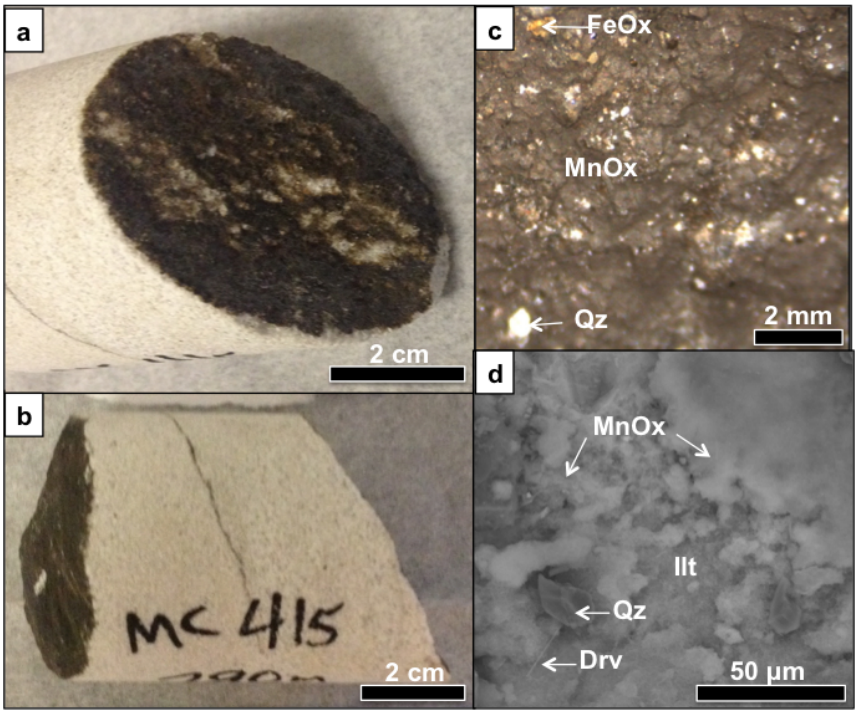

Figure 2.6: Type 4 - Black fracture coating (MC-415-290), showing (a) open fracture face, (b) fracture orientation, (c) optical mineralogy and (d) SEM mineralogy.

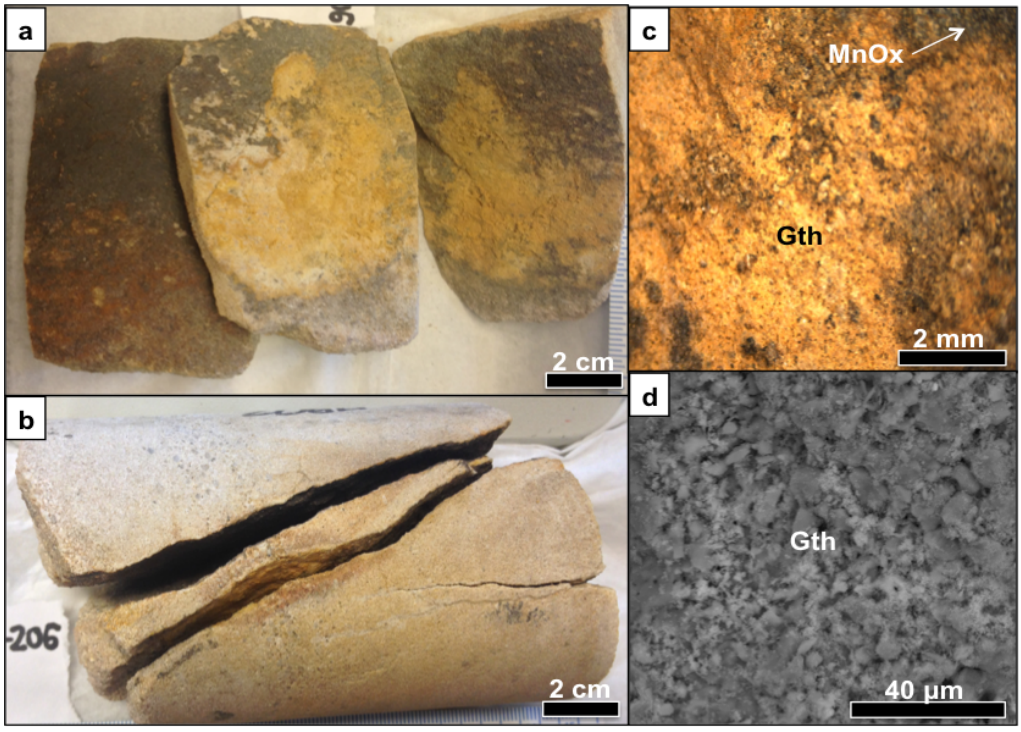

Figure 2.7: Type 5 - Black and orange fracture coating (MC-338-206), showing (a) open fracture face, (b) fracture orientation, (c) optical mineralogy, and (d) SEM mineralogy.

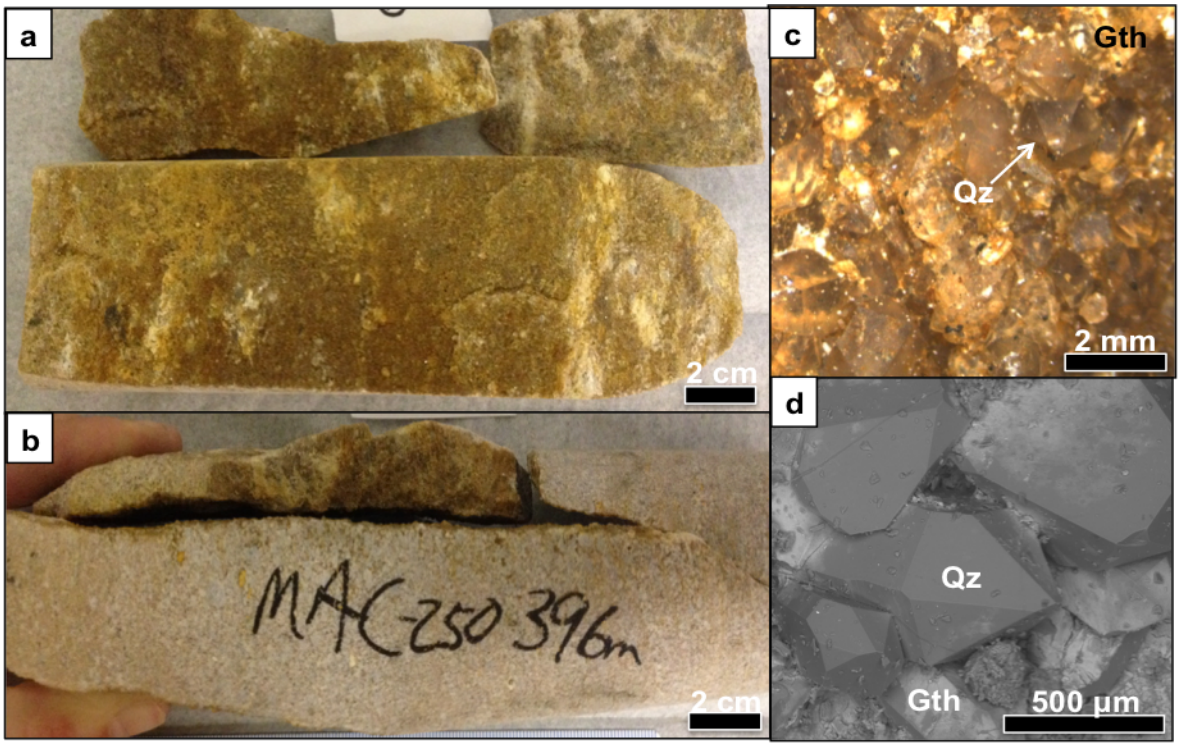

Figure 2.8: Type 6 - Drusy quartz fracture coating (MAC-250-396), showing (a) open fracture face, (b) fracture orientation, (c) optical mineralogy, and (d) SEM mineralogy.

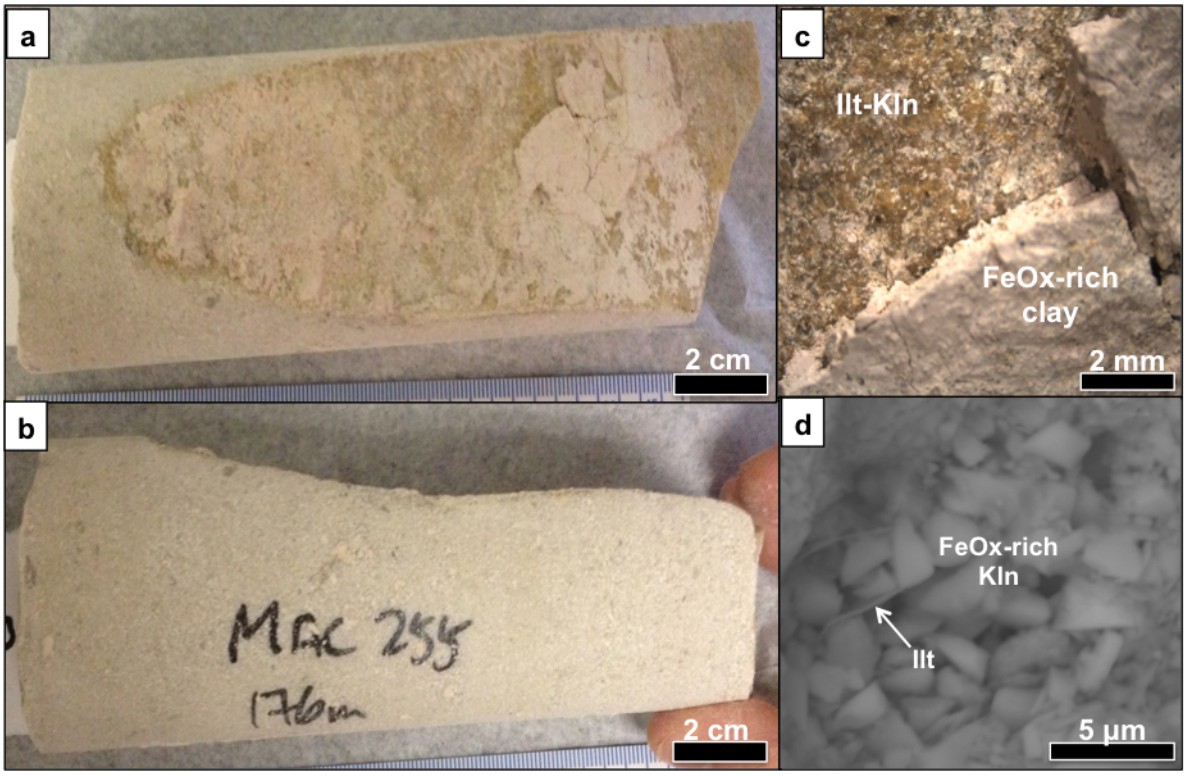

Figure 2.9: Type 7 - Pink fracture coating (MAC-255-176), showing (a) open fracture face, (b) fracture orientation, (c) optical mineralogy, and (d) SEM mineralogy.

All investigated fractures were from the Manitou Falls Formation sandstone. The shallowest sample represents a depth of ~11 m, whereas the deepest sample was at ~580 m. The horizontal extent of the sampling area is ~3150 m along the P2 fault (Figure 2.2b). Type 1 (brown), type 2 (white and yellow), and type 3 (white) fracture types occur at all depths. Black (type 4), black and orange (type 5), and pink (type 7) fractures, which have characteristic Mn-Fe oxides that impart a dark color to the fracture, occur at shallower depths (Figure 2.10). Drusy quartz (type 6) fractures occur proximal to the unconformity.

Samples from the non-mineralized drill hole, MC-434, are considered to represent a local background signature for the Manitou Falls Formation in the McArthur River region, as the drill hole MC-434 is located ~1 km from the strongly mineralized Zone 4 drill hole (Figure 2.2a). Fractures in MC-434 drill core include brown (type 1), white and yellow (type 2), and white (type 3) types (Figure 2.10), which are rich in dickite and illite. The fracture wall-rock mineralogy is similar to the fracture filling and thus the mineralogy is interpreted to represent a regional background.

Fracture orientations were measured relative to vertical of fractures to assess orientations of the fractures as pathways for fluid movement. All of the studied drill holes are sub-vertical (Table 2.2). Fracture orientations typically occur primarily at shallow angles of less than 50° relative to vertical (Table 2.2; Figure 2.11a), providing sub-vertical permeable pathways for fluid movement. A smaller subset of fractures were found to dip between 50°-90° (Figure 2.11b), including two white fracture coatings (type 3) at 87° and 90° relative to vertical; these fractures occur at shallow depths (<100 m).

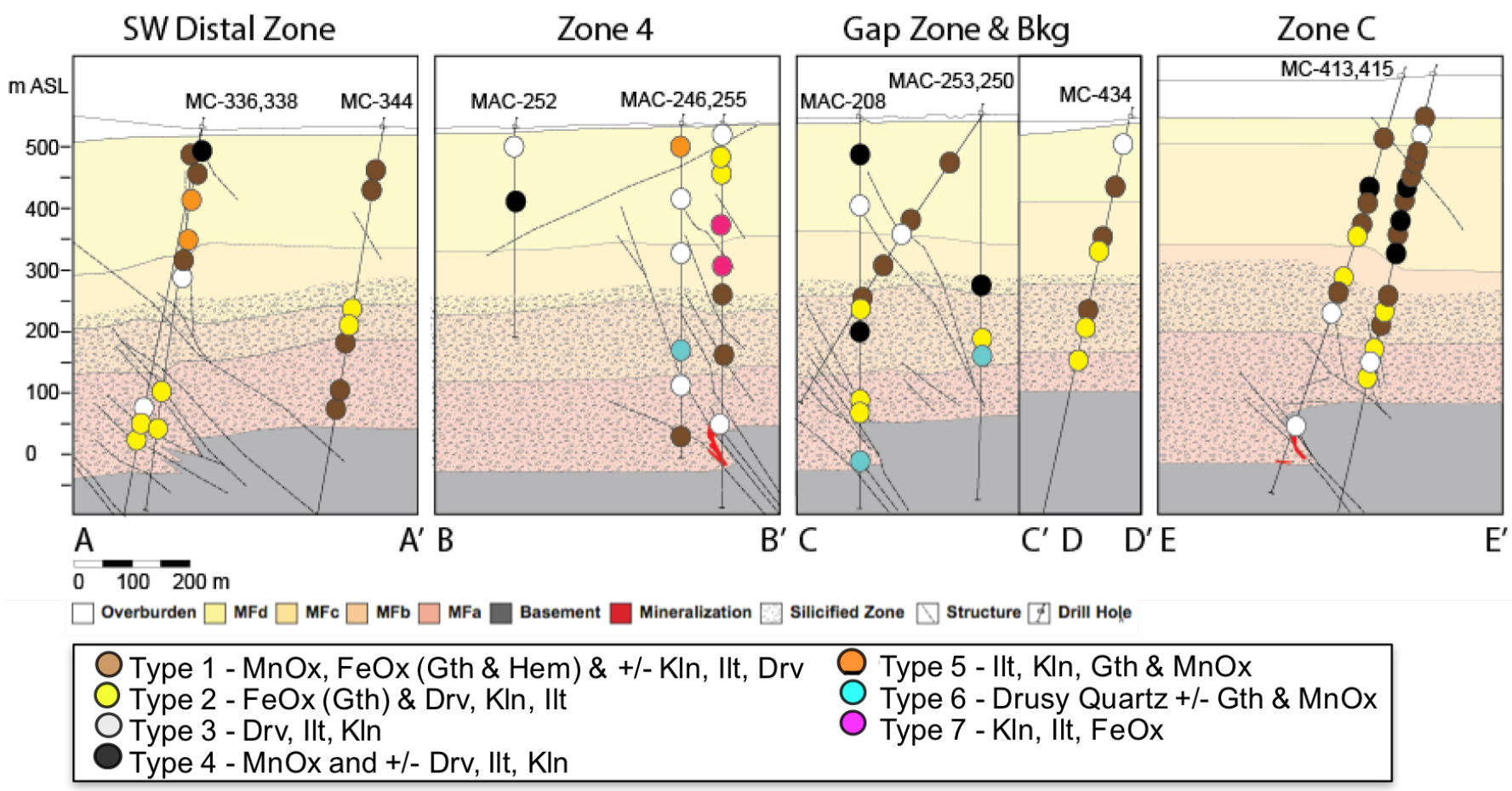

Figure 2.10: Cross-section across the P2 fault at McArthur River (Figure 2.2) showing near-vertical drill core and locations of fracture types. Figure modified from Joyce (2016).

Table 2.2: Depth, drill hole attitude, type, and orientation relative to vertical of fractures from McArthur River.

Sample ID	Drill Hole ID	Depth (m)	Drill Hole Dip (°)	Fracture Type	Fracture Orientation (α)
MAC-208-57.6	MAC-208	57.60	-90	4 - Black	0.0
MAC-208-154.8	MAC-208	154.80	-90	3 - White	20.0
MAC-208-262.5	MAC-208	262.50	-90	1 - Brown	15.0
MAC-208-263	MAC-208	263.00	-90	2 - White & Yellow	15.0
MAC-208-305	MAC-208	305.00	-90	4 - Black	15.0
MAC-208-462	MAC-208	462.00	-90	2 - White & Yellow	10.0
MAC-208-476.5	MAC-208	476.50	-90	2 - White & Yellow	45.0
MAC-208-570	MAC-208	570.00	-90	6 - Drusy Quartz	42.5
MAC-246-23.1	MAC-246	23.10	-90	5 - Black & Orange	15.0
MAC-246-142	MAC-246	142.00	-90	3 - White	20.0
MAC-246-198.5	MAC-246	198.50	-90	3 - White	15.0
MAC-246-395	MAC-246	395.00	-90	6 - Drusy Quartz	3.0
MAC-246-446	MAC-246	446.00	-90	3 - White	40.0
MAC-246-534	MAC-246	534.00	-90	1 - Brown	38.5
MAC-250-276	MAC-250	276.00	-90	4 - Black	20.0
MAC-250-390.5	MAC-250	390.50	-90	2 - White & Yellow	45.0
MAC-250-396	MAC-250	396.00	-90	6 - Drusy Quartz	20.0
MAC-252-21.7	MAC-252	21.70	-90	3 - White	10.0
MAC-252-135.5	MAC-252	135.50	-90	4 - Black	30.0
MAC-253-70.4	MAC-253	70.40	-54	1 - Brown	76.0
MAC-253-235	MAC-253	235.00	-54	1 - Brown	56.0
MAC-253-236	MAC-253	236.00	-54	3 - White	88.5
MAC-253-294.5	MAC-253	294.50	-54	1 - Brown	61.0
MAC-255-11.3	MAC-255	11.30	-90	3 - White	30.0
MAC-255-37	MAC-255	37.00	-90	2 - White & Yellow	0.0
MAC-255-47.2	MAC-255	47.20	-90	2 - White & Yellow	22.5
MAC-255-176	MAC-255	176.00	-90	7 - Pink	15.0
MAC-255-251	MAC-255	251.00	-90	7 - Pink	5.0
MAC-255-305	MAC-255	305.00	-90	1 - Brown	45.0
MAC-255-408	MAC-255	408.00	-90	1 - Brown	5.0
MAC-255-509	MAC-255	509.00	-90	3 - White	10.0
MC-336-28.1	MC-336	28.10	-78	1 - Brown	17.0
MC-336-497	MC-336	497.00	-78	3 - White	32.0
MC-336-503.3	MC-336	503.30	-78	2 - White & Yellow	32.0
MC-336-523.8	MC-336	523.80	-78	2 - White & Yellow	62.0
MC-338-20.7	MC-338	20.70	-81	4 - Black	44.0
MC-338-61.3	MC-338	61.30	-81	1 - Brown	44.0
MC-338-121	MC-338	121.00	-81	5 - Black & Orange	14.0
MC-338-206	MC-338	206.00	-81	5 - Black & Orange	34.0
MC-338-231.8	MC-338	231.80	-81	1 - Brown	24.0
MC-338-234	MC-338	234.00	-81	3 - White	34.0
MC-338-429.7	MC-338	429.70	-81	2 - White & Yellow	17.5
MC-338-504.5	MC-338	504.50	-81	2 - White & Yellow	34.0
MC-344-65.6	MC-344	65.60	-80	1 - Brown	30.0
MC-344-122	MC-344	122.00	-80	1 - Brown	60.0
MC-344-321	MC-344	321.00	-80	2 - White & Yellow	20.0
MC-344-375.5	MC-344	375.50	-80	2 - White & Yellow	40.0
MC-344-379.3	MC-344	379.30	-80	1 - Brown	33.5
MC-344-443	MC-344	443.00	-80	1 - Brown	30.0
MC-344-475	MC-344	475.00	-80	1 - Brown	20.0
MC-413-73.6	MC-413	73.60	-72	1 - Brown	18.0
MC-413-207.52	MC-413	207.52	-72	4 - Black	18.0
MC-413-224	MC-413	224.00	-72	1 - Brown	18.0
MC-413-267.16	MC-413	267.16	-72	1 - Brown	51.0
MC-413-274.5	MC-413	274.50	-72	2 - White & Yellow	18.0
MC-413-346.26	MC-413	346.26	-72	2 - White & Yellow	36.5
MC-413-359.5	MC-413	359.50	-72	1 - Brown	23.0
MC-413-407	MC-413	407.00	-72	3 - White	18.0
MC-413-614	MC-413	614.00	-72	3 - White	63.0
MC-415-80.4	MC-415	80.40	-77	1 - Brown	58.0
MC-415-82.9	MC-415	82.90	-77	3 - White	87.0
MC-415-126	MC-415	126.00	-77	1 - Brown	53.0
MC-415-137	MC-415	137.00	-77	1 - Brown	16.0
MC-415-141.5	MC-415	141.50	-77	1 - Brown	33.0
MC-415-143.1	MC-415	143.10	-77	4 - Black	46.5
MC-415-208.56	MC-415	208.56	-77	1 - Brown	20.5
MC-415-212	MC-415	212.00	-77	4 - Black	23.0
MC-415-246.3	MC-415	246.30	-77	1 - Brown	16.0
MC-415-290	MC-415	290.00	-77	4 - Black	58.0
MC-415-379	MC-415	379.00	-77	1 - Brown	38.0
MC-415-402.97	MC-415	402.97	-77	2 - White & Yellow	28.0
MC-415-405.5	MC-415	405.50	-77	1 - Brown	13.0
MC-415-459.5	MC-415	459.50	-77	2 - White & Yellow	16.0
MC-415-459.69	MC-415	459.69	-77	3 - White	35.5
MC-415-494	MC-415	494.00	-77	2 - White & Yellow	13.0
MC-434-42	MC-434	42.00	-75	3 - White	90.0
MC-434-118	MC-434	118.00	-75	1 - Brown	23.5
MC-434-213	MC-434	213.00	-75	1 - Brown	50.0
MC-434-214	MC-434	214.00	-75	2 - White & Yellow	50.0
MC-434-337	MC-434	337.00	-75	1 - Brown	45.0
MC-434-342	MC-434	342.00	-75	2 - White & Yellow	75.0
MC-434-408	MC-434	408.00	-75	2 - White & Yellow	65.0

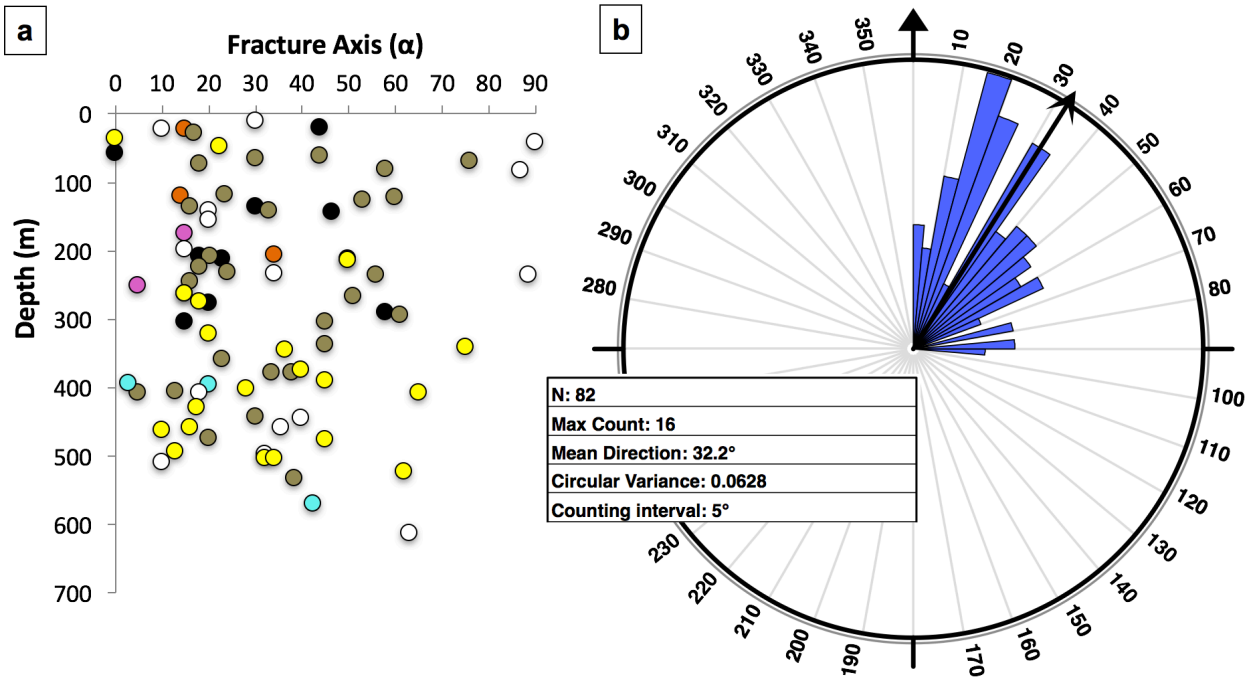

Figure 2.11: a) Orientation relative to vertical of fractures (α) versus depth, showing various fracture types by color for McArthur River samples. See Figure 2.10 for color legend. b) Rose diagram of fracture orientations, highlighting the mean fracture orientation of 32.2°.

2.4.2 Mineral paragenesis

Petrographic relationships derived from visible examination, optical microscopy, and SEM-BSE images and EDS spectra, were used to formulate a generalized paragenetic sequence of minerals from individual fracture types at McArthur River (Figure 2.12). Well-formed ~30 μm polygonal dickite formed early in the paragenesis in brown (type 1), white and yellow (type 2), white (type 3), black (type 4), and drusy quartz (type 6) fractures. This dickite is followed by minor well-crystallized kaolinite (K1; Figure 2.13c) and interlocking fibrous illite (2.13d, e), in brown (type 1) and white (type 3) fractures. Several authors (Hoeve and Quirt, 1984; Halter *et al*., 1989; Kotzer and Kyser, 1995) indicate that illite, euhedral quartz, dravite, and chlorite are associated with the hydrothermal alteration in areas of intense fracturing and can be part of the late ore-forming system, but are primarily post-ore. Kaolinite and illite are overprinted by fine-grained chlorite in white (type 3) and drusy quartz (type 6) fractures proximal to the unconformity, and at intermediate depths (~250 m) for brown (type 1) and black (type 4) fractures. Acicular alkali-deficient dravite (T1; Figure 2.13i) and euhedral quartz (Q1; Figure 2.13f) are paragenetically later in brown (type 1), white and yellow (type 2), white (type 3), black (type 4), and drusy quartz (type 6) fractures in MFd. In contrast, euhedral quartz is present as crystals <0.4 mm in size in the lower sandstones (MFa and MFb) in proximity to the P2 fault and in the silicified zone in drusy quartz (type 6) fractures. Alkali-deficient dravite (T2; Figure 2.13j) occurs as acicular rods and interstitial aggregates within most fractures.

Diagenetic and hydrothermal mineral assemblages were subsequently altered and variably overprinted by minerals that formed from late low-temperature meteoric fluids, similar to the late kaolinite in fractures (K2) previously documented by Wilson and Kyser (1987), Kotzer and Kyser (1995), and Quirt (2001). Another late paragenetic mineral is framboidal pyrite, with crystals that are ~10-20 μm in size (Figure 2.13k) in white and yellow (type 2) and white (type 3)

fracture types from the lower sandstones and silicified zone. This pyrite can be associated with elongate siderite grains in white and yellow fracture coatings (type 2) and as ~120 μm rhombohedral crystals (Figure 2.13f) in drusy quartz (type 6) fracture coatings within the MFa and silicified zone, similar to what Ng *et al*. (2013) reported for hydrothermal post-ore minerals at McArthur River.

Small (<15 μm) pseudocubic APS minerals (Figure 2.13d), pervasive kaolinite (K2) (Figure 2.13a), and Fe-(Ti-Mn) oxy-hydroxides (Figure 2.13b, d-i, k, l) are also late phases present on the fracture surfaces. The APS minerals are associated with Fe-Mn oxides and late kaolinite in brown (type 1), white and yellow (type 2), white (type 3), black (type 4), and drusy quartz (type 6) fractures. Hematite is likely the Fe oxide shown on pink fracture coatings of pink colored clay in type 7 fractures, as well as a dark-red-to-maroon color associated with brown Fe oxides in type 1 fractures. Goethite is observed as a yellow crust in type 2 fractures and an orange crust in type 5 fractures. Mn oxy-hydroxide minerals occur as microfibers (Figure 2.13h) or botryoidal structures and are found with Fe oxides on fracture coatings which occur as late black crusts or stains. Iron and Mn oxides also occur as amorphous staining late in the paragenesis.

Titanium oxides occur in clusters similar to APS minerals, with a tetragonal to orthorhombic habit (Figure 2.13i) in brown (type 1), white and yellow (type 2), white (type 3), and black (type 4) fractures. Organic material occurs in most fracture types as paragenetically late black spots (Figure 2.13l), strings, and amorphous forms (Figure 2.14h).

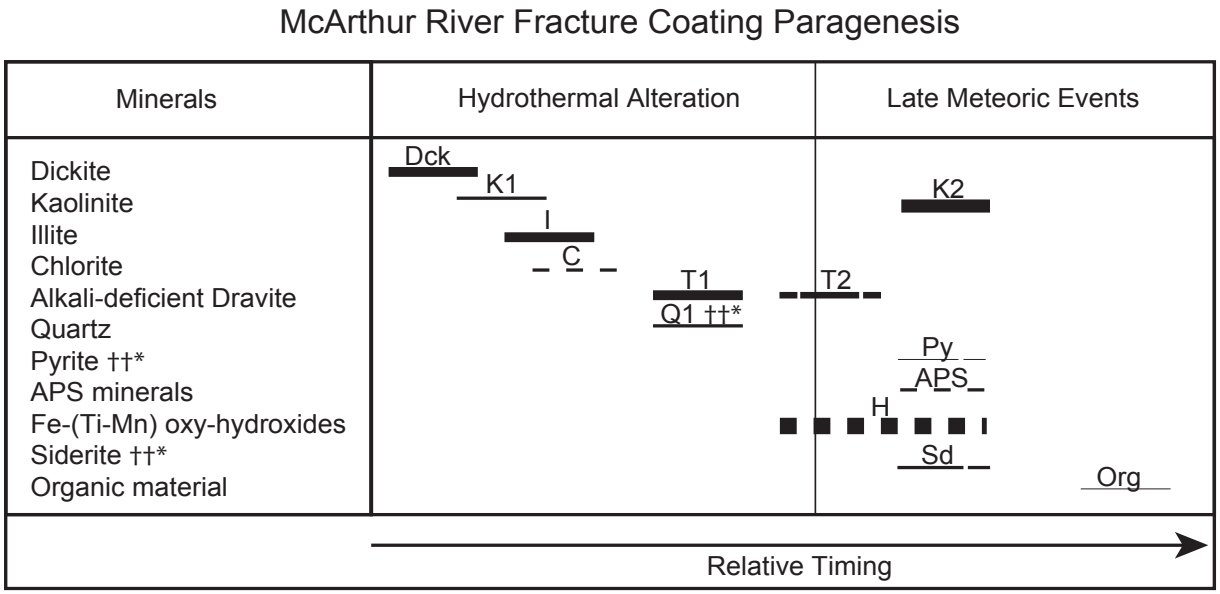

Figure 2.12: Generalized mineral paragenetic sequence of fracture coatings from the Athabasca sandstone in the McArthur River area, reflecting hydrothermal alteration and late meteoric water origins as determined by petrography and stable isotopic composition. The thickness of the line represents the relative abundance of each mineral and the dashed lines represent uncertainty in the timing of mineral formation. Figure modified from Kotzer and Kyser (1995), Fayek and Kyser (1997), and Ng *et al* (2013).

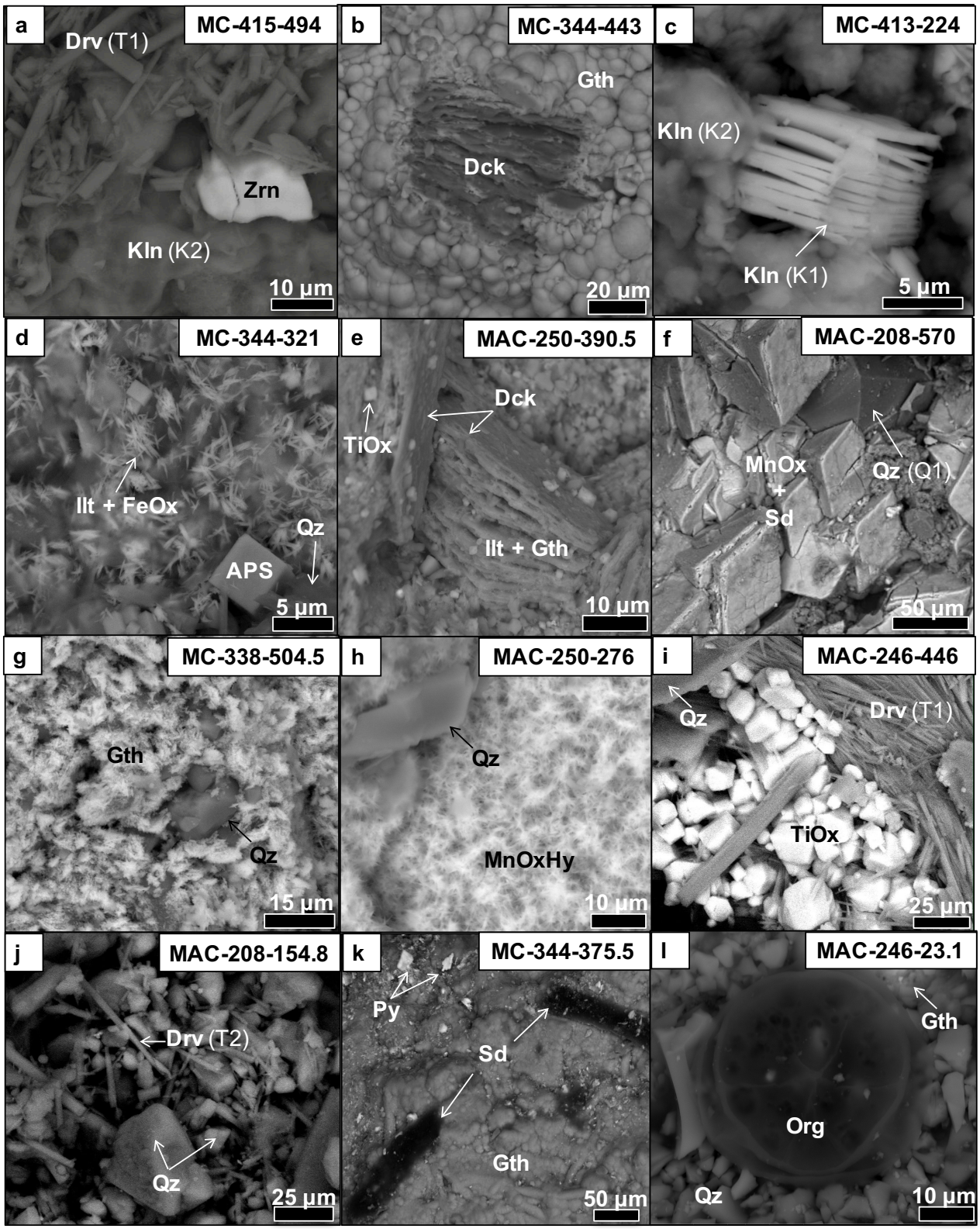

Figure 2.13: BSE images showing mineral assemblages of fracture coatings within the Athabasca sandstones. a) A detrital zircon (Zrn) grain is present with dravite (T1), followed

by late kaolinite (K2) from Zone C MFa sample MC-415-494 (type 2 - white and yellow fracture coating). b) Dickite is followed by botryoidal goethite from the South West Distal Zone MFa sample MC-344-443 (type 1 – brown fracture coating). c) Well-crystalline kaolinite (K1) followed by poorly-crystalline kaolinite (K2) from Zone C MFb sample MC-413-224 (type 1 - brown fracture coating). d) Detrital quartz from the sandstone is present with interlocking fibrous illite with Fe oxide staining and later pseudo-cubic APS minerals from the South West Distal Zone MFb sample MC-344-321 (type 2 - white and yellow fracture coating). e) Well-crystalline dickite (Dck) grains being replaced by illite with goethite staining, followed by Ti oxides from the Gap Zone MFb sample MAC-250-390.5 (type 2 – white and yellow fracture coating). f) Euhedral quartz (Q1) followed by rhombohedral siderite and then Mn oxide staining from Gap Zone MFa sample MAC-208-570 (type 6 - drusy quartz fracture coating). g) Fibrous goethite precipitating on detrital quartz grains within the South West Distal Zone MFa sample MC-338-504.5 (type 2 - white and yellow fracture coating). h) Fibrous Mn oxy-hydroxide staining on detrital quartz within the Gap Zone MFc sample MAC-250-276 (type 4 - black fracture coating). i) Detrital quartz grains with spherulitic dravite (T1) grains followed by Ti oxide from Zone 4 MFa sample MAC-246-446 (type 3 - white fracture coating). j) Interstitial dravite (T2) aggregates and partially dissolved detrital quartz from the Gap Zone MFd sample MAC-208-154.8 (type 3 - white fracture coating). k) Goethite associated with elongate siderite grains and framboidal pyrite crystals from the South West Distal Zone MFb sample MC-344-375.5 (type 2 - white and yellow fracture coating). l) Late goethite staining on detrital quartz followed by organic material from Zone 4 MFd sample MAC-246-23.1 (type 5 - black and orange fracture coating).

2.4.3 Stable isotopes

Stable isotope analyses were conducted on minerals from various fracture types with a known mineral paragenesis (Table 2.3). Pure mineral separates (>70%) were only possible from a limited number of samples because of the complexity of the mineral paragenesis in the fracture coatings and the small size of many of the minerals. Clay minerals range in $\delta^{18}O$ from +5.5 to +13.7 ‰ and in $\delta^{2}H$ from -155 to -44 ‰. Oxy-hydroxide minerals, specifically goethite, have more variable $\delta^{18}O$ and $\delta^{2}H$ values, ranging from +0.6 to +13.2 ‰ and -198 to -70 ‰, respectively (Table 2.3).

Table 2.3: $\delta^{18}O$ and $\delta^{2}H$ values of minerals from different types of fracture coatings. Dominant mineral phase indicates the sample was >70% of that mineral.

Sample ID	Fracture Type	Dominant Mineral Phase	$\delta^{2}H$ (‰)	$\delta^{18}O$ (‰)
MAC-255-408	1-Brown	Dck	-55	+8.5
MC-413-346.26	2-White & Yellow	Dck	-85	+13.2
MC-413-614	3-White	Kln	-85	+9.2
MAC-250-396	6-Drusy Quartz	Ilt	-104	+13.7
MC-344-321	2-White & Yellow	Ilt	-155	+5.5
MAC-246-446	3-White	Drv	-44	+9.7
MC-336-503.3	2-White & Yellow	Drv	-52	+9.8
MC-336-523.8	2-White & Yellow	Drv	-55	+10.1
MAC-255-176	7-Pink	Kln	-115	+12.3
MAC-208-462	2-White & Yellow	Gth	-102	+8.8
MC-388-504.5	2-White & Yellow	Gth	-70	+13.2
MC-434-408	2-White & Yellow	Gth	-97	+9.6
MC-338-206	5-Black & Orange	Gth	-115	+9.8
MC-344-375.5	2-White & Yellow	Gth	-162	+5.9
MC-344-379.3	1-Brown	Gth	-198	+0.6
MC-344-443	1-Brown	Gth	-169	+5.0
MAC-208-305	4-Black	MnOxHy	-69	+9.8
MAC-250-276	4-Black	MnOxHy	-75	+10.4

Dickite (Dck)

Well-crystallized polygonal dickite in samples MAC-255-408 (type 1 – brown) from Zone 4 and MC-413-346.26 (type 2 – white and yellow) from Zone C provides $\delta^{2}H$ values of -55 ‰ and -85 ‰ and $\delta^{18}O$ values of +8.5 ‰ and +13.2 ‰, respectively (Table 2.3; Figure 2.14a). These two samples are located ~100-200 m above uranium mineralization and are within the range of $\delta^{2}H$ and $\delta^{18}O$ values of high-temperature diagenetic kaolin and illite alteration in sandstones at 200°C (Kotzer and Kyser, 1995).

Kaolinite (K1)

Well-crystallized kaolinite (K1; Figure 2.14e) in MC-413-614, a type 3 white fracture from Zone C near uranium mineralization, has isotopic compositions that plot close to the values

for high-temperature diagenetic kaolin and illite in sandstones at 200°C (Kotzer and Kyser, 1995). The crystallinity of this kaolinite is also high, with a value of 0.73 on the Hinckley scale (Hinckley, 1962; Quirt, 2001).

Illite (Ilt)

Illite occurs on fracture coatings as fibrous interlocking grains (Figure 2.14f, g), contemporaneous with and post-dating K1 kaolinite (Figure 2.12). Illites from a type 2 white and yellow fracture in MAC-344-321 from the South West Distal Zone and from MAC-250-396 type 6 drusy quartz fracture from the Gap Zone have $\delta^{18}O$ values consistent with formation near 200°C from basinal fluids (Kotzer and Kyser, 1995) (Table 2.3; Figure 2.14a). However, these illite have anomalously low $\delta^{2}H$ values that could not have been derived by mixing of basinal fluids with other similar fluids present at the time of illite formation in the sandstone (Kotzer and Kyser, 1995). Therefore, preferential hydrogen isotope exchange likely occurred between illite and ^{2}H-depleted meteoric waters (Bird and Chivas, 1988; Longstaffe, 1989; Kyser and Kerrich, 1991; Percival *et al*., 1993).

Alkali-deficient dravite (T1)

Alkali-deficient dravite (T1) occurs as acicular grains on fracture coatings, typically with clay minerals such as illite and kaolinite. Dravite samples from MC-336-503.3 and MC-336-523.8, white and yellow type 2 fractures from the South West Distal Zone, and MAC-246-446 from Zone 4, a white fracture (type 3) ~100 m above uranium mineralization, have similar $\delta^{2}H$ values of -55 to -44 ‰ and $\delta^{18}O$ values between +9.7 to +10.1 ‰ (Table 2.3; Figure 2.14a). These values are similar to diagenetic illite and kaolinite in sandstones at 200°C (Kotzer and Kyser, 1995).

Kaolinite (K2)

Poorly-crystallized kaolinite (K2; Figure 2.14d) that is paragenetically late in sample MAC-255-176, a type 7 pink fracture from Zone 4 at ~300 m above uranium mineralization, has δ^2H and $\delta^{18}O$ values within the range of late low-temperature kaolinite in fractures (Kotzer and Kyser, 1995). The crystallinity of this kaolinite is low, with a value of 0.09 on the Hinckley scale (Hinckley, 1962; Quirt, 2001).

Goethite

Goethite also occurs paragenetically late, typically with Mn oxides and oxy-hydroxides. The presence of fibrous goethite from samples MAC-208-462 (white and yellow type 2 fracture; Gap Zone), MC-338-504.5 (South West Distal Zone (Figure 2.14b)), MC-434-408 (Background), and MC-338-206 (black and orange type 5 fracture; South West Distal Zone) have δ^2H values from -115 to -70 ‰ and $\delta^{18}O$ values from +5.8 and +13.2 ‰, respectively (Figure 2.14a). Botryoidal goethite (Figure 2.14c) from samples MC-344-379.3 (brown type 1 fracture), MC-344-443 (brown type 1 fracture), and MC-344-375.5 (white and yellow type 2 fracture), all from the South West Distal Zone, have very low δ^2H values of -198 to -162 ‰ and $\delta^{18}O$ values of +0.6 to +5.9 ‰, respectively.

The shift in δ^2H toward lower values in the botryoidal goethite is most likely due to either the contribution from organic material on samples that could not be removed (Figure 2.14h) or to preferential H isotope exchange with late meteoric waters (Bird and Chivas, 1988; Longstaffe, 1989; Kyser and Kerrich, 1991; Percival *et al*., 1993). To address this issue, mass balance equations were used to evaluate the effect of organic material on δ^2H. Assuming a δ^2H value of -280 ‰ for the organic matter (e.g. Friedman and O'Neil, 1978; Schimmelmann *et al*., 2006), the

percentage of organic material contaminant required to change the δ^2H value of a goethite-bearing sample such as MC-344-443 from a value of -80 ‰ a value typical for goethite that formed near 25°C (Rainbow *et al*., 2006) (Figure 2.14) to the -180 ‰ value obtained from this sample is 50%. This value is higher than the percentage of organic material determined to be in the sample (10%) using SEM, XRD, and 10% H_2O_2 leach extraction. Therefore, preferential isotope exchange between goethite and ^2H-depleted waters likely had a greater effect on the shift in δ^2H toward lower values.

Mn oxy-hydroxide

Microfibrous Mn oxy-hydroxides in samples MAC-208-305 and MAC-250-276 (black type 4 fractures; Gap Zone), typically occur with Fe oxides and oxy-hydroxides. They have δ^2H values of -69 ‰ and -75 ‰ and $\delta^{18}O$ values of +9.8 and +10.4 ‰ (Figure 2.14a), respectively.

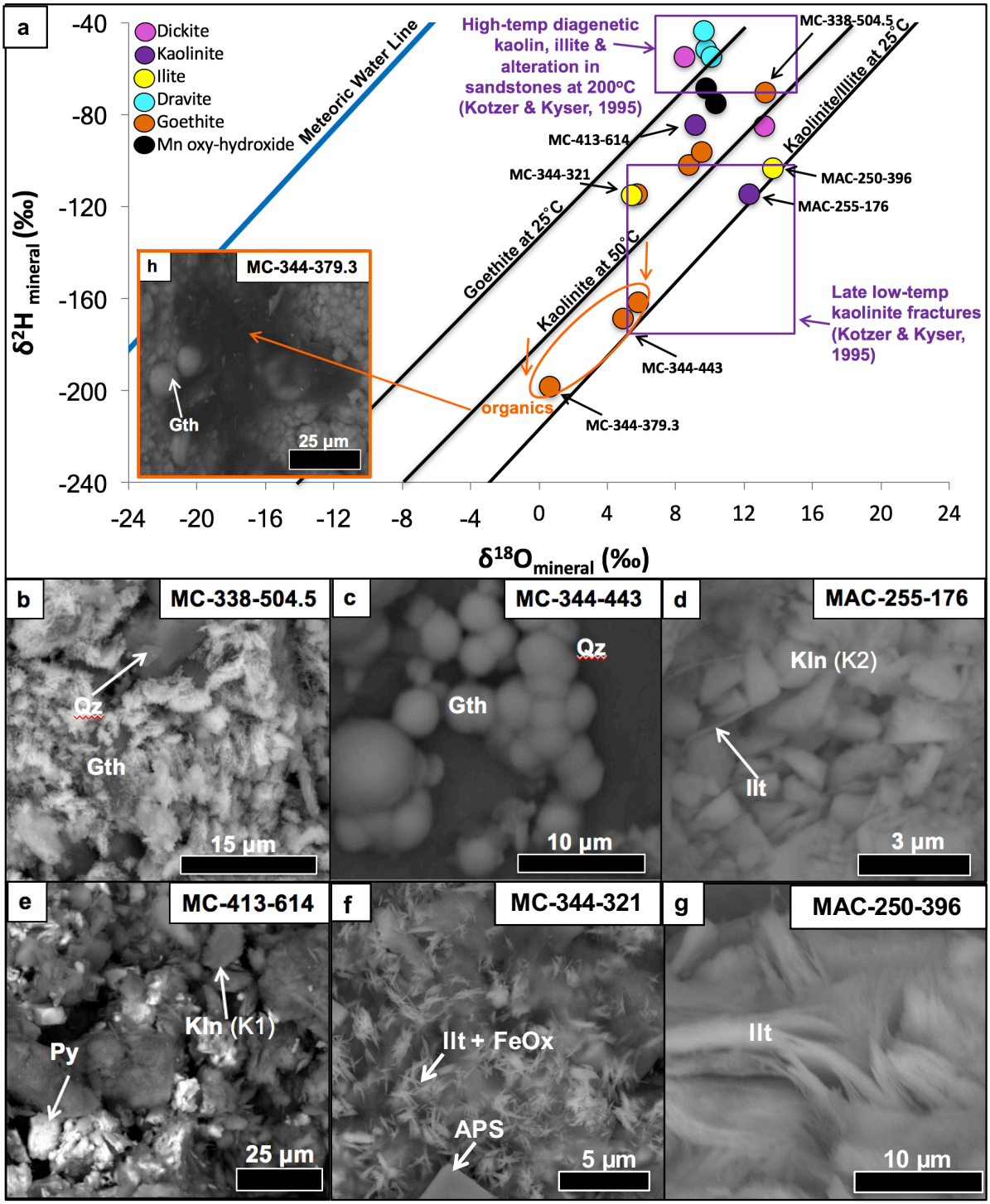

Figure 2.14: a) Relationship between $\delta^{18}O$ and $\delta^{2}H$ values of clay and oxy-hydroxide minerals of fracture coatings from the McArthur River uranium deposit (Table 2.3). Goethite 25°C, kaolinite 25°C, 50°C and illite 25°C lines represent the $\delta^{18}O$ and $\delta^{2}H$ values of kaolinite, dickite, goethite, Mn oxy-hydroxide, dravite, and illite, in equilibrium with meteoric waters at the specified temperature. b) SEM BSE images showing mineral assemblages of fracture coatings within the McArthur River sandstones - fibrous goethite precipitating on quartz

grains from the sandstone within the South West Distal Zone MFa sample MC-338-504.5 (type 2 - white and yellow fracture coating), c) botryoidal goethite precipitating on quartz from the sandstone within the South West Distal Zone MFb sample MC-344-443 (type 1 – brown fracture coating), d) fibrous illite followed by pervasive kaolinite (K2) from Zone 4 MFd sample MAC-255-176 (type 7 – pink fracture coating), e) well-crystalline kaolinite (K1) followed by framboidal pyrite crystals from Zone C MFa sample MC-413-614 (type 3 – white fracture coating), f) interlocking fibrous illite with Fe oxide staining and later pseudo-cubic APS minerals from the South West Distal Zone MFb sample MC-344-321 (type 2 - white and yellow fracture coating), g) interlocking fibrous illite from the Gap Zone MFb sample MAC-250-396 (type 6 – drusy quartz fracture coating), and h) botryoidal goethite followed by amorphous organic material from the South West Distal Zone MFb sample MC-344-379.3 (type 1 – brown fracture coating).

2.4.4 Hyperspectral Imaging

The mineral parageneses of fracture fillings and near-fracture materials were refined using SWIR hyperspectral imaging. The minerology of the near-fracture material was compared to the mineralogy of the fracture coatings/fillings to examine how fluids might have affected the wall-rocks along the fractures.

Hyperspectral imaging indicates that approximately one-third of the samples record a distinct mineralogical zonation from the fracture coating mineralogy into the near-fracture mineralogy. This zoning is exemplified by samples MC-338-429.7 and MC-338-121, in which the fracture surface is coated by kaolinite and Fe oxide; a mineral assemblage that grades within a few millimeters from the fracture edge into a near-fracture background mineralogy of white mica (e.g. illite). In sample MAC-255-251, the fracture coating of kaolinite similarly transitions to the near-fracture background mineralogy of white mica (e.g. illite) over a distance of about 1 cm (Figure 2.15c). Therefore, the influence of the fracture fluids interacting with the fracture surface can be seen in the near-fracture, but the effect decreases with distance from the fracture.

The remaining two-thirds of the samples demonstrate that the fracture-hosted fluid, that produced the fracture filling/coating had only a minimal effect on the wall rock mineral

assemblage. In these samples, few differences were observed between the fracture coating mineral assemblage and the respective near-fracture mineral assemblage. For example, in sample MAC-255-305 (Figure 2.15d), kaolinite, white mica, and traces of Fe oxides are similarly distributed on the fracture surface and in the near-fracture material.

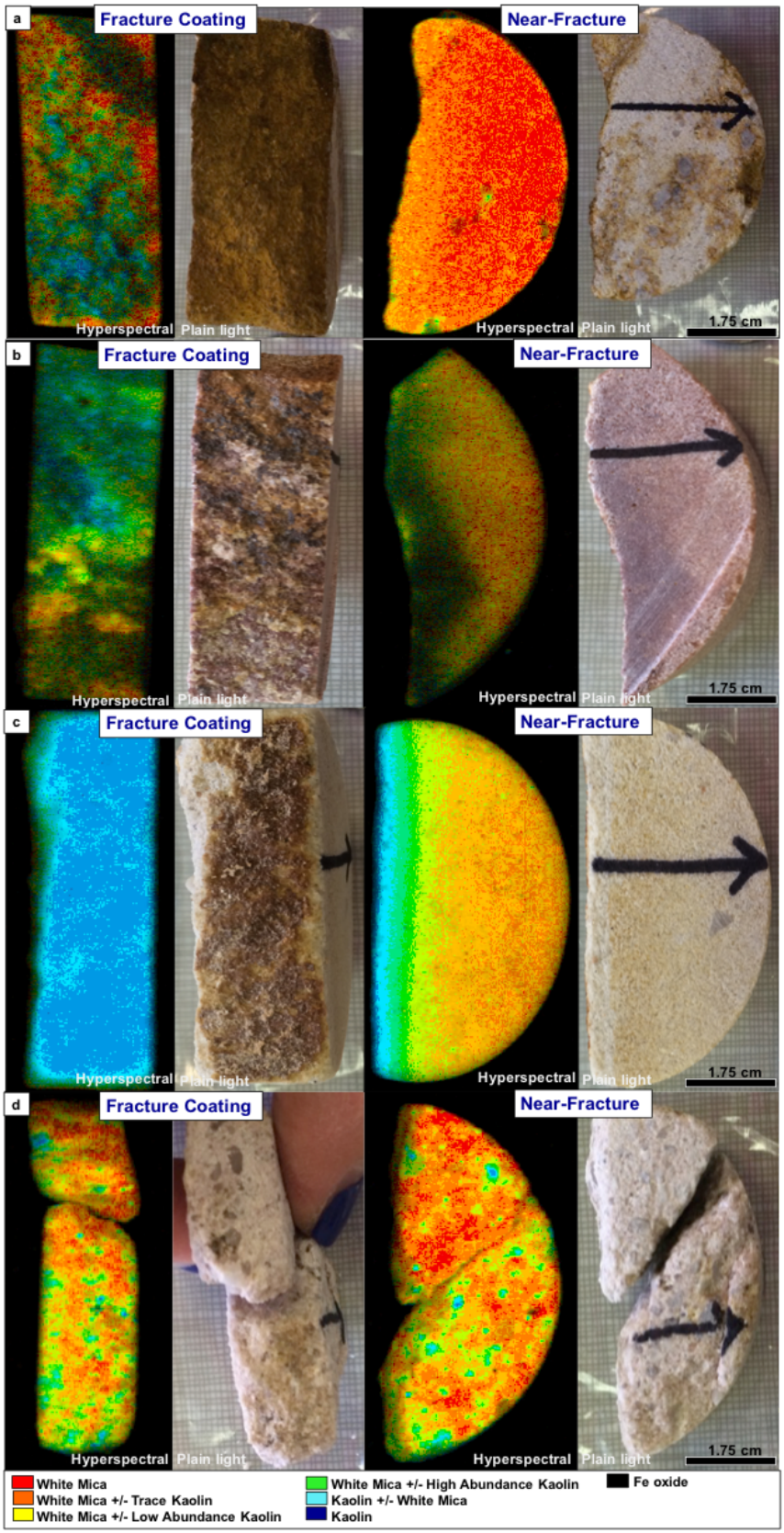
a
Fracture Coating
Near-Fracture
Hyperspectral
Plain light
1.75 cm
b
Fracture Coating
Near-Fracture
Hyperspectral
Plain light
1.75 cm
c
Fracture Coating
Near-Fracture
Hyperspectral
Plain light
1.75 cm
d
Fracture Coating
Near-Fracture
Hyperspectral
Plain light
1.75 cm
White Mica
White Mica +/- Trace Kaolin
White Mica +/- Low Abundance Kaolin
White Mica +/- High Abundance Kaolin
Kaolin +/- White Mica
Kaolin
Fe oxide

Figure 2.15: Comparison of mineral assemblages in the fracture fillings/coatings and the near-fracture material. a) White and yellow fracture coating (MC-338-429.7), b) black and orange fracture coating (MC-338-121), c) pink fracture coating (MAC-255-251), and d) brown fracture coating (MAC-255-305), showing the fracture surface (map view of sample) and near-fracture surface (cross-section of sample) in false-color image from hyperspectral analysis and plain light.

2.4.5 pH

The pH of fluids buffered by the fracture coatings from McArthur River reflect the pH of the fluids from which cations and anions were adsorbed onto the fracture surface and from which the fracture minerals were precipitated (Thornber, 1985). Goethite has a point of zero charge of 7.8 (Figure 2.16a), resulting in an excess of positive surface sites for anything below that pH, and would attract anions (Nickel and Daniels, 1985). At a high pH, many of the elements that would exist as cations at a lower pH tend to be immobilized, and many anions will tend to be immobilized at low pH (Thornber, 1985). The fracture surface minerals buffer the pH of the fluid carrying the elements that are being adsorbed onto the mineral surface.

Fluids associated with the mineralizing system are stable at a neutral pH near 200°C (Kotzer and Kyser, 1995; Cuney and Kyser, 2014) and thus, fracture coatings with values close a near neutral pH are indicative of primary dispersion of elements from the mineralizing system, such as white and yellow (type 2) and white (type 3) fractures (Figure 2.16a). Primary dispersion of elements in the fluid are buffered by the fracture minerals within these types at a pH between 4.5-5. White and yellow (type 2) and white (type 3) fractures also show a high pH (Figure 2.16b) due to the presence of Fe oxides in some fractures. Brown (type 1) fractures also show a near neutral pH (Figure 2.16a) due to Mn oxides present on their surface. As depth increases, the pH of fracture minerals increase, especially for white and yellow (type 2) fractures that are rich in clay at a low pH in comparison to fractures rich in Fe oxides at a high pH. This variation with

depth could also be due to the presence of hematite on some fractures (e.g. brown (type 1) fractures), which has a point of zero charge of 8.5 (Strumm, 1992).

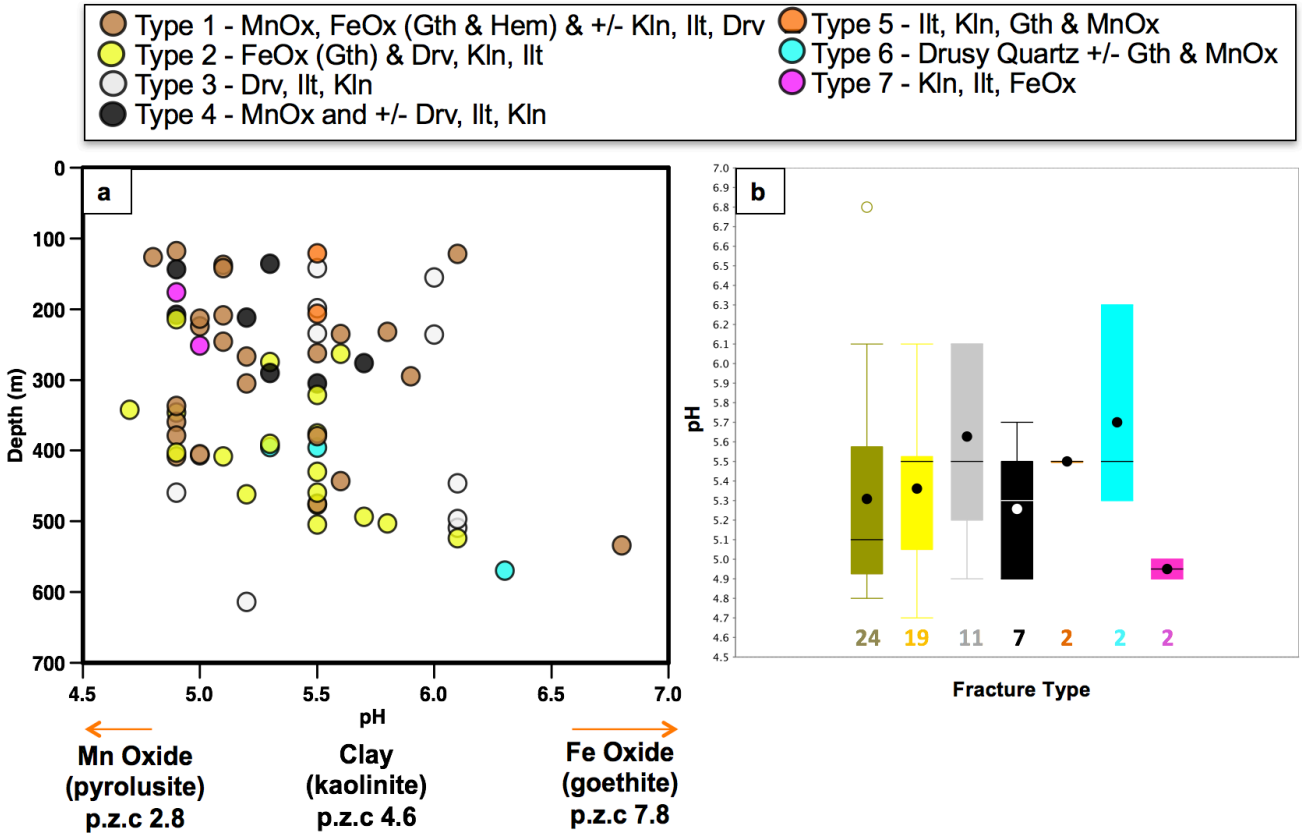

Figure 2.16: a) Relationship between depth and pH of fracture coatings at McArthur River showing the typical point of zero charges for Mn oxide (pyrolusite), clay (kaolinite), and Fe oxide (goethite). Point of zero charges (pzc) of minerals from Stumm (1992). b) Box and whisker plot of the pH for each fracture type, showing the number of samples for each fracture type. The black dot represents the mean, horizontal black line the median, the upper and lower half of the box are Q1 and Q3 whereas the whiskers represent extreme values that are not outliers. Outliers are shown beyond the whiskers.

2.5 Discussion

Seven fracture types and their distributions are identified in this study (Figure 2.10). The mineralogy and chemistry of the fracture fillings in the McArthur River area reflect the most recent and dominant fluids that flowed through the fractures (Figure 2.17) and have affected

some of the wall rock materials adjacent to the fractures (Figure 2.15). The crystallinities and $\delta^{18}O$ and $\delta^{2}H$ values of primary minerals in the fractures indicate that the minerals that fill the fractures formed from hydrothermal and meteoric fluids (Figure 2.14). Dickite formed at temperatures above *ca*. 130°C in the Athabasca Basin from diagenetic basinal fluids (Kotzer and Kyser, 1995) and was likely overprinted by a diagenetic-hydrothermal fluid from later hydrothermal alteration, precipitating dickite on fracture fillings. Dickite was followed by well-crystallized kaolinite (K1) in the mineral paragenesis (Figure 2.12) and likely formed from hydrothermal fluids. Illite and dravite also precipitated on fracture fillings from hydrothermal fluids, as they are associated with the hydrothermal alteration in areas of intense fracturing and can be part of the late ore-forming system (Hoeve and Quirt, 1984; Halter *et al*., 1989; Kotzer and Kyser, 1995). Fibrous goethite is indicative of formation by moderate-temperature fluids near 60°C (Yapp, 1987) based on their $\delta^{18}O$ and $\delta^{2}H$ values (Figure 2.14a). Similarly, $\delta^{18}O$ and $\delta^{2}H$ values of Mn oxy-hydroxides are consistent with formation from similar fluids that formed the fibrous goethite. Botryoidal goethite formed by low-temperature meteoric waters ≤50°C (Rainbow *et al*., 2006). Meteoric fluids also precipitated poorly-crystallized kaolinite (K2) at low temperatures near 25°C (Savin and Epstein, 1970).

During hydrothermal alteration, fluids in the basin with temperatures near 200°C (Figure 2.17) precipitated dickite, kaolinite (K1), illite, and dravite (T1) (Figure 2.14a). This process is preserved in white and yellow (type 2) and white (type 3) fractures from the South West Distal Zone, which is weakly mineralized, as well as the Zone 4 and Zone C mineralized areas (Figure 2.17). These are moderately to strongly mineralized areas at McArthur River, we assume that hydrothermal fluids associated with the uranium mineralizing system transported pathfinder elements from the mineralization and host-rock alteration halos, located below, along fractures thus enlarging the footprint of the McArthur River uranium deposit through the primary

dispersion processes. Primary dispersion occurred mainly above the mineralization. These high temperature fluids associated with the mineralizing system are similar to those of basinal fluids at 200°C in the dominant paleoaquifer in the Manitou Falls Formation and the slightly lower temperatures of 150°C for fluids in late quartz (e.g. Pagel *et al*., 1980; Kotzer and Kyser, 1995; Derome *et al*., 2005).

Later influx of low-temperature meteoric fluids down the fractures variably overprinted earlier-formed minerals through precipitation of Fe oxides, such as botryoidal goethite and late poorly-crystalline kaolinite (K2) (Figure 2.14a). These overgrowths suggest that many fractures have experienced protracted fluid histories, with several fluid incursion events being recorded by some fracture fillings. The sub-vertical orientation of most of the fractures, along with several basin uplift events, causing fault reactivation and basin fracturing (Kotzer and Kyser, 1995), promoted fluid movement. These late fluid events are mainly recorded in brown fractures (type 1), rich in botryoidal goethite, that are in the lower Manitou Falls formations in the weakly mineralized South West Distal Zone (Figure 2.17). The late uplift events and sub-vertical orientation of fractures allowed meteoric fluids from above to transport elements in the fractures and variably overprint the earlier hydrothermal signature in the fractures. The low temperatures and relatively recent meteoric origin for some of these fluids was proposed by Kotzer and Kyser (1995) and Kyser and Kerrich (1991) to explain the apparent preferential hydrogen isotope exchange in kaolinite, illite and dravite in environments with high integrated fluid-flux, such as in fractures. Although, oxy-hydroxide minerals are shown to occur mainly later in the fracture mineral paragenesis (Figure 2.12), the high $\delta^{18}O$ and $\delta^{2}H$ values from microfiber Mn oxy-hydroxides in black (type 4) fractures and fibrous goethite in white and yellow (type 2) and black and orange (type 5) fractures, suggest that these minerals formed from a higher temperature fluid >50°C and thus, represent an earlier stage of formation in the mineral paragenesis (Figure 2.12).

This higher temperature fluid is shown in Figure 2.17 as the second phase of high-temperature hydrothermal input from below.

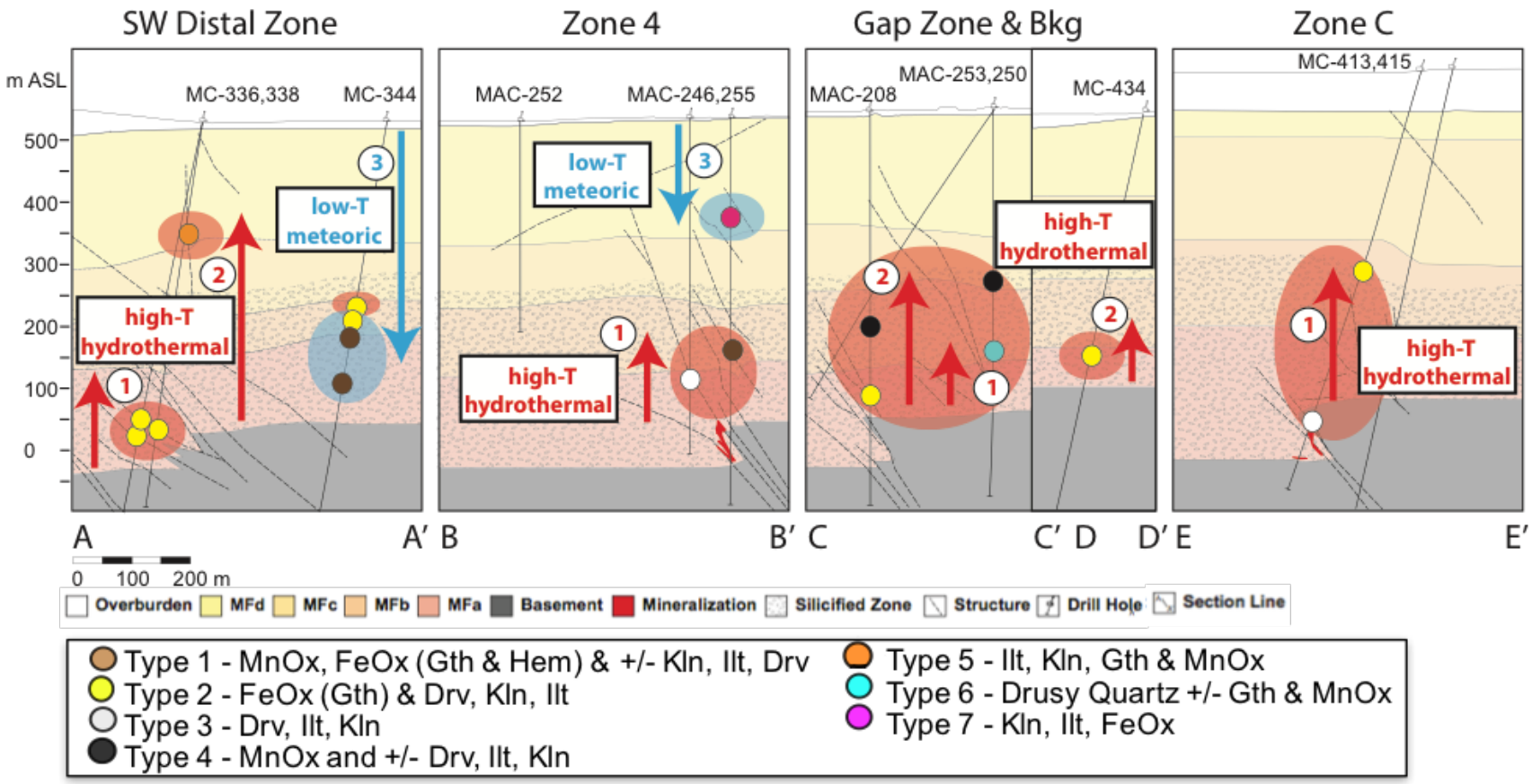

Figure 2.17: Cross section across the P2 fault at McArthur River (Figure 2.2) showing the location of the fracture samples in the Manitou Falls Formation that were analyzed for stable isotopes in the Manitou Falls Formation, highlighting the fracture type, shown by various colors. The red arrows and ellipses reflect fractures associated with high-temperature hydrothermal fluid input from below, while the blue arrows and ellipses reflect fractures associated with low-temperature meteoric fluid input from above, with the order (labelled 1-3) in which they occur. Figure modified from Joyce (2016).

SWIR hyperspectral imaging of fracture coatings and their adjacent wall rock material show that multiple fluids were involved in the precipitation of various alteration minerals on and near the fracture surface. The background mineralogy of the Athabasca Group sandstone is dickite (+/- kaolinite) +/- illite (Hoeve and Quirt, 1984) and the clay mineral assemblage in samples from Background hole MC-434 also consists of dickite and illite on both the fracture surface and wall rock, these fracture filling samples likely represent formation from diagenetic brine. There is little difference between the mineral assemblages of the fracture fillings/coatings and the near-fracture material for about two-thirds of the sample set (Figure 2.15d), indicating that white mica (illite) underwent minimal alteration by fracture fluids and that the fluids were in equilibrium with the host rocks.

The dominant primary fracture fluid that affected the fracture fillings in about one-third of the sample set differed from diagenetic brine, as the influence of this fluid is shown by gradational mineral zoning from the fracture filling adjacent to the fracture surface into the background mineral assemblage within the near-surface material (Figures 2.15a-c). In Figures 2.15a-c, the fracture mineral assemblage of kaolinite and Fe oxide can be observed to transition to the near-fracture mineral assemblage of white mica (illite), indicating that fracture fluids altered the background mineralogy to form kaolinite (K2) and Fe oxide on the fracture surface and near-fracture surface. So, the various layers of alteration minerals recorded on fractures and gradational mineral zoning into the wall rock (Figures 2.15a-c) represent a protracted fluid history for these fractures and a possible record of secondary dispersion of pathfinder elements from uranium mineralization.

Synopsis

Each fracture type displays a unique mineral paragenesis (Figure 2.18) based on petrographic characteristics and hosts a dominant mineral species: brown (type 1) - botryoidal

goethite; white and yellow (type 2) – fibrous goethite; white (type 3) – clay mineral-rich with variably-crystallized kaolinite; black (type 4) – microfibrous Mn oxy-hydroxide; black and orange (type 5) – fibrous goethite; drusy quartz (type 6) – euhedral quartz; pink (type 7) – poorly crystallized kaolinite. Stable isotope analyses of these fracture minerals indicate formation from hydrothermal fluids for some of them and meteoric fluids for others (Yapp, 1987; Kotzer and Kyser, 1995; Rainbow *et al*., 2006).

White and yellow (type 2) and white (type 3) fractures precipitated dickite, well-crystallized kaolinite (K1) in white (type 3) fractures, illite, and dravite (T1) that are early in the paragenesis. These minerals formed from hydrothermal fluids, with temperatures near 200°C (Figure 2.18). These minerals reflect primary dispersion primarily during the waning stages of the mineralizing process. The waning stages of the mineralizing process are also recorded in assemblages of illite and quartz in drusy quartz (type 6) fractures, given that the fluid inclusions in these record slightly lower temperatures near 150°C (e.g. Pagel *et al*., 1980; Kotzer and Kyser, 1995; Derome *et al*., 2005). This mineral assemblage is followed by fibrous goethite in white and yellow (type 2) and black and orange (type 5) fractures and microfibrous Mn oxy-hydroxide in black (type 4) fractures, which also probably formed from hydrothermal fluids.

Brown (type 1) and pink (type 7) fracture coatings are host to botryoidal goethite, Mn oxides and poorly-crystallized kaolinite (K2) that formed from late low-temperature meteoric waters. This influx of meteoric waters altered and variably overprinted the earlier hydrothermal mineral assemblages due to downward migration of fluids/elements to at least 200 m below the surface. This meteoric mineral assemblage variably replaced high-temperature minerals on the fracture surface and the adjacent wall rock. Organic material is younger than these late low-temperature minerals and occurs on most fractures (Figure 2.18). Meteoric waters having low δ^2H values, such as those from high latitudes and cold climates like those of the present

Athabasca Basin, moved down some fractures and affected the H isotopic composition of some minerals such as goethite and illite.

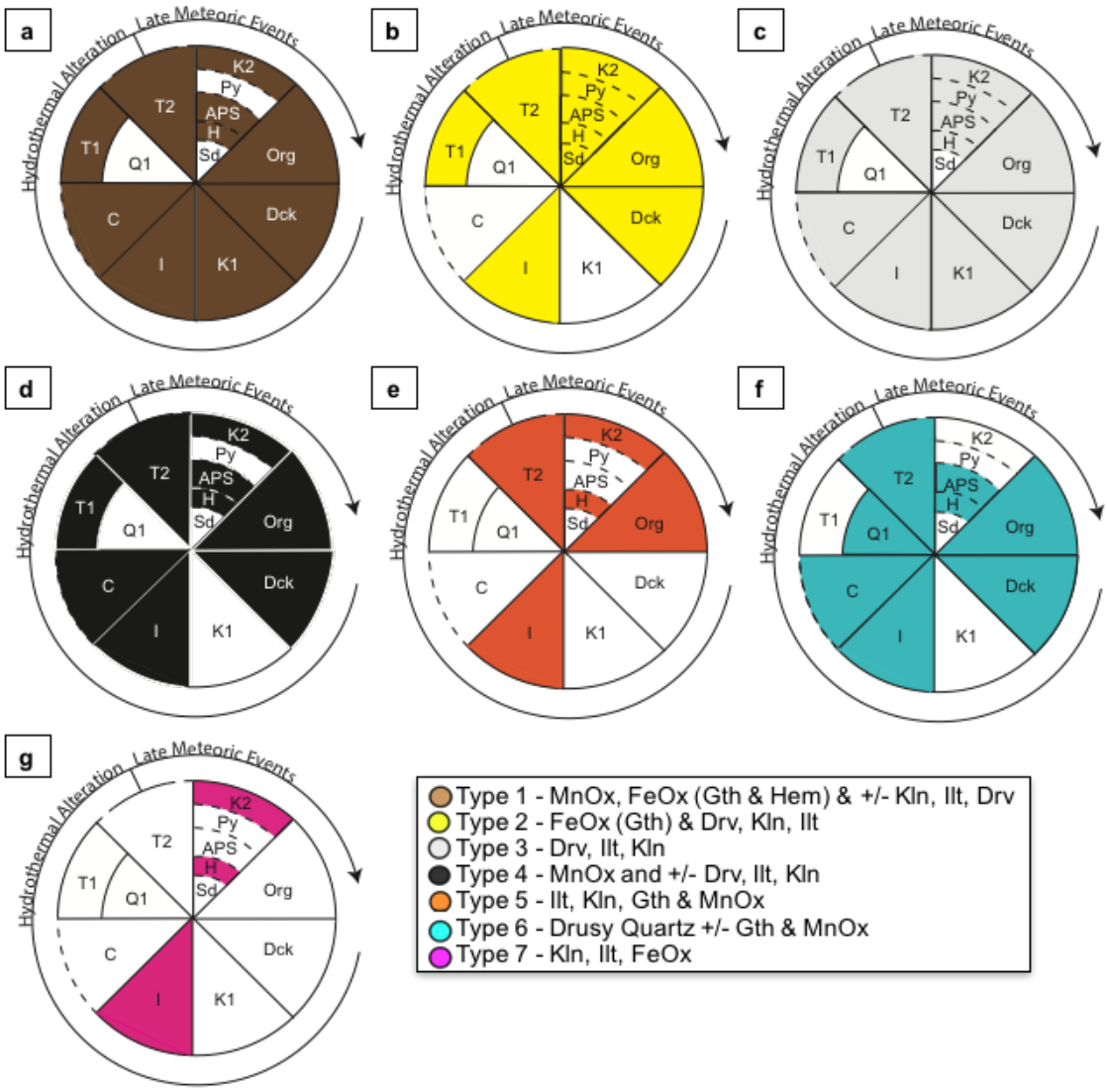

Figure 2.18: Paragenetic sequence of each fracture type beginning with dickite as the earliest fracture fill and phases associated with hydrothermal alteration, followed by later minerals formed from meteoric waters, as by crystallinities and stable isotopic compositions: a) Type 1 – Brown, b) Type 2 – White and Yellow, c) Type 3 – White, d) Type 4 – Black, e) Type 5 – Black and Orange, f) Type 6 – Drusy Quartz, and g) Type 7 – Pink. The dashed lines represent uncertainty in the timing of mineral formation.

Fracture mineralogy appears to be an overlooked aspect of mineral exploration. However,

from this study, sampling and characterizing sandstone-hosted fracture fillings can be a highly effective way to trace geochemical dispersion, as fractures act as conduits for the migration of fluids that extend all the way to the surface through >500 m of Athabasca Group sandstone. Colors of the fractures reflect the mineralogy of the fracture fill and show initial evidence that fractures act as conduits for elements from the deposit, recording primary and secondary dispersion. However, the usefulness of each fracture type can vary due to differences in the fracture fill mineralogy (Table 2.4). For example, white and yellow (type 2) fractures containing dickite, illite, and dravite (T1) are most useful for exploration, as they reflect primary dispersion primarily during the waning stages of the mineralizing process. This mineral assemblage is followed by fibrous goethite in white and yellow (type 2) fractures, which is the dominant and most obvious mineral observed in white and yellow (type 2) fractures. Thus, fibrous goethite on white and yellow (type 2) fractures is the most useful indication of mineralization in the field as it records both primary and secondary dispersion.

Table 2.4: Fracture types, fracture filling mineralogy, sample distance to the P2 fault (distal is > 300 m and proximal is < 200 m) and their usefulness for exploration, using a rating scale from 1 to 7 (1 = most useful and 7 = least useful).

Fracture Type	Fracture Mineralogy	Distance to P2 Fault	Usefulness (1-7)
1 – Brown	MnOx, FeOx (goethite & hematite) ± kaolinite, illite, dravite	distal to proximal	**6** - botryoidal goethite (low-temperature fluid indicator)
2 – White & Yellow	FeOx (goethite) & dravite, kaolinite, illite	distal to proximal	**1** - fibrous goethite (higher temperature fluid indicator)
3 – White	dravite, kaolinite, illite ± dickite, clinochlore	distal to proximal	**2** - well-crystalline kaolinite (high-temperature fluid indicator)
4 – Black	MnOx ± dravite, illite, kaolinite	distal	**5** - microfiber Mn oxy-hydroxides

			(hydrothermal fluid indicator)
5 – Black & Orange	illite, kaolinite, goethite & MnOx	distal	**4** - fibrous goethite (hydrothermal fluid indicator)
6 – Drusy Quartz	drusy quartz, goethite and MnOx	proximal	**3** - fibrous interlocking illite (hydrothermal fluid indicator during waning stages of the mineralizing system)
7 – Pink	illite, kaolinite & FeOx	distal	**7** - poorly-crystalline kaolinite (low-temperature fluid indicator)

2.6 Conclusions

Based on petrography and stable isotopic compositions ($\delta^{18}O$ and $\delta^{2}H$) of fracture coatings and associated wall rock materials from the area around the McArthur River unconformity-related uranium deposit, a number of conclusions about the information recorded by fractures and how these fractures relate to element migration can be made:

1. Seven fracture types are recognized, representing distinct colors, mineral assemblages, and chemical compositions.
2. The generalized mineral paragenesis and origin involves formation of dickite, well-crystalline kaolinite (K1), illite, drusy quartz, and spherulitic dravite (T1) formed by hydrothermal fluids at *ca*. 200°C and associated with the waning mineralizing system. This mineral assemblage is followed by precipitation of fibrous goethite and microfibrous Mn oxy-hydroxide by lower temperature hydrothermal fluids as reflected by their habits and high $\delta^{2}H$ values. Late influx of low-temperature meteoric fluids variably overprinted earlier minerals with botryoidal goethite, Mn oxides, and poorly crystalline kaolinite (K2), indicating

that some fractures have had protracted fluid histories, including some fractures at significant depth.

3. Multiple fluid events are observed on many fracture surfaces and in their wall rock due to their generally moderately to steeply-dipping orientation (<50°) that allows permeable pathways for fluid movement within the Athabasca sandstone from both above and below.
4. White and yellow (type 2) fractures were formed from hydrothermal fluids, reflected by a near neutral pH and high δ^2H values of fibrous goethite, and was likely associated with the mineralizing event. They thus record primary dispersion of pathfinder elements, and therefore extend the deposit footprint away from the deposit. High δ^2H values of microfibrous Mn oxy-hydroxides in black (type 4), fibrous goethite in black and orange (type 5), and well-formed polygonal dickite, well-crystalline kaolinite, fibrous interlocking illite, and spherulitic dravite in some white and yellow (type 2), white (type 3), and drusy quartz (type 6) fractures also indicate formation from hydrothermal fluids, reflecting an upward migration of elements.
5. Brown (type 1) and pink (type 7) fractures are indicative of meteoric fluids due to low δ^2H values in botryoidal goethite and poorly crystalline kaolinite.

Fractures are ideal conduits for the migration of elements by basinal fluids associated with the uranium mineralizing system as they extend from areas near uranium mineralization to the present-day surface. With due diligence, the color, mineralogy, and chemistry of fracture fillings can be used in exploration to detect syn-mineralization and post-mineralization dispersion from the McArthur River uranium deposit.

2.7 Acknowledgments

Funding for this project was provided through the mult-sponsor, multi-researcher CMIC-NSERC Collaborative Research and Development (CRD) grant for the Footprints Project. Many thanks to Dr. Kevin Ansdell and Ken Wasyliuk from the University of Saskatchewan for their revisions on this manuscript. Sample collection in the field was facilitated by in-kind support by Cameco Corporation. Special thanks to Nick Joyce for assisting in sample collection and Queen's Facility for Isotope Research for providing analytical assistance and QFIR staff including, Donald Chipley, Evelyne Leduc, Alexandre Voinot, Steve Beyer, April Vuletich, Agatha Dobosz, and Christabel Jean.

References

Alexandre, P., Kyser, K., Polito, P. and Thomas, D. 2005. Alteration mineralogy and stable isotope geochemistry of Paleoproterozoic basement-hosted unconformity-type uranium deposits in the Athabasca Basin, Canada. Economic Geology, 100(8), 1547-1563.

Alexandre, P., Kyser, K., Jiricka, D. and Witt, G. 2012. Formation and evolution of the Centennial unconformity-related uranium deposit in the south-central Athabasca Basin, Canada. Economic Geology, 107(3), 385-400.

Annesley, I. R., Madore, C. and Portella, P. 2005. Geology and thermotectonic evolution of the western margin of the Trans-Hudson Orogen: evidence from the eastern sub-Athabasca basement, Saskatchewan. Canadian Journal of Earth Sciences, 42(4), 573-597.

Beaufort, D., Patrier, P., Laverret, E., Bruneton, P. and Mondy, J. 2005. Clay alteration associated with Proterozoic unconformity-type uranium deposits in the East Alligator Rivers uranium field, Northern Territory, Australia. Economic Geology, 100(3), 515-536.

Bernier, S. 2004. Stratigraphy of the late Paleoproterozoic Manitou Falls Formation in the vicinity of the McArthur River uranium deposit, Athabasca Basin, Saskatchewan, Canada.

Bird, M. I. and Chivas, A. R. 1988. Stable-isotope evidence for low-temperature kaolinitic weathering and post-formational hydrogen-isotope exchange in Permian kaolinites. Chemical Geology: Isotope Geoscience Section, 72(3), 249-265.

Cameron, E.M., Hamilton, S.M., Leybourne, M.I., Hall, G.E.M., McClenaghan, M.B. 2004. Finding deeply buried deposits using geochemistry; Geochemistry: Exploration, Environments and Analysis. Vol. 4, p. 7-32.

Capuano, R. M. 1992. The temperature dependence of hydrogen isotope fractionation between clay minerals and water: Evidence from a geopressured system. Geochimica et Cosmochimica Acta, 56(6), 2547-2554.

Clayton, R. N. and Mayeda, T. K. 1963. The use of bromine pentafluoride in the extraction of oxygen from oxides and silicates for isotopic analysis. Geochimica et cosmochimica acta, 27(1), 43-52.

Cloutier, J., Kyser, K., Olivo, G. R., Alexandre, P. and Halaburda, J. 2009. The Millennium uranium deposit, Athabasca Basin, Saskatchewan, Canada: an atypical basement-hosted unconformity- related uranium deposit. Economic Geology, 104(6), 815-840.

Cumming, G. L. and Krstic, D. 1992. The age of unconformity-related uranium mineralization in the Athabasca Basin, northern Saskatchewan. Canadian Journal of Earth Sciences, 29(8), 1623-1639.

Cuney, M. and Kyser, K. (Eds.). 2014. Recent and not-so-recent developments in uranium deposits and implications for exploration.

Derome, D., Cathelineau, M., Cuney, M., Fabre, C., Lhomme, T. and Banks, D. A. 2005. Mixing of sodic and calcic brines and uranium deposition at McArthur River, Saskatchewan, Canada: a Raman and laser-induced breakdown spectroscopic study of fluid inclusions. Economic Geology, 100(8), 1529-1545.

Devine, M. 2016. Sources and pathways of radiogenic elements in surface media above the Millennium and McArthur River uranium deposits in the Athabasca Basin, Saskatchewan, Canada (Master's thesis). June

Duke, E. F. 1994. Near infrared spectra of muscovite, Tschermak substitution, and metamorphic reaction progress: Implications for remote sensing. Geology, 22(7), 621-624.

Earle, S. 1997. MINSPEC3 program for estimation of clay contents in Athabasca Group sandstones from reflectance spectral data. Internal Report, Grasswood Geosciences.

Earle, S., Wheatley, K. and Wasyliuk, K. 1999. Application of reflectance spectrometry to assessment of alteration mineralogy at the Key Lake uranium deposit, Saskatchewan.

Ey, F., Piquard, J. P., Baudemont, D. and Zimmerman, J. 1992. The sue uranium deposits, Saskatchewan, Canada (No. IAEA-TECDOC--650).

Fayek, M. and Kyser, T.K. 1997. Characterization of multiple fluid-flow events and rare-earth-element mobility associated with formation of unconformity-type uranium deposits in the Athabasca Basin, Saskatchewan: The Canadian Mineralogist, v. 35, p. 627-658.

Friedman, I. and O'Neil, J. R. 1978. Hydrogen. Handbook of geochemistry, 1.

Gustafson, L. B. and Curtis, L. W. 1983. Post-Kombolgie metasomatism at Jabiluka, Northern Territory, Australia, and its significance in the formation of high-grade uranium mineralization in lower Proterozoic rocks. Economic Geology, 78(1), 26-56.

Hajnal, Z., White, D. J., Takacs, E., Gyorfi, I., Annesley, I. R., Wood, G., O'Dowd, C. and Nimeck, G. 2010. Application of modern 2-D and 3-D seismic-reflection techniques for uranium exploration in the Athabasca Basin This article is one of a series of papers published in this Special Issue on the theme Lithoprobe—parameters, processes, and the evolution of a continent. Canadian Journal of Earth Sciences, 47(5), 761-782.

Halter, G., Pagel, M., Sheppard, S. M. F. and Weber, F. 1989. Alterations in the Carswell structure (Saskatchewan, Canada): Petrology, mineralogy and stable isotopes geochemistry (No. IAEA-TECDOC--500).

Hiatt, E. E. and Kyser, T. K. 2007. Sequence stratigraphy, hydrostratigraphy, and mineralizing fluid flow in the Proterozoic Manitou Falls Formation, eastern Athabasca Basin, Saskatchewan. BULLETIN-GEOLOGICAL SURVEY OF CANADA, 588, 489.

Hiatt, E. E., Kyser, T. K., Fayek, M., Polito, P., Holk, G. J. and Riciputi, L. R. 2007. Early quartz cements and evolution of paleohydraulic properties of basal sandstones in three Paleoproterozoic continental basins: Evidence from in situ δ 18 O analysis of quartz cements. Chemical Geology, 238(1), 19-37.

Hinckley, D. N. 1962. Variability in "crystallinity" values among the kaolin deposits of the coastal plain of Georgia and South Carolina. Clays and Clay Minerals, 11, 229-235.

Hoeve, J., Sibbald, T. I. I., Ramaekers, P. and Lewry, J. F. 1980. Athabasca basin unconformity-type uranium deposits. A special class of sandstone-type deposits. In Uranium in the Pine Creek geosyncline.

Hoeve, J. and Quirt, D. H. 1984. Mineralization and host rock alteration in relation to clay mineral diagenesis and evolution of the Middle-Proterozoic, Athabasca Basin, northern Saskatchewan, Canada.

Hoffman, P. F. 1988. United Plates of America, the birth of a craton-Early Proterozoic assembly and growth of Laurentia. Annual Review of Earth and Planetary Sciences, 16, 543-603.

Holk, G.J., Kyser, T.K., Chipley, D., Hiatt, E.E. and Marlatt, J. 2003. Mobile Pb-isotopes in Proterozoic sedimentary basins as guides for exploration of uranium deposits: Journal of Geochemical Exploration, v. 80, p. 297-320.

International Atomic Energy Agency. 2009. World distribution of uranium deposits (UDEPO), with uranium deposit classification: IAEA-TECDOC-1629, Vienna, 117 p.

Jeanneret, P., Goncalves, P., Durand, C., Trap, P., Marquer, D., Quirt, D. and Ledru, P. 2016. Tectono-metamorphic evolution of the pre-Athabasca basement within the Wollaston–Mudjatik Transition Zone, Saskatchewan. Canadian Journal of Earth Sciences, 53(3), 231-259.

Jefferson, C. W., Thomas, D. J., Gandhi, S. S., Ramaekers, P., Delaney, G., Brisbin, D., Cutts, C., Portella, P. and Olson, R. A. 2007. Unconformity-associated uranium deposits of the Athabasca Basin, Saskatchewan and Alberta. Bulletin-Geological Survey of Canada, 588, 23.

Joyce, N. 2016. Alteration mineralogy and pathfinder element inventory of the McArthur River unconformity related uranium deposit, Saskatchewan, Canada (Master's thesis). 25October

Kotzer, T.G. and Kyser, T.K. 1993. O, U, and Pb isotopic and chemical variations in uraninite: implications for determining the tempo-ral and fluid history of ancient terrains. American Mineralogist 78, 1262–1274.

Kotzer, T. G. and Kyser, T. K. 1995. Petrogenesis of the Proterozoic Athabasca Basin, northern Saskatchewan, Canada, and its relation to diagenesis, hydrothermal uranium mineralization and paleohydrogeology. Chemical Geology, 120(1), 45-89.

Kyser, T. K., Wilson, M. R. and Ruhrmann, G. 1989. Stable isotope constraints on the role of graphite in the genesis of unconformity-type uranium deposits. Canadian Journal of Earth Sciences, 26(3), 490-498.

Kyser, T. K. and Kerrich, R. 1990. Geochemistry of fluids in tectonically active crustal regions. Short Course on Fluids in Tectonically Active Regimes of the Continental Crust, Mineralogical Association of Canada, Short Course Handbook, 18, 133-230.

Kyser, T. K. and Kerrich, R. 1991. Retrograde exchange of hydrogen isotopes between hydrous minerals and water at low temperatures. In Stable isotope geochemistry: a tribute to Samuel Epstein (Vol. 3, pp. 409-424). The Geochemical Society Spec. Pub.

Kyser, K., Hiatt, E., Renac, C., Durocher, K., Holk, G. and Deckart, K. 2000. Diagenetic fluids in Paleo-and Meso-Proterozoic sedimentary basins and their implications for long protracted fluid histories: Fluids and basin evolution: Mineralogical Association of Canada Short Course, v. 28, p. 225-262.

Laverret, E., Mas, P. P., Beaufort, D., Kister, P., Quirt, D., Bruneton, P. and Clauer, N. 2006. Mineralogy and geochemistry of the host-rock alterations associated with the Shea Creek unconformity-type uranium deposits (Athabasca Basin, Saskatchewan, Canada). Part 1. Spatial variation of illite properties. Clays and Clay Minerals, 54(3), 275-294.

LeCheminant, A. N. and Heaman, L. M. 1989. Mackenzie igneous events, Canada: Middle Proterozoic hotspot magmatism associated with ocean opening. Earth and Planetary

Science Letters, 96(1-2), 38-48.

Lesher, M., Hannington, M., Galley, A., Ansdell, K., Astic, T., Banerjee, N., Beauchamp, S., Beaudoin, G., Bertelli, M., Bérubé, C., Beyer, S., Blacklock, N., Byrne, K., Cheng, L.-Z., Chouinard, R., Chouteau, M., Clark, J., D'Angelo, M., Darijani, M., Devine, M., Dupuis, C., El Goumi, N., Enkin, R., Farquharson, C., Fayol, N., Feltrin, L., Feng, J., Gaillard, N., Gleeson, S., Gouiza, M., Grenon, C., Guffey, S., Guilmette, C., Guo, K., Hart, C., Hattori, K., Hollings, P., Joyce, N., Kamal, D., King, J., Kyser, K., Layton-Matthews, D., Lee, R., Lesage, G., Leybourne, M., Linnen, R., Lypaczewski, P., McGaughey, J., Mitchinson, D., Milkereit, B., Mir, R., Morris, W., Oldenburg, D., Olivo, G., Perrouty, S., Piercey, S., Piette-Lauzière, N., Raskevicius, T., Reman, A., Rivard, B., Ross, M., Samson, I., Scott, S., Shamsipour, P., Shi, D., Smith, R., Sundaralingam, N., Taves, R., Taylor, C., Valentino, M., Vallée, M., Wasyliuk, K. and Williams-Jones, A., Winterburn, P. 2017. Integrated Multi-Parameter Exploration Footprints of the Canadian Malartic Disseminated Au, McArthur River-Millennium Unconformity U, and Highland Valley Porphyry Cu Deposits: Preliminary Results from the NSERC-CMIC Mineral Exploration Footprints Research Network. Available at: http://cmic-footprints.ca/home/ publications.

Lewry, J.F. and Sibbald, T.I. 1980. Thermotectonic evolution of the Churchill Province in northern Saskatchewan: Tectonophysics, v. 68, p. 45-82.

Longstaffe, F. J. 1989. Stable isotopes as tracers in clastic diagenesis. Short course in burial diagenesis, 201-284.

Lorilleux, G., Jébrak, M., Cuney, M. and Baudemont, D. 2002. Polyphase hydrothermal breccias associated with unconformity-related uranium mineralization (Canada): from fractal analysis to structural significance. Journal of Structural Geology, 24(2), 323-338.

Marlatt, J., McGill, B., Matthews, R., Sopuck, V. and Pollock, G. 1992. The discovery of the McArthur River uranium deposit, Saskatchewan, Canada (No. IAEA-TECDOC--650).

McGill, B. D., Marlatt, J. L., Matthews, R. B., Sopuck, V. J., Homeniuk, L. A. and Hubregtse, J. J. 1993. The P2 north uranium deposit, Saskatchewan, Canada. Exploration and Mining Geology, 2(4), 321-331.

McQueen, K. G. 2005. Ore deposit types and their primary expressions. Regolith Expression of Australian Ore Systems. CRC LEME, Perth, website: http://www. crcleme. org. au/Pubs/Monographs/RegExpOre. html [Last accessed January 2013.].

Mwenifumbo, C. J., Elliott, B. E., Jefferson, C. W., Bernius, G. R. and Pflug, K. A. 2004. Physical rock properties from the Athabasca Group: designing geophysical exploration models for unconformity uranium deposits. Journal of Applied Geophysics, 55(1), 117-135.

Ng, R., Alexandre, P. and Kyser, K. 2013. Mineralogical and geochemical evolution of the unconformity-related McArthur River Zone 4 Orebody in the Athabasca Basin, Canada: implications of a silicified zone. Economic Geology, 108(7), 1657-1689.

Nickel, E. H. and Daniels, J. L. 1985. Gossans. Handbook of Strata-bound and Stratiform Ore Deposits. Part IV, 13, 261-390.

Pagel, M., Poty, B. and Sheppard, S. M. F. 1980. Contribution to some Saskatchewan uranium deposits mainly from fluid inclusion and isotopic data. In Uranium in the Pine Creek Geosyncline.

Pan, Y. M., Botis, S. and Nokhrin, S. 2006. Applications of natural radiation-induced paramagnetic defects in quartz to exploration in sedimentary basins. Journal of China University of Geosciences, 17(3), 258-271.

Percival, J. B., Bell, K. and Torrance, J. K. 1993. Clay mineralogy and isotope geochemistry of the alteration halo at the Cigar Lake uranium deposit. Canadian Journal of Earth Sciences, 30(4), 689-704.

Post, J. L. and Noble, P. N. 1993. The near-infrared combination band frequencies of dioctahedral smectites, micas, and illites. Clays and clay minerals, 41, 639-639.

Quirt, D. H. 2001. Kaolinite and dickite in the Athabasca sandstone, Northern Saskatchewan, Canada. Saskatchewan Research Council, publication number.

Rainbird, R. H., Stern, R. A., Rayner, N. and Jefferson, C. W. 2007. Age, provenance, and regional correlation of the Athabasca Group, Saskatchewan and Alberta, constrained by igneous and detrital zircon geochronology. BULLETIN-GEOLOGICAL SURVEY OF CANADA, 588, 193.

Rainbow, A., Kyser, T. K. and Clark, A. H. 2006. Isotopic evidence for microbial activity during supergene oxidation of a high-sulfidation epithermal Au-Ag deposit. Geology, 34(4), 269-272.

Ramaekers, P. P. and Dunn, C. E. 1977. Geology and geochemistry of the eastern margin of the Athabasca Basin.

Ramaekers, P., Christopher, J.E., and MacDonald, R. 1979. Stratigraphy of the Athabasca Basin; in Summary of Investigations 1979; Saskatchewan Geological Survey; Saskatchewan Mineral Resources, Miscellaneous Report 79-10, p. 154–160.

Ramaekers, P., Christopher, J.E., and MacDonald, R. 1980. Stratigraphy and tectonic history of the Athabasca Group (Helikian) of northern Saskatchewan; in Summary of Investigations 1980; Saskatchewan Geological Survey, Saskatchewan Mineral Resources, Miscellaneous Report 80-4, p. 99–106.

Ramaekers, P. 1990. Geological Maps of the Athabasca Group (Helikian) in Northern Saskatchewan. Saskatchewan Energy and Mines, Saskatchewan Geology Survey.

Ramaekers, P. and Catuneanu, O. 2004. Development and sequences of the Athabasca basin,

early Proterozoic, Saskatchewan and Alberta, Canada. The Precambrian Earth: Tempos and Events. Developments in Precambrian Geology, 12, 705-723.

Ramaekers, P., Yeo, G. M., Jefferson, C. W., Collier, B., Long, D. G. F., Catuneanu, O., Bernier, S., Kupsch, B., Post, R., Drever, G., McHardy, S., Jiricka, D., Cutts, C. and Wheatley, K. 2007. Revised geological map and stratigraphy of the Athabasca Group, Saskatchewan and Alberta. Bulletin-Geological Survey of Canada, 588, 155.

Savin, S. M. and Epstein, S. 1970. The oxygen and hydrogen isotope geochemistry of clay minerals. Geochimica et Cosmochimica Acta, 34(1), 25-42.

Schimmelmann, A., Sessions, A. L. and Mastalerz, M. 2006. Hydrogen isotopic (D/H) composition of organic matter during diagenesis and thermal maturation. Annu. Rev. Earth Planet. Sci., 34, 501-533.

Sheppard, S. M. F. and Gilg, H. A. 1996. Stable isotope geochemistry of clay minerals. Clay Minerals, 31(1), 1-24.

Thornber, M. R. 1985. Supergene alteration of sulphides: VII. Distribution of elements during the gossan-forming process. Chemical Geology, 53(3), 279-301.

Tran, H. T., Ansdell, K. M., Bethune, K. M., Ashton, K. and Hamilton, M. A. 2008. Provenance and tectonic setting of Paleoproterozoic metasedimentary rocks along the eastern margin of Hearne craton: Constraints from SHRIMP geochronology, Wollaston Group, Saskatchewan, Canada. Precambrian Research, 167(1), 171-185.

Vorres, K. S. 1995. Coal slurry pH studies (No. CONF-950402--). American Chemical Society, Washington, DC (United States).

Wallis, R. H., Saracoglu, N., Brummer, J. J., and Golightly, J. P. 1985. The geology of the McClean uranium deposits, northern Saskatchewan; in Sibbald, T.I.I. and Petruk, W. (eds.), Geology of Uranium Deposits, CIM Spec. Vol. 32, p101-131.

Whitney, D. L. and Evans, B. W. 2010. Abbreviations for names of rock-forming minerals. American mineralogist, 95(1), 185.

Wilde, A. R., Mernagh, T. P., Bloom, M. S. and Hoffmann, C. F. 1989. Fluid inclusion evidence on the origin of some Australian unconformity-related uranium deposits. Economic Geology, 84(6), 1627-1642.

Wilson, M. R. and Kyser, T. K. 1987. Stable isotope geochemistry of alteration associated with the Key Lake uranium deposit, Canada. Economic Geology, 82(6), 1540-1557.

Wood, J. R. and Hewett, T. A. 1982. Fluid convection and mass transfer in porous sandstones—A theoretical model. Geochimica et Cosmochimica Acta, 46(10), 1707-1713.

Yapp, C. J. and Pedley, M. D. 1985. Stable hydrogen isotopes in iron oxides—II. DH variations

among natural goethites. Geochimica et Cosmochimica Acta, 49(2), 487-495.

Yapp, C. J. 1987. Oxygen and hydrogen isotope variations among goethites (α-FeOOH) and the determination of paleotemperatures. Geochimica et Cosmochimica Acta, 51(2), 355-364.

Yapp, C. J. 1990. Oxygen isotopes in iron (III) oxides: 1. Mineral-water fractionation factors. Chemical Geology, 85(3-4), 329-335.

Yeh, H. W. 1980. DH ratios and late-stage dehydration of shales during burial. Geochimica et Cosmochimica Acta, 44(2), 341-352.

Yeo, G., Jefferson, C. W. and Ramaekers, P. 2002. A preliminary comparison of Mantiou Falls Formation stratigraphy in Four Athabasca Basin Deposystems. Summary of Investigations, 2, 2002-4.

Yeo, G., Jefferson, C.W. and Ramaekers, P. 2007. Comparison of lower Athabasca Group stratigraphy among depositional systems, Saskatchewan and Alberta: Geological Survey of Canada, Bulletin 588, p. 465–488.

Chapter 3

Mineral Chemistry of Fracture Coatings in Athabasca Group Sandstones as Records of Elemental Dispersion from the McArthur River Uranium Deposit

M. Valentino[1], T.K. Kyser[1], M. Leybourne[2], T. Kotzer[3], D. Quirt[4]

[1]Department of Geological Sciences and Geological Engineering, Queen's University, Kingston, ON;
[2]Mineral Exploration Research Centre, Department of Earth Sciences, Laurentian University, Sudbury, ON;
[3]Cameco Corporation, Saskatoon, SK;
[4]AREVA Resources Canada Inc., Saskatoon, SK

Abstract

A crystal chemical study of minerals on seven types of fracture fillings from near and above the McArthur River unconformity-related U deposit were analyzed to determine if fracture fillings and their wall rocks record primary and secondary dispersion of elements from the deposit. This study shows that Pb extracted from weak acid (2% HNO_3) leaching provides Pb-Pb model ages near 1100 Ma for fractures with any of the three REE patterns: 1) LREE-enriched patterns, 2) REE patterns that are concave and similar to uraninites in the deposit, and 3) fractures with flat REE patterns. The REE patterns and ages indicate the fractures are an open system to post-mineralization dispersion of radiogenic Pb from a U-rich source, with a major mobilization of Pb from the U deposit at ca. 1100 Ma.

Brown (type 1) fractures, which host Mn-Fe oxides and clay minerals, best record evidence of U mineralization through post-mineralization dispersion, as shown by elevated concentrations of pathfinder elements Co, Ba, Tl, Mn and radiogenic Pb near the surface and at depth. Post-mineralization dispersion is also observed through brown (type 1) and pink (type 7) fractures and their wall rock, showing low $^{207}Pb/^{206}Pb$ values of 0.29-0.50 that were subsequently overprinted by fluids with more common Pb, as recorded in fractures with higher $^{207}Pb/^{206}Pb$

values of 0.51-0.84.

Fracture fillings were analyzed by continuous leach inductively-coupled plasma mass spectrometry (CL-ICP-MS) to determine the relationship between trace elements and their release from specific mineral phases. CL-ICP-MS results indicate that common Pb (with $^{207}Pb/^{206}Pb$ values >0.7) and anomalous Co (360 ppm) and V (220 ppm) contents are resident in organic phases that are dissolved during the 10% H_2O_2 leach phase. CL-ICP-MS also indicates that radiogenic Pb, as well as Ni and V, are resident in clay minerals and Fe-Mn oxy-hydroxides that breakdown during leaching with 30% HNO_3. Uranium contents are low during release of Fe, Al, Mn, and Pb with 10% and 30% HNO_3 leaches, reflecting post-mineralization dispersion of radiogenic Pb, but not U. Thus, secondary dispersion of elements into fractures enhances the size of the deposit footprint, particularly in deep fractures near the P2 fault, but also in some fractures near the surface. The results of this study strongly suggest that fractures can indeed act as conduits for dispersion of elements from the deposit, reaching all the way to the surface, providing viable exploration targets for U mineralization in sedimentary basins.

3.1 Introduction

The Athabasca Basin is a Paleo- to Mesoproterozoic basin located in northern Saskatchewan and Alberta (Figure 3.1) that hosts significant U deposits near the unconformity between the Athabasca Group sandstones and underlying Paleoproterozoic and Archean metamorphic basement rocks (IAEA, 2009). These unconformity-related U deposits formed under reducing conditions near the unconformity, when an oxidizing basinal fluid interacted with reduced basement lithologies or a reducing basement fluid (Hoeve and Sibbald, 1978; Hoeve and Quirt, 1984; Wallis *et al*., 1985; Wilson and Kyser, 1987; Kotzer and Kyser, 1995; Fayek and Kyser, 1997). Fluids associated with these deposits produced alteration zones of variable extent

in the overlying sandstone or more restricted zones in basement rocks surrounding the deposit (Wilson and Kyser, 1987; Kotzer and Kyser, 1995; Fayek and Kyser, 1997). The flow of fluids that affect the formation of the deposits and subsequent alteration of them are associated with high-angle fault structures most commonly associated with graphite-rich gneisses and pelites and quartzites that form a competency contrast (Kyser *et al*., 1989). These fault systems are pre-cursors for later structural features (i.e. fractures in the overlying sandstone), which ultimately control uranium deposition (Kyser *et al*., 1989). The alteration zones associated with unconformity-related U deposits can be used for exploration because they significantly enhance the footprint of the deposit by up to several hundred meters from the ore (Gustafson and Curtis, 1983; Wilde *et al*., 1989), extending along structural discontinuities including permeable zones such as faults, fractures, and breccias on both sides of the unconformity (Beaufort *et al*., 2005).

The mineralogy and geochemistry of some alteration zones are related to two temporally distinct processes that are directly associated with the mineralizing system: (1) primary (syn-mineralization) and (2) secondary (post-mineralization) dispersion. Primary dispersion occurs during hydrothermal alteration associated with the mineralizing system, wherein elements are dispersed to the surrounding rocks, creating a dispersion halo around the deposit itself and along fractures with enhanced permeability (McQueen, 2005). Secondary dispersion occurs when post-ore events such as later hydrothermal fluids, low-temperature meteoric fluids, or microbial activity (Cameron *et al*., 2004) variably mobilize elements from the ore zone and/or surrounding alteration halo; a process also facilitated by the enhanced permeability of open fractures. Mobilized post-mineralization elements can be present in fracture coatings where they are absorbed onto Fe- and Al-oxy-hydroxides and Fe-Mn hydroxides that can precipitate during primary dispersion processes or from fluids that flow down fractures from the surface. These phases typically have negative charges that are capable of attracting metal cations including

elements that may be mobilized from the deposit, thereby trapping them on fracture surfaces during secondary dispersion from the deposit (e.g. Cameron *et al*., 2004). Fractures are important to both primary and secondary dispersion processes and are therefore critical in defining the extended footprint of the deposit and the possible processes by which elements in surface media can reflect the deposit at depth.

The McArthur River deposit is the largest high-grade unconformity-related U deposit in the world. The alteration and mineralizing processes that occurred in the McArthur River area between the middle Proterozoic Athabasca Basin and the Archean to lower Proterozoic basement are thought to have resulted from basinal brines (Hoeve and Sibbald, 1978; Pagel *et al*., 1980). The basinal brines circulated at the basement-cover interface and strongly interacted with various lithologies, producing a large illite-sudoite-dravite alteration halo surrounding the deposit (Wilson and Kyser, 1987; Kotzer and Kyser, 1995; Fayek and Kyser, 1997; Renac et al., 2002; Alexandre et al., 2005). The mineral paragenesis of the deposit and the surrounding area (Figure 3.1) was examined by Kotzer and Kyser (1995), Fayek and Kyser (1997), and Ng *et al*. (2013), among others, who characterized the origin and type of fluids in the mineralizing system using O and H isotopic compositions of clay and silicate minerals. The stable isotope work suggests several generations of mineral formation: illite, euhedral quartz, and dravite at *ca*. 200°C from early hydrothermal fluids, and also later kaolinite and Fe-Mn oxide minerals on fractures that formed from low-temperature meteoric fluids. Pb present in drusy quartz fracture coatings from around the McArthur River area and other unconformity-related deposits contains high $^{206}Pb/^{204}Pb$ values, consistent with migration of radiogenic Pb from the ore body along fractures (Holk *et al*., 2003). Devine (2016) showed that fractures near the surface have coatings of illite, kaolinite, and Fe-Mn oxy-hydroxides, the latter hosting Ra (≤32.2 pg/g). Thus, fractures

potentially record both primary and secondary processes associated with unconformity-related U deposits, thereby enhancing the footprint of the deposits, as well as late meteoric processes.

In this study, the mineralogy and geochemistry of coatings from fractures and adjacent wall rock in the Athabasca Group sandstones above the McArthur River deposit are evaluated to determine if these fractures reflect the presence of U mineralization at depth (>500 m) and so reflect mobilization processes. The purpose of this study is to investigate which mineral phases on the fractures are host to various pathfinder elements and whether components within fractures, located at depths from close to the mineralization to the surface, may be related to mineralization and therefore constitute an effective exploration tool. The presence/absence of elements trapped in the fractures depends on the interaction between elements and the geochemical barriers they encounter. Precipitation as phosphates and sulfates, adsorption onto reactive mineral surfaces such as Mn-Fe oxides, clays and organic material, and co-precipitation and substitution within minerals are all processes that can come into play in these fracture systems (Goldberg, 1998; Hall, 1998). The mineral chemistry of fractures can therefore be used to document large-scale fluid activity in sedimentary basins, because any fluid that migrates through permeable rocks will leave some evidence of water-rock interactions (e.g. Bath *et al*., 1987; Bethke and Marshak, 1990). The main objectives of this study are (1) to examine these fractures near the McArthur River U deposit to aid in the Canadian Mining Innovation Council (CMIC) NSERC-CRD Footprints project determination of the footprint of the McArthur River U deposit, and (2) to generate more effective approaches to integrate and visualize multi-parameter data sets and thus improve exploration within the footprint of unconformity-related uranium deposits (e.g. Lesher *et al*., 2017).

3.2 Geological setting

3.2.1 Regional geology

The Athabasca Basin is an intracratonic basin located in Northern Saskatchewan and Alberta (Figure 3.1), and covers an area greater than 85,000 km^2 (Ramaekers, 1990). The Paleo- to Mesoproterozoic basin unconformably overlies Archean and Paleoproterozoic basement composed of metamorphic and igneous rocks of the western Churchill Province (Figure 3.1), which is further divided into the Rae and Hearne Sub-Provinces. The western Churchill province is located between the remains of two orogenic belts: the Taltson-Thelon orogenic belt (*ca*. 1.9 Ga) and the Trans-Hudson Orogen (*ca*. 1.8 Ga) (Hoffman, 1988). In the Athabasca region, the contact between the Rae and Hearne Provinces is the Snowbird Tectonic Zone (Hoffman, 1988), comprised of the Virgin River shear zone to the south of the Athabasca and the Black Lake shear zone to the north (Figure 3.1).

There are three domains within the Hearne Province in the Athabasca region, all containing metamorphosed Archean and Paleoproterozoic granitic gneiss and overlying the supracrustal meta-sedimentary sequences. Boundaries between the domains exhibit lithological, structural, and metamorphic continuity (Lewry and Sibbald, 1980). Differences between the domains include spatial variation in a related and similar sequence of evolutionary events (Lewry and Sibbald, 1980). From east to west the domains are: the Wollaston Domain, the Mudjatik Domain, and the Virgin River Domain (Annesley *et al*., 2005; Tran *et al*., 2008), with the Wollaston-Mudjatik Transition Zone (WMTZ) separating the Wollaston and Mudjatik domains (Annesley *et al*., 2005; Jeanneret *et al*., 2016). Most of the unconformity-type U deposits in the eastern Athabasca region are located within the WMTZ.

The Wollaston Group basement is composed of pelitic, semipelitic and arkosic gneissic rocks, with calc-silicate and quartzite units in the footwall, and pegmatitic veins in the hanging

wall of the P2 fault zone, which transects the deposit (McGill *et al*., 1993). Prior to the deposition of the Athabasca Group, a paleoweathering profile was established on basement rocks (Ramaekers, 1990). The paleoweathering profile is composed of kaolinite upper layers, chlorite, and illite lower layers and is partially preserved, up to 50 m thick (Ramaekers, 1990). The upper portion of the paleoweathering profile contains pervasive hematite staining; however, the profile can be altered in some areas to chlorite by superimposed reduction (Ramaekers, 1990). Along the hanging wall of the P2 fault lies a 25 m-thick sequence of graphite-bearing pelitic gneiss (McGill *et al*., 1993).

The circa 1700-1500 Ma Athabasca Group (Figure 3.1) consists of flat-lying, quartz-rich sandstone and conglomerate, which was deposited in major river systems and near-shore to shallow-shelf environments (Ramaekers, 1990; Ramaekers *et al*., 2007). Sedimentary basin fill has a maximum current thickness around 1.5 km, although temperature estimates from fluid inclusions suggest that these sequences reached depths of up to 5 km during peak diagenesis (Pagel *et al*., 1980). The units are cut by reactivated Hudsonian faults that are periodically active to the present day (Hoeve and Quirt, 1984; Kyser *et al*., 2000). The northwest-trending 1267 Ma Mackenzie dike swarm (LeCheminant and Heaman, 1989) also cuts the sedimentary sequences of the Athabasca Basin and underlying basement rocks.

Four unconformity-bound stratigraphic sequences form the Athabasca Group (Figure 3.1; Yeo *et al*., 2002; Ramaekers and Catuneanu, 2004; Ramaekers *et al*., 2007). In ascending order: 1) the Fair Point Formation; 2) the Smart and Manitou Falls formations, which make up the majority of the Athabasca Group (Ramaekers *et al*., 2007); 3) the Lazenby Lake and Wolverine Point formations, and 4) the Locker Lake, Otherside, Douglas, and Carswell formations (Ramaekers *et al*., 1979, 1980; Ramaekers, 1990). This Athabasca strata present in the McArthur River area consist of Manitou Falls Formation sandstone and microconglomerate.

3.2.2 Manitou Falls Formation

The Manitou Falls Formation is divided into four members which are, from youngest to oldest, the MFd, MFc, MFb and MFa (Figure 3.1; Ramaekers, 1990). Members a, b, and c were formed from clastic sediments deposited primarily within alluvial fans (MFa) and high-energy, proximal braided streams (MFa, MFb, MFc) (Ramaekers, 1990). MFd reflects deposition in more distal portions of a braided stream, such as an estuary or a braided delta setting (Hiatt and Kyser, 2007).

The MFa is composed of interbedded matrix-supported quartz pebble conglomerate and well-to-poorly-sorted, medium-grained sandstone, accompanied by minor hematitic siltstone beds (Ramaekers, 1990), while the MFb consists of medium-grained sandstone with significant poorly-sorted and clast-supported conglomerate sandstone (Ramaekers, 1990). The MFc contains sandstone that has very minor conglomerate beds less than 2 cm thick and contains less than 1% clay intraclasts (Ramaekers, 1990). The MFd is gradational from the MFc and is composed of well-sorted sandstone with greater than 1% clay intraclast-rich layers (Ramaekers, 1990). In the MFd, bedded siltstone can locally occur as up to 5 cm thick beds (Ramaekers, 1990). This study uses nomenclature from Ramaekers (1990) to remain consistent with historical literature and current exploration terminology.

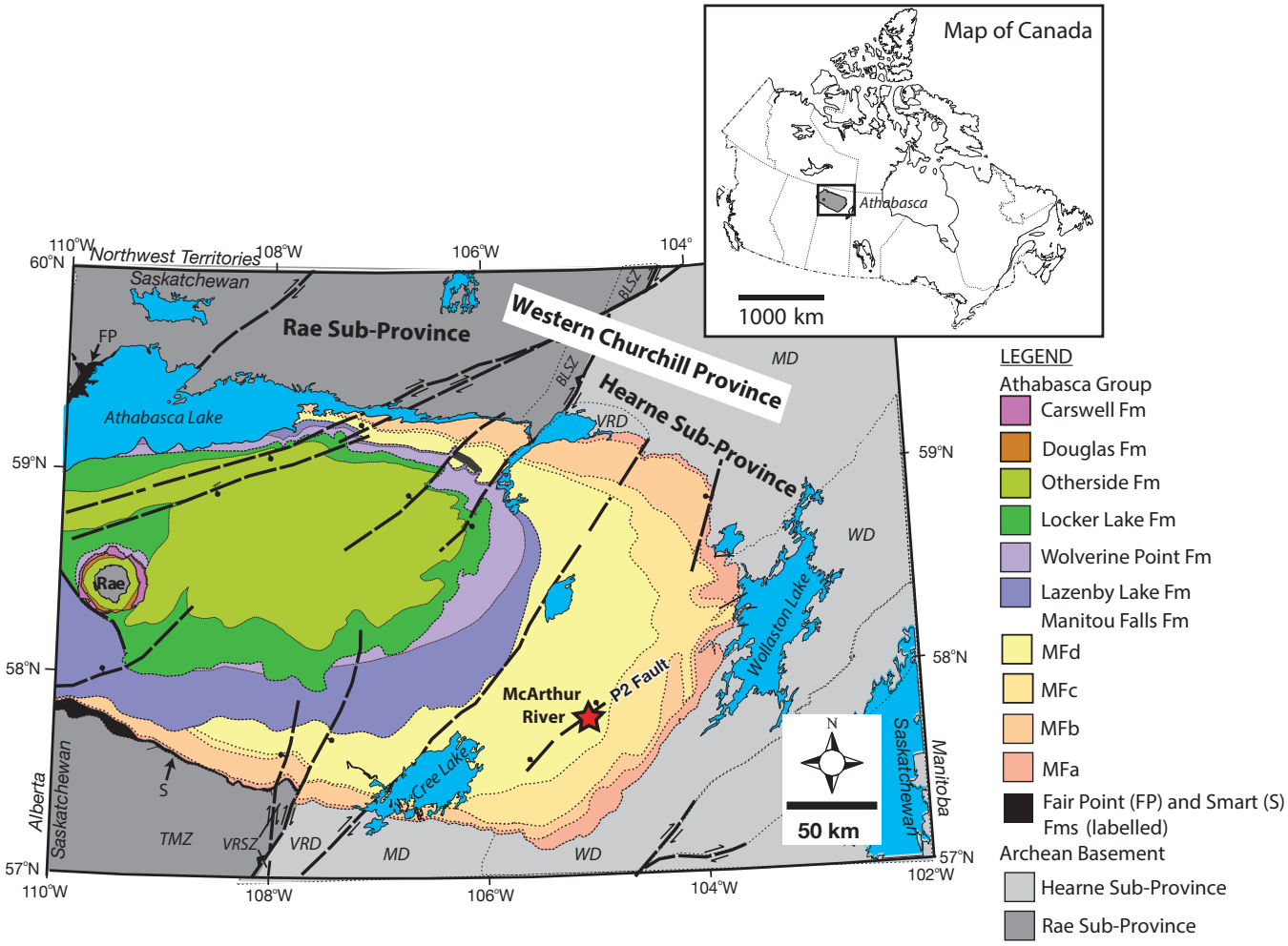

Figure 3.1: Geological map of the Athabasca Basin, highlighting basement provinces (grey; names in bold), fault structures (dashed lines) such as the P2 fault, stratigraphic sections of the Athabasca Group, and the McArthur River deposit (red star). Figure modified from Ng *et al.* (2013). Domain abbreviations: VRD = Virgin River, MD = Mudjatik, WD = Wollaston. Shear/magmatic zones: BLSZ = Black Lake shear zone, VRSZ = Virgin River shear zone, TMZ = Taltson magmatic zone.

3.2.3 McArthur River unconformity-related U deposit

The McArthur River unconformity-related U deposit (Figure 3.1) occurs around the unconformity between the Manitou Falls Formation of the Athabasca Group and Wollaston Group basement rocks, along the P2 structure (Ng *et al*., 2013). The P2 fault is a major reverse thrust fault with a strike length of approximately 13 km, striking N45°E, and dipping 40° to 45° SE (McGill *et al*., 1993). The P2 fault has been traced seismically at least 2 km from the unconformity (Hajnal *et al*., 2010). As displacement along the fault occurred along the graphite-rich basement rocks, the hanging wall block was uplifted by 60-80 m (Figure 3.2). The P2 structure underwent multiple episodes of reactivation during sedimentation (Bernier, 2004; Yeo *et al*., 2007) and was displaced by three sets of steeply-dipping transcurrent faults, which strike 100° to 110° (McGill *et al*., 1993).

Intense silicification is present within the Manitou Falls Formation, especially in the lower 200 m (MFa and MFb) of the Manitou Falls Formation at Zone 4 (Figure 3.2b; Ng *et al*., 2013). Hiatt *et al*. (2007) suggested that this silicified zone formed primarily due to early pre-compaction quartz cementation, whereas Derome *et al*. (2005) suggested that silicification was the result of post-diagenetic, but pre-ore in timing. Pan *et al*. (2006), who used electron paramagnetic resonance (EPR) spectroscopy to observe the effects of U on quartz cements suggest that both previously mentioned processes operated. Either process would limit syn-mineralization or post-mineralization dispersion of elements from the deposit to fracture-controlled migration (Kyser *et al*., 2000; Holk *et al*., 2003; Hiatt and Kyser, 2007; Ng *et al*., 2013; Joyce, 2016). Reactivation of the P2 fault later caused widespread fracturing of silicified sandstone, with a 50-75 m fracture zone being present in the lower MFa (McGill *et al*., 1993; Mwenifumbo *et al*., 2004).

Alteration mineralogy within the Manitou Falls Formation includes quartz cements, iron oxides, dravite, dickite, sudoite and illite (McGill *et al*., 1993). Chlorite-dravite solution breccias are associated with massive quartz dissolution (Lorilleux *et al*., 2002; Derome *et al*., 2005). Basement alteration proximal to the P2 fault zone consists of an inner illite-sudoite alteration and a distal clinochlore alteration (Ng *et al*., 2013). At the hanging wall of the P2 fault, dravite, apatite and carbonate are locally present, (McGill *et al*., 1993; Alexandre *et al*., 2005) together with intense uranium mineralization associated with significant hematite alteration (Ng *et al*., 2013). In proximity to hydrothermally-altered fault zones, these early formed diagenetic and hydrothermal assemblages, were altered and overprinted by late meteoric fluids (Kotzer and Kyser, 1995). Kaolinite mainly occurs within fractures in the upper Manitou Falls Formation, (MFc and MFd), from meteoric fluid infiltration and adjacent to the P2 fault zone in the sandstone from hydrothermal fluids (Kotzer and Kyser, 1995).

The Zone 4 ore body is a strongly mineralized region located at a depth of 500-570 m along the P2 fault (McGill *et al*., 1993; Ng *et al*., 2013). It is partially hosted within the uplifted Wollaston Group basement hanging wall and adjacent Athabasca Group sedimentary rocks, along the P2 fault (Ng *et al*., 2013). The Zone 4 ore body is dominantly monometallic and composed of uraninite, with minor galena, pyrite, chalcopyrite, and Ni-Co-Au sulfides (Ng *et al*., 2013). Late coffinite, late poorly-crystallized uraninite, and recent secondary uranyl minerals also occur in the deposit (McGill *et al*., 1993; Fayek and Kyser, 1997).

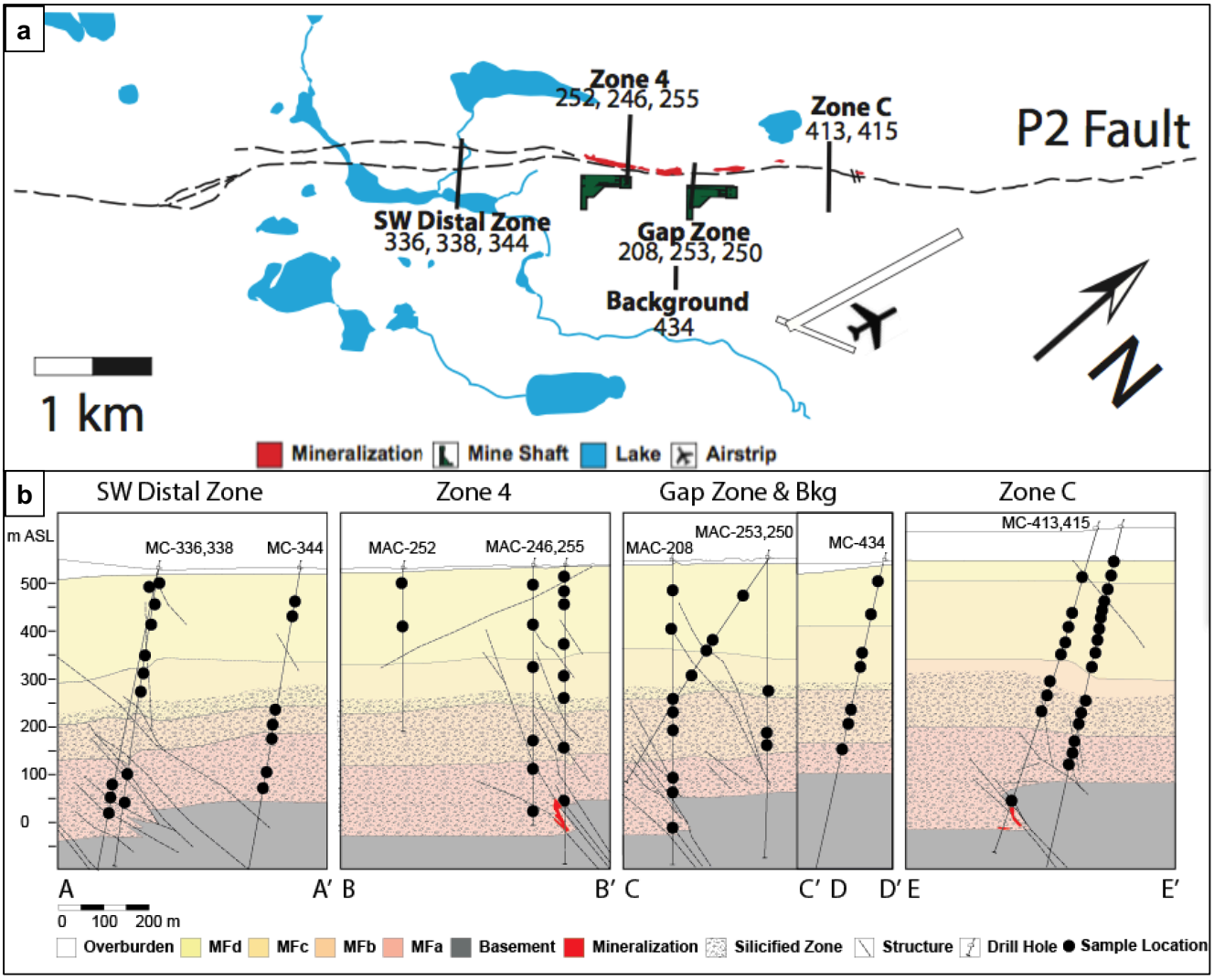

Figure 3.2: (a) Map view of the McArthur River area, highlighting the five zones and drill holes where the fractures for this study were collected; (b) cross section of the McArthur River area, showing the five zones and drill holes where the fractures for this study were collected. Sample locations indicated as a solid circle. Figure modified from Joyce (2016).

The Athabasca sandstones and conglomerates in the McArthur River area consist of *ca.* 95% quartz (+ minor heavy minerals) and 0-5% matrix minerals by volume (Kotzer and Kyser, 1995; Hiatt *et al.*, 2007). The underlying Paleoproterozoic Wollaston Group metasedimentary rocks contain mainly quartz, plagioclase, biotite, cordierite, garnet, and minor tourmaline, with anatectic pegmatite and graphite layers, unconformably overlie the Archean granitoid gneiss (Ey

et al., 1991; Marlatt *et al*., 1992). The graphite layers include an approximately 25 m thick sequence of graphitic pelitic gneiss (McGill *et al*., 1993). Early diagenesis of the basin formed quartz overgrowths, an APS (aluminum-phosphate-sulphate) mineral, and hematite on detrital quartz of the Manitou Falls Formation (Kotzer and Kyser, 1993, 1995; Derome *et al*., 2005). The Aluminum-Phosphate-Sulphate (APS) group mineral is associated with the hydrothermal clay and silicate minerals that comprise the alteration halo of U deposits in the basin (Cuney and Kyser, 2014). Kotzer and Kyser (1995) used increasing $\delta^{18}O$ values, increasing salinities, and homogenization temperatures in fluid inclusions of diagenetic quartz to indicate that continued water interactions modified the basinal fluids, and to some extent, basement fluids, chemically and isotopically. Prior to interaction of fluids along fractures, illite and dickite were produced throughout the entire basin by alteration of detrital silicates during peak diagenesis of the Athabasca Group (Percival, 1993; Kotzer and Kyser, 1995; Laverret *et al*., 2006). Therefore, the predominant clay assemblage of the Athabasca Group is dickite (+/- kaolinte) +/- illite (Hoeve and Quirt, 1984).

The study examined five zones in the McArthur River deposit area, represented by drill fences that are perpendicular to the structural trend of the P2 fault (Figure 3.2). These areas include, from southwest to northeast, the South West Distal Zone (weakly mineralized), Zone 4 (strongly mineralized), the Gap Zone (between zones of mineralization), Background (drill hole MC-434) and Zone C (moderately mineralized) (Figure 3.2).

3.3 Methods

Eighty-two samples of fracture material and their wall rocks were selected to reflect a spectrum of fracture types based on mineralogical characteristics, from near-ore to distal areas.

Major elements, trace elements and Pb isotopic analyses were conducted on fracture coatings through weak acid leach (WAL; 2% HNO_3) to extract mobile elements, and *Aqua Regia* (AR), a more aggressive leaching technique using a modified mixture (1:1:1) of distilled HCl, HNO_3 and deionized water, to study more refractory elements. Leached solutions were measured using a Thermo Scientific Element II XR high resolution inductively coupled plasma mass spectrometry (HR-ICP-MS). A detailed analysis of fractures is presented in the methods section of Chapter 2. Abbreviations of minerals throughout the text and figures are those of Whitney and Evans (2010).

A Continuous Leach Inductively Coupled Plasma Mass Spectrometry (CL-ICP-MS) method was used on eighteen fracture coatings from the McArthur River deposit (Table 3.1) from near-ore to distal areas to observe the relationship between trace elements and Pb isotopes released from specific mineral phases using real-time data produced by leaching by progressively increasingly reactive solutions, from deionized water to 30% nitric acid (MacFarlane *et al*., 2005). These samples were chosen for comparison on the basis on U concentration, $^{207}Pb/^{206}Pb$ isotope values, depth, and fracture type. Multiple isotopes of elements were determined with multiple resolutions to monitor for interferences (MacFarlane *et al*., 2005). Spectral interferences were minimized using three mass resolutions: low (R>300), medium (R>4000), and high (R>10000); HR-ICP-MS operating parameters used in this study, shown in Table 3.2, were optimized daily for sensitivity, stability, and lowest oxides (typically less than 5%). Table 3.3 provides a list of isotopes analyzed by CL-ICP-MS using various analytical resolutions.

Table 3.1: Summary of fracture coating samples analysed by CL-ICP-MS analysis.

Sample ID	Fracture Type	Mineral Phases
MAC-208-262.5	1-Brown	Ilt, Kln, Gth
MAC-208-305	4-Black	Ilt, Dck, MnOx, FeOx
MAC-208-462	2-White & Yellow	Dck, Ilt, Drv, Gth
MAC-208-476.5	2-White & Yellow	Ilt, Kln, FeOx
MAC-208-570	6-Drusy Quartz	Sd, MnOx, Clc, Drv, FeOx
MAC-250-276	4-Black	MnOx, Ilt, Kln, Drv, APS
MAC-250-396	6-Drusy Quartz	Ilt, Dck, Gth, APS
MAC-252-21.7	3-White	Ilt, Kln, Drv, FeOx
MAC-255-37	2-White & Yellow	Kln, Ilt, Drv, FeOx
MAC-255-251	7-Pink	Ilt, Kln, FeOx
MAC-255-509	3-White	Clc, Ilt, Drv, TiOx
MC-336-523.8	2-White & Yellow	Drv, Kln, Ilt, FeOx
MC-338-121	5-Black & Orange	Ilt, Kln, FeOx, MnOx
MC-338-206	5-Black & Orange	Ilt, Kln, Gth
MC-338-429.7	2-White & Yellow	Ilt, Kln, Gth
MC-344-122	1-Brown	Ilt, Drv, Kln, FeOx, MnOx
MC-413-73.6	1-Brown	Ilt, Kln, Drv, FeOx, TiOx
MC-413-614	3-White	Kln, Drv, Ilt, Clc, Py

Table 3.2. HR-ICP-MS parameters.

Tune parameters	
sample gas flow	1 l/min
auxiliary gas	0.8 l/min
cool gas	18 l/min
guard electrode	in
Low resolution aquisition parameters	
mass window	150%
samples/peak	30
sample time	0.01 sec
detection mode	triple
integration window	80%
runs/passes	65/1
Medium resolution aquisition parameters	
mass window	125%
samples/peak	20
sample time	0.01 sec
detection mode	triple
integration window	70%
runs/passes	65/1
High resolution aquisition parameters	
mass window	125%
samples/peak	20
sample time	0.01 sec
detection mode	triple
integration window	70%
runs/passes	65/1

Table 3.3. Isotopes measured at low, medium, and high resolution using CL-ICP-MS.

Low	Medium		High	
^{9}Be	^{7}Li	^{79}Br	^{13}C	^{166}Er
^{10}B	^{13}C	^{81}Br	^{32}S	^{169}Tm
^{11}B	^{24}Mg	^{85}Rb	^{34}S	^{172}Yb
^{13}C	^{25}Mg	^{88}Sr	^{35}Cl	^{175}Lu
^{23}Na	^{27}Al	^{89}Y	^{37}Cl	^{178}Hf
^{115}In	^{28}Si	^{90}Zr	^{39}K	^{183}W
^{118}Sn	^{29}Si	^{91}Zr	^{69}Ga	^{185}Re
^{138}Ba	^{31}P	^{93}Nb	^{72}Ge	^{195}Pt
^{139}La	^{35}Cl	^{97}Mo	^{75}As	^{197}Au
^{140}Ce	^{37}Cl	^{98}Mo	^{77}Se	
^{200}Hg	^{42}Ca	^{101}Ru	^{79}Br	
^{202}Hg	^{44}Ca	^{107}Ag	^{81}Br	
^{203}Tl	^{45}Sc	^{109}Ag	^{105}Pd	
^{205}Tl	^{47}Ti	^{110}Cd	^{110}Cd	
^{204}Pb	^{49}Ti	^{105}Pd	^{111}Cd	
^{206}Pb	^{51}V	^{111}Cd	^{115}In	
^{207}Pb	^{52}Cr	^{115}In	^{118}Sn	
^{208}Pb	^{53}Cr	^{118}Sn	^{121}Sb	
^{209}Bi	^{55}Mn	^{121}Sb	^{126}Te	
^{232}Th	^{56}Fe	^{133}Cs	^{127}I	
^{235}U	^{59}Co	^{139}La	^{140}Ce	
^{238}U	^{60}Ni	^{182}W	^{141}Pr	
	^{62}Ni	^{183}W	^{146}Nd	
	^{63}Cu		^{147}Sm	
	^{65}Cu		^{153}Eu	
	^{64}Zn		^{157}Gd	
	^{66}Zn		^{159}Tb	
	^{77}Se		^{163}Dy	

The original CL-ICP-MS method used four reagents: deionized water (18MΩ resistivity), 1% HNO_3, 10% HNO_3, and 30% HNO_3 (MacFarlane *et al*., 2005). This study used a modification of the original method and added a 10% hydrogen peroxide step between the deionized water step and the 1% HNO_3 step to break down organic material in the fracture coating before the

dissolution of carbonate in nitric acid (van Geffen *et al*., 2015). Nitric acid was chosen as a leaching solution for CL-ICP-MS due to its nature as a low-interference medium (e.g. enabling Cl concentrations to be determined), and its ability, at high concentrations, to attack resistant phases. For CL-ICP-MS, approximately 50 mg of fracture coating material was removed from the fracture surface as a powder using a dental drill. The sample was then weighed into a sampler holder (sample column) consisting of Teflon tubing of approximately 9 cm in length. Quartz wool was used to plug each end of the Teflon tubing to prevent coarse particulate sediment from moving into the HR-ICP-MS (Figure 3.3). A Teflon frit was also used, at the downstream end of the sample column to prevent fine particles from getting through. A 0.6 mL/min glass concentric nebulizer and a cyclonic spray chamber were used to introduce the leachate into the mass spectrometer. The column is connected to a peristaltic pump that is used to send progressively increasingly reactive solutions through the sample, at a flow rate of 556 μL/min, and into the mass spectrometer (Figure 3.3). Each leaching solution cycles through low, medium, and high resolution analyses continuously for 45 minutes, resulting in a total analytical time of 225 minutes per sample. The frequency of the sample solution uptake is controlled by the peristaltic pump set at 0.6 mL/minute, allowing elements to be measured in each 25 mL of leaching solution and 318 data points per sample analyses to be obtained. Each leaching solution is spiked with 10 ppb In as an internal standard. The data is normalized to the In internal standard signal, within each solution, and further normalized to the In response in the DI (deionized) water step to correct data for fluctuations in sample flow rate, matrix effects and instrument sensitivity (MacFarlane *et al*., 2005). A 10-point moving average is then applied to the data, which is converted from counts per second (cps) to parts per million (ppm), shown in appendix G. This conversion from counts to quantity is made by measuring the leaching solutions spiked with calibration standard solutions and introduced through a ‘blank sample’ apparatus to keep flow

rates consistent. The 'blank sample' apparatus is the same CL-ICP-MS apparatus, shown in Figure 3.8, but with no sample in the sample column. A multiplication factor is then applied to the release patterns, bringing the elements to a common scale to allow comparisons between elements.

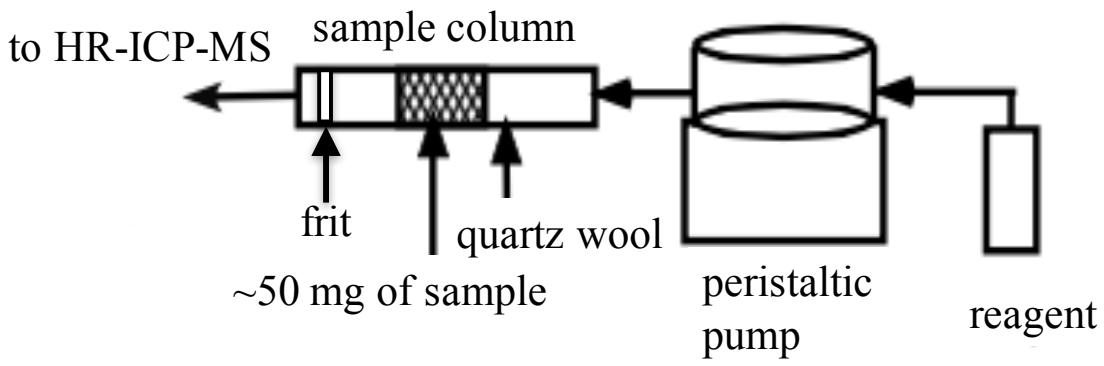

Figure 3.3: Continuous Leach (CL-ICP-MS) apparatus modified from MacFarlane *et al.* (2005).

3.4 Results

3.4.1 Fracture characteristics

Mineralogical and petrographic characteristics of the fracture coatings (Chapter 2) indicate that there are seven distinct types of fracture coatings:

1. Brown – Mn oxides, Fe oxides (goethite and hematite) and ± kaolinite, illite, dravite (30 samples)
2. White & Yellow – Fe oxides (goethite) and dravite, kaolinite, illite (20 samples)
3. White – Contains 1 or more of dravite, illite, kaolinite (15 samples)
4. Black – Mn oxides and ± dravite, illite, kaolinite (9 samples)
5. Black & Orange – illite, kaolinite, goethite, and Mn oxides (3 samples)
6. Drusy Quartz – also commonly contains goethite and Mn oxides (3 samples)
7. Pink – illite, kaolinite, and Fe oxides (2 samples)

All investigated fractures at McArthur River occur within the Manitou Falls Formation. The shallowest sample represents a true vertical depth of ~11 m and ~520 m above the unconformity, compared to the deepest sample at ~580 m at the P2 fault. The horizontal extent of the sampling area is ~3150 m along the P2 fault. Type 1 (brown), type 2 (white and yellow), and type 3 (white) fracture fillings occur over the entire depth range. Black (type 4), black and orange (type 5), and pink (type 7) fracture fillings occur close to the surface (Figure 3.4). Drusy quartz (type 6) fractures occur deep, close to the unconformity.

Samples from the non-mineralized drill hole (MC-434) represent a local background signature for the Manitou Falls Formation in the McArthur River region, as the drill hole is located ~1 km from the deposit (e.g. strongly mineralized Zone 4 drill holes; Figure 3.2a). Fracture fillings present in this background area, including samples near the P2 fault, are brown (type 1), white and yellow (type 2), and white (type 3) (Figure 3.4), which are rich in the pre-ore diagenetic clay minerals (dickite and illite; Hoeve and Quirt, 1984; Jefferson *et al*., 2007).

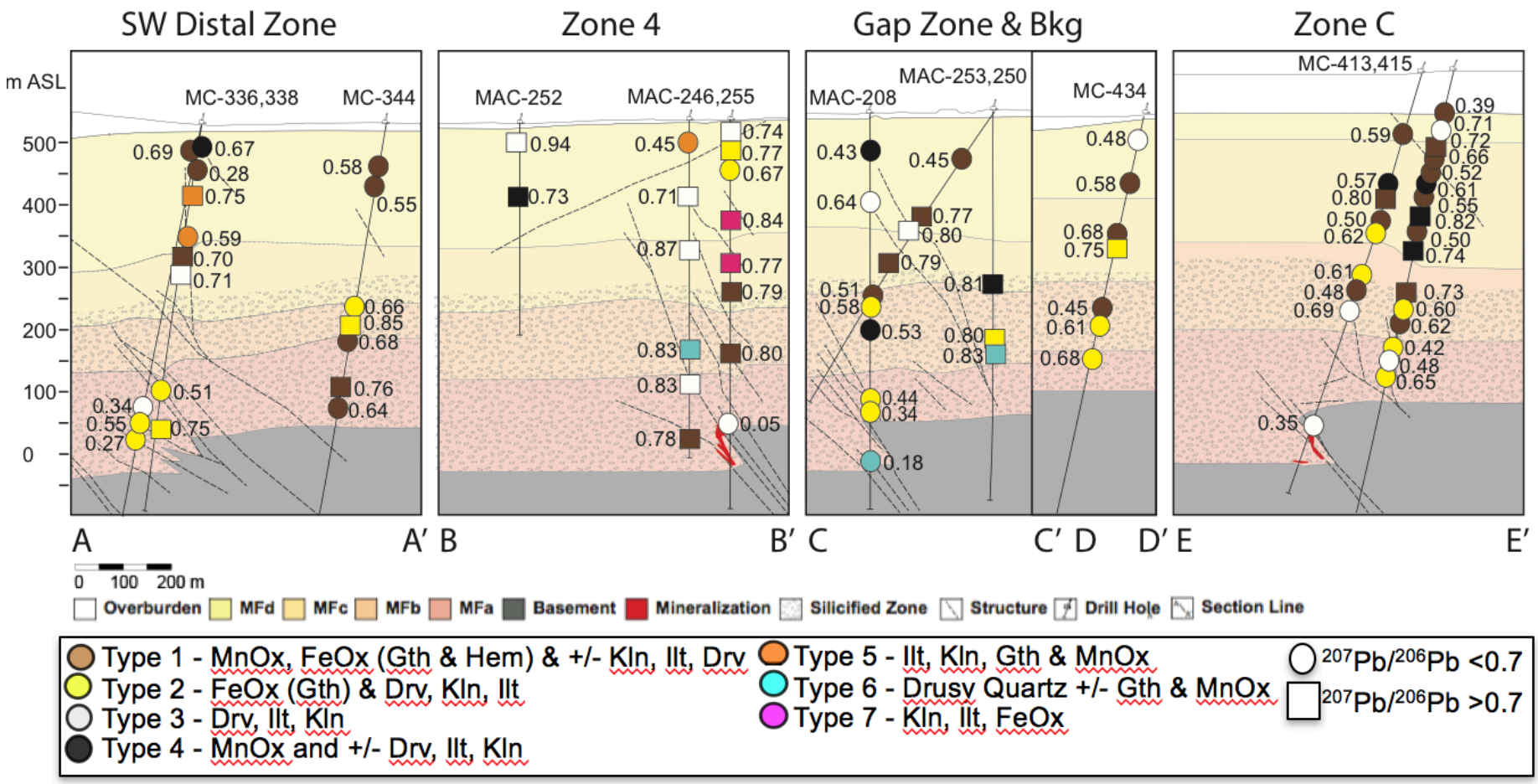

Figure 3.4: Cross-section across the P2 fault at McArthur River (Figure 3.2) showing the location of fracture samples in the Manitou Falls Formation, highlighting fracture type by various colors and $^{207}Pb/^{206}Pb$ isotope ratios. Figure modified from Joyce (2016).

3.4.2 Pb isotopes and REE patterns

Rare earth element (REE) patterns and Pb isotope data obtained from weak acid leaching of fracture coatings were used to group the fracture types into three groups (Table 3.4). The weak acid leach was used rather than *aqua regia* or total digestion because the elements are mobile phases precipitated and absorbed on mineral surfaces. The various chondrite-normalized (Nakamura, 1974) REE patterns observed are: 1) Group 1; light REEs (LREEs)-enriched, 2) Group 2; concave-down ("bell-shaped" elevated middle REEs (MREEs)) patterns, and 3) Group 3; generally flat REE patterns (Figure 3.5). Calculated Pb-Pb isotope model ages, based on the two-stage Pb evolution model of Stacey and Kramers (1975), for the three patterns range from 1070 Ma to 1201 Ma.

Group 1 is composed of clay-rich (type 3, type 7), drusy quartz (type 6) and oxide-rich (type 1, type 2) fracture coatings, that show enrichment in LREEs (Figure 3.5a) and an imprecise Pb-Pb model age of 1163 +/- 130 Ma (Figure 3.5b). Group 2 consists of drusy quartz (type 6) and oxide-rich (type 1, type 2, type 4, type 5) fracture coatings, that display a bell-shaped, concave-down REE pattern that shows enrichment in the MREEs (Figure 3.5c; Mercadier *et al*., 2011) and an imprecise Pb-Pb model age of 1201 +/- 240 Ma (Figure 3.5d). Group 3 is composed of oxide-rich (type 1, type 2, type 4) fracture coatings that show a flat REE pattern (Figure 3.5e) and also record an imprecise Pb-Pb model age of 1070 +/- 290 Ma (Figure 3.5f). The Pb-Pb model ages for all groups coincide roughly with the Grenville Orogen (McLelland *et al*., 1996; Rivers, 1997; Carr *et al*., 2004).

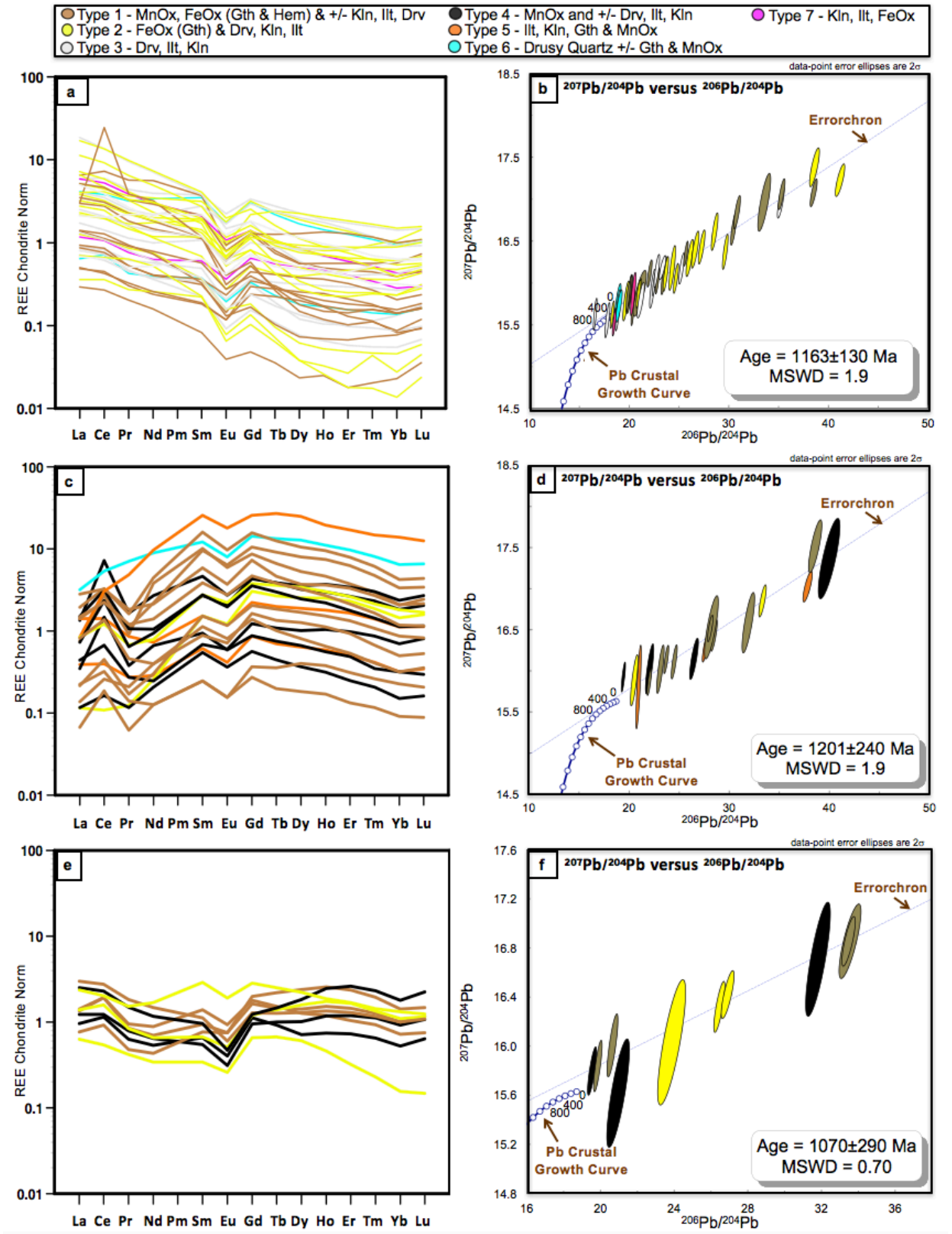

Figure 3.5: a) Chondrite normalized (Nakamura, 1974) LREE enriched patterns of clay-rich (type 3, type 7), drusy quartz (type 6), and oxide-rich (type 1, type 2) fracture types

obtained from weak acid leaching; b) relationship between $^{207}Pb/^{204}Pb$ and $^{206}Pb/^{204}Pb$ and model age of fracture coatings for Group 1; c) concave-down REE pattern from drusy quartz (type 6) and oxide-rich (type 1, type 2, type 4, type 5) fracture types; d) relationship between $^{207}Pb/^{204}Pb$ and $^{206}Pb/^{204}Pb$ graph and model age of fracture coatings for Group 2; e) flat REE pattern of oxide-rich (type 1, type 2, type 4) fracture types; f) relationship between $^{207}Pb/^{204}Pb$ and $^{206}Pb/^{204}Pb$ graph and model age of fracture coatings for Group 3. Data from Table 3.4.

Table 3.4: REE concentrations, U concentrations, and $^{207}Pb/^{204}Pb$, $^{206}Pb/^{204}Pb$, and $^{238}U/^{206}Pb$ values from WAL analyses of fractures from McArthur River.

Sample ID	La (ppm)	Ce (ppm)	Pr (ppm)	Nd (ppm)	Sm (ppm)	Eu (ppm)	Gd (ppm)	Tb (ppm)	Dy (ppm)	Ho (ppm)	Er (ppm)	Tm (ppm)	Yb (ppm)	Lu (ppm)	U (ppm)	$^{207}Pb/^{204}Pb$	$^{206}Pb/^{204}Pb$	$^{238}U/^{206}Pb$
MAC-208-57.6	0.12	1.28	0.05	0.42	0.19	0.04	0.24	0.04	0.23	0.04	0.04	0.01	0.07	0.01	2.33	17.37	40.02	8.96
MAC-208-154.8	0.23	0.53	0.06	0.24	0.07	0.02	0.10	0.02	0.11	0.02	0.02	0.01	0.06	0.01	1.22	16.18	25.30	15.25
MAC-208-262.5	0.02	0.05	0.01	0.02	0.01	0.00	0.02	0.00	0.02	0.01	0.00	0.00	0.01	0.00	1.90	16.96	33.60	63.33
MAC-208-263	0.91	2.13	0.20	0.72	0.14	0.02	0.14	0.02	0.14	0.03	0.02	0.02	0.10	0.02	10.90	16.62	28.62	9.48
MAC-208-305	0.40	1.07	0.10	0.41	0.11	0.02	0.26	0.05	0.35	0.09	0.02	0.04	0.20	0.04	10.17	16.71	31.83	508.50
MAC-208-462	1.69	3.83	0.47	2.17	0.64	0.14	0.88	0.12	0.65	0.12	0.14	0.04	0.22	0.04	257.62	17.08	38.56	74.46
MAC-208-476.5	0.17	0.54	0.08	0.41	0.12	0.03	0.18	0.03	0.17	0.03	0.03	0.01	0.07	0.01	77.69	17.89	52.86	98.34
MAC-208-570	1.05	4.66	0.91	5.63	2.46	0.61	3.96	0.67	4.37	0.85	0.61	0.28	1.42	0.22	279.31	22.87	126.85	27.63
MAC-246-23.1	0.28	2.63	0.62	6.14	5.20	1.38	7.05	1.36	8.53	1.49	1.38	0.51	3.06	0.42	445.73	17.03	37.87	87.23
MAC-246-142	1.96	5.16	0.57	2.49	0.77	0.17	0.92	0.14	0.78	0.15	0.17	0.05	0.31	0.05	20.00	15.94	22.38	3.42
MAC-246-198.5	0.57	1.23	0.15	0.63	0.22	0.05	0.32	0.05	0.28	0.05	0.05	0.02	0.09	0.01	9.07	15.56	17.85	1.15
MAC-246-395	1.36	3.31	0.41	2.13	0.71	0.13	0.84	0.11	0.57	0.11	0.13	0.04	0.20	0.03	76.72	15.76	18.89	3.11
MAC-246-446	0.29	0.71	0.08	0.36	0.10	0.01	0.09	0.01	0.04	0.01	0.01	0.00	0.03	0.01	7.24	15.73	19.01	0.56
MAC-246-534	0.10	0.23	0.03	0.10	0.02	0.00	0.01	0.00	0.01	0.00	0.00	0.00	0.01	0.00	3.04	15.87	20.44	0.20
MAC-250-276	0.32	0.99	0.08	0.34	0.13	0.03	0.31	0.05	0.24	0.06	0.03	0.02	0.12	0.02	4.08	15.80	19.56	17.00
MAC-250-390.5	1.25	2.78	0.30	1.25	0.39	0.07	0.60	0.12	0.77	0.16	0.07	0.06	0.33	0.05	27.67	15.79	19.72	3.30
MAC-250-396	0.21	0.62	0.06	0.25	0.08	0.01	0.09	0.01	0.06	0.01	0.01	0.00	0.03	0.01	4.08	15.68	18.91	0.69
MAC-252-21.7	0.22	0.55	0.07	0.33	0.13	0.03	0.20	0.03	0.18	0.04	0.03	0.01	0.07	0.01	0.96	15.63	16.62	0.02
MAC-252-135.5	0.44	6.21	0.21	1.69	0.94	0.21	1.22	0.19	1.10	0.23	0.21	0.08	0.40	0.07	3.07	16.03	22.08	8.53
MAC-253-70.4	0.02	0.16	0.01	0.08	0.05	0.01	0.07	0.01	0.06	0.01	0.01	0.00	0.02	0.00	2.10	17.52	38.63	1.69
MAC-253-235	0.47	1.67	0.12	0.56	0.28	0.07	0.49	0.08	0.43	0.09	0.07	0.03	0.16	0.03	4.29	16.01	20.67	5.80
MAC-253-236	0.26	0.62	0.06	0.23	0.05	0.01	0.04	0.01	0.03	0.01	0.01	0.00	0.01	0.00	0.55	16.35	20.53	0.54
MAC-253-294.5	0.29	0.66	0.07	0.25	0.06	0.01	0.10	0.02	0.07	0.01	0.01	0.01	0.03	0.01	1.17	15.87	20.07	1.86
MAC-255-11.3	0.70	1.74	0.28	1.40	0.44	0.10	0.50	0.07	0.39	0.07	0.10	0.02	0.14	0.02	22.30	15.80	21.20	50.68
MAC-255-37	0.28	1.05	0.09	0.50	0.56	0.17	1.04	0.18	1.17	0.23	0.17	0.07	0.40	0.06	34.07	15.89	20.55	22.41
MAC-255-47.2	0.78	1.75	0.20	1.06	0.59	0.15	0.78	0.13	0.76	0.14	0.15	0.05	0.29	0.04	30.51	16.03	23.88	32.46
MAC-255-176	1.93	4.56	0.50	1.90	0.43	0.08	0.38	0.05	0.29	0.05	0.08	0.02	0.10	0.01	15.59	15.54	18.54	3.66
MAC-255-251	0.39	0.92	0.10	0.40	0.12	0.03	0.18	0.03	0.18	0.04	0.03	0.01	0.06	0.01	5.66	15.71	20.42	6.43
MAC-255-305	0.16	0.39	0.04	0.15	0.04	0.01	0.08	0.01	0.09	0.02	0.01	0.01	0.03	0.01	0.63	15.91	20.11	5.25
MAC-255-408	2.14	6.30	0.73	3.52	0.75	0.07	0.39	0.04	0.20	0.04	0.07	0.02	0.09	0.02	6.36	15.84	19.92	0.81
MAC-255-509	1.04	3.12	0.40	1.56	0.24	0.06	0.22	0.03	0.21	0.05	0.06	0.02	0.12	0.02	2.11	19.79	434.27	1.24
MC-336-28.1	0.04	0.22	0.03	0.25	0.23	0.06	0.38	0.05	0.28	0.05	0.06	0.01	0.07	0.01	12.16	16.02	23.16	67.56
MC-336-497	6.11	11.71	1.23	4.49	0.77	0.11	0.50	0.05	0.20	0.03	0.11	0.01	0.09	0.02	1.56	19.08	55.61	3.25
MC-336-503.3	0.71	1.69	0.22	1.09	0.38	0.08	0.38	0.05	0.29	0.06	0.08	0.03	0.24	0.05	20.26	16.38	29.68	20.89
MC-336-523.8	2.18	4.04	0.42	1.46	0.27	0.05	0.22	0.03	0.17	0.03	0.05	0.01	0.08	0.01	5.72	19.10	72.06	7.15
MC-338-20.7	0.24	2.03	0.08	0.59	0.56	0.15	0.98	0.15	0.85	0.17	0.15	0.05	0.25	0.04	6.03	17.38	26.08	27.41
MC-338-61.3	0.07	0.39	0.02	0.19	0.31	0.09	0.56	0.09	0.58	0.12	0.09	0.04	0.19	0.03	13.04	19.51	68.36	76.71
MC-338-121	0.47	1.23	0.11	0.46	0.31	0.09	0.61	0.10	0.65	0.14	0.09	0.05	0.24	0.04	25.04	15.81	20.98	15.65
MC-338-206	0.13	0.34	0.04	0.18	0.12	0.03	0.24	0.04	0.22	0.05	0.03	0.01	0.07	0.01	11.60	16.27	27.62	52.73
MC-338-231.8	0.11	0.26	0.03	0.17	0.10	0.02	0.15	0.02	0.12	0.02	0.02	0.01	0.03	0.01	3.16	16.02	22.86	13.17
MC-338-234	1.32	3.04	0.32	1.36	0.56	0.13	0.81	0.12	0.69	0.14	0.13	0.04	0.20	0.03	30.71	15.98	22.55	35.30

(Cont.)

Sample ID	La (ppm)	Ce (ppm)	Pr (ppm)	Nd (ppm)	Sm (ppm)	Eu (ppm)	Gd (ppm)	Tb (ppm)	Dy (ppm)	Ho (ppm)	Er (ppm)	Tm (ppm)	Yb (ppm)	Lu (ppm)	U (ppm)	$^{207}Pb/^{204}Pb$	$^{206}Pb/^{204}Pb$	$^{238}U/^{206}Pb$
MC-338-429.7	0.04	0.09	0.02	0.16	0.31	0.09	0.84	0.14	0.87	0.19	0.09	0.06	0.32	0.05	94.59	16.85	33.37	859.91
MC-338-504.5	5.59	11.74	1.27	4.63	0.82	0.15	0.70	0.08	0.39	0.07	0.15	0.02	0.12	0.02	34.57	15.88	21.09	30.06
MC-344-65.6	0.07	0.28	0.02	0.08	0.05	0.01	0.10	0.02	0.14	0.03	0.01	0.01	0.05	0.01	1.54	16.53	28.26	1.45
MC-344-122	0.31	0.74	0.07	0.26	0.07	0.02	0.12	0.02	0.13	0.03	0.02	0.01	0.04	0.01	1.93	16.85	30.87	2.10
MC-344-321	0.12	0.31	0.04	0.16	0.04	0.01	0.04	0.00	0.01	0.00	0.01	0.00	0.00	0.00	1.01	16.18	24.36	25.25
MC-344-375.5	0.41	0.94	0.11	0.47	0.07	0.01	0.05	0.00	0.02	0.00	0.01	0.00	0.01	0.00	12.17	15.63	18.34	9.29
MC-344-379.3	0.06	0.22	0.04	0.19	0.02	0.00	0.01	0.00	0.00	0.00	0.00	0.00	0.00	0.00	0.57	16.09	23.53	4.75
MC-344-443	0.46	1.10	0.12	0.46	0.07	0.01	0.05	0.01	0.03	0.01	0.01	0.00	0.02	0.00	9.39	15.87	20.97	14.90
MC-344-475	0.45	0.97	0.12	0.50	0.12	0.02	0.11	0.01	0.08	0.02	0.02	0.01	0.03	0.01	16.46	16.35	25.73	21.10
MC-413-73.6	0.27	1.18	0.06	0.25	0.18	0.06	0.45	0.07	0.43	0.09	0.06	0.02	0.11	0.02	6.28	16.52	28.14	1.41
MC-413-207.52	0.14	0.58	0.04	0.15	0.14	0.05	0.34	0.05	0.35	0.08	0.05	0.03	0.15	0.03	1.22	16.85	29.36	30.50
MC-413-224	0.44	1.67	0.11	0.44	0.19	0.06	0.45	0.07	0.49	0.12	0.06	0.04	0.22	0.04	2.46	15.84	19.87	2.62
MC-413-267.16	0.25	0.80	0.06	0.27	0.16	0.06	0.55	0.11	0.82	0.20	0.06	0.07	0.31	0.05	8.63	16.86	33.50	37.52
MC-413-274.5	0.46	1.38	0.11	0.41	0.14	0.04	0.33	0.07	0.54	0.13	0.04	0.05	0.24	0.04	30.03	16.32	26.48	13.41
MC-413-346.26	0.21	0.47	0.05	0.21	0.07	0.02	0.18	0.03	0.21	0.04	0.02	0.01	0.03	0.01	1.85	16.42	26.93	26.43
MC-413-359.5	0.16	0.37	0.04	0.16	0.04	0.01	0.07	0.01	0.07	0.01	0.01	0.00	0.02	0.00	0.94	17.06	35.34	11.75
MC-413-407	0.44	0.94	0.10	0.38	0.08	0.01	0.07	0.01	0.05	0.01	0.01	0.00	0.02	0.00	1.77	16.19	23.39	7.70
MC-413-614	2.48	5.38	0.62	2.42	0.66	0.09	0.56	0.09	0.56	0.12	0.09	0.06	0.43	0.08	290.61	17.85	50.61	0.18
MC-415-80.4	0.49	1.94	0.15	0.88	0.78	0.21	1.30	0.19	1.11	0.21	0.21	0.06	0.26	0.04	2.04	21.49	55.17	25.50
MC-415-82.9	2.98	6.07	0.67	2.53	0.81	0.19	1.28	0.24	1.65	0.36	0.19	0.13	0.75	0.12	6.01	16.15	22.81	3.01
MC-415-126	0.47	1.98	0.14	1.39	1.94	0.49	2.90	0.46	2.75	0.57	0.49	0.16	0.74	0.12	5.99	15.87	22.05	19.32
MC-415-137	0.64	2.85	0.21	2.80	3.24	0.75	4.31	0.64	3.62	0.73	0.75	0.21	0.94	0.15	5.33	16.11	24.54	12.69
MC-415-141.5	0.25	2.37	0.12	2.42	2.05	0.46	2.40	0.34	1.82	0.35	0.46	0.10	0.46	0.07	1.15	16.59	31.95	38.33
MC-415-143.1	0.04	0.14	0.01	0.13	0.11	0.03	0.16	0.02	0.13	0.02	0.03	0.01	0.03	0.01	0.18	16.15	26.52	6.00
MC-415-208.56	0.98	2.39	0.23	0.93	0.23	0.05	0.35	0.06	0.44	0.10	0.05	0.04	0.22	0.04	5.27	16.65	30.52	2.26
MC-415-212	0.49	2.71	0.14	0.66	0.55	0.16	1.19	0.20	1.22	0.28	0.16	0.10	0.52	0.09	0.96	15.93	19.46	6.00
MC-415-246.3	0.22	0.65	0.06	0.22	0.08	0.03	0.31	0.07	0.50	0.13	0.03	0.05	0.22	0.04	2.16	16.86	33.57	43.20
MC-415-290	0.82	1.99	0.19	0.74	0.20	0.04	0.34	0.07	0.63	0.19	0.04	0.08	0.39	0.08	3.53	15.62	20.98	353.00
MC-415-379	1.15	2.65	0.29	1.15	0.24	0.03	0.16	0.01	0.05	0.01	0.03	0.00	0.02	0.00	3.79	16.12	22.09	4.41
MC-415-402.97	2.37	5.06	0.53	1.89	0.35	0.04	0.23	0.02	0.09	0.02	0.04	0.01	0.05	0.01	7.18	16.43	27.32	11.97
MC-415-405.5	1.70	3.99	0.42	1.83	0.43	0.06	0.35	0.04	0.19	0.04	0.06	0.02	0.12	0.02	21.70	16.30	26.11	46.17
MC-415-459.5	3.70	8.00	0.83	3.10	0.56	0.09	0.45	0.05	0.29	0.05	0.09	0.02	0.13	0.02	13.43	17.23	41.21	10.49
MC-415-459.69	0.83	1.79	0.21	0.87	0.24	0.05	0.28	0.04	0.29	0.06	0.05	0.03	0.20	0.04	6.70	16.96	35.26	13.67
MC-415-494	1.06	2.47	0.28	1.17	0.29	0.06	0.32	0.05	0.32	0.07	0.06	0.03	0.20	0.03	11.78	16.06	24.73	8.60
MC-434-42	1.64	3.38	0.34	1.24	0.24	0.04	0.19	0.03	0.16	0.03	0.04	0.02	0.13	0.02	2.62	17.71	37.12	7.08
MC-434-118	0.24	0.71	0.07	0.33	0.16	0.04	0.21	0.03	0.15	0.03	0.04	0.01	0.04	0.01	4.96	16.43	28.51	8.41
MC-434-213	0.92	2.79	0.23	1.34	1.19	0.28	2.00	0.24	1.27	0.28	0.28	0.09	0.46	0.08	43.16	16.14	23.75	166.00
MC-434-214	0.76	1.69	0.19	0.74	0.24	0.05	0.36	0.05	0.26	0.05	0.05	0.02	0.09	0.02	10.81	15.85	21.03	3.59
MC-434-337	1.01	21.27	0.49	2.03	0.24	0.02	0.15	0.01	0.06	0.01	0.02	0.01	0.03	0.01	20.57	17.38	38.64	32.14
MC-434-342	1.32	3.57	0.43	1.94	0.40	0.05	0.31	0.03	0.12	0.02	0.05	0.01	0.05	0.01	6.82	16.40	26.67	10.18
MC-434-408	0.23	0.57	0.08	0.33	0.05	0.01	0.03	0.00	0.01	0.00	0.01	0.00	0.01	0.00	1.95	16.11	23.71	7.22

3.4.3 Pb isotope ratios

Fracture materials and their adjacent wall rock can record evidence of various fluid flow events before the precipitation of the fracture coating. These events can be recorded by differences in $^{207}Pb/^{206}Pb$ isotope values and mineralogical zoning from the fracture surface, decreasing with distance from the fracture (Figure 3.6). However, the wall rock can also contain a mineralogy similar to the fracture filling (Chapter 2).

Anomalously low $^{207}Pb/^{206}Pb$ values can be indicative of U-rich sources, with common Pb having ratios near 0.9 and radiogenic Pb having ratios near 0.1 (Holk *et al*., 2003). The P2 fault is interpreted to have acted as a conduit for mineralizing fluids (Jefferson *et al*., 2007) and could act as a pathway for secondary mobilization of radiogenic Pb. White and yellow (type 2), white (type 3), and drusy quartz (type 6) fracture fillings show similar $^{207}Pb/^{206}Pb$ values for fracture coatings and Pb in the near-fracture material for samples proximal to the P2 fault (Figure 3.6; Table 3.5). As distance increases from the P2 fault, $^{207}Pb/^{206}Pb$ values of extractable Pb from near-fracture material for brown (type 1), black (type 4), black and orange (type 5), and pink (type 7) fracture fillings are lower than the Pb isotope ratios for the corresponding fracture fill. If the fracture fill and the wall rock had been altered by the same fluid, they should have the same Pb isotopic composition, as is recorded by types 2, 3 and 6 located nearest to the P2 fault. The fracture types 1, 4, 5 and 7 that occur further from the P2 fault and from shallower depths tend to have more radiogenic Pb in the wall rock relative to the fracture filling. This suggests that the filling records elements that have not been dispersed from the deposit or that more recent fluids have either replaced or overprinted an earlier formed Pb isotopic signature that was originally similar to that in the wall rocks.

Table 3.5: Uranium concentrations and $^{207}Pb/^{206}Pb$ values from WAL of fracture coatings and some near-fractures at McArthur River.

Sample ID	Depth (m)	U (ppm) (Fracture Coating)	$^{207}Pb/^{206}Pb$ (Fracture Coating)	$^{207}Pb/^{206}Pb$ (Near-Fracture)	Sample ID	Depth (m)	U (ppm) (Fracture Coating)	$^{207}Pb/^{206}Pb$ (Fracture Coating)	$^{207}Pb/^{206}Pb$ (Near-Fracture)
McArthur River									
MAC-208-57.6	57.60	2.33	0.43		MC-338-429.7	429.70	94.59	0.51	0.25
MAC-208-154.8	154.80	1.22	0.64		MC-338-504.5	504.50	34.57	0.75	
MAC-208-262.5	262.50	1.90	0.51	0.29	MC-344-65.6	65.60	1.54	0.58	
MAC-208-263	263.00	10.90	0.58		MC-344-122	122.00	1.93	0.55	0.64
MAC-208-305	305.00	10.17	0.53	0.54	MC-344-321	321.00	1.01	0.66	
MAC-208-462	462.00	257.62	0.44	0.49	MC-344-375.5	375.50	12.17	0.85	
MAC-208-476.5	476.50	77.69	0.34	0.52	MC-344-379.3	379.30	0.57	0.68	
MAC-208-570	570.00	279.31	0.18	0.19	MC-344-443	443.00	9.39	0.76	
MAC-246-23.1	23.10	445.73	0.45		MC-344-475	475.00	16.46	0.64	
MAC-246-142	142.00	20.00	0.71		MC-413-73.6	73.60	6.28	0.59	
MAC-246-198.5	198.50	9.07	0.87		MC-413-207.52	207.52	1.22	0.57	
MAC-246-395	395.00	76.72	0.83	0.75	MC-413-224	224.00	2.46	0.80	
MAC-246-446	446.00	7.24	0.83		MC-413-267.16	267.16	8.63	0.50	
MAC-246-534	534.00	3.04	0.78		MC-413-274.5	274.50	30.03	0.62	
MAC-250-276	276.00	4.08	0.81	0.33	MC-413-346.26	346.26	1.85	0.61	
MAC-250-390.5	390.50	27.67	0.80		MC-413-359.5	359.50	0.94	0.48	0.48
MAC-250-396	396.00	4.08	0.83	0.57	MC-413-407	407.00	1.77	0.69	
MAC-252-21.7	21.70	0.96	0.94		MC-413-614	614.00	290.61	0.35	0.27
MAC-252-135.5	135.50	3.07	0.73	0.84	MC-415-80.4	80.40	2.04	0.39	
MAC-253-70.4	70.40	2.10	0.45		MC-415-82.9	82.90	6.01	0.71	
MAC-253-235	235.00	4.29	0.77		MC-415-126	126.00	5.99	0.72	
MAC-253-236	236.00	0.55	0.80	0.81	MC-415-137	137.00	5.33	0.66	
MAC-253-294.5	294.50	1.17	0.79		MC-415-141.5	141.50	1.15	0.52	
MAC-255-11.3	11.30	22.30	0.74		MC-415-143.1	143.10	0.18	0.61	
MAC-255-37	37.00	34.07	0.77		MC-415-208.56	208.56	5.27	0.55	
MAC-255-47.2	47.20	30.51	0.67		MC-415-212	212.00	0.96	0.82	
MAC-255-176	176.00	15.59	0.84	0.46	MC-415-246.3	246.30	2.16	0.50	
MAC-255-251	251.00	5.66	0.77	0.50	MC-415-290	290.00	3.53	0.74	
MAC-255-305	305.00	0.63	0.79		MC-415-379	379.00	3.79	0.73	
MAC-255-408	408.00	6.36	0.80		MC-415-402.97	402.97	7.18	0.60	
MAC-255-509	509.00	2.11	0.05	0.05	MC-415-405.5	405.50	21.70	0.62	
MC-336-28.1	28.10	12.16	0.69		MC-415-459.5	459.50	13.43	0.42	
MC-336-497	497.00	1.56	0.34		MC-415-459.69	459.69	6.70	0.48	
MC-336-503.3	503.30	20.26	0.55		MC-415-494	494.00	11.78	0.65	
MC-336-523.8	523.80	5.72	0.27	0.48	MC-434-42	42.00	2.62	0.48	
MC-338-20.7	20.70	6.03	0.67		MC-434-118	118.00	4.96	0.58	
MC-338-61.3	61.30	13.04	0.28		MC-434-213	213.00	43.16	0.68	
MC-338-121	121.00	25.04	0.75	0.76	MC-434-214	214.00	10.81	0.75	
MC-338-206	206.00	11.60	0.59	0.14	MC-434-337	337.00	20.57	0.45	
MC-338-231.8	231.80	3.16	0.70		MC-434-342	342.00	6.82	0.61	
MC-338-234	234.00	30.71	0.71		MC-434-408	408.00	1.95	0.68	

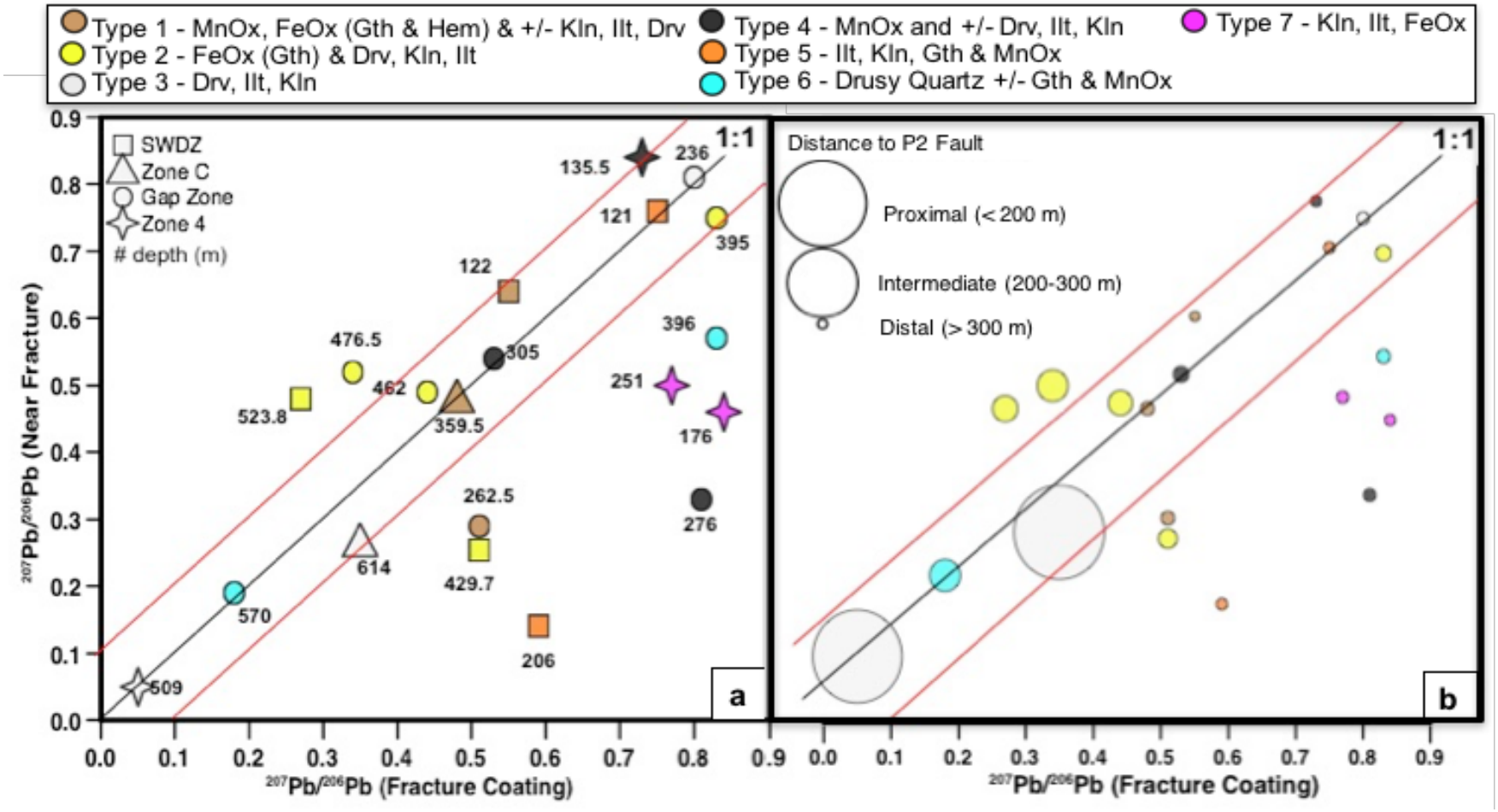

Figure 3.6: (a) $^{207}Pb/^{206}Pb$ isotope values of fracture coatings from McArthur River versus the near-fracture surface wall-rock for samples from various depths as indicated and (b) with symbol size proportional to distance from the P2 fault, approximated by using Figure 3.4. Numbers next to symbols refer to depth of the sample and red lines are 2σ errors around the line of equal ratios of material in the fractures and the material adjacent to the fracture.

3.4.4 Pathfinder elements

Typical pathfinder elements of unconformity-related U deposits include Ba, Co, Mn, Ni, S, Tl, V, and Zn (Cuney and Kyser, 2014; Table 3.6). While their concentrations in the fracture fillings increase towards the unconformity, they also increase toward the surface for McArthur River samples (Figure 3.7). Increased concentrations of these elements are most prominent in drill holes 252, 246, and 255 (Zone 4), and 413 and 415 (Zone C); locations that are closest to the mineralization at McArthur River. Brown (type 1) and black (type 4) fracture coatings (Fe and Mn hydroxides) show elevated concentrations of Ba, Co, Tl, and Mn (up to 540.8, 88.7, 0.19 and 10343 ppm) whereas white and yellow (type 2) and black and orange (type 5) fracture fills, commonly containing limonite stain or crusts, show elevated concentrations of V (up to 126.7 ppm). Although white and yellow (type 2) fractures show elevated concentrations of V (up to 69.7 ppm), the brown (type 1) and black and orange (type 5) fracture coatings show the most elevated concentrations, especially in MAC-246-534 (type 1 – brown; 91.6 ppm) and MAC-246-23.1 (type 5 - black and orange; 126.7 ppm) in Zone 4. Drusy quartz (type 6) fracture coatings show elevated concentrations of Co, Mn and S (up to 312.5, 8827 and 2204.5 ppm) at depth, while pink (type 7) fracture fillings show pathfinder element concentrations similar to background values. White (type 3) fracture fillings also show elevated pathfinder element concentrations in both the surface and at depth, including Ni (MC-415-82.9; 1611.1 ppm) and Zn (MC-413-73.6; 110.3 ppm) near the surface (<100 m) and elevated S (up to 1652.5 ppm) concentrations at a vertical depth of ~530 m for three samples at the unconformity.

Table 3.6: Concentrations of pathfinder elements Ba, Co, Mn, Ni, S, Tl, V, and Zn, from WAL extraction of fractures from McArthur River.

Sample ID	Depth (m)	Ba (ppm)	Co (ppm)	Mn (ppm)	Ni (ppm)	S (ppm)	Tl (ppm)	V (ppm)	Zn (ppm)
McArthur River									
MAC-208-57.6	57.60	26.2	12.2	1055	198.7	3.5	0.03	3.3	17.6
MAC-208-154.8	154.80	2.1	0.3	9	0.2	3.2	0.00	0.4	0.5
MAC-208-262.5	262.50	0.6	0.1	13	0.1	1.2	0.00	0.4	0.3
MAC-208-263	263.00	9.0	25.5	27	57.9	4.0	0.00	5.5	1.2
MAC-208-305	305.00	239.8	69.7	3479	23.2	34.6	0.11	1.6	7.7
MAC-208-462	462.00	47.7	14.9	260	54.7	1.1	0.03	38.1	50.0
MAC-208-476.5	476.50	18.8	6.7	47	3.3	1.0	0.00	2.1	4.3
MAC-208-570	570.00	16.8	312.5	8827	133.3	2204.5	0.12	5.8	40.2
MAC-246-23.1	23.10	11.9	19.0	113	31.2	2.3	0.01	126.7	43.3
MAC-246-142	142.00	20.7	2.8	108	3.5		0.01	17.8	3.6
MAC-246-198.5	198.50	6.3	0.9	63	0.4	32.5	0.01	4.4	3.0
MAC-246-395	395.00	27.1	7.7	216	9.1	7.4	0.01	20.9	45.6
MAC-246-446	446.00	5.4	4.5	82	5.0	1.6	0.03	1.2	4.0
MAC-246-534	534.00	4.1	5.6	45	3.8		0.00	91.6	5.5
MAC-250-276	276.00	32.9	19.1	1330	34.1	7.5	0.01	0.6	5.6
MAC-250-390.5	390.50	17.8	18.1	166	47.7	8.8	0.02	11.6	9.9
MAC-250-396	396.00	13.6	10.6	164	2.3	4.5	0.02	2.5	3.6
MAC-252-21.7	21.70	16.1	25.0	71	68.9	12.9	0.01	1.3	7.5
MAC-252-135.5	135.50	529.0	75.3	10343	9.4		0.02	0.5	17.1
MAC-253-70.4	70.40	12.2	8.4	524	158.6	2.5	0.02	3.8	13.1
MAC-253-235	235.00	38.7	46.8	738	60.5	10.0	0.01	5.2	8.3
MAC-253-236	236.00	3.1	12.0	73	4.5	15.9	0.00	0.4	1.4
MAC-253-294.5	294.50	17.7	65.6	2852	41.1	2.3	0.01	0.4	24.5
MAC-255-11.3	11.30	26.9	0.9	31	1.8	4.7	0.01	5.8	5.0
MAC-255-37	37.00	13.8	19.7	63	131.9	21.8	0.01	69.7	15.6
MAC-255-47.2	47.20	15.1	14.2	690	1071.9	1.6	0.02	18.1	77.3
MAC-255-176	176.00	113.2	1.2	35	0.5	19.9	0.01	5.4	14.7
MAC-255-251	251.00	6.3	0.4	29	0.2	2.5	0.00	6.6	9.9
MAC-255-305	305.00	2.1	1.1	99	0.5	1.7	0.00	0.3	7.5
MAC-255-408	408.00	118.4	88.7	1857	205.1	7.0	0.17	8.6	83.5
MAC-255-509	509.00	12.1	10.3	74	8.0	1027.7	0.01	5.2	2.4
MC-336-28.1	28.10	17.8	1.2	281	2.7	13.7	0.01	3.9	3.3
MC-336-497	497.00	7.1	1.2	3	0.5	5.2	0.00	0.7	0.8
MC-336-503.3	503.30	3.1	5.4	13	200.0	3.3	0.00	7.1	13.1
MC-336-523.8	523.80	4.0	3.0	5	2.8		0.00	2.0	2.3
MC-338-20.7	20.70	540.8	37.6	2660	82.0	4.2	0.08	0.6	29.5
MC-338-61.3	61.30	56.8	15.5	757	19.6	0.9	0.02	4.7	3.8
MC-338-121	121.00	32.8	12.2	595	2.8	9.2	0.03	31.1	8.9
MC-338-206	206.00	9.2	4.2	225	0.4		0.00	4.3	1.6
MC-338-231.8	231.80	7.1	1.3	97	0.9	2.3	0.01	1.0	4.7
MC-338-234	234.00	18.9	4.6	368	0.6	2.2	0.01	11.0	4.9

(Cont.)

Sample ID	Depth (m)	Ba (ppm)	Co (ppm)	Mn (ppm)	Ni (ppm)	S (ppm)	Tl (ppm)	V (ppm)	Zn (ppm)
MC-338-429.7	429.70	0.8	2.3	84	2.4		0.00	4.2	8.3
MC-338-504.5	504.50	14.6	5.3	29	1.4	1.8	0.01	8.9	3.2
MC-344-65.6	65.60	202.0	18.5	2249	1509.5	5.0	0.10	15.2	94.4
MC-344-122	122.00	46.4	15.3	870	4.0	4.6	0.02	1.4	6.9
MC-344-321	321.00	1.2	1.3	10	0.6	2.0	0.00	0.2	0.5
MC-344-375.5	375.50	2.8	5.8	15	1.3	8.7	0.00	0.4	3.0
MC-344-379.3	379.30	1.1	1.3	4	0.5		0.00	0.1	1.8
MC-344-443	443.00	3.0	4.5	17	1.8	3.9	0.00	5.4	3.8
MC-344-475	475.00	11.6	17.8	18	4.6	3.3	0.01	3.1	4.0
MC-413-73.6	73.60	100.9	13.9	4149	1727.4	10.9	0.19	16.8	110.3
MC-413-207.52	207.52	24.7	8.8	650	5.0	0.9	0.00	3.1	2.6
MC-413-224	224.00	21.8	37.0	1055	33.1	4.6	0.01	3.8	10.0
MC-413-267.16	267.16	71.8	13.0	1596	5.0	1.1	0.03	19.8	3.5
MC-413-274.5	274.50	9.9	1.6	317	3.8	3.8	0.01	34.4	3.9
MC-413-346.26	346.26	6.3	0.5	149	0.5	1.8	0.00	1.8	0.9
MC-413-359.5	359.50	2.6	0.2	39	0.6	0.8	0.00	1.2	0.4
MC-413-407	407.00	17.8	3.2	13	1.1	4.7	0.00	1.2	1.5
MC-413-614	614.00	30.9	127.7	17	424.0	1652.5	0.14	45.1	223.9
MC-415-80.4	80.40	150.6	22.1	1895	61.2	0.6	0.05	8.6	10.0
MC-415-82.9	82.90	15.3	8.8	733	1611.1		0.01	10.8	97.8
MC-415-126	126.00	19.2	1.8	935	1.5		0.01	25.4	2.3
MC-415-137	137.00	34.8	8.3	990	5.3	0.8	0.01	14.3	3.9
MC-415-141.5	141.50	52.4	9.0	1031	4.4	0.9	0.00	5.4	2.7
MC-415-143.1	143.10	3.0	0.2	38	0.2	0.6	0.00	0.6	0.6
MC-415-208.56	208.56	14.1	2.9	315	2.4	1.6	0.00	2.3	1.7
MC-415-212	212.00	137.7	35.5	1898	63.8	3.8	0.02	1.2	3.8
MC-415-246.3	246.30	24.5	4.9	596	6.1	0.3	0.00	0.4	3.6
MC-415-290	290.00	364.6	19.9	3756	30.4	0.7	0.06	3.9	25.1
MC-415-379	379.00	15.1	16.6	266	81.6	7.6	0.03	3.4	2.4
MC-415-402.97	402.97	15.9	8.2	279	2.7	3.2	0.04	5.2	4.9
MC-415-405.5	405.50	22.5	17.8	584	10.2	2.1	0.02	15.6	3.9
MC-415-459.5	459.50	19.1	6.9	44	3.9	6.0	0.01	18.9	2.4
MC-415-459.69	459.69	5.6	1.4	12	2.6	2.7	0.01	2.3	1.5
MC-415-494	494.00	13.2	3.3	534	8.4	2.8	0.00	3.2	3.9
MC-434-42	42.00	10.1	0.1	64	4.6	1.7	0.01	2.0	2.4
MC-434-118	118.00	19.2	2.5	158	2.4	0.9	0.00	4.5	2.0
MC-434-213	213.00	42.0	30.3	1611	11.2	1.3	0.01	22.7	3.7
MC-434-214	214.00	7.9	3.9	160	0.9	2.4	0.01	9.0	6.2
MC-434-337	337.00	12.2	4.2	481	2.6	1.3	0.01	0.5	3.9
MC-434-342	342.00	5.1	1.3	31	0.7	0.9	0.00	1.1	0.9
MC-434-408	408.00	0.8	2.1	5	5.0	1.2	0.00	0.2	0.7

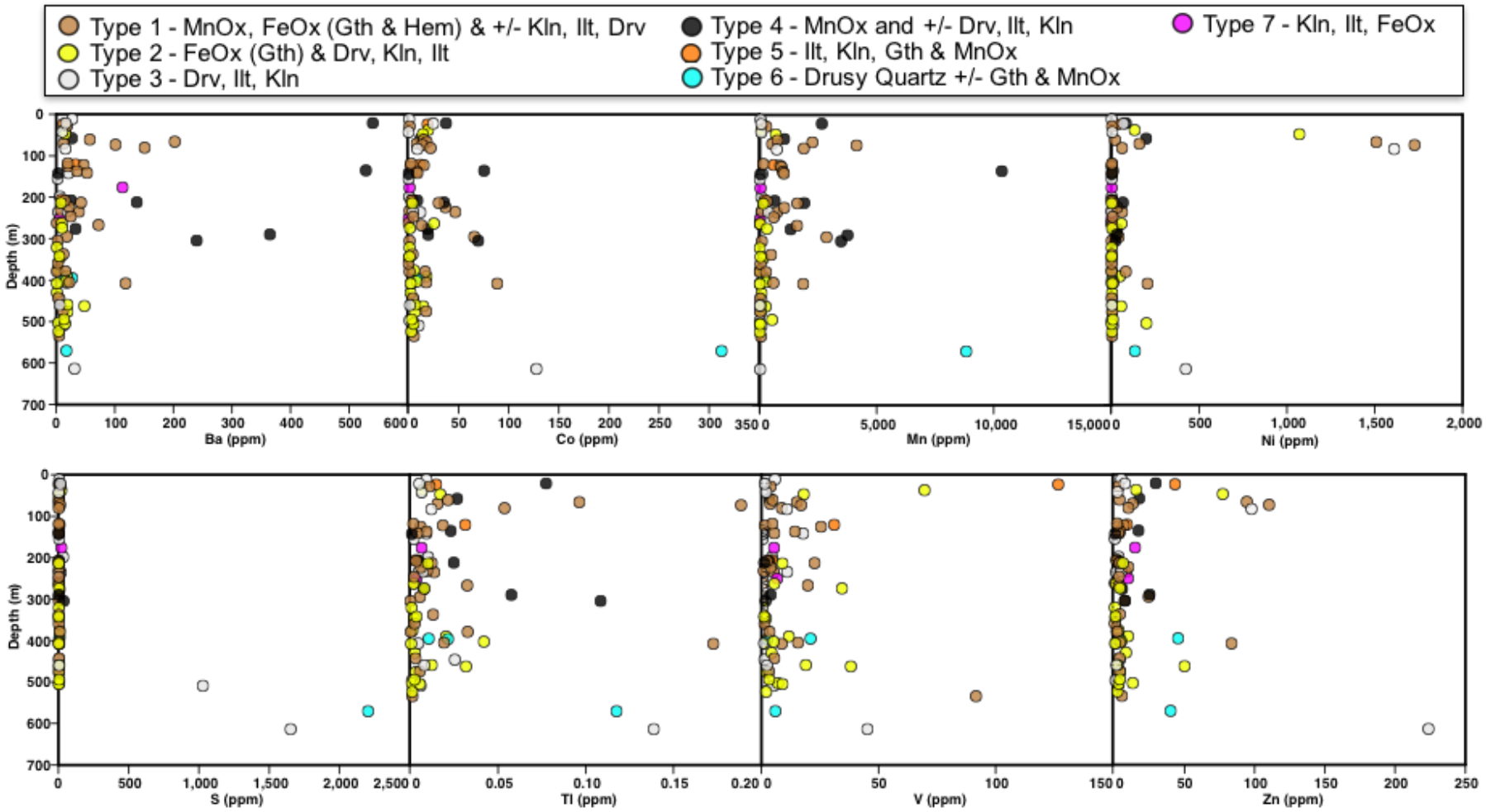

Figure 3.7: Relationship between depth and concentration of Ba, Co, Mn, Ni, S, Tl, V, and Zn for fracture fill from McArthur River extracted using WAL.

3.4.5 Continuous leach ICP-MS

Continuous leach ICP-MS analysis provides data indicating the residence location of the various chemical components (Pb isotopes, trace elements, and major elements) using real time data acquired through the use of leaching by a series of progressively increasingly-reactive solutions from DI water to 30% HNO_3 acid (MacFarlane *et al*., 2005). A variety of factors affect the rate at which minerals react with fluids during CL-ICP-MS analyses, including mineral/grain surface area, surface structure, structure defects, elemental solubility, and diffusion rate of components through the mineral structure (MacFarlane *et al*., 2005). Dissolution reactions commonly occur at a rapid rate initially (Krauskopf and Bird, 1995), as surface layers or defect areas in the crystal structure react and begin to dissolve (MacFarlane *et al*., 2005). Release patterns of major elements reflect the results of specific mineral phases reacting at each leaching stage and can be apportioned provided the mineralogy is well characterized. This mineralogical knowledge allows association of the release patterns of trace elements to mineral phase dissolution reactions through observations concerning which specific trace elements are associated with a mineral phase. The release pattern of $^{207}Pb/^{206}Pb$ values can also be compared to the release of major and trace elements to interpret which mineral phases may host the common or radiogenic Pb.

The breakdown and dissolution of major phases that typify the samples from McArthur River is exemplified by tracking C, S, and Fe release during CL-ICP-MS of a sample above Zone C, which is slightly mineralized (Figure 3.8). Carbon and S are released when the samples are attacked with 10% H_2O_2; hydrogen peroxide reacts with organic matter releasing elements that are adsorbed to or resident within organic matter (Figure 3.9). Reaction with 1% HNO_3 then attacks carbonate minerals, releasing elements on reactive surfaces, and/or in poorly crystalline phases such as chlorite or Fe oxides, as shown by Fe (Figure 3.8). If there is no carbonate in the

sample, there will be no release of C (e.g. in the sample in Figure 3.8). Phosphate minerals in the samples will begin to react as well. As more aggressive reagents are used (10% HNO_3, 30% HNO_3), surface-controlled dissolution reactions on silicates will continue, as reflected by continued release of Fe (Figure 3.8). Reaction with 30% HNO_3 will dissolve sulphides, attack well-crystalline Fe-Mn oxides, and incongruently dissolve phyllosilicates. Dissolution of sulphides is evident by the concurrent increase in Fe and S release (Figure 3.8).

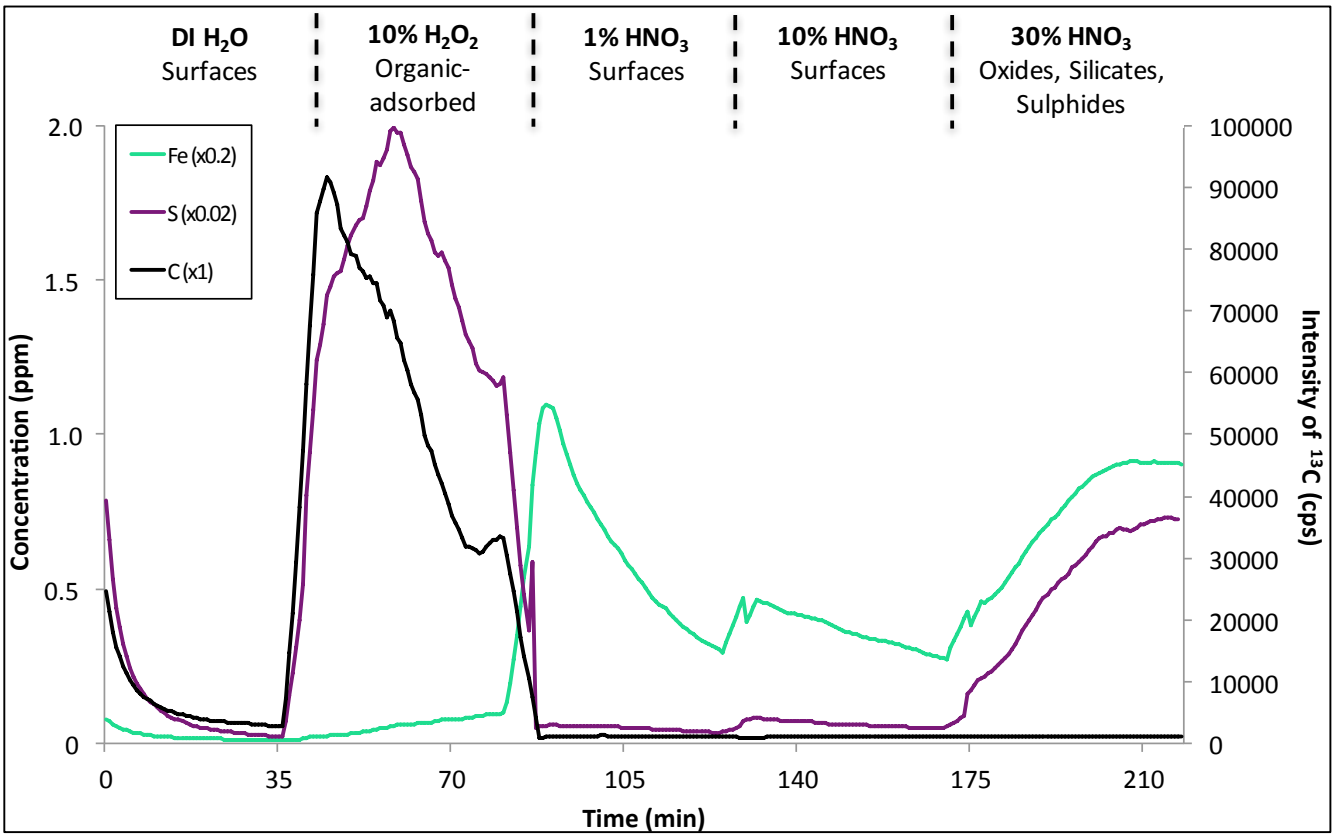

Figure 3.8: White (type 3) fracture coating (MC-413-614 from deep in slightly mineralized hole; kaolinite, dravite, illite, clinochlore, pyrite) showing typical release patterns of Fe, S, and C.

Each leach solution causes various phases to react (Figure 3.8 and 3.9). During water extraction, weakly-held particles and fine-grained particles on surfaces of minerals are released. The frit of the sample column has pores 15-20 μ, is 2 mm thick and only allows very fine-grained

particles to pass through to the ICP-MS. Significant amounts of C, reflecting oxidized organic C, are released during the 10% H_2O_2 leach phase (Figure 3.8 and 3.9). Associated major and trace elements also released at this time are likely adsorbed onto organic material. Elements undergoing dissolution during 1% HNO_3 are similar to those leached during the batch WAL (2% HNO_3) and include elements on the surfaces of many minerals and inorganic C from carbonates (Figure 3.9). Leachates with 1% HNO_3 tend to have the lowest (most radiogenic) $^{207}Pb/^{206}Pb$ values (Figure 3.9), with concomitant low U concentrations. Uranium is released in greatest concentration during the 30% HNO_3 stage (Figure 3.9) and is likely present in the crystalline structure of these phases (e.g. U in uraninite [UO_2]). Elements extracted with 30% HNO_3 are similar to those leached with AR (Chapter 2).

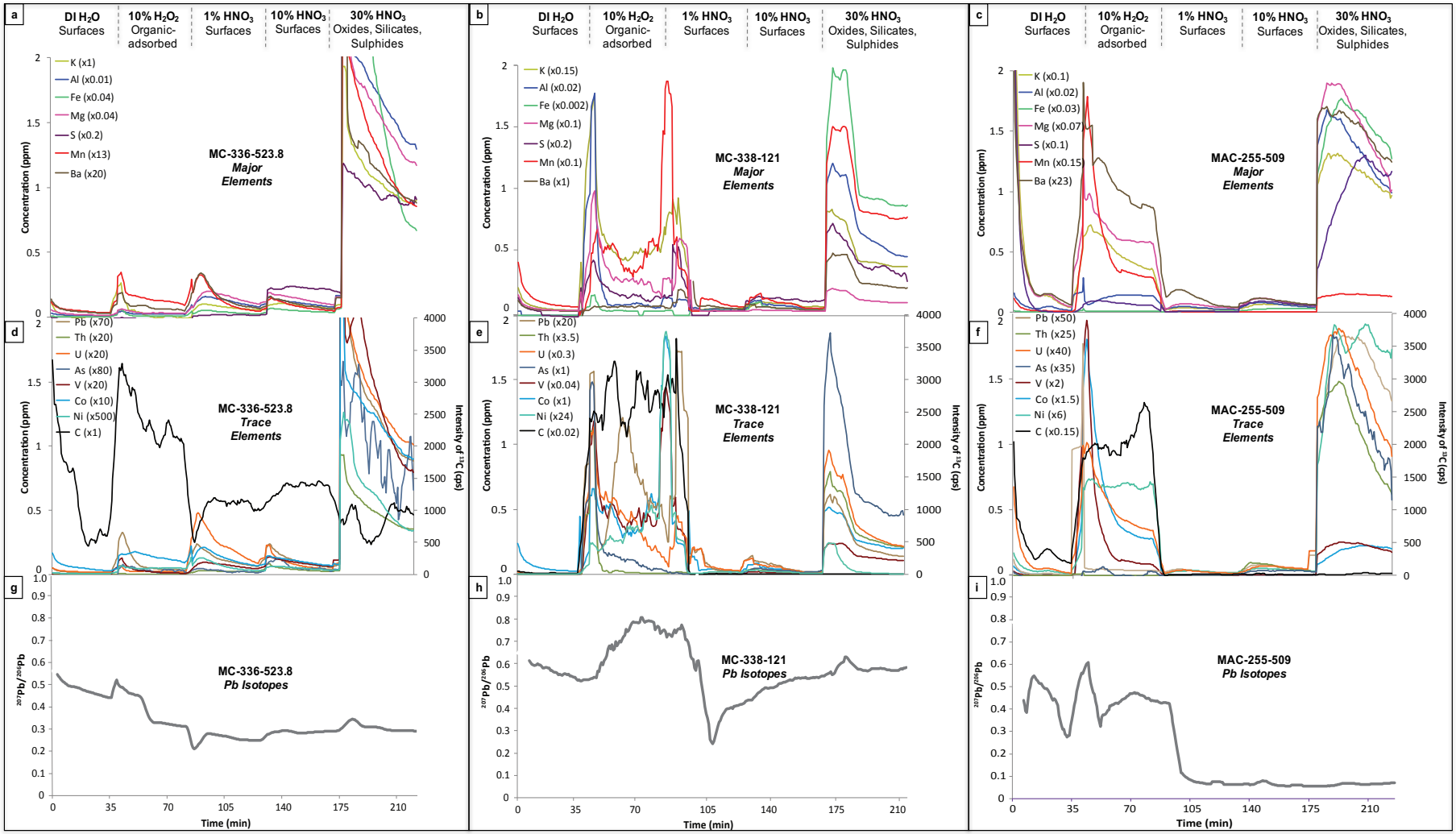

Figure 3.9: Typical real-time release patterns of elements following CL-ICP-MS analyses, showing (a-c) major elements, (d-f) trace elements and (g-i) $^{207}Pb/^{206}Pb$ isotope ratios from MC-336-523.8 (type 2 - white and yellow fracture from the South West Distal Zone), MC-338-121 (type 5 - black and orange fracture from the South West Distal Zone) and MAC-255-509 (type 3 - white fracture from Zone 4). Type of leach solution is indicated at the top of the graphs.

Vanadium and Co in many samples have similar release patterns during 10% H_2O_2 leach and 30% HNO_3 leach (Figure 3.10a) and are thus associated with highest concentrations during the 10% leach during which organic phases are attacked (Figure 3.10b, h, k and n). All fracture coatings show a significant release of C during the 10% H_2O_2 leach (Figure 3.8, 3.9 and 3.10). Some major elements (e.g. Mg, K, Al, Mn, Ca, Ba) and many trace elements (e.g. Co and V) appear to be adsorbed onto organics in some fracture coatings, particularly type 2 fractures – white and yellow (e.g. MAC-208-476.5) and type 3 fractures – white (e.g. MAC-255-509). During the 30% HNO_3 leach, Ni is typically released simultaneously with Fe from Fe oxides or sulphides (Figure 3.9) (e.g. MAC-250-396 (type 6 – drusy quartz fracture coating; Figure 3.10d). Vanadium is also released during 30% HNO_3 acid extraction in samples MC-344-122 (type 1 – brown), MAC-208-462 (type 2 – white and yellow), MAC-208-305 (type 4 – black) and MAC-208-570 (type 6 – drusy quartz). Nickel is interpreted to be mainly hosted by Fe oxide, as shown by the association between V and Fe during 30% HNO_3 acid leach (Figure 3.10g, j and m).

A summary of mineral phases and the most likely dispersion processes involved in the dispersion of pathfinder elements in the fracture fillings is presented in Table 3.7. The process types include primary dispersion associated with the mineralizing system, post-ore secondary dispersion, and dispersion from surficial meteoric fluids moving down or along fractures. Primary dispersion indicates that the radiogenic Pb could have been produced by the U in the sample over the past 1500 m.y. and primary and secondary dispersion indicate that either process could have operated for both U and Pb. The origin of the fluids that formed the mineral hosts of these pathfinder elements are based on mineral paragenesis, mineral crystallinities, and H and O isotopic compositions of the minerals as described in Chapter 2.

White and yellow (type 2) fractures host the pathfinder elements V, Ni, Co, Zn, and S from primary and secondary dispersion processes as indicated by their release with 10% H_2O_2

and 30% HNO_3. Brown (type 1) and drusy quartz (type 6) fractures have low concentrations of the pathfinder elements V, Pb, and Ni, but demonstrate major release of K from phyllosilicates during 10% H_2O_2 and 30% HNO_3 acid leach. The K release is due to dissolution of potassic phyllosilicates; the more highly-soluble phases have been already removed. The highly soluble phases may have been removed by relatively acidic low-temperature meteoric waters that migrated from above to the lower regions of the Manitou Falls Formation (Kotzer and Kyser, 1995). The sub-vertical orientation of the fractures along with the probable occurrence of one or more basin uplift events (Kotzer and Kyser, 1995) promoted this fluid movement (Chapter 2). This process is referred to as 'surficial' within the text and in Tables 7, 8 and 9. 'Surficial' processes are likely involved in the dispersion of the common Pb from the surface because the $^{207}Pb/^{206}Pb$ values in these fractures are higher than in the background sandstones.

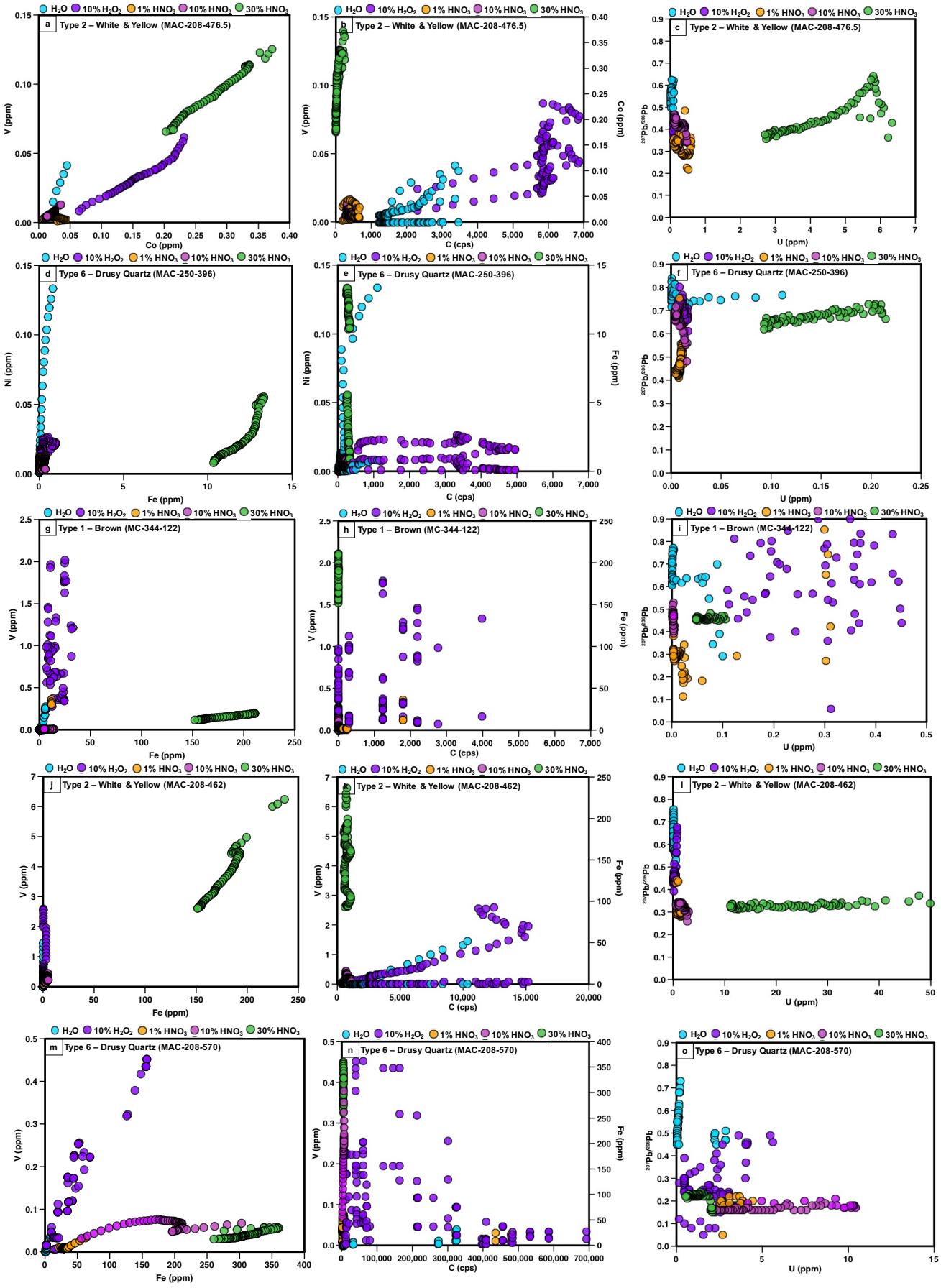
H2O
10% H2O2
1% HNO3
10% HNO3
30% HNO3
a
Type 2 – White & Yellow (MAC-208-476.5)
V (ppm)
Co (ppm)
b
Type 2 – White & Yellow (MAC-208-476.5)
V (ppm)
Co (ppm)
C (cps)
c
Type 2 – White & Yellow (MAC-208-476.5)
Pbdisol/Pbzirc
U (ppm)
d
Type 6 – Drusy Quartz (MAC-250-396)
Ni (ppm)
Fe (ppm)
e
Type 6 – Drusy Quartz (MAC-250-396)
Ni (ppm)
Fe (ppm)
C (cps)
f
Type 6 – Drusy Quartz (MAC-250-396)
Pbdisol/Pbzirc
U (ppm)
g
Type 1 – Brown (MC-344-122)
V (ppm)
Fe (ppm)
h
Type 1 – Brown (MC-344-122)
V (ppm)
Fe (ppm)
C (cps)
i
Type 1 – Brown (MC-344-122)
Pbdisol/Pbzirc
U (ppm)
j
Type 2 – White & Yellow (MAC-208-462)
V (ppm)
Fe (ppm)
k
Type 2 – White & Yellow (MAC-208-462)
V (ppm)
Fe (ppm)
C (cps)
l
Type 2 – White & Yellow (MAC-208-462)
Pbdisol/Pbzirc
U (ppm)
m
Type 6 – Drusy Quartz (MAC-208-570)
V (ppm)
Fe (ppm)
n
Type 6 – Drusy Quartz (MAC-208-570)
V (ppm)
Fe (ppm)
C (cps)
o
Type 6 – Drusy Quartz (MAC-208-570)
Pbdisol/Pbzirc
U (ppm)

Figure 3.10: Bivariate scatter plots for (a) V and Co, (b) V, Co and C and (c) $^{207}Pb/^{206}Pb$ and U, from MAC-208-476.5 (type 2 - white and yellow fracture from the Gap Zone), (d) Ni and Fe, (e) Ni, Fe and C and (f) $^{207}Pb/^{206}Pb$ and U, from MAC-250-396 (type 6 - drusy quartz fracture from the Gap Zone), (g) V and Fe, (h) V, Fe and C and (i) $^{207}Pb/^{206}Pb$ and U, from MC-344-122 (type 1 - brown fracture from the South West Distal Zone), (j) V and Fe, (k) V, Fe and C and (l) $^{207}Pb/^{206}Pb$ and U (type 2 - white and yellow fracture from the Gap Zone), and (m) V and Fe, (n) V, Fe and C and (o) $^{207}Pb/^{206}Pb$ and U (type 6 - drusy quartz fracture from the Gap Zone). Type of leach solution is indicated at the top of each graph.

Major elements including Fe, Al, Mg, as well as S and Ba show release patterns reflective of their respective host phases, which undergo dissolution primarily during the 30% HNO_3 leach step for most fractures fillings analyzed. For example, leaching of sample MC-413-614 (type 3 – white fracture coating) demonstrates the breakdown of pyrite, as Fe and S are simultaneously released during the 30% HNO_3 leach phase (Figure 3.8). This pattern contrasts with the pattern from MC-336-523.8 (type 2 - white and yellow fracture coating) that shows the dissolution of Fe oxide in the 30% HNO_3 leach phase, rather than pyrite, as Fe and S are not released together (Figure 3.9a).

Samples proximal to mineralization with low U concentrations and anomalously low $^{207}Pb/^{206}Pb$ values (0.05) suggest secondary dispersion has occurred from a U-rich source (e.g. samples MC-336-523.8 and MAC-255-509, Figure 3.9), in contrast to background samples distal to mineralization with high $^{207}Pb/^{206}Pb$ values (0.8) (e.g. MC-338-121, Figure 3.9). Low $^{207}Pb/^{206}Pb$ values (0.05) and high U concentrations (605 ppm) in samples proximal to mineralization obtained during leaching with 30% HNO_3 indicate both primary and secondary dispersion of U and Pb (Figure 3.10c and l). As the mineral host dissolves, U concentrations decrease near the end of 30% HNO_3 leach (Figure 3.10c and l).

Mineral phases hosting common Pb (Table 3.9) indicate that there is dominantly an organic control on common Pb. Low U concentrations (≤ background values ~10 ppm) and high

$^{207}Pb/^{206}Pb$ values (>0.7) during breakdown of the paragenetically-late organic matter (Chapter 2) during leaching with 10% H_2O_2 likely reflect surficial sources of both the organic matter and Pb. The CL-ICP-MS data also indicate an association between Fe-Mn oxy-hydroxides and clay minerals with radiogenic Pb (Table 3.8), because higher concentrations of Pb, Al, Fe, and Mn are released along with low $^{207}Pb/^{206}Pb$ values (<0.7) during the 30% HNO_3 leach phase. However, low U concentrations (≤ background values) in many of these fracture fillings also indicate that the Pb reflects post-mineralization dispersion, either without U or that U was removed by a later fluid. Fractures showing a radiogenic Pb signature near the surface, such as MC-413-73.6 (type 1 – brown), reflect post-mineralization dispersion of radiogenic Pb from a U-rich source released with 10% H_2O_2. In this case, organic material acts as a host for the radiogenic Pb.

Table 3.7: Various fracture types and interpreted mineral phases hosting pathfinder elements released during CL-ICP-MS. Also listed is the likely process associated with dispersion of the pathfinder elements.

Sample ID	Fracture type	Leaching step and pathfinder elements released	Mineral phase(s) hosting pathfinder elements	Dispersion
MAC-208-262.5	1-Brown	10% H_2O_2 – Pb, V	organic	Secondary
MAC-208-305	4-Black	30% HNO_3 – Co, V	clays, FeOx	Secondary
MAC-208-462	2-White & Yellow	30% HNO_3 – Co, V	clays, goethite	Primary & Secondary
MAC-208-476.5	2-White & Yellow	10% H_2O_2 – Co, V 30% HNO_3 – Ni, Zn	organic, FeOx	Primary (Ni, Zn) Secondary (Co, V)
MAC-208-570	6-Drusy Quartz	30% HNO_3 - V	altered MnOx, FeOx	Surficial
MAC-250-276	4-Black	10% H_2O_2 – Mn, Co	organic	Secondary
MAC-250-396	6-Drusy Quartz	10% H_2O_2 – V 30% HNO_3 – Ni	organic, FeOx	Primary (Ni) Surficial (V)

MAC-252-21.7	3-White	10% H_2O_2 – Co, Zn, Mn	organic, FeOx	Secondary (Co, Zn) Surficial (Mn)
MAC-255-37	2-White & Yellow	10% H_2O_2 – Co, Zn, Mn	organic, dravite	Surficial
MAC-255-251	7-Pink	10% H_2O_2 - V	organic, FeOx	Secondary
MAC-255-509	3-White	10% H_2O_2 – Co, V 30% HNO_3 – Pb, As, Ni	organic, MnOx clinochlore	Secondary
MC-336-523.8	2-White & Yellow	30% HNO_3 - V	FeOx	Secondary
MC-338-121	5-Black & Orange	10% H_2O_2 – Co, V 30% HNO_3 –Ni	organic, clays, Mn-FeOx	Primary (Co & V) Secondary (Ni)
MC-338-206	5-Black & Orange	10% H_2O_2 – Co, Mn	organic, goethite	Secondary
MC-338-429.7	2-White & Yellow	10% H_2O_2 – S, Zn	organic	Secondary
MC-344-122	1-Brown	30% HNO_3 - V	FeOx	Secondary
MC-413-73.6	1-Brown	10% H_2O_2 – V	organic	Secondary
MC-413-614	3-White	10% H_2O_2 – Ni, Co, Pb, Mn	organic, clays, dravite	Primary & Secondary

Table 3.8: Continuous leach ICP-MS results for mineral phases hosting radiogenic Pb. Also shown is the likely process involved in the dispersion of the radiogenic Pb and U. N/A = not applicable.

Sample ID	Fracture type	Leaching step releasing radiogenic Pb	Mineral phase(s) hosting radiogenic Pb	Dispersion
MAC-208-262.5	1-Brown	30% HNO_3	illite	Secondary
MAC-208-305	4-Black	30% HNO_3	dickite	Secondary
MAC-208-462	2-White & Yellow	30% HNO_3	illite	Primary or Secondary (U & Pb)
MAC-208-476.5	2-White & Yellow	30% HNO_3	kaolinite	Primary & Secondary (U & Pb)
MAC-208-570	6-Drusy Quartz	30% HNO_3	altered clinochlore & dravite	Primary & Secondary (U & Pb)
MAC-250-276	4-Black	10% H_2O_2	organic, APS minerals	Secondary
MAC-250-396	6-Drusy Quartz	1% HNO_3	surfaces	Secondary
MAC-252-21.7	3-White	none	none	N/A

MAC-255-37	2-White & Yellow	none	none	N/A
MAC-255-251	7-Pink	10% H_2O_2	organic, illite, kaolinite, FeOx	Secondary
MAC-255-509	3-White	30% HNO_3	clinochlore	Secondary
MC-336-523.8	2-White & Yellow	30% HNO_3	dravite, clays, FeOx	Secondary
MC-338-121	5-Black & Orange	30% HNO_3	kaolinite, FeOx	Primary & Secondary (U & Pb)
MC-338-206	5-Black & Orange	10% H_2O_2	clays, goethite	Secondary
MC-338-429.7	2-White & Yellow	30% HNO_3	kaolinite, goethite	Secondary
MC-344-122	1-Brown	30% HNO_3	FeOx, clays, dravite, MnOx	Secondary
MC-413-73.6	1-Brown	10% H_2O_2	organic, clays, FeOx, TiOx	Secondary
MC-413-614	3-White	10% H_2O_2	organic, illite, dravite	Primary & Secondary (U & Pb)

Table 3.9: Continuous leach ICP-MS results for mineral phases hosting common Pb and the associated dispersion. N/A = not applicable.

Sample ID	Fracture type	Leaching step releasing common Pb	Mineral phase(s) hosting common Pb	Dispersion
MAC-208-262.5	1-Brown	10% H_2O_2	organic, clays, goethite	Surficial
MAC-208-305	4-Black	10% H_2O_2	organic, clays, Mn-FeOx	Surficial
MAC-208-462	2-White & Yellow	none	none	N/A
MAC-208-476.5	2-White & Yellow	none	none	N/A
MAC-208-570	6-Drusy Quartz	none	none	N/A
MAC-250-276	4-Black	H_2O	surfaces	Surficial
MAC-250-396	6-Drusy Quartz	H_2O	surfaces	Surficial
MAC-252-21.7	3-White	10% H_2O_2	organic, clays, dravite, FeOx	Surficial
MAC-255-37	2-White & Yellow	10% H_2O_2	organic, clays, dravite, FeOx	Surficial
MAC-255-251	7-Pink	H_2O	surfaces	Surficial
MAC-255-509	3-White	none	none	N/A

MC-336-523.8	2-White & Yellow	none	none	N/A
MC-338-121	5-Black & Orange	10% H_2O_2	organic, illite, MnOx	Surficial
MC-338-206	5-Black & Orange	H_2O	surfaces	Surficial
MC-338-429.7	2-White & Yellow	10% H_2O_2	organic, clays, goethite	Surficial
MC-344-122	1-Brown	10% H_2O_2	organic, clays, dravite, MnOx	Surficial
MC-413-73.6	1-Brown	H_2O	surfaces	Surficial
MC-413-614	3-White	none	none	N/A

Although the CL-ICP-MS analysis time is long and the resulting data patterns are complex, sample preparation is minimal and potential for contamination is reduced due to leaching in a closed system. Other techniques, such as sequential leach (increasing concentrations of HNO_3) used by Devine *et al*. (2016) on fracture coatings of the top 100 m of the MFd sandstone, do not have the time resolution of CL-ICP-MS analysis (e.g. Gatehouse *et al*., 1977; Hall *et al*., 1996; Silva *et al*., 2007). Devine *et al*. (2016) used sequential leach on "surficial" (<100 m) fracture coatings to determine the potential mineralogical hosts of various elements and compared these results to Ra concentrations (in pg/g). Fracture surfaces were leached with different strengths of nitric acid, which resulted in the dissolution of Fe-Mn oxy-hydroxide minerals throughout the nitric acid leaches (Devine *et al*., 2016). Fe-Mn oxy-hydroxide minerals (Ames *et al*., 1983; Sajih *et al*., 2014) are potential hosts for Ra on fracture surfaces due to their electronegativity and chemical affinity (Devine *et al*., 2016). A moderate correlation between Ra and Mn (Devine *et al*., 2016) suggests that Ra is indeed likely adsorbed to Mn oxy-hydroxides (Herczeg *et al*., 1988). Although the time resolution of CL-ICP-MS analysis cannot be achieved by sequential leach, the sequential leach data supports the Fe-Mn oxy-hydroxide association with

radiogenic decay products in fracture coatings also observed in this study, especially for fractures near the surface that record radiogenic Pb (e.g. MC-413-73.6; type 1 - brown).

3.5 Discussion

Fracture coatings and related wall rock alterations in Athabasca Group sandstones will be effective in exploration for U resources if they record the syn-mineralization and post-mineralization dispersion of components from unconformity-type U deposits, such as the McArthur River U deposit. These dispersions may be able to enhance the deposit footprint and establish the link for element dispersion/migration from the deposit to their surficial geochemical signatures. For fracture fillings to be effective indicators of dispersion from the U deposits, a crystal chemical context of fracture filling mineralogy is critical to determine which minerals are host to certain pathfinder elements.

3.5.1 Pb isotopes

The seven fracture types have variable $^{207}Pb/^{206}Pb$ values, which are the most definitive pathfinders for U deposits (Cuney and Kyser, 2014). Low $^{207}Pb/^{206}Pb$ values occur throughout the depth profile (Figure 3.4), but the lowest (most radiogenic) ratios (0.05-0.35) are typically associated with white (type 3) fractures located near to the P2 fault and are representative of syn-mineralization dispersion (Zone C and Zone 4, Figure 3.4). The color of the type 3 fractures is reflective of the kaolinitic and illitic clay minerals that comprise the fracture fill. Brown (type 1) and black (type 4) also have low $^{207}Pb/^{206}Pb$ values (0.28-0.45), but they occur primarily at shallow depths (e.g. at SW Distal Zone, Gap Zone, Zone C, Figure 3.4) and with mostly background (~10 ppm or less) U concentrations. These fractures record radiogenic Pb that is expected from an unconformity-type U deposit. Additionally, they also have concave-down

chondrite-normalized REEs patterns that match those of the uraninites (Mercadier *et al*., 2011).

Uraninite and coffinite are unstable in oxidizing surficial environments and are easily altered by meteoric fluids (Dyck, 1978; Baadsgaard *et al*., 1984; Kotzer and Kyser, 1995). This makes the establishment of a reliable age of initial emplacement for U deposits challenging, and determination of the timing of the fluids mobilizing the U difficult. Uranium deposits contain ^{238}U and ^{235}U that decay to daughter products of ^{206}Pb and ^{207}Pb at a known rate (Holk *et al*., 2003). The decay of U isotopes does not affect ^{204}Pb, the stable isotope of Pb. Thus, $^{206}Pb/^{204}Pb$ and $^{207}Pb/^{204}Pb$ values will reflect the initial U/Pb values and residence time within a system (Holk *et al*., 2003). In open systems, such as basins having structurally-hosted U deposits like the Athabasca Basin, the $^{206}Pb/^{204}Pb$ value away from the deposit will be elevated if either radiogenic Pb or U are mobilized from the deposit, depending on the timing of the mobilization (Holk *et al*., 2003).

$^{206}Pb/^{204}Pb$ and $^{207}Pb/^{204}Pb$ values are elevated throughout the Manitou Falls Formation above the McArthur River deposit (Guffey, 2017), consistent with post-mineralization dispersion of radiogenic Pb from the deposit. The Pb-Pb model ages near 1100 Ma for all fractures suggest a major mobilization of Pb at the time of the Grenville Orogeny. Although this was a major event of mobilization that affected the deposits in the basin (Cuney and Kyser, 2014), the significant errors in all model ages indicate an open system that reflects Pb mobility during multiple events. The U-Pb isotope ratios (Table 3.4) of most of these fracture materials suggest that in many fractures, the Pb isotopic system was reset more recently (~250 Ma), related to fluid-rock interactions with the influx of meteoric fluids from ~250 Ma ago (Figure 3.11). Lead mobilization events from U deposits within Proterozoic basins are thought to have been ongoing for at least the last 1500 Ma (Kyser *et al*., 2000), with particularly significant episodes occurring at 1100, ~300-400 Ma, and 0 Ma that resulted in considerable Pb loss from most ores due to the

interaction with later fluids (Wilson and Kyser, 1987; Kotzer and Kyser, 1991, 1993, 1995). Much of this radiogenic Pb is now resident in the fractures, as was reported for this and other U deposits by Holk et al. (2003).

3.5.2 REE patterns

Fracture coatings can be divided into three distinct groups according to their REE patterns. These patterns reflect REEs that were mobilized by fluids that flowed through the fractures. The REEs in fractures tend to be hosted by mineral surfaces or in APS minerals because they are released during weak acid leaching, which does not attack most other minerals. Group 1 fracture coatings have variable REE concentrations (Figure 3.5a), LREE-enriched chondrite normalized patterns with LREE/HREE values of > 1 and negative Eu anomalies. Such REE patterns are typical of background sandstone (Fayek and Kyser, 1997), the likely source of the REEs.

Group 2 fractures have bell-shaped, concave-down MREE-enriched patterns and LREE/HREE values of ~1 (Figure 3.5c), which are typical of uraninites from unconformity-type U deposits in the Athabasca Basin (Mercadier *et al*., 2011). This pattern has been proposed to result from the crystallization of LREE-rich APS minerals that diminishes the LREE available for uraninite (Gaboreau *et al*., 2007). The REE patterns in Group 2 fractures also exhibit positive Ce and negative Eu anomalies for black (type 4) and brown (type 1) types (Figure 3.5c). Positive Ce anomalies are indicative of precipitation of REEs by oxidizing fluids (Fayek and Kyser, 1997), causing Ce^{4+} to be precipitated with the fracture minerals.

Group 3 fractures have flat REE patterns, weaker positive Ce anomalies for some brown (type 1) and black (type 4) fracture types relative to Group 2 fractures, and negative Eu anomalies (Figure 3.5e). The weaker positive Ce anomalies indicate the influence of more anoxic fluids

(Fayek and Kyser, 1997). These fractures have LREE/HREE values that range between 0.20 and 75.68, consistent with REE distributions intermediate between background sandstone and mineralization patterns (Fayek and Kyser, 1997; Mercadier *et al*., 2011).

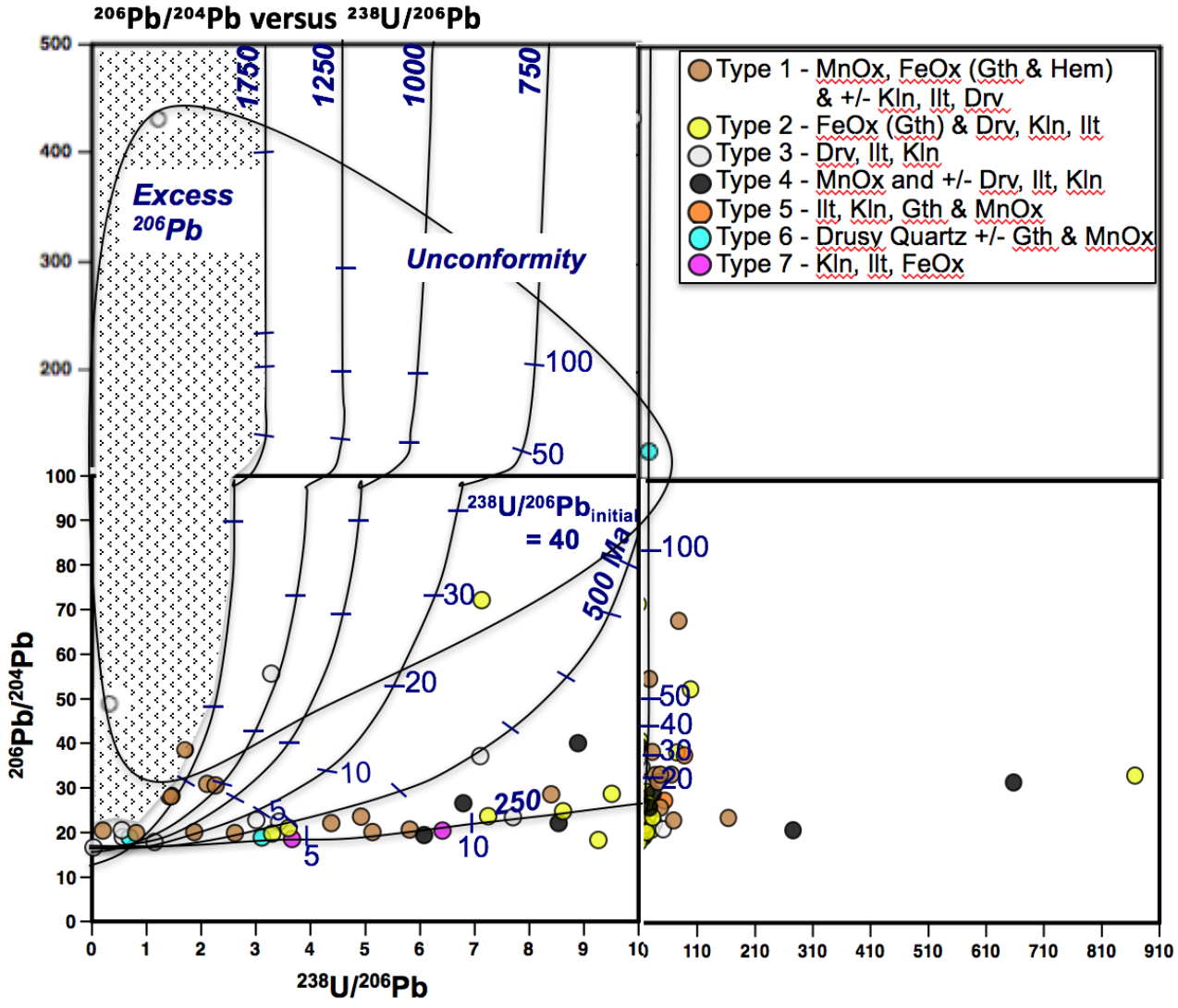

Figure 3.11: $^{206}Pb/^{204}Pb$ versus $^{238}U/^{206}Pb$ data from WAL of fracture fillings. The lines show the closed system evolution of isotope ratios in uraninites with ages from 1750-250 Ma. The shaded area indicates samples that have ^{206}Pb contents in excess of the amount that can be obtained from the leachable U in the sample. The isotope evolution curves show the initial $^{238}U/^{206}Pb$ values of 10, 20, 30, 40, 50 and 100. Figure modified from Holk *et al.* (2003).

3.5.3 Origins of fluids recorded by fractures at McArthur River

Comparison of the mineralogy and geochemistry of fracture coatings, with their associated near-fracture samples, from McArthur River indicate fluid-rock interactions in both fracture coatings and the surrounding wall rock consistent with post-mineralization dispersion fluids that mobilized radiogenic Pb having low $^{207}Pb/^{206}Pb$ values of 0.05-0.50 from a U-rich source. In some fractures, the fracture fill was subsequently replaced by minerals deposited from a fluid with higher $^{207}Pb/^{206}Pb$ values of 0.51-0.84, but leaving radiogenic Pb signature in the near-fracture material (Figure 3.6). This is especially evident for brown (type 1) and pink (type 7) fractures, present nearest the surface, that are characterized by botryoidal goethite and late poorly-crystallized kaolinite, which are low-temperature minerals with isotopic compositions and habits consistent with formation from meteoric waters (Chapter 2). These late meteoric fluids migrated downward from surface and variably overprinted earlier formed minerals that are preserved in the near-fracture material. Figure 3.6 shows that pink (type 7) fracture coatings exhibit a common Pb ($^{207}Pb/^{206}Pb$ >0.7) signature compared to a brown (type 1) fracture coating, at the surface, that exhibits a radiogenic Pb signature ($^{207}Pb/^{206}Pb$ <0.7) due to accumulation of radiogenic Pb from post-mineralization dispersion. These fluid-rock interactions can be indicated by mineralogical zoning in the wall rock adjacent to the fracture for one-third of the samples, as shown by hyperspectral imaging in Chapter 2, whereas the other two-thirds of the samples show minimal differences in mineralogy and element inventory between the fracture and wall rock. Two possible causes of this outcome are either that a late fluid overprinted the wall rock entirely or the fluid precipitated minerals that were similar to those already present in the fracture fill. Therefore, based on Pb isotope values, pink (type 7) and brown (type 1) fractures, occurring nearest the surface in the McArthur River area, can be used to detect post-mineralization

dispersion of radiogenic Pb within the wall rock adjacent to the fracture. The timing of these events using $^{207}Pb/^{204}Pb$-$^{206}Pb/^{204}Pb$ model ages indicates ages of 781 +/- 210 Ma for these fracture coatings and slightly older ages of 1128 +/- 150 Ma for the McArthur River near-fracture wall rock materials.

Brown (type 1), white and yellow (type 2), black (type 4), and black and orange (type 5) fractures contain Fe oxides that facilitate fixation of metal cations, including mobile pathfinder elements (Cameron *et al*., 2004). Brown (type 1) and black (type 4) fractures generally record variable overprinting by Fe and Mn oxides of earlier formed minerals and the WAL data indicate that they contain elevated concentrations of Co, Ba, Tl, and Mn (Figure 3.7). Brown (type 1) fractures at depth, for example MAC-246-534, also record syn-mineralization dispersion with the presence of elevated concentrations of V and alkali-deficient dravite (T1; Chapter 2). White and yellow (type 2) and black and orange (type 5) fractures have a fibrous goethite crystal habit, indicative of hydrothermal fluid input, in contrast to botryoidal goethite in brown (type 1) fractures from meteoric waters, and also recorded by the $\delta^{18}O$ and $\delta^{2}H$ values of the goethite (Chapter 2). Black and orange (type 5) fractures located near the surface, such as sample MAC-246-23.1, also have elevated U and V concentrations and radiogenic Pb associated with fibrous goethite. White and yellow (type 2) fractures generally record syn-mineralization dispersion of V at depth (MAC-208-462; 38 ppm), but also in the near-surface (MAC-255-37; 70 ppm). Continuous leach ICP-MS data indicate syn-mineralization dispersion of V and Co during 30% HNO_3 leach that is hosted in clay minerals and goethite from MAC-208-462, a white and yellow (type 2) fracture. However, V can also be trapped in organic material, as evident in MAC-208-476.5 (type 2 - white and yellow) and MAC-255-251 (type 7 – pink) during 10% H_2O_2 leach and hosted in Fe oxide from MC-336-523.8 (type 2 – white and yellow) and MC-344-122 (type 1 –

brown) released during 30% HNO_3 leach. The organic matter and the Fe oxide in these samples are paragenetically late (Chapter 2), consistent with trapping of V from post-mineralization dispersion from the deposit. Continuous leach ICP-MS data also indicate that most pathfinder elements including, V, Co, Ni, Pb, Mn, S, and Zn are released during 10% H_2O_2 and 30% HNO_3 leaching. Thus, many pathfinder elements are hosted both in organic material that reacts during 10% H_2O_2 and in Fe oxides and clays with 30% HNO_3 leaching. Similarly, radiogenic Pb is released during 30% HNO_3 and is also hosted in Fe-Mn oxy-hydroxides and clays.

Fracture fill samples can have low $^{207}Pb/^{206}Pb$ values (<0.5), both from near the surface locations and at depth, but not at intermediate levels (Figure 3.4). Similarly, pathfinder elements are enriched in fractures located both near the surface and at depth, especially Ba, Co, Mn, and Tl in brown (type 1) and black (type 2) fractures (Figure 3.7). From stable isotope data in Chapter 2, most near-surface samples with low $^{207}Pb/^{206}Pb$ ratios (<0.5) at McArthur River record post-mineralization hydrothermal fluids associated with fibrous goethite on fracture coatings. However, some samples record the effects of meteoric fluids by the presence of botryoidal Fe oxide, such as within a brown fracture (type 1), MC-338-61.3, near the surface. Meteoric fluids can also affect some fractures located at depth where these fluids have migrated downward carrying common Pb to areas proximal to the unconformity through the fractures, precipitating low-temperature mineral phases such as botryoidal goethite on brown (type 1) fractures (e.g. MC-344-379.3 and MC-344-443 from the South West Distal Zone). The distribution of radiogenic Pb (Figure 3.4) and enrichments of pathfinder elements (Figure 3.7) indicates that the silicified zone generally obstructed the spatial dispersion of radiogenic Pb and pathfinder elements into the overlying strata (Figure 3.4). Thus, some of the secondary dispersion of radiogenic Pb and pathfinder elements in the upper MFd may have originated from meteoric waters carrying components leached from the surface or even the till. There is a correlation between the

geochemistry of composite samples from Manitou Falls Formation boulders and the underlying bedrock (Earle *et al*., 1990), and alteration halos and perched mineralization from the McArthur River deposit extend upward to near the present bedrock surface. Surface media such as boulders, soils, lake sediments and vegetation have been used to identify post-mineralization components at the surface related to the underlying bedrock (Dunn and Ramaekers, 1978). Geophysics, till lithology, and geomorphology have also been used, at McArthur River, to analyze Quaternary sediments and develop an understanding of till provenance and production (Scott and Ross, 2016). Scott and Ross (2016) suggested that exploration programs should select sampling areas that are shown to be more local in provenance and exclude areas that are distally derived. Therefore, from this study, some elements were dispersed from the deposit and accumulated near the surface, including in the till, must have been mobilized by later fluids and carried downward along some fractures.

Of the seven fracture types, the brown (type 1) type is the most indicative of U mineralization at depth because these fracture fillings show the greatest number of chondrite-normalized concave-down, bell-shaped REE patterns. They also display low $^{207}Pb/^{206}Pb$ values (0.28-0.69) and elevated Ba, Co, Tl, and Mn concentrations in fracture fillings at both the near-surface and at depth. Brown fractures can contain both high (illite, dravite), moderate (kaolinite and MnOx) and low-temperature (botryoidal goethite, organics) phases. Their wall rocks can have a more radiogenic Pb signature (e.g. Figure 3.6, sample MAC-208-262.5) than the fracture coatings, suggesting that meteoric fluids overprinted some of the radiogenic Pb signature that was in the fracture. Radiogenic Pb is mainly released during the most aggressive leach phase (30% HNO_3) in brown (type 1) fractures and is mostly hosted in Fe oxide (e.g. Table 3.8, MC-344-122), whereas some brown (type 1) fractures (e.g. MC-413-73.6, Table 3.8) and other types near the surface have radiogenic Pb that is released during 10% H_2O_2 and is hosted in organic

material.

Dispersion processes

The relationship between $^{207}Pb/^{206}Pb$ ratios and U concentrations (Table 3.5) should reflect whether syn- or post-mineralization dispersion processes have affected the fractures, depending on how open the system has been. Fluid events related to syn-mineralization and post-mineralization dispersion can be separated into three end members based on the concentration of U and the $^{207}Pb/^{206}Pb$ values (Figure 3.12): (1) dispersion of radiogenic Pb without U, (2) primary/secondary dispersion of both U and Pb in open systems, and (3) secondary mobilization of U without Pb. Low U concentrations and low $^{207}Pb/^{206}Pb$ values reflect dispersion of radiogenic Pb without the U that produced it, or later removal of the U. High U concentrations and low $^{207}Pb/^{206}Pb$ values reflect primary or secondary dispersion of U and Pb in an open system at various times in the evolution of the fracture. High U concentrations and high $^{207}Pb/^{206}Pb$ values reflect recent mobilization of U without the radiogenic Pb that would have been produced by the decay of the U. Background Pb and U in the Athabasca Group sandstones is present on fracture coatings as variable but high $^{207}Pb/^{206}Pb$ values and low U concentrations (Figure 3.12). Using the relationship between Pb isotopes and U concentrations in the fractures and near-fractures shown in Figure 3.12, the processes involved and the significance of the fractures in the evolution of the basin can be better constrained.

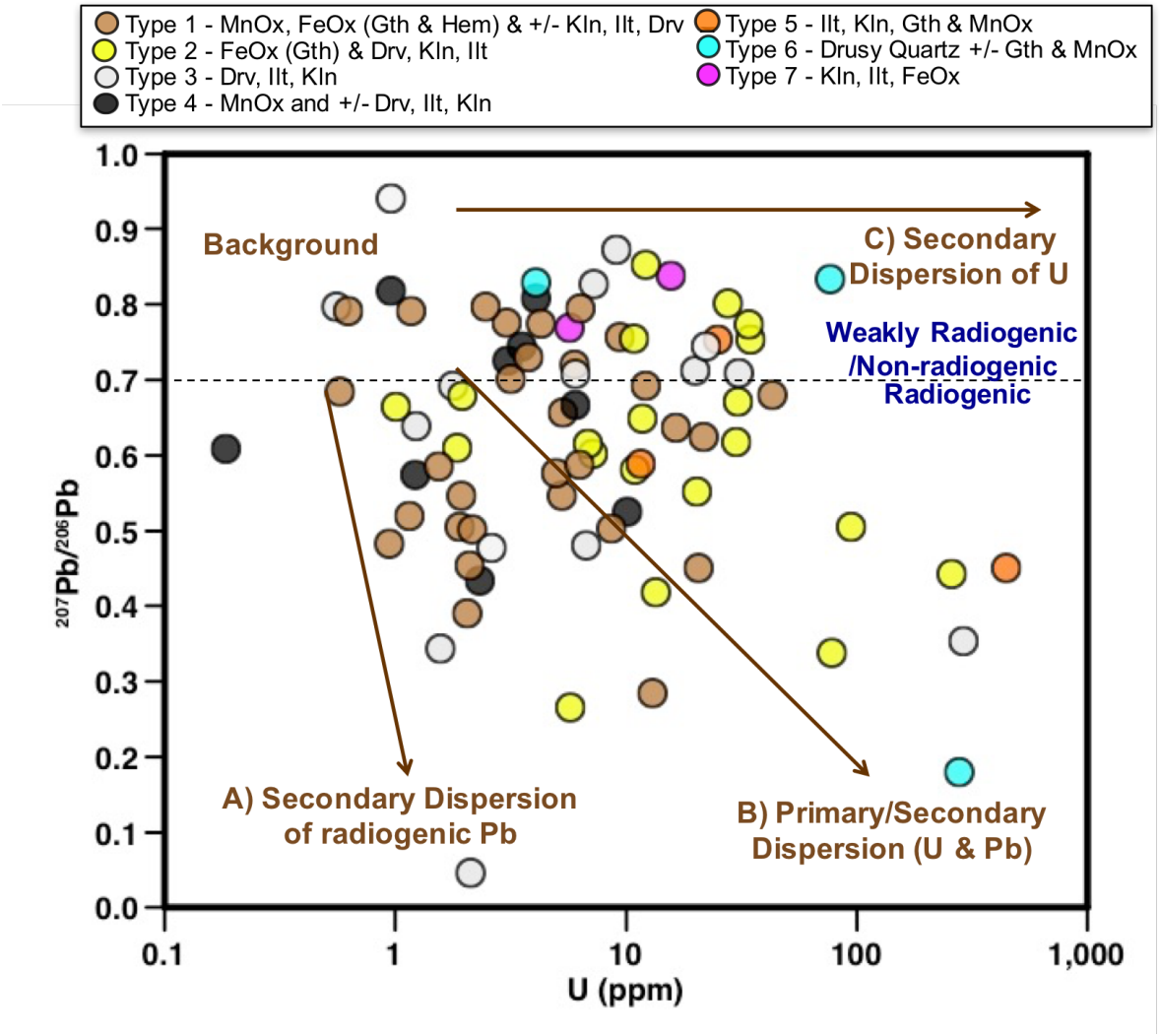

Figure 3.12: Relationship between $^{207}Pb/^{206}Pb$ ratios and U concentrations in fracture coatings showing the effect of syn-mineralization and post-mineralization dispersion processes from WAL data. The line at $^{207}Pb/^{206}Pb$ value of 0.7 divides weakly radiogenic/background from radiogenic Pb in the basin (Holk *et al.*, 2003).

3.5.4 Implications for surface exploration

Sampling and characterizing sandstone-hosted fracture fillings can be a highly effective way to trace geochemical dispersion, as fractures act as conduits for the migration of fluids that extend all the way to the surface through >500 m of Athabasca Group sandstone. Colors of the fractures reflect the mineralogy of the fracture fill and show initial evidence that fractures act as conduits for elements from the deposit, recording primary and secondary dispersion. However,

the usefulness of each fracture type can vary due to differences in the fracture fill mineralogy (Table 3.10). For example, brown (type 1) fractures are useful in terms of the higher concentration of pathfinder elements, specifically Ba, Co, Mn, Tl and radiogenic Pb. This geochemical signature is evident near the surface and at depth through high concentrations of pathfinder elements and low $^{207}Pb/^{206}Pb$ values, but not at intermediate depths due to the silicified zone. The silicified zone limited the mobility of hydrothermal and late meteoric post-ore fluids and the dispersion of elements above and below its barrier, causing low concentrations of U pathfinder elements and variable $^{207}Pb/^{206}Pb$ values at intermediate depths. In comparison, white and yellow (type 2) and white (type 3) fractures are useful in terms of recording primary dispersion of elements during the waning stages of the mineralizing system through early-formed minerals such as dickite, well-crystallized kaolinite (K1) in white (type 3) fractures, illite, and dravite (T1) from hydrothermal fluids rising from below with temperatures near 200ºC (Chapter 2). These fracture types extend from areas near U mineralization to the surface, allowing the migration of elements by basinal fluids associated with the U mineralizing system from depth to shallow levels in the basin. Therefore, two sources of U deposition occur in the McArthur River area including the deposit at depth and accumulation at the surface from mobilized components.

Table 3.10: Fracture types, fracture filling mineralogy, sample distance to the P2 fault (distal is > 300 m and proximal is < 200 m) and their usefulness for exploration, using a rating scale from 1 to 7 (1 = most useful and 7 = least useful).

Fracture Type	Fracture Mineralogy	Distance to P2 Fault	Usefulness (1-7)
1 – Brown	MnOx, FeOx (goethite & hematite) ± kaolinite, illite, dravite	distal to proximal	**1** - high Ba, Co, Mn & Tl; post-mineralization dispersion of radiogenic Pb in the fracture & wall rock; botryoidal goethite (low-temperature fluid indicator)

2 – White & Yellow	FeOx (goethite) & dravite, kaolinite, illite	distal to proximal	**2** - high V; fibrous goethite (higher temperature fluid indicator)
3 – White	dravite, kaolinite, illite ± dickite, clinochlore	distal to proximal	**3** - well-crystalline kaolinite (high-temperature fluid indicator)
4 – Black	MnOx ± dravite, illite, kaolinite	distal	**4** - high Ba, Co, Mn & Tl; microfiber Mn oxy-hydroxides (hydrothermal fluid indicator)
5 – Black & Orange	illite, kaolinite, goethite & MnOx	distal	**5** - high V; fibrous goethite (hydrothermal fluid indicator)
6 – Drusy Quartz	drusy quartz, goethite and MnOx	proximal	**7** - fibrous interlocking illite (hydrothermal fluid indicator during waning stages of the mineralizing system)
7 – Pink	illite, kaolinite & FeOx	distal	**6** - post-mineralization dispersion of radiogenic Pb in the fracture & wall rock; poorly-crystalline kaolinite (low-temperature fluid indicator)

3.6 Conclusions

Fracture fillings and their adjacent wall rock materials can record various fluid events even before the current fracture coating was deposited. These fracture events can be observed by mineralogical zoning in the wall rock decreasing with distance from the fracture and/or from paragenetically distinct minerals present in the fracture. Based on the petrography and chemistry of fracture fillings and their wall rock materials, a number of conclusions can be drawn:

1. Brown (type 1) fracture coatings containing Mn oxides, Fe oxides (goethite and hematite) ± kaolinite, illite, and dravite are the most viable fracture type to detect

U mineralization, as they record low $^{207}Pb/^{206}Pb$ values and elevated Co, Ba, Tl, and Mn concentrations at surface, suggesting post-mineralization dispersion of radiogenic Pb accumulated at the surface from a U-rich source. At depth, these fractures reflect post-mineralization dispersion of radiogenic Pb from the McArthur River U deposit. Brown fractures also have chondrite-normalized REE patterns similar to those in unconformity-related U deposits in the Athabasca Basin.

2. REE patterns of drusy quartz (type 6) and oxide-rich (type 1 - brown, type 2 – white and yellow, type 4 – black, type 5 – black and orange) fractures also have REE patterns similar to those in unconformity-related U deposits in the Athabasca Basin, including fractures located near the surface. The $^{206}Pb/^{204}Pb$ and $^{207}Pb/^{204}Pb$ isotope ratios in many of these fracture fillings are elevated throughout the Manitou Falls Formation above the McArthur River deposit, consistent with post-mineralization dispersion of radiogenic Pb from a U-rich source and providing evidence that fractures act as conduits for element migration from the deposits to the surface.
3. Pink (type 7) and brown (type 1) fractures near the surface can be used as an exploration technique to detect post-mineralization dispersion within the fracture and its adjacent wall rock. The $^{207}Pb/^{206}Pb$ values of their wall rock reveal post-mineralization dispersion processes via low $^{207}Pb/^{206}Pb$ values compared to higher $^{207}Pb/^{206}Pb$ ratios on the fracture surface. Multiple fluid events have effected both the fracture and the wall rock and more recent fluids have either replaced or overprinted earlier formed minerals on the fractures.

4. Trace and major elements can be correlated with mineral chemistry through CL-ICP-MS analyses to reveal the mineral phase that hosts the elements. CL-ICP-MS data indicate an organic control on common Pb, as well as Co and V, during leaching with 10% H_2O_2, likely reflecting surficial processes wherein these elements are trapped by organic matter that originated from the surface. The CL-ICP-MS data indicate that radiogenic Pb is associated with Fe-Mn oxy-hydroxides and clays, as well as pathfinders Ni and V during leaching with 30% HNO_3, and reflecting post-mineralization dispersion from the deposit. The sequential leach analyses carried out by Devine *et al*. (2016) support the Fe-Mn oxy-hydroxide association with radiogenic decay products on fracture coatings, especially for fractures near the surface. CL-ICP-MS of fracture coatings provides useful exploration information as it identifies suites of mobile elements, thereby enlarging the footprint of the McArthur River U deposit.

The mineral chemistry of fracture coatings relative to that of the host rock indicates that, although multiple fluid events have affected some fractures, they still preserve evidence of syn-mineralization and post-mineralization dispersion of elements, including radiogenic Pb from a U-rich source at the surface and at depth, but not intermediate depths because of a silicified zone in the sandstone. The mineralogy and geochemistry of fracture fillings indicate syn- and post-mineralization mobilization of pathfinder elements from the deposit at depth, but also provide evidence of a downward migration of elements from surface. The footprint of the deposit appears concentrated at depth, as exhibited by deep fractures proximal to the P2 fault, but may also be detectable in the overlying surficial media, evidenced by near surface fractures.

3.7 Acknowledgments

Funding for this project was provided through the multi-sponsor, multi-researcher CMIC-NSERC Collaborative Research and Development (CRD) grant for the Footprints Project. Many thanks to Dr. Kevin Ansdell and Ken Wasyliuk from the University of Saskatchewan for their revisions on this manuscript. Sample collection in the field was facilitated by in-kind support from Cameco Corporation. Special thanks to Nick Joyce for assisting in sample collection and Queen's Facility for Isotope Research for providing analytical assistance and QFIR staff including, Donald Chipley, Evelyne Leduc, Alexandre Voinot, Steve Beyer, April Vuletich, Agatha Dobosz and Christabel Jean.

References

Alexandre, P., Kyser, K., Polito, P. and Thomas, D. 2005. Alteration mineralogy and stable isotope geochemistry of Paleoproterozoic basement-hosted unconformity-type uranium deposits in the Athabasca Basin, Canada. Economic Geology, 100(8), 1547-1563.

Alexandre, P., Kyser, K., Jiricka, D. and Witt, G. 2012. Formation and evolution of the Centennial unconformity-related uranium deposit in the south-central Athabasca Basin, Canada. Economic Geology, 107(3), 385-400.

Ames, L. L., McGarrah, J. E., Walker, B. A. and Salter, P. F. 1983. Uranium and radium sorption on amorphous ferric oxyhydroxide. Chemical Geology, 40(1-2), 135-148.

Annesley, I. R., Madore, C. and Portella, P. 2005. Geology and thermotectonic evolution of the western margin of the Trans-Hudson Orogen: evidence from the eastern sub-Athabasca basement, Saskatchewan. Canadian Journal of Earth Sciences, 42(4), 573-597.

Baadsgaard, H., Cummino, G. L. and Worden, J. M. 1984. U-Pb geochronology of minerals from the Midwest uranium deposit, northern Saskatchewan. Canadian Journal of Earth Sciences, 21(6), 642-648.

Bath, A. H., Milodowski, A. E. and Strong, G. E. 1987. Fluid flow and diagenesis in the East Midlands Triassic sandstone aquifer. Geological Society, London, Special Publications, 34(1), 127-140.

Beaufort, D., Patrier, P., Laverret, E., Bruneton, P. and Mondy, J. 2005. Clay alteration associated with Proterozoic unconformity-type uranium deposits in the East Alligator

Rivers uranium field, Northern Territory, Australia. Economic Geology, 100(3), 515-536.

Bernier, S. 2004. Stratigraphy of the late Paleoproterozoic Manitou Falls Formation in the vicinity of the McArthur River uranium deposit, Athabasca Basin, Saskatchewan, Canada.

Bethke, C. M. and Marshak, S. 1990. Brine migrations across North America-the plate tectonics of groundwater. Annual Review of Earth and Planetary Sciences, 18(1), 287-315.

Cameron, E.M., Hamilton, S.M., Leybourne, M.I., Hall, G.E.M., McClenaghan, M.B. 2004. Finding deeply buried deposits using geochemistry; Geochemistry: Exploration, Environments and Analysis. Vol. 4, p. 7-32.

Carr, S.D., Easton, R.M., Jamieson, R.A., Culshaw, N.G. and White, D.J. 2004. The Grenville Orogen of Ontario and New York—a Himalayan-scale mountain belt: Significance of along strike-variations: In: The Celebratory Conference, From Parameters to Processes—Revealing the Evolution of a Continent, October 12–15, 2004, Toronto, Program and Abstract, Lithoprobe Secretariat, University of British Columbia, Vancouver, British Columbia, Lithoprobe Report No. 86, 4 pp.

Cloutier, J., Kyser, K., Olivo, G. R., Alexandre, P. and Halaburda, J. 2009. The Millennium uranium deposit, Athabasca Basin, Saskatchewan, Canada: an atypical basement-hosted unconformity- related uranium deposit. Economic Geology, 104(6), 815-840.

Cuney, M. and Kyser, K. (Eds.). 2014. Recent and not-so-recent developments in uranium deposits and implications for exploration.

Derome, D., Cathelineau, M., Cuney, M., Fabre, C., Lhomme, T. and Banks, D. A. 2005. Mixing of sodic and calcic brines and uranium deposition at McArthur River, Saskatchewan, Canada: a Raman and laser-induced breakdown spectroscopic study of fluid inclusions. Economic Geology, 100(8), 1529-1545.

Devine, M. 2016. Sources and pathways of radiogenic elements in surface media above the Millennium and McArthur River uranium deposits in the Athabasca Basin, Saskatchewan, Canada (Master's thesis). June

Dunn, C. E. and Ramaekers, P. 1978. Surface geochemical patterns associated with uranium in and beneath the Athabasca sandstone, Saskatchewan, Canada. In Geochemical Exploration 1978, Proceedings of the Seventh International Geochemical Exploration Symposium, Association of Exploration Geochemists, Ontario (pp. 9-15).

Dyck, W. 1978. The mobility and concentration of uranium and its decay products in temperate surficial environments. Uranium deposits, their mineralogy and origin. Mineralogical Association of Canada Short Course Handbook, 3.

Earle, S., McGill, B. and Murphy, J. 1990. Glacial till boulder geochemistry: an effective new exploration technique in the Athabasca Basin, Saskatchewan. Modern Exploration Techniques (BECK, LS, SIBBALD, TII, Eds.).

Ey, F., Piquard, J. P., Baudemont, D. and Zimmerman, J. 1992. The sue uranium deposits, Saskatchewan, Canada (No. IAEA-TECDOC--650).

Fayek, M. and Kyser, T.K. 1997. Characterization of multiple fluid-flow events and rare-earth-element mobility associated with formation of unconformity-type uranium deposits in the Athabasca Basin, Saskatchewan: The Canadian Mineralogist, v. 35, p. 627-658.

Gaboreau, S., Cuney, M., Quirt, D., Patrier, P., and Mathieu, R. 2007. Significance of aluminum phosphate-sulfate minerals associated with U unconformity-type deposits: The Athabasca basin, Canada. American Mineralogist, 92(2-3), 267-280.

Gatehouse, S., Russell, D. W. and Van Moort, J. C. 1977. Sequential soil analysis in exploration geochemistry. Journal of Geochemical Exploration, 8(1-2), 483-494.

Goldberg, I. S. 1998. Vertical migration of elements from mineral deposits. Journal of Geochemical Exploration, 61(1), 191-202.

Goulden, W. D., Hendry, M. J., Clifton, A. W. and Barbour, S. L. 1998. Characterization of radium-226 in uranium mill tailings. In Tailings and mine waste (Vol. 98, pp. 561-570).

Guffey, S. 2017. 3D Lithogeochemical footprint of the Millennium-McArthur River unconformity-type uranium deposits, Saskatchewan, Canada (Master's thesis). May

Gustafson, L. B. and Curtis, L. W. 1983. Post-Kombolgie metasomatism at Jabiluka, Northern Territory, Australia, and its significance in the formation of high-grade uranium mineralization in lower Proterozoic rocks. Economic Geology, 78(1), 26-56.

Hajnal, Z., White, D. J., Takacs, E., Gyorfi, I., Annesley, I. R., Wood, G., O'Dowd, C. and Nimeck, G. 2010. Application of modern 2-D and 3-D seismic-reflection techniques for uranium exploration in the Athabasca Basin This article is one of a series of papers published in this Special Issue on the theme Lithoprobe—parameters, processes, and the evolution of a continent. Canadian Journal of Earth Sciences, 47(5), 761-782.

Hall, G. E. M., Valve, J. E., Beer, R. and Hoashi, M. 1996. Phase selective leaches for use in exploration geochemistry. BULLETIN-GEOLOGICAL SURVEY OF CANADA, 169-200.

Hall, G. E. 1998. Analytical perspective on trace element species of interest in exploration. Journal of Geochemical Exploration, 61(1), 1-19.

Herczeg, A. L., Simpson, H. J., Anderson, R. F., Trier, R. M., Mathieu, G. G. and Deck, B. L. 1988. Uranium and radium mobility in groundwaters and brines within the Delaware Basin, southeastern New Mexico, USA. Chemical Geology: Isotope Geoscience section, 72(2), 181-196.

Hiatt, E. E. and Kyser, T. K. 2007. Sequence stratigraphy, hydrostratigraphy, and mineralizing fluid flow in the Proterozoic Manitou Falls Formation, eastern Athabasca Basin, Saskatchewan. BULLETIN-GEOLOGICAL SURVEY OF CANADA, 588, 489.

Hiatt, E. E., Kyser, T. K., Fayek, M., Polito, P., Holk, G. J. and Riciputi, L. R. 2007. Early quartz cements and evolution of paleohydraulic properties of basal sandstones in three Paleoproterozoic continental basins: Evidence from in situ δ 18 O analysis of quartz cements. Chemical Geology, 238(1), 19-37.

Hoeve, J. and Sibbald, T. I. 1978. On the genesis of Rabbit Lake and other unconformity-type uranium deposits in northern Saskatchewan, Canada. Economic Geology, 73(8), 1450-1473.

Hoeve, J. and Quirt, D. H. 1984. Mineralization and host rock alteration in relation to clay mineral diagenesis and evolution of the Middle-Proterozoic, Athabasca Basin, northern Saskatchewan, Canada.

Hoffman, P. F. 1988. United Plates of America, the birth of a craton-Early Proterozoic assembly and growth of Laurentia. Annual Review of Earth and Planetary Sciences, 16, 543-603.

Holk, G.J., Kyser, T.K., Chipley, D., Hiatt, E.E. and Marlatt, J. 2003. Mobile Pb-isotopes in Proterozoic sedimentary basins as guides for exploration of uranium deposits: Journal of Geochemical Exploration, v. 80, p. 297-320.

International Atomic Energy Agency. 2009. World distribution of uranium deposits (UDEPO), with uranium deposit classification: IAEA-TECDOC-1629, Vienna, 117 p.

Jeanneret, P., Goncalves, P., Durand, C., Trap, P., Marquer, D., Quirt, D. and Ledru, P. 2016. Tectono-metamorphic evolution of the pre-Athabasca basement within the Wollaston–Mudjatik Transition Zone, Saskatchewan. Canadian Journal of Earth Sciences, 53(3), 231-259.

Jefferson, C. W., Thomas, D. J., Gandhi, S. S., Ramaekers, P., Delaney, G., Brisbin, D., Cutts, C., Portella, P. and Olson, R. A. 2007. Unconformity-associated uranium deposits of the Athabasca Basin, Saskatchewan and Alberta. Bulletin-Geological Survey of Canada, 588, 23.

Joyce, N. 2016. Alteration mineralogy and pathfinder element inventory of the McArthur River unconformity related uranium deposit, Saskatchewan, Canada (Master's thesis). 25October

Kotzer, T. G. and Kyser, T. K. 1991. Retrograde alteration of clay minerals in uranium deposits: Radiation catalyzed or simply low-temperature exchange? Chemical Geology: Isotope Geoscience section, 86(4), 307-321.

Kotzer, T.G. and Kyser, T.K. 1993. O, U, and Pb isotopic and chemical variations in uraninite:

implications for determining the tempo-ral and fluid history of ancient terrains. American Mineralogist 78, 1262–1274.

Kotzer, T. G. and Kyser, T. K. 1995. Petrogenesis of the Proterozoic Athabasca Basin, northern Saskatchewan, Canada, and its relation to diagenesis, hydrothermal uranium mineralization and paleohydrogeology. Chemical Geology, 120(1), 45-89.

Krauskopf, K. and Bird, D. 1995. Surface chemistry: the solution-mineral interface. Introduction to geochemistry (Ed MG-HI Editions) Mc Graw-Hill International Editions edn. Earth Sciences and Geology Series, 135-163.

Kyser, T. K., Wilson, M. R. and Ruhrmann, G. 1989. Stable isotope constraints on the role of graphite in the genesis of unconformity-type uranium deposits. Canadian Journal of Earth Sciences, 26(3), 490-498.

Kyser, K., Hiatt, E., Renac, C., Durocher, K., Holk, G. and Deckart, K. 2000. Diagenetic fluids in Paleo-and Meso-Proterozoic sedimentary basins and their implications for long protracted fluid histories: Fluids and basin evolution: Mineralogical Association of Canada Short Course, v. 28, p. 225-262.

Kyser, K., Lahusen, L., Drever, G., Dunn, C., Leduc, E., and Chipley, D. 2015. Using Pb isotopes in surface media to distinguish anthropogenic sources from undercover uranium sources. Comptes Rendus Geoscience, 347(5), 215-226.

Laverret, E., Mas, P. P., Beaufort, D., Kister, P., Quirt, D., Bruneton, P. and Clauer, N. 2006. Mineralogy and geochemistry of the host-rock alterations associated with the Shea Creek unconformity-type uranium deposits (Athabasca Basin, Saskatchewan, Canada). Part 1. Spatial variation of illite properties. Clays and Clay Minerals, 54(3), 275-294.

LeCheminant, A. N. and Heaman, L. M. 1989. Mackenzie igneous events, Canada: Middle Proterozoic hotspot magmatism associated with ocean opening. Earth and Planetary Science Letters, 96(1-2), 38-48.

Lesher, M., Hannington, M., Galley, A., Ansdell, K., Astic, T., Banerjee, N., Beauchamp, S., Beaudoin, G., Bertelli, M., Bérubé, C., Beyer, S., Blacklock, N., Byrne, K., Cheng, L.-Z., Chouinard, R., Chouteau, M., Clark, J., D'Angelo, M., Darijani, M., Devine, M., Dupuis, C., El Goumi, N., Enkin, R., Farquharson, C., Fayol, N., Feltrin, L., Feng, J., Gaillard, N., Gleeson, S., Gouiza, M., Grenon, C., Guffey, S., Guilmette, C., Guo, K., Hart, C., Hattori, K., Hollings, P., Joyce, N., Kamal, D., King, J., Kyser, K., Layton-Matthews, D., Lee, R., Lesage, G., Leybourne, M., Linnen, R., Lypaczewski, P., McGaughey, J., Mitchinson, D., Milkereit, B., Mir, R., Morris, W., Oldenburg, D., Olivo, G., Perrouty, S., Piercey, S., Piette-Lauzière, N., Raskevicius, T., Reman, A., Rivard, B., Ross, M., Samson, I., Scott, S., Shamsipour, P., Shi, D., Smith, R., Sundaralingam, N., Taves, R., Taylor, C., Valentino, M., Vallée, M., Wasyliuk, K. and Williams-Jones, A., Winterburn, P. 2017. Integrated Multi-Parameter Exploration Footprints of the Canadian Malartic Disseminated Au, McArthur River-Millennium Unconformity U, and Highland Valley

Porphyry Cu Deposits: Preliminary Results from the NSERC-CMIC Mineral Exploration Footprints Research Network. Available at: http://cmic-footprints.ca/home/ publications.

Lewry, J.F. and Sibbald, T.I. 1980. Thermotectonic evolution of the Churchill Province in northern Saskatchewan: Tectonophysics, v. 68, p. 45-82.

Lorilleux, G., Jébrak, M., Cuney, M. and Baudemont, D. 2002. Polyphase hydrothermal breccias associated with unconformity-related uranium mineralization (Canada): from fractal analysis to structural significance. Journal of Structural Geology, 24(2), 323-338.

MacFarlane, W. R., Kyser, T. K., Chipley, D., Beauchemin, D. and Oates, C. 2005. Continuous leach inductively coupled plasma mass spectrometry: applications for exploration and environmental geochemistry. Geochemistry: Exploration, Environment, Analysis, 5(2), 123-134.

Marlatt, J., McGill, B., Matthews, R., Sopuck, V. and Pollock, G. 1992. The discovery of the McArthur River uranium deposit, Saskatchewan, Canada (No. IAEA-TECDOC--650).

McGill, B. D., Marlatt, J. L., Matthews, R. B., Sopuck, V. J., Homeniuk, L. A. and Hubregtse, J. J. 1993. The P2 north uranium deposit, Saskatchewan, Canada. Exploration and Mining Geology, 2(4), 321-331.

McQueen, K. G. 2005. Ore deposit types and their primary expressions. Regolith Expression of Australian Ore Systems. CRC LEME, Perth, website: http://www. crcleme. org. au/Pubs/Monographs/RegExpOre. html [Last accessed January 2013.].

Mercadier, J., Cuney, M., Lach, P., Boiron, M. C., Bonhoure, J., Richard, A., Leisen, M., and Kister, P. 2011. Origin of uranium deposits revealed by their rare earth element signature. Terra Nova, 23(4), 264-269.

McLelland, J., Daly, J. S. and McLelland, J. M. 1996. The Grenville orogenic cycle (ca. 1350-1000 Ma): an Adirondack perspective. Tectonophysics, 265(1-2), 1-28.

Mwenifumbo, C. J., Elliott, B. E., Jefferson, C. W., Bernius, G. R. and Pflug, K. A. 2004. Physical rock properties from the Athabasca Group: designing geophysical exploration models for unconformity uranium deposits. Journal of Applied Geophysics, 55(1), 117-135.

Nakamura, N. 1974. Determination of REE, Ba, Fe, Mg, Na and K in carbonaceous and ordinary chondrites. Geochimica et Cosmochimica Acta, 38(5), 757-775.

Ng, R., Alexandre, P. and Kyser, K. 2013. Mineralogical and geochemical evolution of the unconformity-related McArthur River Zone 4 Orebody in the Athabasca Basin, Canada: implications of a silicified zone. Economic Geology, 108(7), 1657-1689.

Pagel, M., Poty, B. and Sheppard, S. M. F. 1980. Contribution to some Saskatchewan uranium deposits mainly from fluid inclusion and isotopic data. In Uranium in the Pine Creek Geosyncline.

Pan, Y. M., Botis, S. and Nokhrin, S. 2006. Applications of natural radiation-induced paramagnetic defects in quartz to exploration in sedimentary basins. Journal of China University of Geosciences, 17(3), 258-271.

Percival, J. B., Bell, K. and Torrance, J. K. 1993. Clay mineralogy and isotope geochemistry of the alteration halo at the Cigar Lake uranium deposit. Canadian Journal of Earth Sciences, 30(4), 689-704.

Ramaekers, P. P. and Dunn, C. E. 1977. Geology and geochemistry of the eastern margin of the Athabasca Basin.

Ramaekers, P., Christopher, J.E., and MacDonald, R. 1979. Stratigraphy of the Athabasca Basin; in Summary of Investigations 1979; Saskatchewan Geological Survey; Saskatchewan Mineral Resources, Miscellaneous Report 79-10, p. 154–160.

Ramaekers, P., Christopher, J.E., and MacDonald, R. 1980. Stratigraphy and tectonic history of the Athabasca Group (Helikian) of northern Saskatchewan; in Summary of Investigations 1980; Saskatchewan Geological Survey, Saskatchewan Mineral Resources, Miscellaneous Report 80-4, p. 99–106.

Ramaekers, P. 1990. Geological Maps of the Athabasca Group (Helikian) in Northern Saskatchewan. Saskatchewan Energy and Mines, Saskatchewan Geology Survey.

Ramaekers, P. and Catuneanu, O. 2004. Development and sequences of the Athabasca basin, early Proterozoic, Saskatchewan and Alberta, Canada. The Precambrian Earth: Tempos and Events. Developments in Precambrian Geology, 12, 705-723.

Ramaekers, P., Yeo, G. M., Jefferson, C. W., Collier, B., Long, D. G. F., Catuneanu, O., Bernier, S., Kupsch, B., Post, R., Drever, G., McHardy, S., Jiricka, D., Cutts, C. and Wheatley, K. 2007. Revised geological map and stratigraphy of the Athabasca Group, Saskatchewan and Alberta. Bulletin-Geological Survey of Canada, 588, 155.

Renac, C., Kyser, T. K., Durocher, K., Dreaver, G. and O'Connor, T. 2002. Comparison of diagenetic fluids in the Proterozoic Thelon and Athabasca Basins, Canada: implications for protracted fluid histories in stable intracratonic basins. Canadian Journal of Earth Sciences, 39(1), 113-132.

Rivers, T. 1997. Lithotectonic elements of the Grenville Province: review and tectonic implications. Precambrian Research, 86(3-4), 117-154.

Sajih, M., Bryan, N. D., Livens, F. R., Vaughan, D. J., Descostes, M., Phrommavanh, V., Nos, J. and Morris, K. 2014. Adsorption of radium and barium on goethite and ferrihydrite: a kinetic and surface complexation modelling study. Geochimica et Cosmochimica Acta,

146, 150-163.

Scott, S. and Ross, M. 2016. Quaternary stratigraphy and till provenance across the drumlinized terrain of the McArthur River uranium mine area in the Eastern Athabasca Basin. Poster originally presented at the Prospectors and Developers Association of Canada, Society of Economic Geologists Student Minerals Colloquium, Toronto, Ontario.

Silva, M., Kyser, K., Oates, C. and Beauchemin, D. 2007. Microwave-assisted continuous leaching on-line with inductively coupled plasma mass spectrometry for exploration and environmental geochemistry. Journal of Geochemical Exploration, 94(1), 30-42.

Stacey, J. T. and Kramers, 1. 1975. Approximation of terrestrial lead isotope evolution by a two-stage model. Earth and planetary science letters, 26(2), 207-221.

Tran, H. T., Ansdell, K. M., Bethune, K. M., Ashton, K. and Hamilton, M. A. 2008. Provenance and tectonic setting of Paleoproterozoic metasedimentary rocks along the eastern margin of Hearne craton: Constraints from SHRIMP geochronology, Wollaston Group, Saskatchewan, Canada. Precambrian Research, 167(1), 171-185.

van Geffen, P. W., Kyser, T. K., Oates, C. J. and Ihlenfeld, C. 2015. Evaluation of partial digestions for soils to detect a deeply buried VMS Cu-Zn prospect in boreal forests. Geochemistry: Exploration, Environment, Analysis, 15(1), 27-38.

Wallis, R. H., Saracoglu, N., Brummer, J. J., and Golightly, J. P. 1985. The geology of the McClean uranium deposits, northern Saskatchewan; in Sibbald, T.I.I. and Petruk, W. (eds.), Geology of Uranium Deposits, CIM Spec. Vol. 32, p101-131.

Whitney, D. L. and Evans, B. W. 2010. Abbreviations for names of rock-forming minerals. American mineralogist, 95(1), 185.

Wilde, A. R., Mernagh, T. P., Bloom, M. S. and Hoffmann, C. F. 1989. Fluid inclusion evidence on the origin of some Australian unconformity-related uranium deposits. Economic Geology, 84(6), 1627-1642.

Wilson, M. R. and Kyser, T. K. 1987. Stable isotope geochemistry of alteration associated with the Key Lake uranium deposit, Canada. Economic Geology, 82(6), 1540-1557.

Yeo, G., Jefferson, C. W. and Ramaekers, P. 2002. A preliminary comparison of Mantiou Falls Formation stratigraphy in Four Athabasca Basin Deposystems. Summary of Investigations, 2, 2002-4.

Yeo, G., Jefferson, C.W. and Ramaekers, P. 2007. Comparison of lower Athabasca Group stratigraphy among depositional systems, Saskatchewan and Alberta: Geological Survey of Canada, Bulletin 588, p. 465–488.

Chapter 4

Mineral Chemistry of Fracture Coatings in Athabasca Group Sandstones as Records of Elemental Dispersion from the Stewardson Lake Uranium Project

M. Valentino[1], T.K. Kyser[1], S.R. Beyer[1], L. Lahusen[2]

[1]Department of Geological Sciences and Geological Engineering, Queen's University, Kingston, ON;
[2]Uravan Mineral Incorporated, Calgary, AB

Abstract

The Stewardson Lake unconformity-related U project in the Athabasca Basin, Saskatchewan, Canada, contains elevated U concentrations (>100 ppm) at a depth of ~1100 meters in the lower Manitou Falls Formation sandstone of drill holes SL15-003 and SL15-004. In this study, the mineralogy and geochemistry of drill core fractures and adjacent wall rock from Stewardson Lake, were used to determine the paragenetic sequence and origin of minerals on and near fractures in the sandstone to determine if the minerals they host record elements associated with the U occurance at depth (~1100 m) and can be used to guide exploration.

Fracture orientations indicate that most fractures are moderately to steeply-dipping (<50°), allowing permeable pathways for fluid movement in the basin from below and above. Five types of fracture fillings were identified, representing distinct colors, mineralogies, and chemistry. These are white (type 1), drusy quartz (type 2), white and yellow (type 3), brown (type 4) and pink (type 5). White and yellow (type 3), brown (type 4), and pink (type 5) fractures host paragenetically late Fe oxides that variably replaced higher-temperature minerals (e.g. dickite in white (type 1) and white and yellow (type 3) fractures), which are rarely preserved on the fractures or in wall-rock near the fractures. Additionally, brown (type 4) and pink (type 5) fractures and their wall rock reflect the effect of post-mineralization dispersion fluids imprinted

on near-fractures with low $^{207}Pb/^{206}Pb$ values of 0.09-0.49 that were subsequently overprinted by a less radiogenic fluid recorded in the fractures with higher $^{207}Pb/^{206}Pb$ values of 0.50-0.82. White (type 1) fractures are the most indicative of mineralization through syn-mineralization dispersion, as shown by elevated concentrations of pathfinder elements Ni, Co and radiogenic Pb, both near the surface and at depth. Model Pb-Pb ages, from weak acid (2% HNO_3) leach, are 1529 +/- 440 Ma for fractures with chondrite-normalized LREE-enriched patterns ($[La/Yb]_n$ = 4.5-65.7) and 1115 +/- 370 Ma for fractures with flat REE patterns ($[La/Yb]_n$ = 2.0-17.0). The large errors on ages represent an open system, where exchange of Pb occurred, with post-mineralization dispersion of radiogenic Pb from a U-rich source. As such, fractures can be used to detect dispersion of elements, including radiogenic Pb from U mineralization at depth to intermediate levels. This indicates that the footprint of the U occurence extends upwards through some fracture networks.

4.1 Introduction

The Athabasca Basin is a Paleo- to Mesoproterozoic basin located in northern Saskatchewan and Alberta (Figure 4.1) that hosts significant U deposits near the unconformity between the Athabasca Group sandstone and underlying Paleoproterozoic and Archean metamorphic basement rocks (IAEA, 2009). These unconformity-related U deposits formed under reducing conditions near the unconformity, when a U-rich oxidizing basinal fluid interacted with reduced basement lithologies or a reducing basement fluid (Hoeve and Sibbald, 1978; Hoeve and Quirt, 1984; Wallis *et al*., 1985; Wilson and Kyser, 1987; Kotzer and Kyser, 1995; Fayek and Kyser, 1997) at temperatures around 200ºC. The ore-forming fluids produced alteration chimneys that can extend >300 m above the unconformity into the overlying sandstone, or more restricted zones in basement rocks surrounding the deposit (Hoeve and Quirt, 1984;

Clark, 1987; Leppin and Goldak, 2005; Cuney and Kyser, 2014). The alteration zones associated with unconformity-related U deposits can be used for exploration because they significantly enhance the footprint of the deposit by up to several hundred meters from the mineralization (Gustafson and Curtis, 1983; Hoeve and Quirt, 1984; Wilde *et al*., 1989).

The mineralogy and geochemistry of some alteration zones are related to two temporally distinct processes that are directly associated with the mineralizing system: (1) primary (syn-mineralization) and (2) secondary (post-mineralization) dispersion. Primary dispersion occurs during hydrothermal alteration associated with the mineralizing system, wherein elements are dispersed by fluids to the surrounding rocks, creating a dispersion halo around the deposit and along permeable fractures (McQueen, 2005). Secondary dispersion occurs when post-ore events such as hydrothermal, low-temperature meteoric, or microbial activity (Cameron *et al*., 2004) variably mobilize elements from the ore zone or surrounding alteration halo, facilitated by enhanced permeability of open fractures. For example, drusy quartz fracture coatings located in the Kombolgie Basin showed high $^{206}Pb/^{204}Pb$ values, suggesting that radiogenic Pb was being transported from the ore body through fractures (Holk *et al*., 2003). Additionally, elements mobilized by secondary dispersion processes can be adsorbed on Fe and Al oxy-hydroxide mineral coatings on open fractures that originate from fluids that flow down the fractures from the surface. These oxy-hydroxide phases typically have unsatisfied negative charges that are capable of attracting metal cations including elements that may be mobilized from the deposit, thereby trapping them on fracture surfaces during secondary dispersion from the deposit (e.g. Cameron *et al*., 2004). Fractures record both primary and secondary dispersion processes and are therefore critical in defining the footprint of the deposit and the possible processes by which elements in surface media can reflect the deposit at depth.

In this study, the mineralogy and geochemistry of coatings from fractures and adjacent

wall rock in the Athabasca Group sandstones above the Stewardson Lake U occurence are used to determine if fractures record U mineralization at depth and reflect dispersion processes. The purpose of this study is to investigate whether components within fractures from depth to surface may be related to a deposit and therefore constitute an effective exploration tool for U, as well as provide a mechanism to create anomalies in surface media.

4.2 Geological setting

4.2.1 Regional geology

The Athabasca Basin is an intracratonic basin located in northern Saskatchewan and Alberta (Figure 4.1), and covers an area greater than 85,000 km^2 (Ramaekers, 1990). The Paleo- to Mesoproterozoic basin unconformably overlies Archean and Paleoproterozoic basement composed of metamorphic and igneous rocks of the western Churchill Province (Figure 4.1), which is further divided into the Rae and Hearne Sub-Provinces. The western Churchill province is located between the remains of two orogenic belts, the Taltson magmatic zone and Thelon tectonic zone (*ca*. 1.9 Ga) and the Trans-Hudson Orogen (*ca*. 1.8 Ga) (Hoffman, 1988). On the south side of the basin, the contact between the Rae and Hearne Provinces is comprised by the Virgin River shear zones, and to the north, the Black Lake shear zones (Figure 4.1).

There are three domains within the Hearne Province that unconformably underlie the basin. From east to west these are the Wollaston domain, the Mudjatik domain and the Virgin River domains (Hoffman, 1988). The primary composition of the three domains is metamorphosed Archean and Paleoproterozoic granitoid, which is overlain by supracrustal metasedimentary sequences. Boundaries between the domains are defined by lithological, structural, and metamorphic grades (Lewry and Sibbald, 1980).

The circa 1700-1500 Ma Athabasca Group (Figure 4.1) consists of flat-lying, quartz-rich

sandstone and conglomerate, which was deposited in major river systems and near-shore to shallow-shelf environments (Ramaekers, 1990; Ramaekers, *et al*., 2007). Sedimentary basin fill has a maximum current thickness around 1.5 km deep, although temperature estimates from fluid inclusions suggest that these sequences reached depths of up to 5 km during peak diagenesis (Pagel *et al*., 1980). The units are cut by reactivated Hudsonian faults that are periodically active to the present day (Hoeve and Quirt, 1984; Kyser *et al*., 2000). The northwest-trending 1267 Ma Mackenzie dike swarm (LeCheminant and Heaman, 1989), also cuts through the sedimentary sequences of the Athabasca Basin and underlying basement rocks.

Four unconformity-bound stratigraphic sequences divide the Athabasca Group (Figure 4.1; Yeo *et al*., 2002; Ramaekers and Catuneanu, 2004; Ramaekers *et al*., 2007). In ascending order: 1) the Fair Point Formation; 2) the Smart and Manitou Falls formations, which make up the majority of the Athabasca Group (Ramaekers *et al*., 2007); 3) the Lazenby Lake and Wolverine Point formations, and 4) the Locker Lake, Otherside, Douglas, and Carswell formations (Ramaekers *et al*., 1979, 1980; Ramaekers, 1990). The samples used in this study were collected from the Manitou Falls and Lazenby Lake formations.

4.2.2 Manitou Falls Formation

The Manitou Falls Formation is divided into four members that, from youngest to oldest, are known as the MFd, MFc, MFb and MFa (Figure 4.1; Ramaekers, 1990). Members a, b, and c consist of clastic sediments deposited primarily within alluvial fans (MFa) and high energy proximal braided streams (MFa, MFb, MFc) (Ramaekers, 1990), whereas the MFd reflects deposition in distal portions of a braided stream, such as an estuary or a braided delta setting (Hiatt and Kyser, 2007).

The MFa is composed of interbedded matrix-supported quartz pebble conglomerate and

well-to-poorly-sorted, medium-grained sandstone, accompanied by minor hematitic siltstone beds (Ramaekers, 1990). MFb consists of medium-grained sandstone with significant poorly-sorted and clast-supported conglomerate sandstone (Ramaekers, 1990). MFc contains sandstone that has conglomerate beds less than 2 cm thick and less than 1% clay intraclasts (Ramaekers, 1990). The MFd is gradational over the MFc and is composed of well-sorted sandstone with greater than 1% clay intraclast-rich layers (Ramaekers, 1990). In the MFd, bedded siltstone and mudstone can occur up to 5 cm thick (Ramaekers, 1990). This study uses nomenclature from Ramaekers (1990) to remain consistent with historical literature and current exploration terminology.

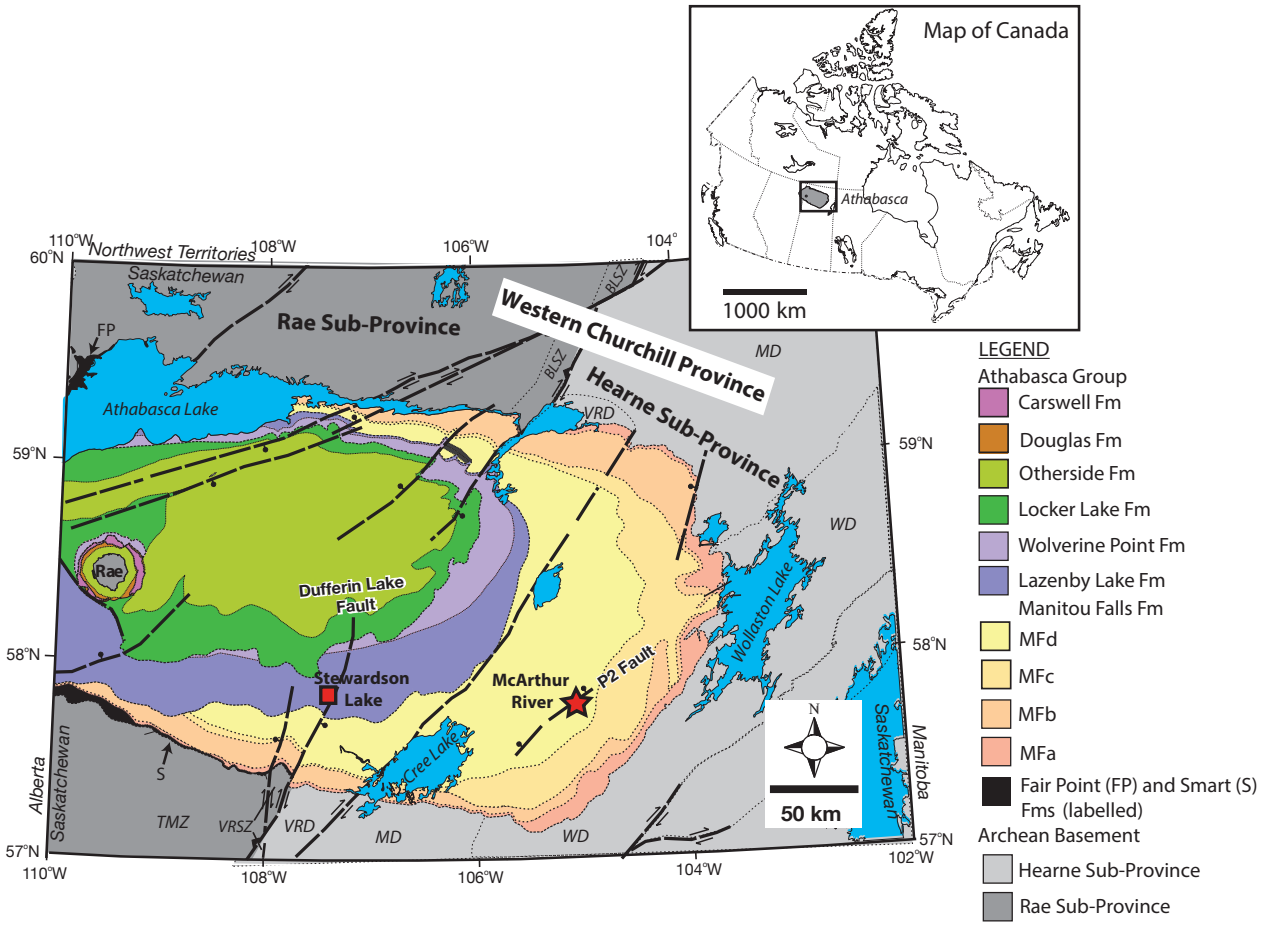

Figure 4.1: Geological map of the Athabasca Basin, highlighting basement provinces (grey; names in bold), fault structures (dashed lines) such as the Dufferin Lake Fault, stratigraphic sections of the Athabasca Group, the Stewardson Lake project (red square), and the McArthur River deposit (red star). Figure modified from Ng *et al.* (2013). Domain abbreviations: VRD = Virgin River, MD = Mudjatik, WD = Wollaston. Shear/magmatic zones: BLSZ = Black Lake shear zone, VRSZ = Virgin River shear zone, TMZ = Taltson magmatic zone.

4.2.3 Stewardson Lake unconformity-related U project

The Stewardson Lake area is a U project currently under exploration by Uravan Minerals Inc. and is located on the Virgin River Shear Zone in the south-central area of the Athabasca Basin, ~180 km west of the world-class McArthur River unconformity-related U deposit (Figure 4.1). Sedimentary units at surface within the Stewardson Lake area include the Lazenby Lake Formation and the underlying Manitou Falls Formation (as described in previous chapters), which overlies the unconformity at Stewardson Lake. The sedimentary package of sediment is greater than 800 m thick and overlies the crystalline basement rocks (felsic gneiss, metavolcanic rocks and graphitic pelitic schist) of the Virgin Schist Group along the Virgin River Shear Zone (Leppin and Goldak, 2005). Ramaekers *et al*. (2007) suggested that the Lazenby Lake Formation represents a shallow marine shoreface depositional environment, with overturned trough cross-bedding within the sequence caused by syn-sedimentary deformation. Three upward-fining cycles of fine- to coarse-grained pebbly quartz arenites with rare clay intraclasts and interbedded mudstone and minor conglomerates occur within the Lazenby Lake Formation (Ramaekers *et al*., 2007).

A 2014 soil geochemical survey, and a conductor (named, the E conductor) defined by a superconducting quantum interference device time-domain electromagnetics (SQUID TDEM) survey identified a target for two drill holes (SL14-001 and SL14-002; Figure 4.2) (Uravan Minerals Inc., 2014). Drill hole SL14-002 also targeted the intersection of a pronounced lineament, defined by z-axis tipper electromagnetic (ZTEM) survey, and the trace of the E conductor. Both drill holes intersected the unconformity, SL14-001 at 1162.03 m and SL14-002 at 1198.0 m (Uravan Minerals Inc., 2014). A fault zone is present directly above the unconformity in the sandstones and is characterized by silicification, desilicification, rubbly recovery, and dravite clay gouge. Basal sandstone from 1170.0 m – 1198.0 m is chloritic

immediately above the unconformity and overlain by an illitic horizon, which has elevated U concentrations (up to 8.1 ppm), Ni, Co, Zn, and radiogenic Pb (Uravan Minerals Inc., 2014).

The Stewardson Lake area was also investigated by drill holes SL15-003 and SL15-004 (Figure 4.2 and 4.3) as follow-up to geophysics and surface geochemical sampling surveys. Drill holes SL15-003 and SL15-004 intersect alteration chimneys that extend greater than 300 m into the sandstone above the unconformity and exhibit bleaching and distinct hematite-chlorite alteration within the MFa (Uravan Minerals Inc., 2017). This bleaching is associated with fracturing, associated with post-sandstone basement fault reactivation, which extends from the basement to the overlying sandstone. Bleaching is also associated with elevated concentrations of pathfinder elements such as U, Ni, Co, Mg, and radiogenic Pb (Uravan Minerals Inc., 2017). The basal 30 m of the MFa in drill hole SL15-003 also hosts fracture-controlled hydrothermal alteration and bleaching including secondary hematite, green chlorite, dravite, kaolinite, and silicification (Uravan Minerals Inc., 2017). This unit also contains smoky quartz veins, elevated U concentrations (>100 ppm), and highly radiogenic Pb ($^{207}Pb/^{206}Pb$ values of ~0.14) (Uravan Minerals Inc., 2017).

The Lazenby Lake Formation and the upper Manitou Falls Formation (MFd-MFb) in drill holes SL15-003 and SL15-004 include a background diagenetic mineral assemblage of hematite and an illite-dominated clay mineral assemblage. Faulting and fracturing that occurred in these stratigraphic sections are associated with bleaching, drusy quartz, chlorite, and kaolinite. Basement rocks at SL15-003 are phyllites interbedded with iron formations (Virgin Schist Group), whereas in SL15-004, basement rocks are mainly felsic gneisses (Uravan Minerals Inc., 2017).

The Stewardson Lake property overlies two strands of the NE-SW trending Dufferin Lake reverse fault. Reactivation of the Dufferin Lake fault (Figure 4.1) occurred after the basin formed

and is characterized by 300 m vertical offset (Leppin and Goldak, 2005). A north-northeast trending antiform has been refolded along the northwest axial planes of the basement rocks in the strain zone; at the limbs of the antiform, graphite is enriched structurally (Leppin and Goldak, 2005). Uranium occurrences are known at saddle structures within the fold arrangement and are typically associated with kaolinite, dravite and chlorite hydrothermal alteration halos (Leppin and Goldak, 2005).

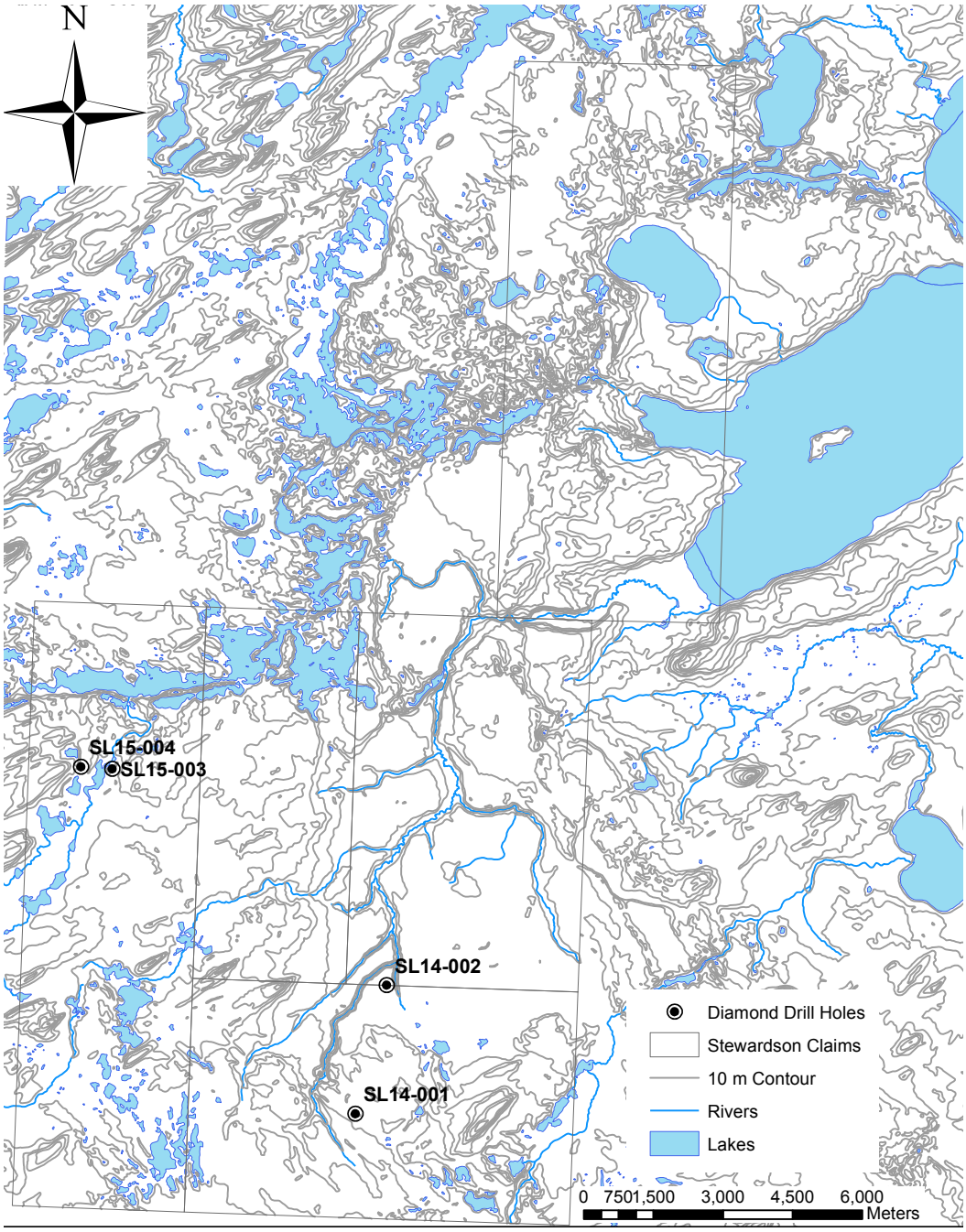

Figure 4.2: Map view of the Stewardson Lake area, highlighting drill holes SL14-001, SL14-002, SL15-003, and SL15-004.

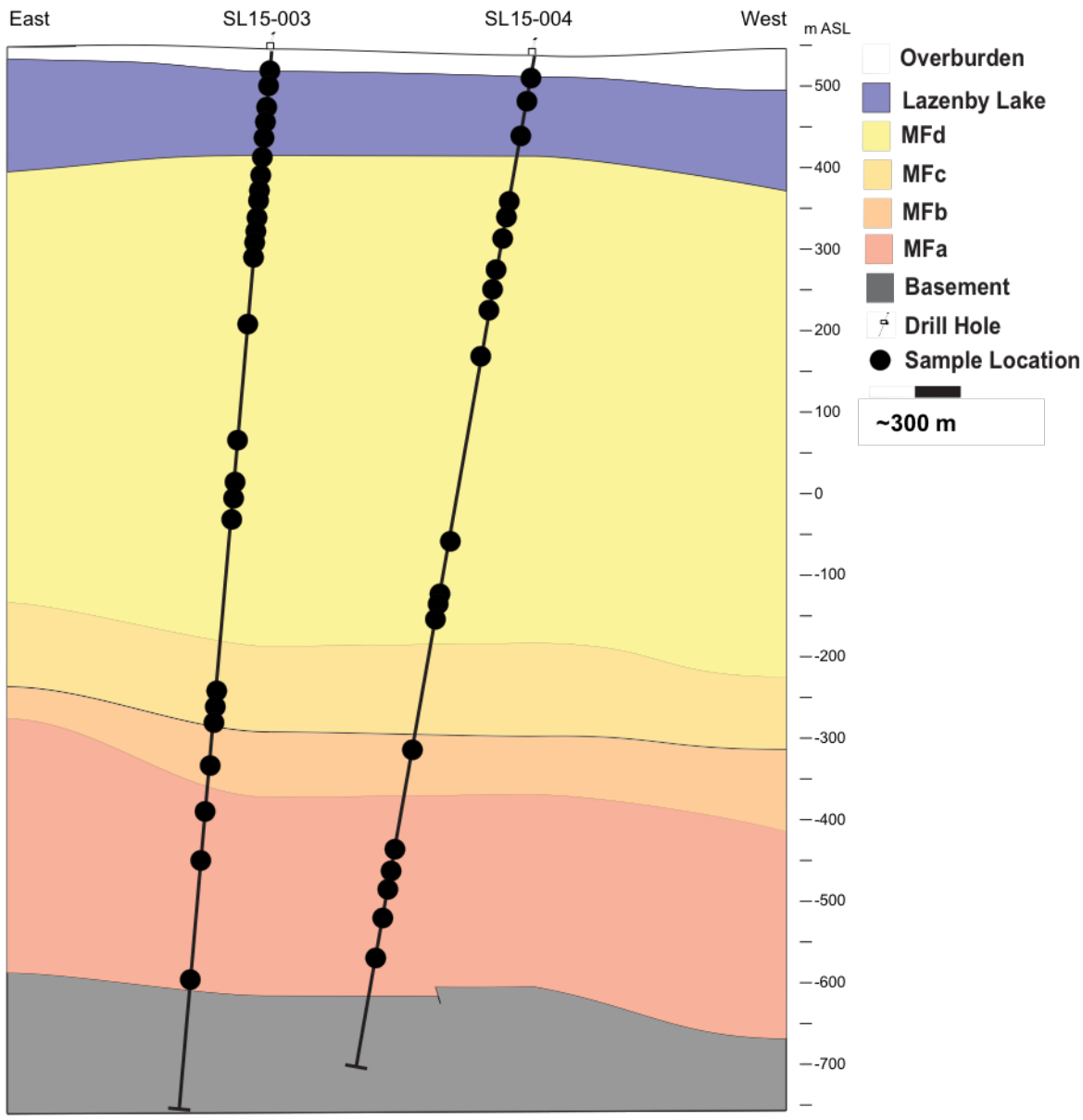

Figure 4.3: Cross section of the Stewardson Lake area (Figure 4.1), showing the two drills holes where the fractures for this study were collected. Figure modified from Uravan Minerals Corporate Website (2017).

The Athabasca sandstones and conglomerates that constitute the Stewardson Lake area presently consist of *ca*. 95% quartz (+ minor heavy minerals) and 0-5% matrix minerals by volume (Kotzer and Kyser, 1995; Hiatt *et al*., 2007). Early diagenesis of the basin formed quartz overgrowths, an APS (aluminum-phosphate-sulphate) mineral, and hematite on detrital quartz of

the Manitou Falls Formation (Kotzer and Kyser, 1993, 1995; Derome *et al*., 2005). The Aluminum-Phosphate-Sulphate (APS) group mineral is associated with the hydrothermal clay and silicate minerals that comprise the alteration halo of U deposits in the basin (Cuney and Kyser, 2014). Kotzer and Kyser (1995) used increasing $\delta^{18}O$ values, increasing salinities, and homogenization temperatures in fluid inclusions of diagenetic quartz to indicate that continued water interactions modified the basinal fluids, and to some extent, basement fluids, chemically and isotopically. Prior to interaction of fluids along fractures, illite and dickite were produced throughout the entire basin by alteration of detrital sheet silicate minerals during peak diagenesis of the Athabasca Group (Percival, 1993; Kotzer and Kyser, 1995; Laverret *et al*., 2006). Therefore, the predominant clay assemblage of the Athabasca Group is dickite (+/- kaolinite) +/- illite (Hoeve and Quirt, 1984).

4.3 Methods

Open fracture surfaces host fracture coatings, which are used as the primary criteria for classifying fractures in this study. The near-fracture area is adjacent to the fracture, and is considered to represent a local background signature or a prior fluid event for that fracture, or an alteration selvedge. 121 fractures were initially collected at Stewardson Lake from drill holes SL15-003 and SL15-004, and a subset of forty-five fractures were selected for more detailed study. Abbreviations of minerals throughout the text and figures are those of Whitney and Evans (2010).

Fracture types were classified based on color, mineralogy and geochemistry of fracture coatings and adjacent wall rock. The orientation (α) relative to vertical of fractures (degrees TCA) was used to establish pathways for fluid movement and the migration of elements from

depth to surface and vice versa. Petrography was done on fracture coatings using a Leica E24D microscope for reflected and transmitted light optical petrography to document mineralogy, grain size and color. A section of fracture surface was mounted on a sample stub for scanning electron microscopy (SEM) to assist in determining the mineralogy and paragenesis of each fracture coating using a FEI Quanta 650 FEG ESEM equipped with a back-scatter detector (BSED) and two Bruker XFlash Si-Drift energy dispersive spectrometers (EDS). Analyses were conducted at a voltage of 25 kV and a spot size of 4 in low vacuum mode at a chamber pressure of 0.45 torr.

A separate aliquot of fracture coating was removed as a fine powder from the fracture surface using a dental drill for geochemistry by weak acid leach (WAL), a technique to leach mobile elements with 2% HNO_3, following a similar method described by Holk *et al*. (2003) (Table 4.1). The WAL was also conducted to document the chemical changes between the near-fracture and fracture coating. The wall rock was isolated from the fracture surface using a diamond rock saw; samples were crushed using a ceramic jaw crusher, and sieved to 0.5-1.18 mm. Leach solutions were analyzed using a Thermo Scientific Element II XR HR-ICP-MS to determine major and trace element concentrations, and Pb isotope ratios including $^{207}Pb/^{206}Pb$, $^{208}Pb/^{206}Pb$, $^{206}Pb/^{204}Pb$, $^{207}Pb/^{204}Pb$ and $^{208}Pb/^{204}Pb$. A list of parameters used by the Thermo Scientific Element II XR HR-ICP-MS are specified in appendix D.

Table 4.1: Sample preparation summary for WAL.

Method	Amount of sample (g)	Acid added (mL)	Reaction time (hr)	Acid removed (mL)	Dilution (g)
Dental drill	0.1	2	2 at 44°C	1	5
Crusher	0.5	2	2 at 44°C	1	10

Shortwave infrared (SWIR) reflectance spectra were collected on the open fracture face and on the side of the core sample using an ASD Inc. Terraspec 4 instrument with a contact probe analyzer having a 10 mm spot diameter, a 100 ms scanning time, and a 3-10 μm spectral resolution across a wavelength range of 350-2500 nm to characterize the clay mineralogy. The data were interpreted using MinSpec4 software (Earle, 1997, *et al*., 1999), which reports relative abundances (%) of illite, chlorite, dickite, kaolinite, and dravite as well as signal-to-noise ratios (Appendix E). Spectra having signal-to-noise ratios of less than 10 are here considered inaccurate and omitted.

4.4 Results

4.4.1 Fracture characteristics

Fracture coatings from Stewardson Lake were grouped into five types using a similar fracture classification to that established on fractures at the McArthur River unconformity-related U deposit (Figure 4.1; Chapter 2 and 3), based on color, mineralogy and chemistry. All fracture types reflect minerals that were formed on the fracture surface and are normally visible in hand specimen.

Type 1 (white) is the most abundant fracture type at Stewardson Lake (20 samples) and is composed of pyrite and white clay (Figure 4.4), including illite, dravite and kaolinite. Type 2 is

the second most abundant fracture type (11 samples) and consists of drusy quartz, the crystals of which are commonly surrounded by pyrite (Figure 4.5), siderite, illite, dravite and chlorite. Type 3 fractures are white and yellow (8 samples) and are rich in Fe oxides, consisting of yellow limonite crusts (Figure 4.6), and siderite, illite and dickite. Type 4 fractures are brown-stained (4 samples) and rich in Fe oxides (Figure 4.7), typically including hematite and limonite. The final fracture type, Type 5, is pink (2 samples from Stewardson Lake) with illite, kaolinite and Fe oxide (Figure 4.8). Therefore, major fracture coating minerals at Stewardson Lake include clays (kaolinite, dravite, illite, chlorite and dickite), Fe oxides of limonite and hematite, siderite, pyrite and drusy quartz.

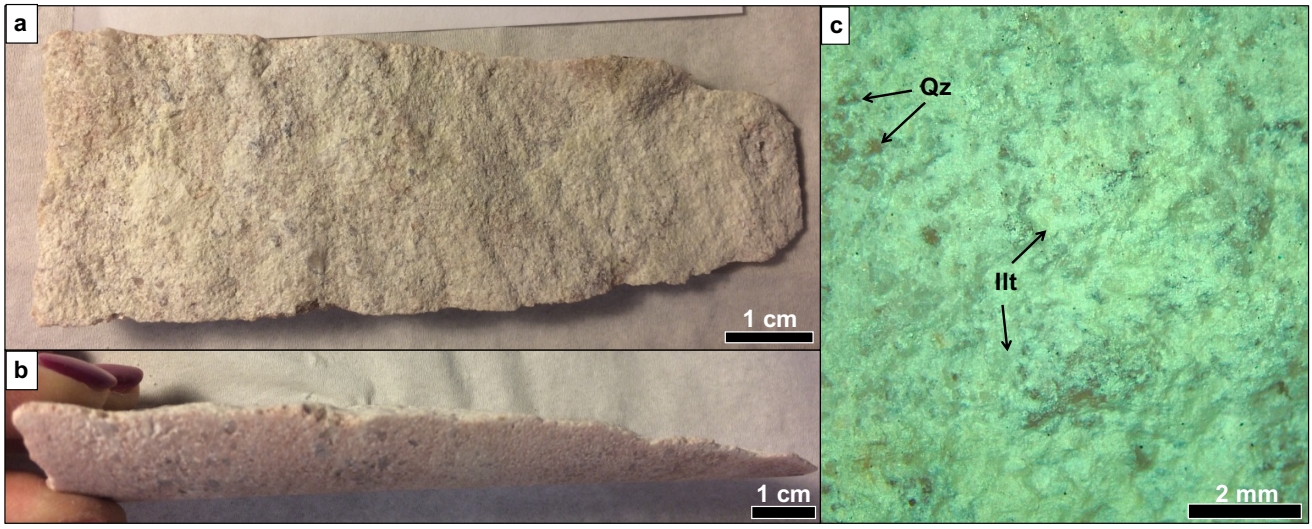

Figure 4.4: Type 1 – White fracture coating (SL3F-036), showing the (a) open fracture face, (b) fracture orientation, and (c) optical mineralogy in plain light.

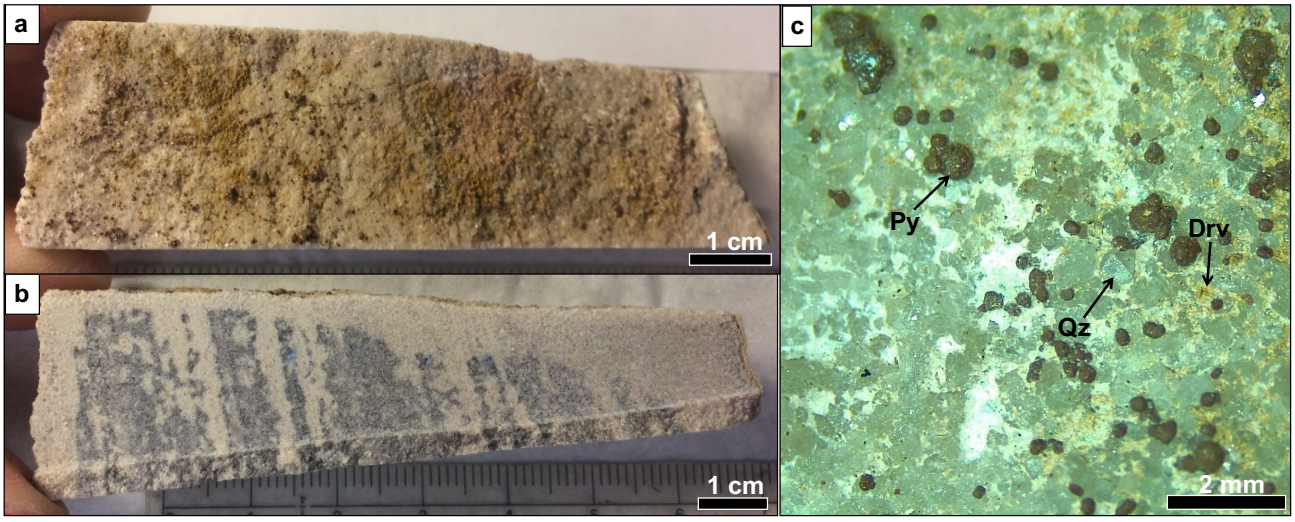

Figure 4.5: Type 2 – Drusy quartz fracture coating (SL3F-026), showing the (a) open fracture face, (b) fracture orientation, and (c) optical mineralogy in plain light.

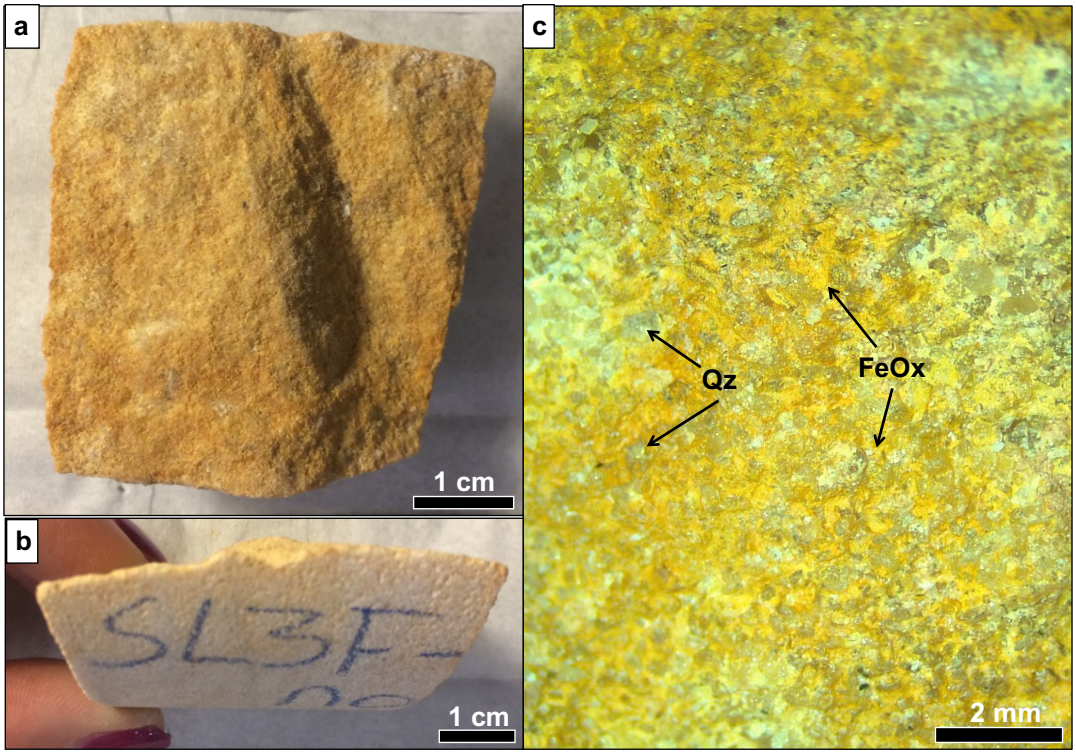

Figure 4.6: Type 3 – White and yellow fracture coating (SL3F-004), showing the (a) open fracture face, (b) fracture orientation, and (c) optical mineralogy in plain light.

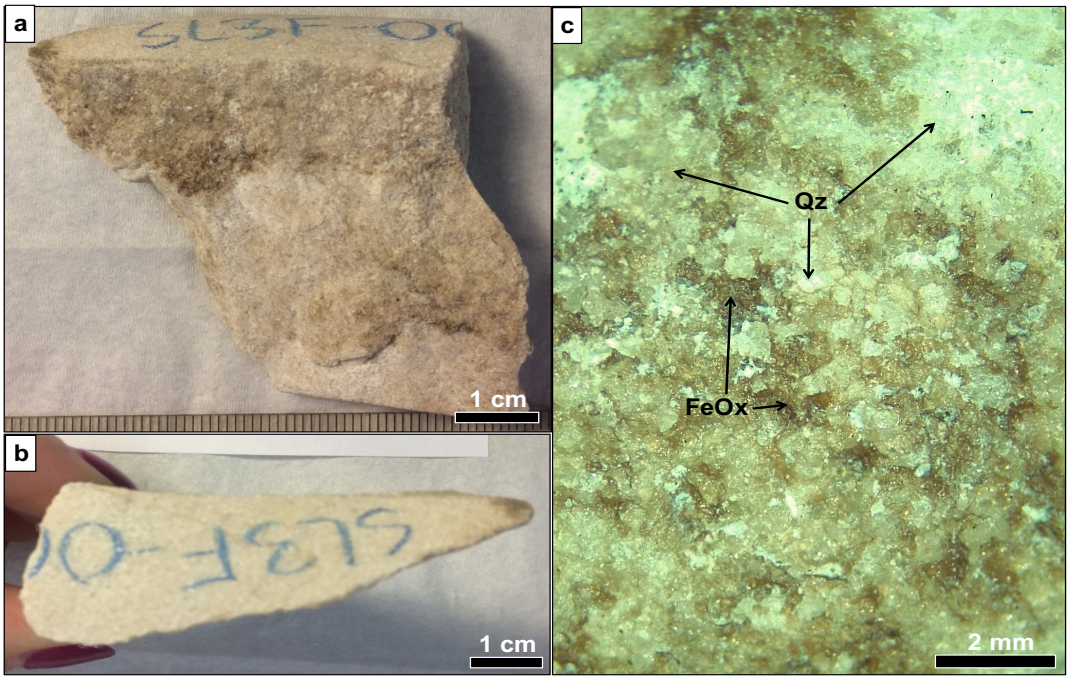

Figure 4.7: Type 4 - Brown fracture coating (SL3F-006), showing the (a) open fracture face, (b) fracture orientation, and (c) optical mineralogy in plain light.

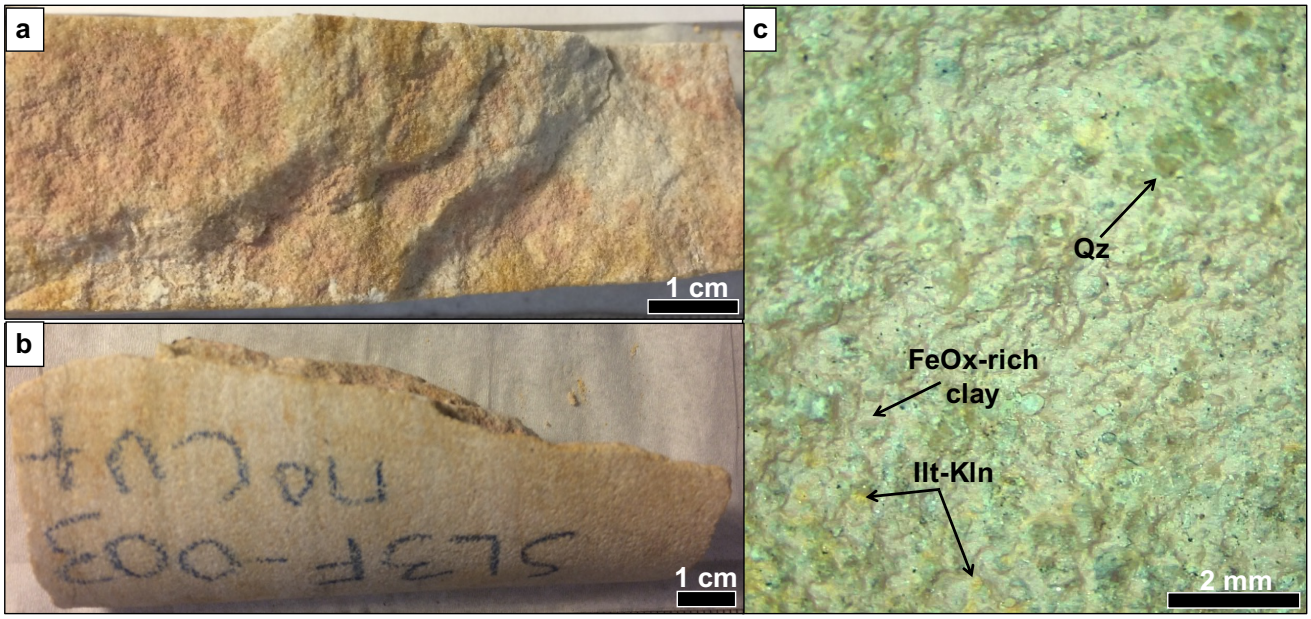

Figure 4.8: Type 5 – Pink fracture coating (SL3F-003), showing the (a) open fracture face, (b) fracture orientation, and (c) optical mineralogy in plain light.

All investigated fracture coatings at Stewardson Lake were found within the Manitou Falls and Lazenby Lake formations. The shallowest sample represents a true vertical depth of ~30

m, the deepest sample at ~1138 m (Figure 4.9). The horizontal extent of the sampling area is ~1000 m from SL15-003 to SL15-004 (Figure 4.2 and 4.3). Type 3 (white and yellow) fractures occur at intermediate levels from the MFd to the surface. Brown (type 4) and pink (type 5) fractures mainly occur close to the surface, whereas type 1 (white) and type 2 (drusy quartz) fracture types occur at all depths.

Samples from drill holes SL14-001 and SL14-002 (Figure 4.2) are considered to represent a local background signature of the Lazenby Lake and Manitou Falls formations at Stewardson Lake. Fractures in this area include white (type 1), drusy quartz (type 2), white and yellow (type 3), brown (type 4), and pink types, which are rich in illite.

Fracture orientations at Stewardson Lake occur primarily at shallow angles of less than 50° relative to core axis (Table 4.2; Figure 4.10b), providing sub-vertical permeable pathways for fluid movement. A smaller subset of fractures, including two type 1 white fractures, were found to dip at 55° and 90° (Figure 4.10a); these fractures samples occur at intermediate depths of 618 m.

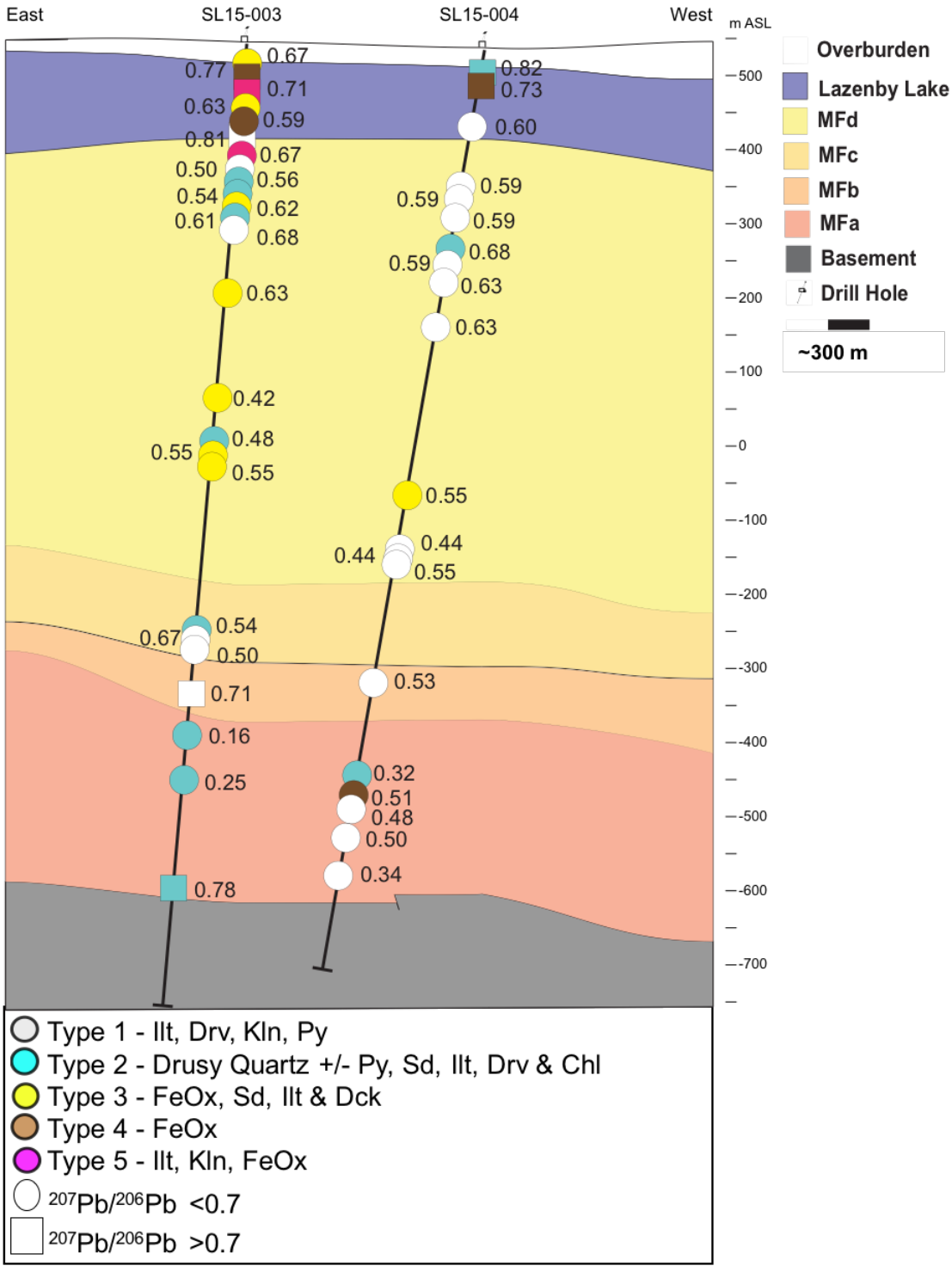

Figure 4.9: Cross-section across the Dufferin Lake fault at Stewardson Lake (Figure 4.1) showing the location of fracture samples in the Manitou Falls and Lazenby Lake formations, highlighting the fracture type, and $^{207}Pb/^{206}Pb$ values. Figure modified from Uravan Minerals Corporate Website (2017).

Table 4.2: Depth, drill hole attitude, type, and orientation relative to vertical of fractures from Stewardson Lake.

Sample ID	Drill Hole ID	Depth (m)	Drill Hole Dip (°)	Fracture Type	Fracture Orientation (α)
SL3F-001	SL15-003	30	-85	3 - White & Yellow	15
SL3F-002	SL15-003	40	-85	4 - Brown	40
SL3F-003	SL15-003	52	-85	5 - Pink	25
SL3F-004	SL15-003	58	-85	3 - White & Yellow	5
SL3F-006	SL15-003	80	-85	4 - Brown	10
SL3F-008	SL15-003	124	-85	1 - White	5
SL3F-009	SL15-003	139	-85	5 - Pink	40
SL3F-010	SL15-003	143	-85	1 - White	45
SL3F-011	SL15-003	153	-85	2 - Drusy Quartz	
SL3F-013	SL15-003	172	-85	2 - Drusy Quartz	
SL3F-014	SL15-003	183	-85	3 - White & Yellow	15
SL3F-017	SL15-003	231	-85	2 - Drusy Quartz	40
SL3F-018	SL15-003	244	-85	1 - White	25
SL3F-022	SL15-003	321	-85	3 - White & Yellow	15
SL3F-023	SL15-003	447	-85	3 - White & Yellow	15
SL3F-026	SL15-003	506	-85	2 - Drusy Quartz	15
SL3F-029	SL15-003	532	-85	3 - White & Yellow	7
SL3F-030	SL15-003	541	-85	3 - White & Yellow	
SL3F-034	SL15-003	792	-85	2 - Drusy Quartz	10
SL3F-035	SL15-003	797	-85	1 - White	
SL3F-036	SL15-003	803	-85	1 - White	20
SL3F-039	SL15-003	861	-85	1 - White	13
SL3F-043	SL15-003	935	-85	2 - Drusy Quartz	
SL3F-044	SL15-003	975	-85	2 - Drusy Quartz	
SL3F-048	SL15-003	1141	-85	2 - Drusy Quartz	
SL4F-001	SL15-004	43	-80	2 - Drusy Quartz	10
SL4F-004	SL15-004	71	-80	4 - Brown	30
SL4F-008	SL15-004	128	-80	1 - White	25
SL4F-010	SL15-004	180	-80	1 - White	10
SL4F-011	SL15-004	194	-80	1 - White	10
SL4F-012	SL15-004	200	-80	1 - White	10
SL4F-014	SL15-004	242	-80	2 - Drusy Quartz	20
SL4F-015	SL15-004	256	-80	1 - White	18
SL4F-016	SL15-004	271	-80	1 - White	12
SL4F-020	SL15-004	350	-80	1 - White	14
SL4F-034	SL15-004	573	-80	3 - White & Yellow	20
SL4F-035	SL15-004	618	-80	1 - White	30
SL4F-036	SL15-004	618	-80	1 - White	55
SL4F-037	SL15-004	618	-80	1 - White	90
SL4F-042	SL15-004	838	-80	1 - White	22
SL4F-046	SL15-004	955	-80	2 - Drusy Quartz	20
SL4F-050	SL15-004	991	-80	3 - Brown	15
SL4F-053	SL15-004	999	-80	1 - White	17
SL4F-058	SL15-004	1067	-80	1 - White	30
SL4F-066	SL15-004	1142	-80	1 - White	23

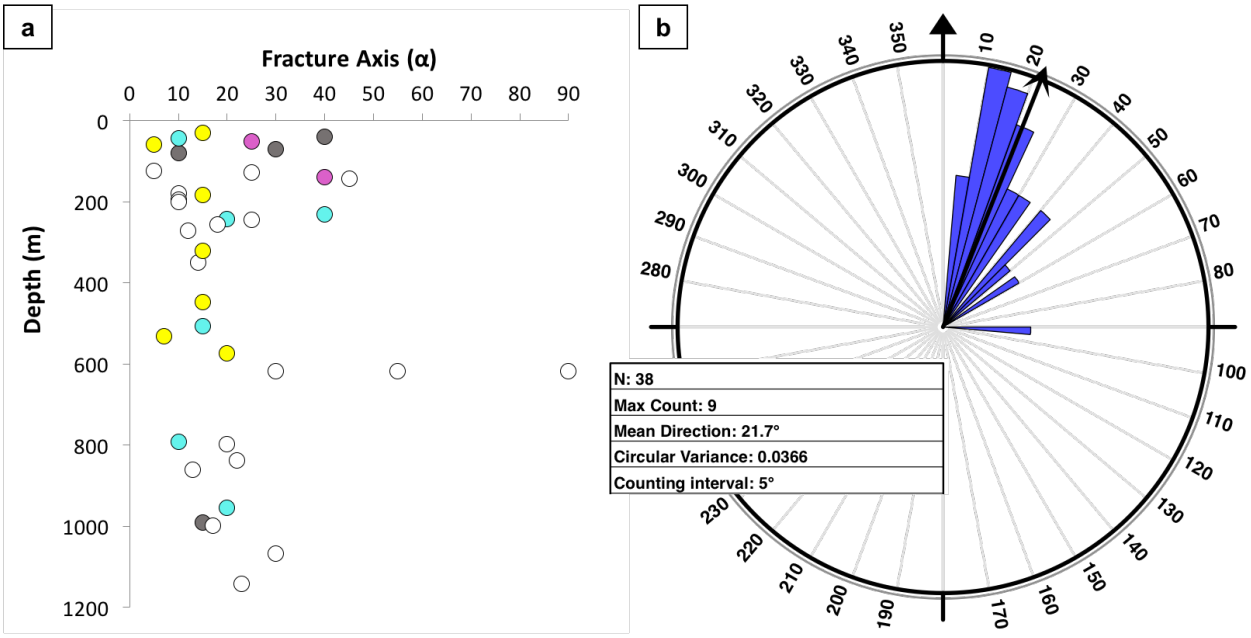

Figure 4.10: a) Orientation relative to vertical of fractures (α) versus depth (m), showing various fracture types. See Figure 4.9 for legend. b) Rose diagram of fracture orientations, highlighting the mean fracture orientation of 21.7° relative to vertical.

4.4.2 Mineral Paragenesis

A generalized paragenetic sequence of fracture coating minerals at Stewardson Lake was formulated using visible examination and SEM-BSE images and EDS spectra. The paragenetic sequence is similar to the paragenetic relationships derived by Kotzer and Kyser (1995) and Fayek and Kyser (1997). There are two origins of mineral formation on the fracture coatings, which are interpreted to be hydrothermal alteration and late meteoric events (Figure 4.11).

Acicular alkali-deficient dravite grains and euhedral quartz (Figure 4.12a) follows the earlier hydrothermal alteration minerals dickite, illite, and chlorite. Dravite primarily occurs in the hydrothermal alteration halos as intergrowths contemporaneously with euhedral quartz (Q1) filling fractures within the MFd (Kotzer and Kyser, 1995; Ng *et al*., 2013), for drusy quartz (type

2) fracture types. Euhedral quartz is present as ~0.5 mm thick crystals and is observed in drusy quartz (type 2) fractures from the unconformity to the surface.

Hydrothermal mineral assemblages were subsequently altered and variably overprinted by minerals formed from late meteoric fluids that precipitated kaolinite in fractures, as previously documented by Kotzer and Kyser, (1995). Kaolinite can be associated with Fe oxides and oxy-hydroxides present as a pink (Fe oxides) powder (kaolinite) in pink (type 5) fractures and as limonite crusts or stain in white and yellow (type 3) and brown (type 4) fractures. Kaolinite can also be associated with ~50-500 μm bladed to tabular siderite crystals (Figure 4.12b, c), which occur in drusy quartz (type 2) and white and yellow (type 3) fracture types. Siderite can also be associated with <10 mm globular pyrite in drusy quartz (type 2) fractures.

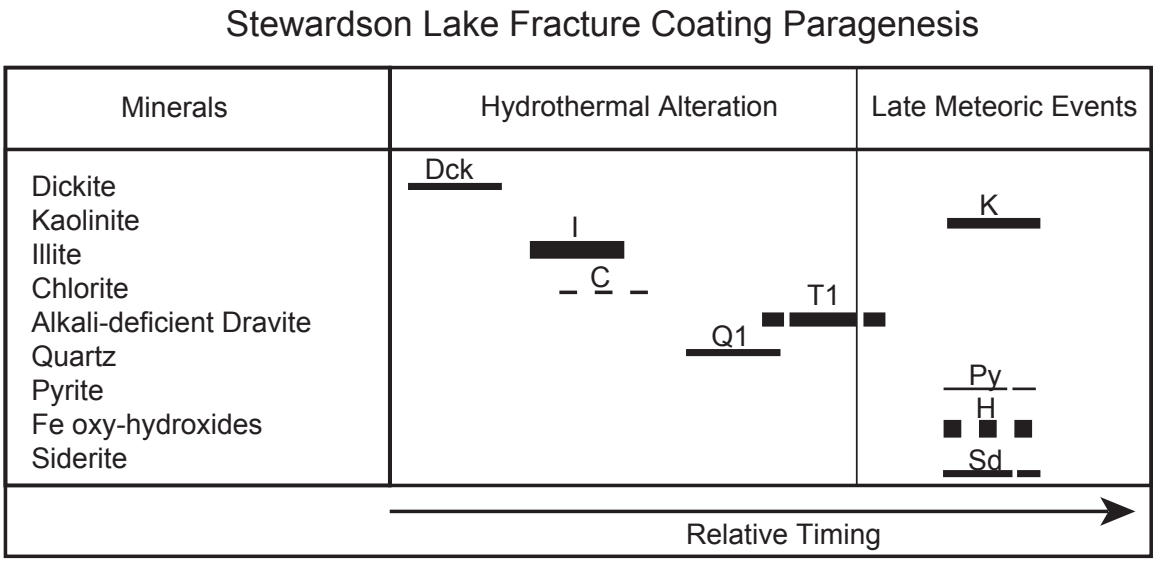

Figure 4.11: Generalized paragenetic sequence of fracture coatings from the Stewardson Lake project. The thickness of the line represents the relative abundance of each mineral and the dashed lines represent uncertainty in the timing of mineral formation. Figure modified from Kotzer and Kyser (1995) and Fayek and Kyser (1997).

Figure 4.12: BSE images showing mineral assemblages of a drusy quartz (type 2) fracture coating (SL3F-043) within the Stewardson Lake MFa sandstone. a) Euhedral quartz followed by acicular dravite grains, overlaid with siderite. b) Euhedral quartz followed by bladed to tabular siderite crystals. c) Siderite precipitation on dravite and euhedral quartz.

4.4.3 Pb isotope ratios

White (type 1), and drusy quartz (type 2) show similarities in $^{207}Pb/^{206}Pb$ values between the fracture coating and near-fracture in proximity to the Dufferin Lake fault (Figure 4.13; Table 4.3). Most white and yellow (type 3) fractures show a similar trend, but at an intermediate distance (360-760 m) from the Dufferin Lake fault. As distance increases from the Dufferin Lake fault, $^{207}Pb/^{206}Pb$ values are increasingly different between the near-fracture and fracture coating for all fracture types, reflecting low $^{207}Pb/^{206}Pb$ values on the near-fracture and high $^{207}Pb/^{206}Pb$ values on the fracture coating. This effect is most prominent for brown (type 4) and pink (type 5) fractures near the surface. If the fracture fill and the wall rock had been altered by the same fluid, they should have the same Pb isotopic composition, as is recorded by types 1, 2 and 3, nearest the Dufferin Lake fault. The fracture types 4 and 5 that are further from the Dufferin Lake fault and from shallower depth tend to have more radiogenic Pb in the wall rock relative to the fracture fill suggesting that the fill records elements that have not been dispersed from the deposit or that more recent fluids have either replaced or overprinted earlier formed minerals, like those in the wall rocks.

Table 4.3: Uranium concentrations and $^{207}Pb/^{206}Pb$ values, from WAL, of fracture coatings and near-fractures at Stewardson Lake. SL3F and SL4F indicate drill holes SL15-003 and SL15-004, respecitively.

Sample ID	Depth (m)	U (ppm) (Fracture Coating)	$^{207}Pb/^{206}Pb$ (Fracture Coating)	$^{207}Pb/^{206}Pb$ (Near-Fracture)
Stewardson Lake				
SL3F-001	30	0.14	0.67	0.10
SL3F-002	40	0.58	0.77	0.09
SL3F-003	52	0.27	0.71	0.12
SL3F-004	58	0.58	0.63	0.09
SL3F-006	80	0.69	0.59	0.15
SL3F-008	124	0.07	0.81	0.12
SL3F-009	139	0.16	0.67	0.10
SL3F-010	143	0.56	0.50	0.34
SL3F-011	153	0.61	0.56	0.23
SL3F-013	172	1.07	0.54	0.31
SL3F-014	183	0.86	0.62	0.46
SL3F-017	231	0.03	0.61	0.50
SL3F-018	244	0.07	0.68	0.68
SL3F-022	321	0.18	0.63	0.45
SL3F-023	447	7.60	0.42	0.40
SL3F-026	506	7.62	0.48	0.49
SL3F-029	532	1.24	0.55	0.43
SL3F-030	541	10.37	0.55	0.37
SL3F-034	792	0.87	0.54	0.43
SL3F-035	797	0.19	0.67	0.35
SL3F-036	803	0.37	0.50	0.47
SL3F-039	861	0.40	0.71	0.42
SL3F-043	935	154.48	0.16	0.19
SL3F-044	975		0.25	0.24
SL3F-048	1141	2.46	0.78	0.21
SL4F-001	43	1.23	0.82	0.36
SL4F-004	71	0.11	0.73	0.63
SL4F-008	128	0.19	0.60	0.55
SL4F-010	180	0.11	0.59	0.59
SL4F-011	194	0.24	0.59	0.59
SL4F-012	200	0.07	0.59	0.59
SL4F-014	242	0.16	0.68	0.67
SL4F-015	256	0.07	0.59	0.59
SL4F-016	271	0.13	0.63	0.65
SL4F-020	350	0.95	0.63	0.66
SL4F-034	573	2.37	0.55	0.54
SL4F-035	618	2.27	0.44	0.44
SL4F-036	618	1.59	0.44	0.46
SL4F-037	618	2.33	0.55	0.49
SL4F-042	838	0.09	0.53	0.48
SL4F-046	955	14.54	0.32	0.32
SL4F-050	991	11.34	0.51	0.51
SL4F-053	999	3.00	0.48	0.48
SL4F-058	1067	0.60	0.50	0.48
SL4F-066	1142	1.18	0.34	0.31

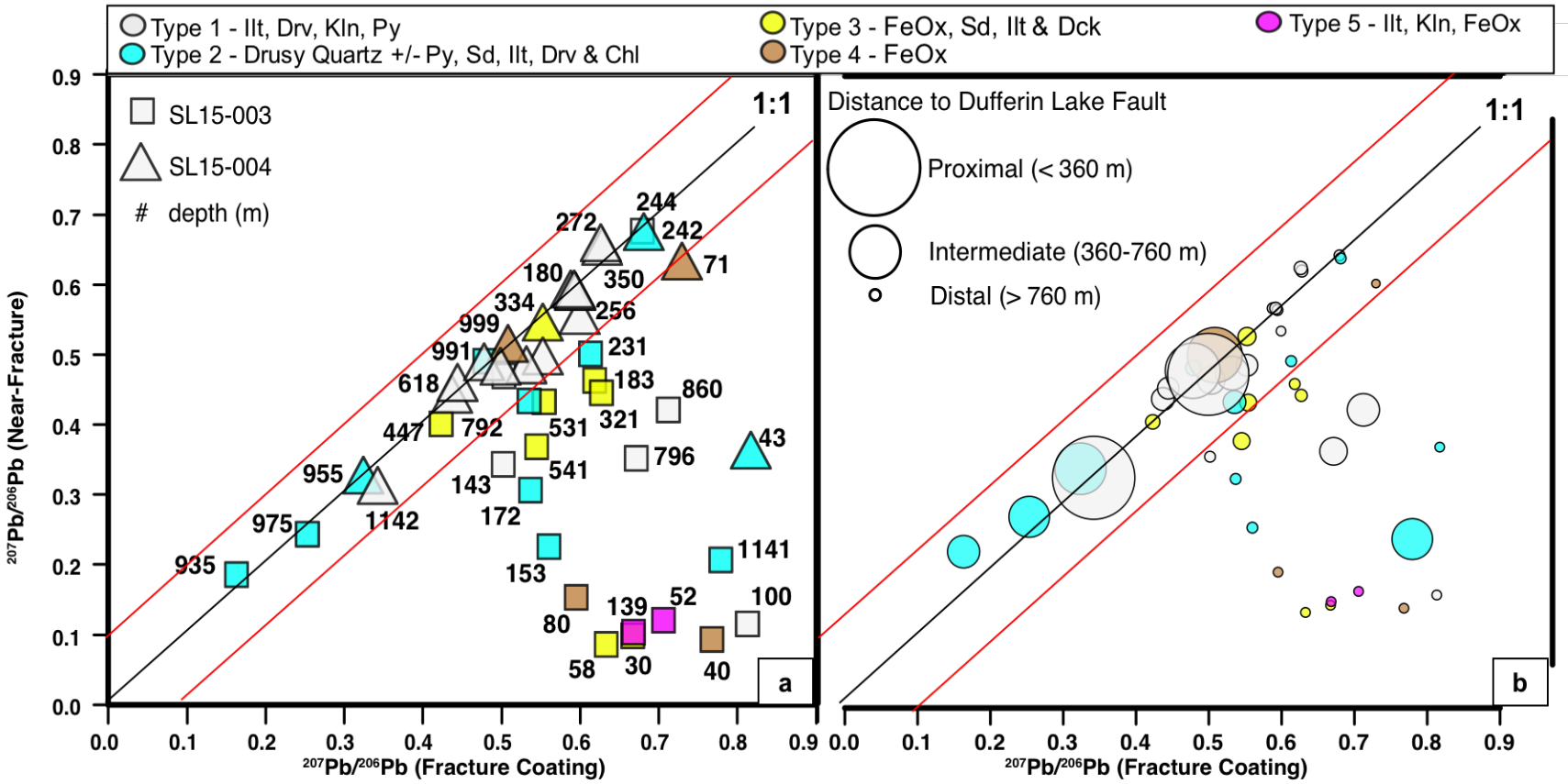

Figure 4.13: a) $^{207}Pb/^{206}Pb$ isotope values of fracture coatings versus the near-fracture surface wall-rock samples from various depths at Stewardson Lake, and b) with symbol size proportional to distance from the Dufferin Lake fault, approximated by using Figure 4.9. Numbers next to symbols refer to depth of the sample and red lines are 2σ errors around the line of equal ratios of material in the fractures and the material adjacent to the fracture.

4.4.4 Model Ages and REE patterns

Rare earth element (REE) patterns and Pb isotopes from weak acid leaching of forty-five fracture coatings (Table 4.4), were used to group the fracture types. Weak acid leach was used rather than *aqua regia* or total digestion to target mobile phases precipitated and absorbed on fracture coatings. Two chondrite-normalized REE patterns are observed; which are Group 1) light REEs (LREEs)-enriched, and Group 2) flat (Figure 4.14). Calculated Pb-Pb isotope model ages for each of the two patterns are based on the two-stage Pb evolution model of Stacey and Kramers (1975). This two-stage model describes the evolution of Pb that began with primordial isotope ratios 4.57 Ga years ago in a reservoir having uniform $^{238}U/^{204}Pb$ and $^{232}Th/^{204}Pb$ values (Faure, 1977).

Group 1 is composed of clay-rich (type 1), drusy quartz (type 2) and oxide-rich (type 3) fracture coatings, showing LREE enrichment (Figure 4.14a) and an imprecise Pb-Pb model age of 1529 +/- 440 Ma (Figure 4.14b). Group 2 consists of additional clay-rich (type 1, type 5) and oxide-rich (type 3, type 4) fracture types, as well as drusy quartz (type 2) fracture coatings, showing a flat REE pattern (Figure 4.14c) and an imprecise Pb-Pb model age of 1115 +/- 370 Ma (Figure 4.14d).

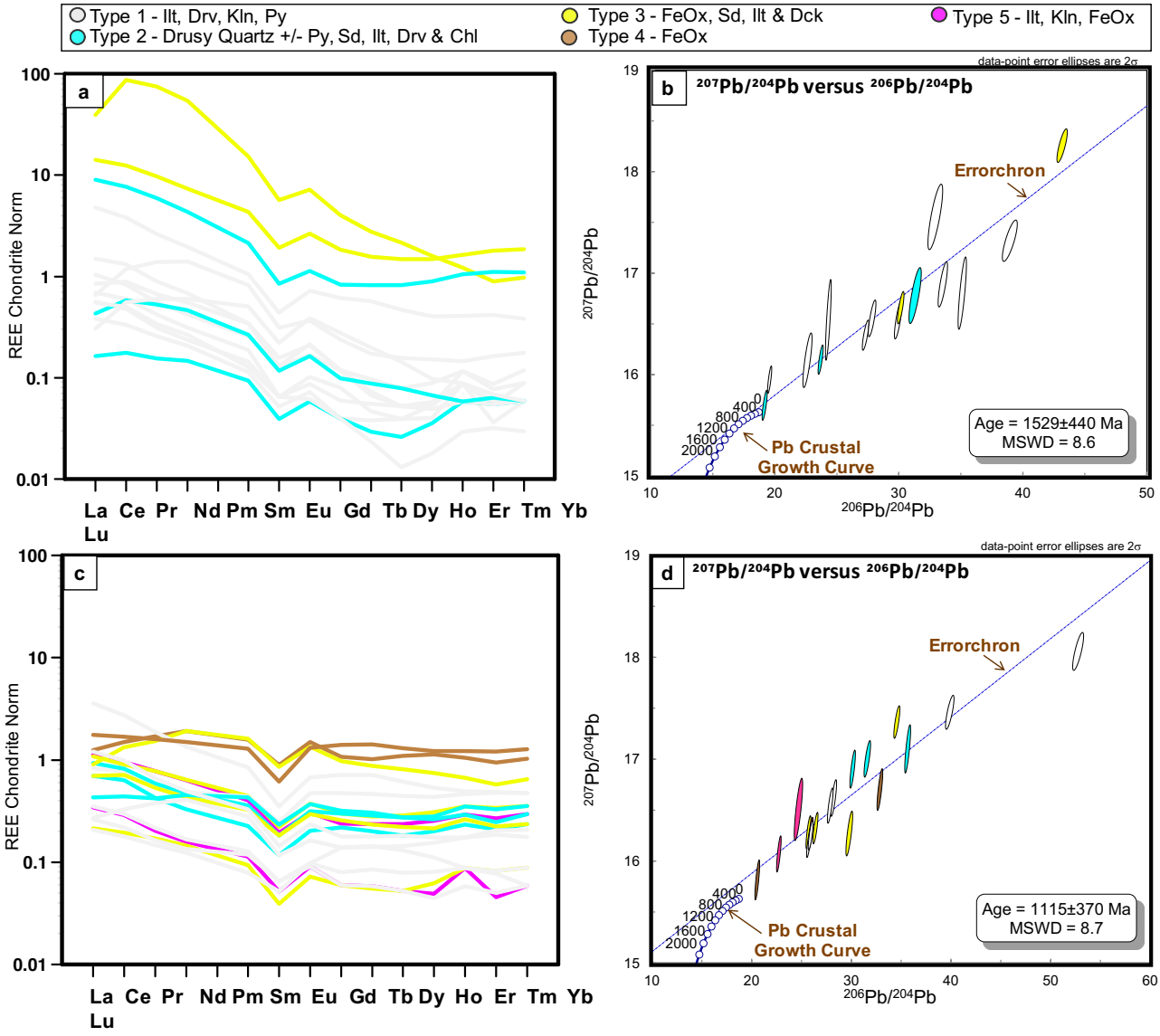

Figure 4.14: a) Chondrite-normalized (Nakamura, 1974) LREE enriched patterns of clay-rich (type 1), drusy quartz (type 2), and oxide-rich (type 3) fracture types obtained from weak acid leaching; b) relationship between $^{207}Pb/^{204}Pb$ and $^{206}Pb/^{204}Pb$ values and model age of fracture coatings for Group 1; c) flat REE patterns of additional clay-rich (type 1, type 5) and oxide-rich (type 3, type 4) fracture types, and drusy quartz (type 2) fractures; d) relationship between $^{207}Pb/^{204}Pb$ and $^{206}Pb/^{204}Pb$ values and model age of fracture coatings for Group 2.

Table 4.4: REE concentrations, U concentrations, and $^{207}Pb/^{204}Pb$, $^{206}Pb/^{204}Pb$, and $^{238}U/^{206}Pb$ values from WAL analyses of fractures from Stewardson Lake. SL3F and SL4F indicate drill holes SL15-003 and SL15-004, respecitively.

Sample ID	La (ppm)	Ce (ppm)	Pr (ppm)	Nd (ppm)	Sm (ppm)	Eu (ppm)	Gd (ppm)	Tb (ppm)	Dy (ppm)	Ho (ppm)	Er (ppm)	Tm (ppm)	Yb (ppm)	Lu (ppm)	U (ppm)	$^{207}Pb/^{204}Pb$	$^{206}Pb/^{204}Pb$	$^{238}U/^{206}Pb$
SL3F-001	0.32	0.97	0.10	0.40	0.08	0.01	0.06	0.01	0.04	0.01	0.02	0.00	0.02	0.00	0.14	17.42	26.10	0.38
SL3F-002	0.41	1.29	0.22	1.21	0.32	0.07	0.41	0.05	0.35	0.08	0.25	0.04	0.21	0.03	0.58	15.82	20.60	1.16
SL3F-003	0.37	0.82	0.10	0.40	0.08	0.01	0.08	0.01	0.08	0.02	0.06	0.01	0.06	0.01	0.27	16.07	22.76	1.83
SL3F-004	0.35	0.78	0.10	0.40	0.09	0.02	0.10	0.02	0.10	0.02	0.07	0.01	0.08	0.01	0.59	16.29	25.73	1.20
SL3F-006	0.28	0.75	0.10	0.42	0.09	0.02	0.08	0.01	0.05	0.01	0.02	0.00	0.02	0.00	0.69	17.26	29.00	4.86
SL3F-008	0.28	0.76	0.09	0.35	0.07	0.01	0.06	0.01	0.02	0.00	0.01	0.00	0.01	0.00	0.07	15.95	19.61	0.02
SL3F-009	0.11	0.25	0.03	0.10	0.02	0.00	0.02	0.00	0.02	0.00	0.01	0.00	0.01	0.00	0.16	16.51	24.73	4.36
SL3F-010	0.27	0.67	0.07	0.31	0.09	0.02	0.13	0.02	0.16	0.03	0.10	0.02	0.11	0.02	0.56	17.37	34.61	0.90
SL3F-011	0.23	0.55	0.05	0.21	0.05	0.01	0.06	0.01	0.07	0.01	0.04	0.01	0.05	0.01	0.61	16.91	30.17	3.25
SL3F-013	0.31	0.71	0.08	0.30	0.07	0.01	0.09	0.02	0.10	0.02	0.06	0.01	0.07	0.01	1.07	17.01	31.65	1.11
SL3F-014	0.23	0.62	0.07	0.27	0.07	0.01	0.08	0.01	0.08	0.02	0.05	0.01	0.05	0.01	0.86	16.33	26.44	2.61
SL3F-017	0.04	0.10	0.01	0.05	0.01	0.00	0.01	0.00	0.01	0.00	0.00	0.00	0.00	0.00	0.03	18.89	30.81	0.22
SL3F-018	0.13	0.29	0.03	0.13	0.02	0.00	0.02	0.00	0.01	0.00	0.01	0.00	0.01	0.00	0.07	16.54	24.35	0.30
SL3F-022	0.07	0.17	0.02	0.09	0.02	0.00	0.02	0.00	0.02	0.00	0.01	0.00	0.02	0.00	0.18	16.27	25.94	0.49
SL3F-023	12.94	75.36	9.70	34.09	3.12	0.44	1.99	0.20	0.95	0.16	0.36	0.04	0.20	0.03	7.60	18.26	43.21	4.40
SL3F-026	0.14	0.38	0.05	0.29	0.09	0.02	0.10	0.02	0.10	0.02	0.06	0.01	0.05	0.01	7.62	17.10	35.70	1.13
SL3F-029	0.19	0.72	0.10	0.44	0.07	0.01	0.08	0.01	0.07	0.02	0.04	0.01	0.03	0.01	1.24	16.28	29.40	57.51
SL3F-030	0.30	1.15	0.20	1.20	0.33	0.07	0.37	0.05	0.30	0.06	0.17	0.02	0.13	0.02	10.37	16.28	29.84	60.85
SL3F-034	0.05	0.15	0.02	0.09	0.02	0.00	0.02	0.00	0.01	0.00	0.01	0.00	0.01	0.00	0.87	16.78	31.35	6.89
SL3F-035	0.48	1.14	0.12	0.43	0.07	0.01	0.06	0.01	0.02	0.00	0.01	0.00	0.01	0.00	0.19	20.62	30.73	1.40
SL3F-036	0.23	0.52	0.05	0.20	0.04	0.00	0.03	0.00	0.02	0.00	0.01	0.00	0.02	0.00	0.37	16.89	33.58	0.00
SL3F-039	0.49	1.14	0.12	0.43	0.07	0.01	0.06	0.01	0.03	0.00	0.01	0.00	0.01	0.00	0.40	16.15	22.67	2.15
SL3F-043	1.06	6.16	1.07	5.36	1.06	0.18	0.60	0.05	0.22	0.03	0.07	0.01	0.05	0.01	154.48	22.31	136.75	104.02
SL3F-044	0.64	2.36	0.34	1.43	0.18	0.02	0.08	0.01	0.04	0.01	0.01	0.00	0.01	0.00		21.65	85.68	0.00
SL3F-048	0.08	0.17	0.02	0.08	0.02	0.00	0.02	0.00	0.01	0.00	0.01	0.00	0.01	0.00	2.47	16.62	21.34	0.95
SL4F-001	2.96	6.67	0.77	2.72	0.43	0.06	0.31	0.04	0.28	0.06	0.20	0.04	0.24	0.04	1.23	15.70	19.21	1.99
SL4F-004	0.08	0.18	0.02	0.09	0.02	0.00	0.02	0.00	0.01	0.00	0.01	0.00	0.01	0.00	0.11	17.28	23.70	1.43
SL4F-008	0.34	0.72	0.07	0.27	0.05	0.01	0.05	0.01	0.03	0.01	0.02	0.00	0.02	0.00	0.19	16.39	27.35	0.11
SL4F-010	0.40	0.85	0.08	0.31	0.07	0.01	0.07	0.01	0.06	0.01	0.04	0.01	0.04	0.01	0.11	16.55	27.92	0.01
SL4F-011	0.09	0.19	0.02	0.09	0.02	0.01	0.03	0.00	0.03	0.01	0.02	0.00	0.02	0.00	0.24	16.62	28.27	0.08
SL4F-012	0.19	0.41	0.04	0.15	0.03	0.00	0.02	0.00	0.02	0.00	0.01	0.00	0.01	0.00	0.07	16.56	27.88	0.03
SL4F-014	0.14	0.50	0.07	0.29	0.05	0.01	0.04	0.01	0.03	0.01	0.02	0.00	0.01	0.00	0.16	16.15	23.72	0.36
SL4F-015	0.01	0.04	0.01	0.04	0.02	0.01	0.03	0.01	0.04	0.01	0.02	0.00	0.02	0.00	0.07	16.55	27.95	0.03
SL4F-016	0.11	0.25	0.03	0.11	0.03	0.00	0.02	0.00	0.02	0.00	0.01	0.00	0.01	0.00	0.13	16.18	25.77	0.25
SL4F-020	0.09	0.28	0.05	0.26	0.06	0.01	0.05	0.01	0.05	0.01	0.04	0.01	0.04	0.01	0.95	16.26	25.96	1.75
SL4F-034	4.67	10.75	1.25	4.65	0.88	0.15	0.73	0.09	0.54	0.11	0.33	0.06	0.40	0.06	2.37	16.66	30.19	0.75
SL4F-035	1.18	2.36	0.24	0.85	0.17	0.03	0.19	0.04	0.24	0.05	0.12	0.02	0.11	0.02	2.27	17.46	39.92	2.55
SL4F-036	0.10	0.48	0.08	0.38	0.10	0.02	0.11	0.01	0.07	0.01	0.02	0.00	0.01	0.00	1.60	17.32	38.99	0.85
SL4F-037	1.57	3.29	0.34	1.23	0.21	0.03	0.20	0.03	0.19	0.04	0.09	0.01	0.09	0.01	2.33	16.54	29.98	5.00
SL4F-042	0.18	0.43	0.04	0.17	0.03	0.00	0.02	0.00	0.01	0.00	0.00	0.00	0.01	0.00	0.09	17.56	32.98	0.76
SL4F-046	7.92	46.11	7.15	31.20	4.21	0.78	2.46	0.22	0.88	0.13	0.23	0.02	0.11	0.02	14.54	17.28	53.33	9.72
SL4F-050	0.58	1.46	0.21	0.94	0.26	0.05	0.36	0.07	0.49	0.10	0.28	0.04	0.27	0.04	11.34	16.71	32.91	6.19
SL4F-053	0.21	1.02	0.18	0.88	0.17	0.02	0.10	0.01	0.06	0.01	0.03	0.01	0.04	0.01	3.00	16.81	35.15	1.87
SL4F-058	0.10	0.21	0.02	0.08	0.01	0.00	0.01	0.00	0.01	0.00	0.00	0.00	0.00		0.60	19.81	39.72	3.94
SL4F-066	0.07	0.15	0.02	0.08	0.02	0.00	0.03	0.01	0.05	0.01	0.02	0.00	0.02	0.00	1.18	18.06	52.81	3.32

4.4.5 Pathfinder elements

Typical pathfinder elements of unconformity-related U deposits include As, Co, Cu, Mo, Ni, and S (Cuney and Kyser, 2014; Table 4.5; Figure 4.15). Enrichments of these elements mainly occur in white (type 1) fractures at ~200 m and ~600-800 m in SL15-003 and SL15-004 drill holes (e.g. SL3F-010: Ni = 101.8 ppm, S = 3914 ppm), which commonly host clay minerals and pyrite. White and yellow (type 3) fractures show elevated concentrations of Ni and S (up to 73.7 and 884 ppm, respectively) at ~600 m, whereas drusy quartz (type 2) fractures show increased concentrations of Co (up to 42.7 ppm) at ~900 m, and Ni and S (up to 44.5 and 526 ppm, respectively) at ~200 m. Brown (type 4) and pink (type 5) fractures show low concentrations of pathfinder elements similar to background values (Figure 4.15).

Table 4.5: Concentrations of pathfinder elements As, Co, Cu, Mo, Ni, and S, from WAL extraction of fractures from Stewardson Lake.

Sample ID	Depth (m)	As (ppm)	Co (ppm)	Cu (ppm)	Mo (ppm)	Ni (ppm)	S (ppm)
Stewardson Lake							
SL3F-001	30	0.06	34.8	2.0	0.02	3.6	1
SL3F-002	40	0.73	10.0	5.0	0.02	10.3	1
SL3F-003	52	0.04	6.0	2.2	0.03	3.6	1
SL3F-004	58	0.11	2.5	3.7	0.00	1.6	10
SL3F-006	80	1.75	20.2	3.2	0.01	4.4	79
SL3F-008	124	0.12	36.9	1.1	0.58	16.6	24
SL3F-009	139	0.24	3.1	0.4	0.04	1.5	397
SL3F-010	143	5.94	8.8	4.3	1.74	101.8	3914
SL3F-011	153	0.03	3.0	1.4	0.22	44.5	10
SL3F-013	172	0.32	7.7	0.5	0.60	19.6	526
SL3F-014	183	0.01	14.0	1.8	0.04	3.5	3
SL3F-017	231	0.04	8.3	0.1	0.00	0.2	7
SL3F-018	244	0.02	5.2	0.2	0.01	0.2	6
SL3F-022	321	0.01	1.0	0.1	0.02	1.2	5
SL3F-023	447	0.17	2.4	1.7	0.03	8.7	315
SL3F-026	506	0.09	0.7	1.8		2.7	42
SL3F-029	532	0.01	1.5	0.0	0.01	73.7	4
SL3F-030	541		1.8	0.6	0.01	21.7	
SL3F-034	792	0.02	0.9	0.0	0.01	0.3	39
SL3F-035	797	0.09	17.3	0.6	0.01	0.5	18
SL3F-036	803	2.72	50.6	0.7	0.52	40.6	14
SL3F-039	861	0.09	109.7	0.5	0.05	0.9	3
SL3F-043	935	0.03	2.5	0.3	0.00	4.3	2
SL3F-044	975	0.02	1.7	0.2	0.05	3.9	5
SL3F-048	1141	0.05	29.1	1.1	0.24	2.9	13
SL4F-001	43	0.11	6.7	3.9	0.18	11.3	
SL4F-004	71	0.28	7.0	0.6	0.02	1.6	55
SL4F-008	128	0.20	22.3	1.8	0.75	29.3	53
SL4F-010	180	3.71	18.0	3.5	2.40	69.1	1699
SL4F-011	194	2.47	6.6	1.0	1.00	8.2	1262
SL4F-012	200	5.47	36.6	0.6	2.21	8.3	828
SL4F-014	242	0.09	9.9	0.7	0.43	10.4	5
SL4F-015	256	0.14	0.1	0.2	0.01	0.3	199
SL4F-016	271	0.02	20.6	1.2	0.06	5.5	5
SL4F-020	350	0.03	1.2	0.2	0.03	3.7	121
SL4F-034	573	3.32	2.0	1.0	0.08	15.9	884
SL4F-035	618	0.04	2.6	3.7	0.02	0.6	1
SL4F-036	618	0.12	0.0	10.9	0.09	0.5	8
SL4F-037	618	0.05	0.2	4.3	0.01	0.7	3
SL4F-042	838	0.07	19.6	1.0	0.02	1.2	32
SL4F-046	955	0.31	42.7	1.9	0.05	3.3	40
SL4F-050	991	0.02	0.0	0.4		0.6	5
SL4F-053	999	0.03	1.0	0.1	0.11	1.5	3
SL4F-058	1067	0.08	10.1	1.0	0.01	0.9	4
SL4F-066	1142	0.02	0.0	0.2		0.6	1

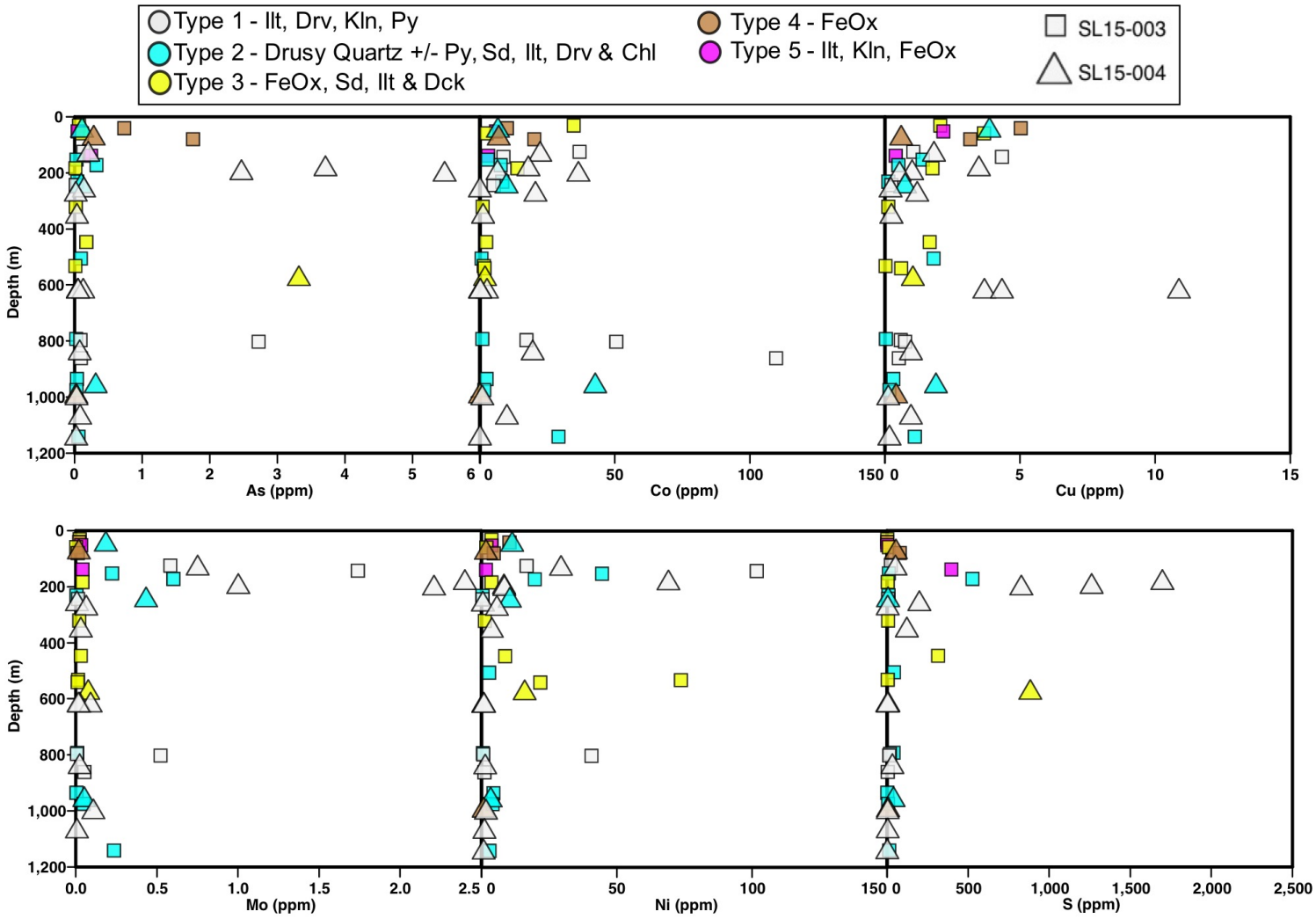

Figure 4.15: Relationship between depth and concentration of As, Co, Cu, Mo, Ni, and S for fracture fill from Stewardson Lake extracted using WAL.

4.5 Discussion

4.5.1 Fracture mineralogy

Five fracture types at Stewardson Lake were identified in this study and vary with depth (Figure 4.9). A petrographic context of fracture coatings at Stewardson Lake allows a better understanding of the fluids involved that formed fracture coatings minerals (Figure 4.11) as well as a comparison to the chemistry of the adjacent wall rock (Figure 4.13). Dickite formed at temperatures above *ca*. 130 °C in the Athabasca Basin from diagenetic basinal fluids (Kotzer and Kyser, 1995) and was likely overprinted by a diagenetic-hydrothermal fluid from later hydrothermal alteration, precipitating dickite on fracture fillings fluids in white (type 1) and white and yellow (type 3) fractures. Illite followed by drusy quartz (type 2) and dravite precipitated on fracture surfaces from hydrothermal fluids, as they are associated with the hydrothermal alteration in areas of intense fracturing and can be part of the late-ore forming system (Hoeve and Quirt, 1984; Halter *et al*., 1989; Kotzer and Kyser, 1995). Late influx of meteoric fluids likely variably overprinted these minerals with Fe oxides and kaolinite in white and yellow (type 3), brown (type 4) and pink (type 5) fracture types, suggesting that some fractures have had protracted fluid histories.

4.5.2 Pb isotopes

Uraninite and coffinite are unstable geochemically in surficial environments and are easily altered by meteoric fluids (Dyck, 1978; Baadsgaard *et al*., 1984; Kotzer and Kyser, 1995). This geochemical instability makes establishing a reliable age of initial emplacement for U deposits and determining the timing of the fluids mobilizing U challenging. Uranium deposits contain ^{238}U and ^{235}U that decay to daughter products of ^{206}Pb and ^{207}Pb at a known rate (Holk *et*

al., 2003). The decay of U isotopes does not affect ^{204}Pb, the stable isotope of Pb. Thus, ^{206}Pb/^{204}Pb and ^{207}Pb/^{204}Pb values will reflect the initial U/Pb values and time in a system (Holk *et al*., 2003). In open systems such as basins having structurally-hosted U deposits like the Athabasca Basin, the ^{206}Pb/^{204}Pb value away from the deposit will be elevated if either radiogenic Pb or U are mobilized from the deposit, depending on the timing of the mobilization (Holk *et al*., 2003).

Leaching of fracture coatings and near-fractures were conducted because it has been shown that ^{207}Pb/^{206}Pb isotopes can be used as a vector for unconformity-related U deposits in the Athabasca Basin (Holk *et al*., 2003; Cloutier *et al*., 2009; Alexandre *et al*., 2012). Five fracture types including white (type 1), drusy quartz (type 2), white and yellow (type 3), brown (type 4), and pink (type 5) fractures have variable ^{207}Pb/^{206}Pb values (Figure 4.9). Low ^{207}Pb/^{206}Pb values occur throughout the depth profile, but the lowest values (0.16-0.32) are typically associated with drusy quartz (type 2) fractures in the MFa in proximity to the Dufferin Lake fault and are representative of syn-mineralization dispersion (SL15-003 and SL15-004; Figure 4.9). White (type 1) fractures also show low ^{207}Pb/^{206}Pb values near the unconformity (0.34) and within the MFd (0.44-0.59) with U concentrations of ~2 ppm, and are interpreted to result from syn-mineralization dispersion. White and yellow (type 3) fractures suggest post-mineralization dispersion of radiogenic Pb due to their low ^{207}Pb/^{206}Pb values (0.42-0.63) in the MFd and commonly low U concentrations (<1 ppm). However, limited white and yellow (type 3) fractures suggest syn-mineralization dispersion due to low ^{207}Pb/^{206}Pb values (0.42-0.55) and higher U concentrations greater than background values (>1 ppm) within the MFd of drill hole SL15-003. Other fracture types including brown (type 4) and pink (type 5) are more representative of a background signature, due to higher ^{207}Pb/^{206}Pb values (>0.7), indicating common Pb, and low U concentrations at background values (<1 ppm), similar to drill holes SL14-001 and SL14-002.

Measured $^{206}Pb/^{204}Pb$ and $^{207}Pb/^{204}Pb$ values are elevated throughout the Manitou Falls Formation above the Stewardson Lake U occurence, consistent with post-mineralization dispersion of radiogenic Pb from a uraniferous source. The significant errors of all model ages indicate an open system where exchange of Pb from multiple fluid events occurred (Kyser *et al*., 2000). White (type 1) and drusy quartz (type 2) fractures show elevated Pb isotope ratios (Figure 4.16) suggesting these fractures were possible avenues for fluid transport, allowing the migration of radiogenic Pb. Much of these fractures are coated with clay minerals that could have incorporated Pb during their crystallization or adsorbed radiogenic Pb from later fluids onto their surfaces. Stewardson Lake $^{206}Pb/^{204}Pb$ and $^{238}U/^{206}Pb$ values (Table 4.4) indicate migration of U and Pb into these fractures any time between 400 and 1700 Ma (Figure 4.16), supported by U mobilization in the basin at 1600-1700 Ma and remobilization at *ca*. 900 and <400 Ma (Kyser *et al*., 2000). Many fractures also have excess ^{206}Pb, which is not internally supported by U or Th, and could record the migration of late-stage fluids through sedimentary basins that host U mineralization (Holk *et al*., 2003).

4.5.3 REE patterns

Fracture coatings can be divided into two distinct groups according to their REE patterns. These patterns reflect REEs that were mobilized by fluids that flowed through the fractures. The REEs in fractures tend to be hosted by mineral surfaces or phosphates because they are released during weak acid leaching, which does not attack most other minerals. Group 1 fracture coatings have variable REE concentrations (Figure 4.14a). They have LREE-enriched chondrite normalized patterns, $[HREE/LREE]_n$ values of <1, ranging from 0.03-0.23, and negative Eu anomalies. Such REE patterns are typical of background sandstone, the likely source of the REEs (Fayek and Kyser, 1997). Group 2 fractures have flat normalized REE patterns and record negative Eu anomalies (Figure 4.14c). These fractures have $[HREE/LREE]_n$ values ranging from

0.09-11.12, consistent with REE distributions intermediate between background sandstone and mineralization patterns (Fayek and Kyser, 1997; Mercadier *et al*., 2011). Although both groups show background signatures, one white (type 1) fracture (SL4F-015) at Stewardson Lake has a concave-down REE pattern and a $[HREE/LREE]_n$ value of ~1, which is typical of uraninite from unconformity-type U deposits in the Athabasca Basin (Mercadier *et al*., 2011), indicating a possible link to U mineralization. This pattern exhibits a negative Eu anomaly and has been proposed to result from the crystallization of LREE-rich APS minerals that decreases the integration of LREE into the U-oxide structure (Gaboreau *et al*., 2007).

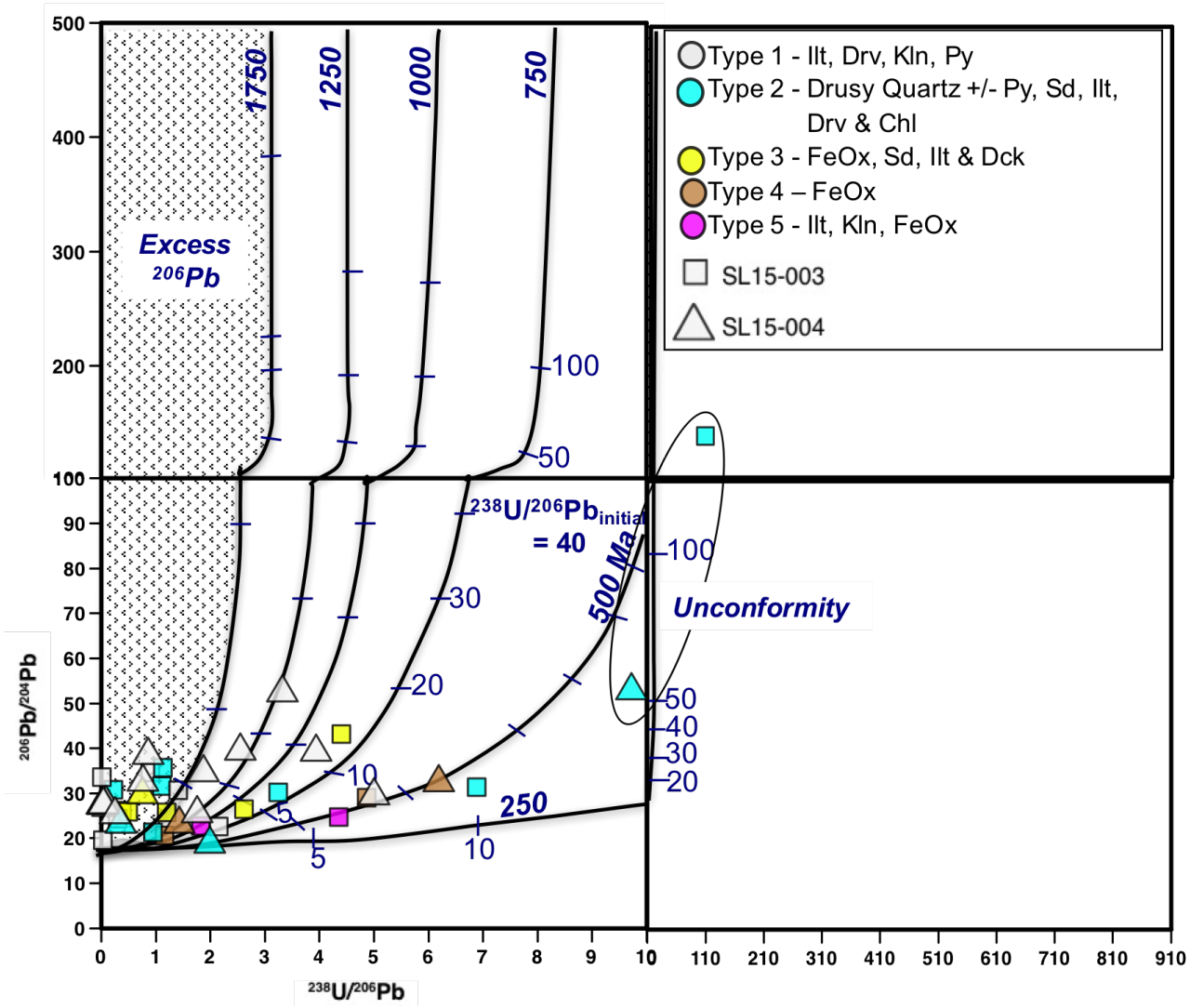

Figure 4.16: $^{206}Pb/^{204}Pb$ versus $^{238}U/^{206}Pb$ data from WAL of fractures. The lines show the closed system evolution of isotope ratios in uraninite with ages from 1750-250 Ma. The shaded area indicates samples that have ^{206}Pb contents in excess of the amount of leachable U in the sample. The isotope evolution curve shows the initial $^{238}U/^{206}Pb$ values of 10, 20, 30, 40, 50 and 100. Figure modified from Holk *et al.* (2003).

4.5.4 Origins of fluids recorded by fractures at Stewardson Lake

Comparison of the mineralogy and geochemistry of fracture coatings with their associated near-fracture samples from Stewardson Lake indicate fluid-rock interactions in both fracture coatings and the surrounding wall rock consistent with post-mineralization dispersion fluids that mobilized radiogenic Pb having low $^{207}Pb/^{206}Pb$ values of 0.09-0.49 from a U-rich source. In

some fractures, the fracture fill was subsequently replaced by minerals from a fluid with higher $^{207}Pb/^{206}Pb$ values of 0.50-0.82, but leaving a radiogenic Pb ratio in the near-fracture (Figure 4.13). This is especially evident for brown (type 4) and pink (type 5) fractures nearest the surface that are characterized by Fe oxides and clay minerals, including kaolinite, which are likely low-temperature minerals formed from meteoric waters (Figure 4.11), that migrated downward from the surface and variably overprinted earlier formed minerals that are preserved in the near-fracture. Figure 4.13 shows that pink (type 5) fracture coatings exhibit more of a common Pb ($^{207}Pb/^{206}Pb$ ~0.7) signature, compared to a brown (type 4) fracture coating that exhibits a radiogenic to common Pb signature ($^{207}Pb/^{206}Pb$ = 0.59-0.77) at the surface due accumulation of radiogenic Pb from post-mineralization dispersion. In summary, brown (type 4) and pink (type 5) fractures nearest the surface at Stewardson Lake can be used to detect post-mineralization dispersion of radiogenic Pb within the wall rock adjacent to the fracture. The timing of these events using $^{207}Pb/^{204}Pb$-$^{206}Pb/^{204}Pb$ model ages indicate ages of 1143 +/- 330 Ma for these fracture coatings and slightly older ages of 1401 +/- 110 Ma for the Stewardson Lake near-fractures.

White (type 1), drusy quartz (type 2), and white and yellow (type 3), fractures are rich in clay minerals that adsorb metal ions, including mobile pathfinder elements, restricting their movement elsewhere (Cameron *et al*., 2004). White (type 1) fractures are interpreted to likely show syn-mineralization dispersion of Co and Ni due to their high concentrations at depth (SL3F-036: Ni = 40.6 ppm, SL3F-039: Co = 109.7 ppm) and near the surface (SL3F-010: Ni = 101.8 ppm, SL3F-008: Co = 36.9 ppm). Brown (type 4) and pink (type 5) reflect low concentrations of pathfinder elements, including U, and common Pb, representing a background signature, which likely formed due to meteoric fluids from above. At the surface, the fracture samples show the highest $^{207}Pb/^{206}Pb$ values (0.71-0.82), indicating common Pb (Figure 4.9). Because the wall rock

shows a more radiogenic Pb signature (Figure 4.13) than the fracture coatings for fractures near the surface, this suggests that meteoric fluids contributed a high proportion of common Pb to the fractures.

Stewardson Lake fracture samples show very low $^{207}Pb/^{206}Pb$ values at depth near the unconformity and in the lower MFd at intermediate levels (~200-800 m; Figure 4.9) with variable U concentrations. Pathfinder elements are mainly enriched at ~200 m (Figure 4.15). The distribution of radiogenic Pb (Figure 4.9), enrichments of pathfinder elements, and variable U concentrations indicates post-mineralization dispersion of elements through permeable fractures into the overlying strata. Therefore, this suggests that these elements have been remobilized by later stages in the system.

From the five fracture types classified, white (type 1) is the most viable fracture type indicative of U mineralization because white fractures show the lowest $^{207}Pb/^{206}Pb$ values near the unconformity (0.34) and within the MFd (0.42-0.59; Figure 4.9) and U concentrations > 1, suggesting these fractures were the possible avenues for fluid transport, including the migration of radiogenic Pb and U. They also show elevated Co and Ni concentrations on fracture coatings near the surface (~100 m) and at depth (~800 m), suggesting syn-mineralization dispersion from a U-rich source (e.g. deposit). Lastly, a white fracture coating (SL4F-015) exhibits a chondrite normalized concave-down REE pattern suggestive of a uraninite signature of unconformity-related U deposits in the Athabasca Basin (Mercadier *et al*., 2011) at a depth of 256 m in the MFd.

The relationship between $^{207}Pb/^{206}Pb$ ratios and U concentrations (Table 4.3) should reflect whether syn- or post-mineralization dispersion processes have affected the fractures, depending on how open the system has been. Fluid events related to syn-mineralization and post-mineralization dispersion can be separated into three end members based on the concentration of

U and the $^{207}Pb/^{206}Pb$ values (Figure 4.17): (1) dispersion of radiogenic Pb without U, (2) primary/secondary dispersion of both U and Pb an open systems, and (3) secondary dispersion of U without Pb. Low U concentrations and low $^{207}Pb/^{206}Pb$ values reflect dispersion of radiogenic Pb without the U that produced it, or later removal of the U. High U concentrations and low $^{207}Pb/^{206}Pb$ ratios reflect primary or secondary dispersion of U and Pb in an open system at various times in the evolution of the fracture. High U concentrations and high $^{207}Pb/^{206}Pb$ values reflect recent mobilization of U without the radiogenic Pb that would have been produced by the decay of the U. Background Pb and U in the Athabasca Group sandstones is present on fracture coatings as variable but high $^{207}Pb/^{206}Pb$ values and low U concentrations (Figure 4.17). Using the relationship between Pb isotopes and U concentrations in the fractures and near-fractures, the processes involved and the significance of the fractures in the evolution of the basin can be better constrained.

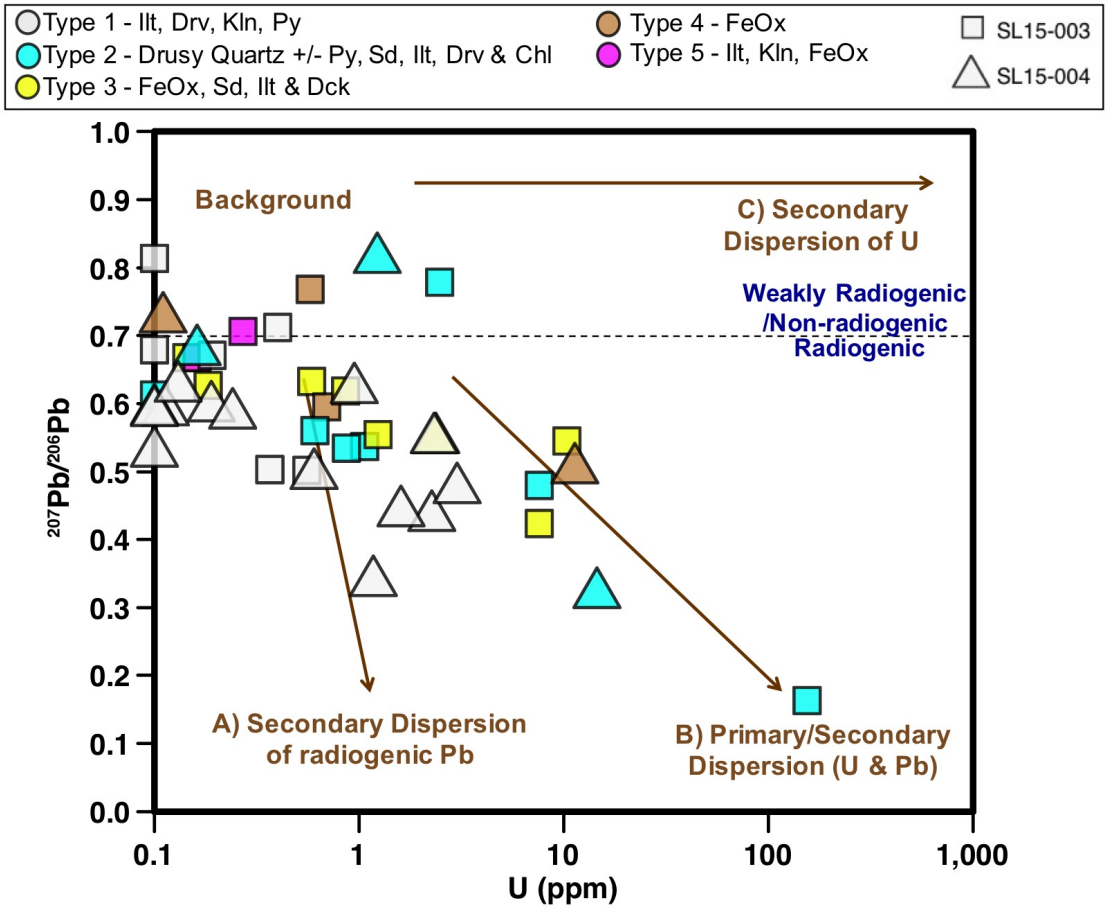

Figure 4.17: Relationship between $^{207}Pb/^{206}Pb$ ratios and U concentrations in fracture coatings showing the effect of syn-mineralization and post-mineralization dispersion processes from WAL data. The line at $^{207}Pb/^{206}Pb$ ratio of 0.7 divides weakly radiogenic/background from radiogenic Pb in the basin (Holk *et al.*, 2003).

4.5.5 Implications for surface exploration

Sampling and characterizing sandstone-hosted fractures can be a highly effective way to trace geochemical dispersion, as fractures act as conduits for the migration of fluids that extend all the way to the surface through about 1100 meters of Athabasca Group sandstone. Colors of the fractures reflect the mineralogy of the fracture fill and show initial evidence that fractures act as conduits for elements from the U occurence, recording primary and secondary dispersion.

However, the usefulness of each fracture type can vary due to differences in the fracture fill (Table 4.6). For example, white (type 1) fractures are most useful in terms of the higher concentration of many pathfinder elements, particularly Co, Ni and radiogenic Pb. This geochemical signature is evident near the surface and at depth through high concentrations of pathfinder elements and low $^{207}Pb/^{206}Pb$ values. These fractures extend from areas near high U concentrations to the near surface, allowing the migration of elements associated with the U mineralizing system from depth to shallow levels in the basin. In comparison, brown (type 4) and pink (type 5) fractures and their wall rock indicate post-mineralization dispersion of radiogenic Pb due to low $^{207}Pb/^{206}Pb$ values in the wall rock adjacent to the fracture surface and higher $^{207}Pb/^{206}Pb$ values on the fracture, reflecting multiple fluid events. Therefore, the source of anomalous U concentrations in the Stewardson Lake area could include the U occurence at depth.

Table 4.6: Fracture types, fracture mineralogy, sample distance to the Dufferin Lake fault (distal is > 760 m, intermediate is 360-760 m and proximal is < 360 m) and their usefulness for exploration, using a rating scale from 1 to 5 (1 = most useful and 5 = least useful).

Fracture Type	Fracture Mineralogy	Distance to Dufferin Lake Fault	Usefulness (1-5)
1 – White	illite, dravite, kaolinite, pyrite	distal to proximal	**1** - high As, Co, Cu, Mo, Ni, S, and radiogenic Pb; syn-mineralization dispersion of U, Pb, Co & Ni; REE uraninite signature of unconformity-related U deposits in the Athabasca Basin (SL4F-015)
2 – Drusy Quartz	drusy quartz +/- pyrite, siderite, illite, dravite, & chlorite	distal to proximal	**2** - high Co, Ni & S; syn-mineralization dispersion of U & Pb
3 – White & Yellow	FeOx, siderite, illite & dickite	intermediate to distal	**3** – high Ni & S; syn- & post-mineralization dispersion of U & Pb

4 – Brown	FeOx	distal	**4** - post-mineralization dispersion of radiogenic Pb in the fracture & wall rock
5 – Pink	illite, kaolinite & FeOx	distal	**5** - post-mineralization dispersion of radiogenic Pb in the fracture & wall rock

4.6 Conclusions

Based on the petrography and chemistry of fractures and their wall rocks from the Stewardson Lake unconformity-related U project, several conclusions about what fractures record and how these relate to element migration can be drawn:

1. During hydrothermal alteration associated with the mineralizing system, fluids likely precipitated dickite in white (type 1) and white and yellow (type 3) fractures and illite followed by drusy quartz (type 2) fractures and dravite. Late influx of meteoric fluids likely variably overprinted these minerals with Fe oxides and kaolinite in white and yellow (type 3), brown (type 4), and pink (type 5) fractures, suggesting that some fractures have had protracted fluid histories.
2. The sub-vertical orientation (<50°) of fractures allows permeable pathways for fluid movement in the basin from both above and below.
3. Measured $^{206}Pb/^{204}Pb$ and $^{207}Pb/^{204}Pb$ isotope values are elevated throughout the Manitou Falls Formation above the Stewardson Lake U occurence, consistent with post-mineralization dispersion of radiogenic Pb from a U-rich source (e.g. deposit).
4. White (type 1) fracture coatings containing pyrite and white clay, including illite, dravite and kaolinite are the most useful fracture type to detect U mineralization, as they show low $^{207}Pb/^{206}Pb$ values and elevated concentrations of Co and Ni near the surface and at depth, reflecting syn-mineralization dispersion from the Stewardson Lake U occurence. A white fracture (SL4F-015) also shows a uraninite signature of unconformity-related U

deposits in the Athabasca Basin through chondrite-normalized REEs. White (type 1) fractures show elevated $^{206}Pb/^{204}Pb$ and $^{207}Pb/^{204}Pb$ values and suggest they were possible avenues for fluid transport, allowing the migration of radiogenic Pb and thus, supporting their viability for U detection at depth.

5. By analyzing fractures and their adjacent wall rock from the Stewardson Lake U project, it can be recognized that brown (type 4) and pink (type 5) fractures near the surface can be used as an exploration technique to detect post-mineralization dispersion within the wall rock adjacent to the fracture through low $^{207}Pb/^{206}Pb$ values. Multiple fluid events have effected these fractures.

The mineral chemistry of fracture coatings, relative to that of the host rock, indicates that they can be used to detect syn-mineralization and post-mineralization dispersion of elements, including radiogenic Pb from U mineralization at depth (~1100 m) to intermediate levels near the surface (~200 m). The mineralogy and geochemistry of fractures indicates post-mineralization of pathfinder elements from the U occurence at depth. These results indicate that the footprint of the U occurence extends upwards, as the concentrated source diffuses outwards and the radiogenic Pb and U gradients diminish away from the occurence, through some fracture networks. Other fractures rich in Fe oxides near the surface show an influence of common Pb from above, likely by low temperature meteoric fluids. These effects tend to lessen with depth and distance to the mineralization, indicating the mineralization as the source of the anomalous values.

4.7 Acknowledgements

Funding for this project, including sample collection in the field, was provided and facilitated by in-kind support from Uravan Minerals Inc. Special thanks to Queen's Facility for

Isotope Research for providing analytical assistance and QFIR staff including, Donald Chipley,

Evelyne Leduc, Alexandre Voinot, April Vuletich, Agatha Dobosz and Christabel Jean.

References

Alexandre, P., Kyser, K., Jiricka, D. and Witt, G. 2012. Formation and evolution of the Centennial unconformity-related uranium deposit in the south-central Athabasca Basin, Canada. Economic Geology, 107(3), 385-400.

Baadsgaard, H., Cummino, G. L. and Worden, J. M. 1984. U-Pb geochronology of minerals from the Midwest uranium deposit, northern Saskatchewan. Canadian Journal of Earth Sciences, 21(6), 642-648.

Cameron, E.M., Hamilton, S.M., Leybourne, M.I., Hall, G.E.M., McClenaghan, M.B. 2004. Finding deeply buried deposits using geochemistry; Geochemistry: Exploration, Environments and Analysis. Vol. 4, p. 7-32.

Carr, S.D., Easton, R.M., Jamieson, R.A., Culshaw, N.G. and White, D.J. 2004. The Grenville Orogen of Ontario and New York—a Himalayan-scale mountain belt: Significance of along strike-variations: In: The Celebratory Conference, From Parameters to Processes—Revealing the Evolution of a Continent, October 12–15, 2004, Toronto, Program and Abstract, Lithoprobe Secretariat, University of British Columbia, Vancouver, British Columbia, Lithoprobe Report No. 86, 4 pp.

Ceyhan, M. 2009. World distribution of uranium deposits (UDEPO) with uranium deposit classification. IAEATECDOC-1629, Division of Nuclear Fuel Cycle.

Clark, L. A. 1987. Near-surface lithogeochemical halo as an aid to discovery of deeply buried unconformity-type uranium deposits, Athabasca Basin, Canada. Journal of Geochemical Exploration, 28(1-3), 71-84.

Cloutier, J., Kyser, K., Olivo, G. R., Alexandre, P. and Halaburda, J. 2009. The Millennium uranium deposit, Athabasca Basin, Saskatchewan, Canada: an atypical basement-hosted unconformity-related uranium deposit. Economic Geology, 104(6), 815-840.

Cuney, M. and Kyser, K. (Eds.). 2014. Recent and not-so-recent developments in uranium deposits and implications for exploration.

Derome, D., Cathelineau, M., Cuney, M., Fabre, C., Lhomme, T. and Banks, D. A. 2005. Mixing of sodic and calcic brines and uranium deposition at McArthur River, Saskatchewan, Canada: a Raman and laser-induced breakdown spectroscopic study of fluid inclusions. Economic Geology, 100(8), 1529-1545.

Dyck, W. 1978. The mobility and concentration of uranium and its decay products in temperate surficial environments. Uranium deposits, their mineralogy and origin. Mineralogical Association of Canada Short Course Handbook, 3.

Earle, S. 1997. MINSPEC3 program for estimation of clay contents in Athabasca Group sandstones from reflectance spectral data. Internal Report, Grasswood Geosciences.

Earle, S., Wheatley, K. and Wasyliuk, K. 1999. Application of reflectance spectrometry to assessment of alteration mineralogy at the Key Lake uranium deposit, Saskatchewan.

Ey, F., Piquard, J. P., Baudemont, D. and Zimmerman, J. 1992. The sue uranium deposits, Saskatchewan, Canada (No. IAEA-TECDOC--650).

Faure, G. 1977. Principles of isotope geology.

Fayek, M. and Kyser, T.K. 1997. Characterization of multiple fluid-flow events and rare-earth-element mobility associated with formation of unconformity-type uranium deposits in the Athabasca Basin, Saskatchewan: The Canadian Mineralogist, v. 35, p. 627-658.

Gaboreau, S., Cuney, M., Quirt, D., Patrier, P., and Mathieu, R. 2007. Significance of aluminum phosphate-sulfate minerals associated with U unconformity-type deposits: The Athabasca basin, Canada. American Mineralogist, 92(2-3), 267-280.

Gustafson, L. B. and Curtis, L. W. 1983. Post-Kombolgie metasomatism at Jabiluka, Northern Territory, Australia, and its significance in the formation of high-grade uranium mineralization in lower Proterozoic rocks. Economic Geology, 78(1), 26-56.

Halter, G., Pagel, M., Sheppard, S. M. F. and Weber, F. 1989. Alterations in the Carswell structure (Saskatchewan, Canada): Petrology, mineralogy and stable isotopes geochemistry (No. IAEA-TECDOC--500).

Hiatt, E. E. and Kyser, T. K. 2007. Sequence stratigraphy, hydrostratigraphy, and mineralizing fluid flow in the Proterozoic Manitou Falls Formation, eastern Athabasca Basin, Saskatchewan. BULLETIN-GEOLOGICAL SURVEY OF CANADA, 588, 489.

Hoeve, J. and Sibbald, T. I. 1978. On the genesis of Rabbit Lake and other unconformity-type uranium deposits in northern Saskatchewan, Canada. Economic Geology, 73(8), 1450-1473.

Hoeve, J. and Quirt, D. H. 1984. Mineralization and host rock alteration in relation to clay mineral diagenesis and evolution of the Middle-Proterozoic, Athabasca Basin, northern Saskatchewan, Canada.

Hoffman, P. F. 1988. United Plates of America, the birth of a craton-Early Proterozoic assembly and growth of Laurentia. Annual Review of Earth and Planetary Sciences, 16, 543-603.

Holk, G.J., Kyser, T.K., Chipley, D., Hiatt, E.E. and Marlatt, J. 2003. Mobile Pb-isotopes in Proterozoic sedimentary basins as guides for exploration of uranium deposits: Journal of Geochemical Exploration, v. 80, p. 297-320.

International Atomic Energy Agency. 2009. World distribution of uranium deposits (UDEPO), with uranium deposit classification: IAEA-TECDOC-1629, Vienna, 117 p.

Kotzer, T.G. and Kyser, T.K. 1993. O, U, and Pb isotopic and chemical variations in uraninite: implications for determining the tempo-ral and fluid history of ancient terrains. American Mineralogist 78, 1262–1274.

Kotzer, T. G. and Kyser, T. K. 1995. Petrogenesis of the Proterozoic Athabasca Basin, northern Saskatchewan, Canada, and its relation to diagenesis, hydrothermal uranium mineralization and paleohydrogeology. Chemical Geology, 120(1), 45-89.

Kyser, K., Hiatt, E., Renac, C., Durocher, K., Holk, G. and Deckart, K. 2000. Diagenetic fluids in Paleo-and Meso-Proterozoic sedimentary basins and their implications for long protracted fluid histories: Fluids and basin evolution: Mineralogical Association of Canada Short Course, v. 28, p. 225-262.

Laverret, E., Mas, P. P., Beaufort, D., Kister, P., Quirt, D., Bruneton, P. and Clauer, N. 2006. Mineralogy and geochemistry of the host-rock alterations associated with the Shea Creek unconformity-type uranium deposits (Athabasca Basin, Saskatchewan, Canada). Part 1. Spatial variation of illite properties. Clays and Clay Minerals, 54(3), 275-294.

LeCheminant, A. N. and Heaman, L. M. 1989. Mackenzie igneous events, Canada: Middle Proterozoic hotspot magmatism associated with ocean opening. Earth and Planetary Science Letters, 96(1-2), 38-48.

Leppin, M. and Goldak, D. 2005. Mapping deep sandstone alteration and basement conductors utilizing audio magnetotellurics: exploration for uranium in the Virgin River area, Athabasca basin, Saskatchewan, Canada. In 2005 SEG Annual Meeting. Society of Exploration Geophysicists.

Lewry, J.F. and Sibbald, T.I. 1980. Thermotectonic evolution of the Churchill Province in northern Saskatchewan: Tectonophysics, v. 68, p. 45-82.

Marlatt, J., McGill, B., Matthews, R., Sopuck, V. and Pollock, G. 1992. The discovery of the McArthur River uranium deposit, Saskatchewan, Canada (No. IAEA-TECDOC--650).

McQueen, K. G. 2005. Ore deposit types and their primary expressions. Regolith Expression of Australian Ore Systems. CRC LEME, Perth, website: http://www. crcleme. org. au/Pubs/Monographs/RegExpOre. html [Last accessed January 2013.].

Mercadier, J., Cuney, M., Lach, P., Boiron, M. C., Bonhoure, J., Richard, A., Leisen, M., and Kister, P. 2011. Origin of uranium deposits revealed by their rare earth element signature. Terra Nova, 23(4), 264-269.

McLelland, J., Daly, J. S. and McLelland, J. M. 1996. The Grenville orogenic cycle (ca. 1350-1000 Ma): an Adirondack perspective. Tectonophysics, 265(1-2), 1-28.

Nakamura, N. 1974. Determination of REE, Ba, Fe, Mg, Na and K in carbonaceous and ordinary chondrites. Geochimica et Cosmochimica Acta, 38(5), 757-775.

Ng, R., Alexandre, P. and Kyser, K. 2013. Mineralogical and geochemical evolution of the unconformity-related McArthur River Zone 4 Orebody in the Athabasca Basin, Canada: implications of a silicified zone. Economic Geology, 108(7), 1657-1689.

Pagel, M., Poty, B. and Sheppard, S. M. F. 1980. Contribution to some Saskatchewan uranium deposits mainly from fluid inclusion and isotopic data. In Uranium in the Pine Creek Geosyncline.

Percival, J. B., Bell, K. and Torrance, J. K. 1993. Clay mineralogy and isotope geochemistry of the alteration halo at the Cigar Lake uranium deposit. Canadian Journal of Earth Sciences, 30(4), 689-704.

Ramaekers, P., Christopher, J.E., and MacDonald, R. 1979. Stratigraphy of the Athabasca Basin; in Summary of Investigations 1979; Saskatchewan Geological Survey; Saskatchewan Mineral Resources, Miscellaneous Report 79-10, p. 154–160.

Ramaekers, P., Christopher, J.E., and MacDonald, R. 1980. Stratigraphy and tectonic history of the Athabasca Group (Helikian) of northern Saskatchewan; in Summary of Investigations 1980; Saskatchewan Geological Survey, Saskatchewan Mineral Resources, Miscellaneous Report 80-4, p. 99–106.

Ramaekers, P. 1990. Geological Maps of the Athabasca Group (Helikian) in Northern Saskatchewan. Saskatchewan Energy and Mines, Saskatchewan Geology Survey.

Ramaekers, P. and Catuneanu, O. 2004. Development and sequences of the Athabasca basin, early Proterozoic, Saskatchewan and Alberta, Canada. The Precambrian Earth: Tempos and Events. Developments in Precambrian Geology, 12, 705-723.

Ramaekers, P., Yeo, G. M., Jefferson, C. W., Collier, B., Long, D. G. F., Catuneanu, O., Bernier, S., Kupsch, B., Post, R., Drever, G., McHardy, S., Jiricka, D., Cutts, C. and Wheatley, K. 2007. Revised geological map and stratigraphy of the Athabasca Group, Saskatchewan and Alberta. Bulletin-Geological Survey of Canada, 588, 155.

Rivers, T. 1997. Lithotectonic elements of the Grenville Province: review and tectonic implications. Precambrian Research, 86(3-4), 117-154.

Stacey, J. T. and Kramers, 1. 1975. Approximation of terrestrial lead isotope evolution by a two-stage model. Earth and planetary science letters, 26(2), 207-221.

Stewardson Lake, Uravan Minerals Inc. 2017. Retrieved from

http://www.uravanminerals.com/properties/outer_ring_project/

Uravan Minerals Inc. 2014. Uravan Completes Stewardson Drill Program. (online) Available at: http://www.uravanminerals.com/_resources/news/PR_100614.pdf (Accessed 27 Aug. 2017).

Uravan Minerals Inc. 2017. Update - Stewardson Project. (online) Available at: http://www.uravanminerals.com/_resources/news/nr_2017_02_09.pdf (Accessed 27 Aug. 2017).

Wallis, R. H., Saracoglu, N., Brummer, J. J., and Golightly, J. P. 1985. The geology of the McClean uranium deposits, northern Saskatchewan; in Sibbald, T.I.I. and Petruk, W. (eds.), Geology of Uranium Deposits, CIM Spec. Vol. 32, p101-131.

Whitney, D. L. and Evans, B. W. 2010. Abbreviations for names of rock-forming minerals. American mineralogist, 95(1), 185.

Wilde, A. R., Mernagh, T. P., Bloom, M. S. and Hoffmann, C. F. 1989. Fluid inclusion evidence on the origin of some Australian unconformity-related uranium deposits. Economic Geology, 84(6), 1627-1642.

Wilson, M. R. and Kyser, T. K. 1987. Stable isotope geochemistry of alteration associated with the Key Lake uranium deposit, Canada. Economic Geology, 82(6), 1540-1557.

Yeo, G., Jefferson, C. W. and Ramaekers, P. 2002. A preliminary comparison of Mantiou Falls Formation stratigraphy in Four Athabasca Basin Deposystems. Summary of Investigations, 2, 2002-4.

Chapter 5

General Discussion

5.1 General conclusions and exploration implications

Fracture coatings and their wall rocks preserve syn-mineralization and post-mineralization dispersion and therefore can be used to detect U mineralization at depth. Colors of the fractures reflect the mineralogy of the fracture fill and show initial evidence that fractures act as conduits for the migration of elements from U mineralization to the surface, recording primary and secondary dispersion. However, the usefulness of each fracture type can vary due to differences in the fracture fill. The most useful fractures include brown (Mn oxides, Fe oxides (goethite and hematite) and +/- kaolinite, illite, dravite) and white and yellow (Fe oxides (goethite) and dravite, kaolinite, illite) fractures at the McArthur River U deposit and white (illite, dravite, kaolinite, pyrite) fractures at the Stewardson Lake U project. For example, white fractures are most useful in detecting U deposition at Stewardson Lake due to low $^{207}Pb/^{206}Pb$ ratios concentrations at intermediate levels and at depth, as well as elevated concentrations of Co and Ni from depth to surface, reflecting syn-mineralization dispersion. At McArthur River, brown fractures are a viable fracture type reflecting post-mineralization dispersion due to high concentrations of Co, Mn, Tl, and Ba, low $^{207}Pb/^{206}Pb$ ratios near the surface and at depth, but not intermediate, and an abundance of chondrite normalized REEs showing a uraninite signature similar to an unconformity-related U deposit in the Athabasca Basin (Figure 3.5c). Analysis of O and H stable isotopes at McArthur River aid in establishing the type of fluids from which the fracture coating minerals formed. These results indicate that the footprint of the deposit extends upwards by hydrothermal fluids at high-temperatures, represented by dominantly white and yellow fracture types rich in fibrous goethite. This indicates that the mineralization is the source of the

anomalous values of U, V, and radiogenic Pb within these white and yellow fractures, reflecting syn-mineralization dispersion. CL-ICP-MS data indicates that minerals within brown and white and yellow fractures at McArthur River, including Fe oxy-hydroxides and clays are associated with radiogenic Pb, Ni and V released during the 30% HNO_3 leach phase, reflecting syn-mineralization and post-mineralization dispersion of U and radiogenic Pb. The sequential leach analysis carried out by Devine *et al*. (2016), confirms the Fe oxy-hydroxide association with radiogenic decay products on fracture coatings, especially for fractures near the surface showing a radiogenic Pb signature. The CL-ICP-MS method applied to fracture coatings is a useful exploration tool as it identifies suites of mobile elements on paragenetically-constrained substrates into distal fracture networks related to a deposit.

A non-prospective fracture type is pink composed of illite, kaolinite, and Fe oxide at both McArthur River and Stewardson Lake. Pink fractures are least likely to detect U mineralization due to high $^{207}Pb/^{206}Pb$ ratios, low concentrations of pathfinder elements similar to background values, as well as LREE-enriched chondrite normalized REE patterns (Figure 3.5a) and HREE/LREE ratios (<1), indicative of background sandstone in the Athabasca Basin. Analysis of O and H stable isotopes at McArthur River indicate that pink fractures were formed by a downward migration of elements in low-temperature meteoric fluids from above. The CL-ICP-MS method was useful in recognizing which pathfinder elements are hosted in a mineral phase for that specific fracture, despite the extensive and complex data analysis. For example, common Pb was released from mineral surfaces on pink fractures during H_2O extraction and is linked to surficial processes.

Post-mineralization dispersion processes are also observed on dark fractures near the surface including, brown and pink fractures and their adjacent wall rock at both McArthur River and Stewardson Lake, showing low $^{207}Pb/^{206}Pb$ ratios on the wall rock and higher $^{207}Pb/^{206}Pb$

ratios on the fracture surface. Mineralogical zoning from the fracture into the wall rock reflects multiple fluid events that have affected both the fracture and the wall rock and more recent fluids have either replaced or overprinted earlier formed minerals on the fractures. Therefore, despite the influence of meteoric fluids from above that cause a less radiogenic signature on some fracture coatings (high $^{207}Pb/^{206}Pb$ ratios), the footprint of the occurence is observed within the wall rock as it extends upwards through some fracture networks both during and after U mineralization at Stewardson Lake and can be detectable in overlying surficial media from till at the McArthur River area, reflecting the protracted fluid history of the Athabasca basin. Because this trend occurs at both the McArthur River U deposit and the Stewardson Lake U project, brown and pink fracture types can be used as an exploration technique to detect U mineralization within the wall rock of fractures elsewhere in the Athabasca Basin and could possibly be applied to other types of deposits. Thus, it is important to use caution when dealing with fracture coatings.

Potential exploration challenges include accessing several historic drill holes at a U exploration project to fully characterize the fractures. Additionally, fractures need to possess certain characteristics in order to be prospective, including a steeply-dipping orientation with an open face to subsequently produce a high fracture permeability, allowing the migration of hydrothermal fluids. The silicified zone at McArthur River can cause obstruction of these fractures, decreasing their permeability and likelihood of adsorbing mobile pathfinder elements from U mineralization.

5.2 Conclusions

Brown and white and yellow fractures are the most viable fracture types that can be used, through their mineral chemistry, as an exploration technique to detect U mineralization at depth.

Both fracture types have Fe oxides in common, including goethite, that make up most these fracture coatings. The fractures typically reflect post-mineralization dispersion of radiogenic Pb, as many fractures have low concentrations of U and low $^{207}Pb/^{206}Pb$ ratios. The footprint of the deposit extends upwards through fractures, including white and yellow fractures rich in fibrous goethite, by hydrothermal fluids, as shown by higher $\delta^{18}O$ and $\delta^{2}H$ values. CL-ICP-MS also shows an association between Ni, V, and radiogenic Pb with Fe oxide and clay minerals during the 30% HNO_3 leach phase for these fracture types.

It is important to be aware of relatively recent meteoric fluids from above. These fluids can erase the radiogenic Pb signature on the fractures themselves causing an abundance of common Pb (high $^{207}Pb/^{206}Pb$ ratios). Some fractures, including those composed of botryoidal goethite (brown fractures from McArthur River) are associated with organic material and meteoric fluids, as shown by lower $\delta^{18}O$ and $\delta^{2}H$ values. CL-ICP-MS also shows an association between common Pb, Co, and V with organic material during the 10% H_2O_2 leach phase.

The mineral chemistry of seven fracture types from McArthur River and five fracture types from Stewardson Lake, relative to the host rock indicates that, although multiple fluid events have affected some fractures, they still preserve evidence of syn-mineralization and post-mineralization dispersion of elements, including radiogenic Pb from a U-rich source at depth. At McArthur River, there is also evidence of syn-mineralization and post-mineralization at the surface, but not intermediate depths because of a silicified zone. The mineralogy and geochemistry of McArthur River fractures indicate syn- and post-mineralization of pathfinder elements from the deposit at depth, but also evidence of a downward migration of elements from surface. These results indicate that the footprint of the McArthur River U deposit and the Stewardson Lake U occurence is concentrated at depth, exhibited in deep fractures proximal to the P2 fault and the Dufferin Lake fault, but also is detectable in the overlying surficial media,

shown by surficial fractures at McArthur River.

5.3 Future research

Geochemical exploration involves plenty of difficulties that have been highlighted throughout this thesis. They include: which pathfinder elements migrate to the surface, what are the processes involved in element migration, which fractures are most useful for surface exploration, and whether the mineralogy and geochemistry of fracture coatings and their wall rock can be used as an exploration technique, in other prospective areas, to detect U at depth through syn-mineralization and post-mineralization dispersion. Further research can be conducted to compliment the research presented here:

- Additional analysis is needed on the near-fracture surface, adjacent to the fracture. This includes WAL extraction on the remaining near-fracture samples and further comparison to the fracture coating WAL data to identify and confirm dispersion processes. The level of alteration from the fracture surface to the near-fracture surface can also be compared to this new near-fracture dataset to identify suites of mobile elements, especially radiogenic Pb. CL-ICP-MS could also be conducted on the near-fracture samples to identify which mineral phases are hosting pathfinder elements.
- Additional stable isotope analyses on a greater spectrum of fracture coating minerals would aid in further discriminating between crystal chemistry characteristics relating to high-temperature and low-temperature systems.
- Additional fractures and their wall rocks could be collected from other deposit types to determine if the mineralogy and geochemistry of fractures and their wall

rocks can be used as an exploration technique for other types of deposits and geological settings.